Identification of Low-wavenumber Wall Pressure Field beneath a Turbulent Boundary Layer

by

Seyedhesamaldin Abtahi

under the supervision of

Dr. Mahmoud Karimi (principal supervisor)
A/Prof. Laurent Maxit (co-supervisor)
Prof. Ray Kirby (co-supervisor)

A thesis submitted in total fulfillment for the degree of Doctor of Philosophy

in the
Centre for Audio, Acoustics and Vibration
School of Mechanical and Mechatronic Engineering
Faculty of Engineering and Information Technology
The University of Technology Sydney

Submission date: 03 February 2025

Certificate of Original Authorship

I, Seyedhesamaldin Abtahi, declare that this thesis is submitted in fulfilment of the requirements for the award of Doctor of Philosophy (C02018), in the School of Mechanical and Mechatronic Engineering at the University of Technology Sydney.

This thesis is wholly my own work unless otherwise referenced or acknowledged. In addition, I certify that all information sources and literature used are indicated in the thesis.

This document has not been submitted for qualifications at any other academic institution.

This research is supported by the Australian Government Research Training Program.

Signed: Production Note: Signature removed prior to publication.

Date: 03/02/2025

Abstract

A turbulent boundary layer (TBL), which occurs when a fluid flows over a surface of a structure at a sufficient speed, can generate pressure fluctuations over the surface, subsequently imposing a wall pressure field (WPF) on the structure that causes vibrations. The spectrum of the WPF in a TBL consists of acoustic and hydrodynamic domains. The hydrodynamic domain is also divided into sub-convective, convective, and viscous regions. At high Mach number flow, the convective region of the WPF significantly contributes to the structural vibrations. However, at low Mach number flow the structure effectively filters out the convective domain and the bending waves of the structure aligns with the low-wavenumber domain of the WPF. Consequently, the primary cause of vibration would be the low-wavenumber components of the WPF. Therefore, accurate estimation of the WPF in the low-wavenumber domain is crucial for understanding and predicting the flow-induced vibrations of structures. Existing TBL WPF models accurately predict the convective region but show significant discrepancies in predicting low-wavenumber levels. This thesis numerically investigates the feasibility of estimating the low-wavenumber WPF using a microphone array (acoustic-based approach) and an accelerometer array (vibration-based approach).

Initially, the key factors in the arrangement of microphones for the WPF estimation are examined, and the challenges of the acoustic approach in estimating the low-wavenumber WPF are highlighted. Subsequently, an inverse vibration method is proposed for the WPF estimation in the low-wavenumber domain, focusing on the critical factors for accurate WPF estimation. In both approaches, a known TBL WPF is used as the input, and the estimated WPF obtained using the microphone or accelerometer arrays is compared with the reference WPF of the input TBL model. To mimic experimental measurements, a virtual experiment is proposed for both approaches, involving the synthesis of snapshots of the WPF. The impact of the number of realizations on the accurate estimation of the low-wavenumber WPF is also studied.

Finally, two methods namely the modal expansion and reciprocity principle for calculating the sensitivity functions, which are needed for vibration based approach, are examined. The modal expansion method requires accurate extraction of the modal properties of the structure to compute the sensitivity functions, while the reciprocity principle method relies on measuring the vibrational response of the structure when excited at specific points where the measurement sensors are located. Experimental investigations have been conducted to illustrate the challenges and effectiveness of each method in computing the sensitivity functions. The results show that both methods are effective and are in good agreement.

List of Publications

Most of the work presented in this thesis has been published or submitted for publication in journals and conference proceedings. The following list of articles includes works that have been completed during the time-frame of the thesis:

Journal publications

1. **Hesam Abtahi**, Mahmoud Karimi, and Laurent Maxit. "On the challenges of estimating the low-wavenumber wall pressure field beneath a turbulent boundary layer using a microphone array". In: *Journal of Sound and Vibration* 574. 2024.

2. **Hesam Abtahi**, Mahmoud Karimi, and Laurent Maxit. "Identification of low-wavenumber wall pressure field beneath a turbulent boundary layer using vibration data". In: *Journal of Fluids and Structures* 127:104135. 2024.

Peer-reviewed conference proceedings

1. **Hesam Abtahi**, Mahmoud Karimi, and Laurent Maxit. "Numerical study on the estimation of the low-wavenumber wall pressure field using vibration data". In: *Inter-Noise 2023*. Chiba, Japan, 20-23 August 2023.

2. **Hesam Abtahi**, Mahmoud Karimi, and Laurent Maxit. "Estimation of the low-wavenumber component of turbulent boundary layer pressure field using vibration data". In: *Acoustics 2023 Sydney*. Sydney, Australia, 4-8 December 2023.

3. **Hesam Abtahi**, Mahmoud Karimi, and Laurent Maxit. "A vibration-based method to estimate the low-wavenumber wall pressure field in a turbulent boundary layer". In: *Inter-Noise 2024*. Nantes, France, 25-29 August 2024.

Acknowledgements

The completion of my thesis marks the end of a research journey enriched by the continual support and guidance of individuals both within and outside of academia. I am deeply grateful to all those who have contributed to shaping both my work and personal life, enabling me to excel in academic research.

The intersection between work and personal life has allowed me to regard my supervisors and colleagues as companions beyond the confines of work. First and foremost, I am especially thankful to my principal supervisor, Dr. Mahmoud Karimi, for giving me the opportunity to conduct this research under his expert guidance. His unwavering support, insightful advice, and engaging scholarly discussions have significantly shaped my research journey and deepened my understanding of fluid-induced vibration. I would also like to acknowledge his enthusiasm for celebrating milestones and organizing social gatherings within our research group.

I extend my heartfelt gratitude to my co-supervisors, A/Prof. Laurent Maxit and Prof. Ray Kirby, for their invaluable insights. Each has taught me unique nuances of research that, when combined, have provided a robust approach to academic investigation. I also thank my colleagues, Mr. Yaser Jazayeri Moghadas, Drs. Shahrokh Sepehrirahnama, Qiaoxi Zhu, and Paul Williams, for their assistance in setting up and conducting experiments.

A special acknowledgment goes to the University of Technology Sydney for their generous support through the UTS President's Scholarship and the International Research Scholarship, which have enabled me to pursue my PhD at this esteemed institution. I am equally grateful to the School of Mechanical and Mechatronic Engineering for their financial support through the MME fund, which facilitated my participation in two significant international conferences: Inter-Noise 2023 in Chiba, Japan, and Inter-Noise 2024 in Nantes, France.

Beyond academia, my personal life has been steadfastly supported by my partner, Negin. Her love and encouragement have ensured that I maintained the focus necessary for such an extensive research project. Her emotional support and belief in me have enabled me to give my best to my work, while also preparing us for financial autonomy and social responsibilities.

Seyedhesamaldin Abtahi
February 2025
Sydney, Australia

Contents

List of Figures

List of Tables

Abbreviations

2D	**T**wo-**D**imensional
3D	**T**hree-**D**imensional
ABA	**A**coustic-**B**ased **A**pproach
AFM	**A**ccelerated **F**orcing **F**unction
ASD	**A**uto **S**spectral **D**ensity
CAAV	**C**entre for **A**udio, **A**coustics, and **V**ibration
CFD	**C**omputational **F**luid **D**ynamics
CMIF	**C**omplex **M**ode **I**ndicator **F**unction
CPU	**C**entral **P**rocessing **U**nit
CSD	**C**ross **S**pectral **D**ensity
CSM	**C**ross **S**pectral **M**atrix
DAF	**D**iffuse **A**cousic **F**ield
DNI	**D**irect **N**umerical **I**ntegration
DNS	**D**irect **N**umerical **S**imulations
DOF	**D**egree **O**f **F**reedom
eFRF	**e**nhanced **F**requency **R**esponse **F**unction
FAT	**F**orce **A**nalysis **T**echnique
FEM	**F**inite **E**lement **M**ethod
FRF	**F**requency **R**esponse **F**unction
GCV	**G**eneralized **C**ross **V**alidation
IFT	**I**nverse **F**ourier **T**ransform
LDV	**L**aser **D**oppler **V**ibrometer
LES	**L**arge **E**ddy **S**imulation
MAE	**M**ean **A**bsolute **E**rror
MIMO	**M**ultiple **I**nput **M**ultiple **O**utput

PDF	**P**robability **D**ensity **F**unction
PSF	**P**oint **S**pread **F**unction
RANS	**R**eynolds **A**veraged **N**ervier-stokes **S**imulation
RFBA	**R**egularized **F**ourier **B**ased **A**pproach
RFP	**R**ational **F**raction **P**olynomial
SEA	**S**tatistical **E**nergy **A**nalysis
SIMO	**S**ingle **I**nput **M**ultiple **O**utput
SR	**S**caling **R**atio
SV	**S**ingular **V**alue
SVD	**S**ingular **V**alue **D**ecomposition
TBL	**T**urbulent **B**oundary **L**ayer
TGSVD	**T**runcated **G**eneralized **S**ingular **V**alue **D**ecomposition
UTS	**U**niversity of **T**echnology **S**ydney
UWPW	**U**ncorrelated **W**all **P**lane **W**ave
VBA	**V**ibration-**B**ased **A**pproach
WPF	**W**all **P**ressure **F**ield

Symbols

A_r	r^{th} residue matrix
a	array dimension along x-axis
b	array dimension along y-axis
c_0	sound speed
c_f	bending wave speed
D	flexural rigidity of the plate
$\mathrm{e}^{(x)}$	exponential function
E	Young's modulus
f	frequency
f_c	coincidence frequency
f_e	critical frequency
F	co-array factor
F_{mn}	modal force
G_{pp}	space-time correlation function
h	thickness of the plate
h_γ	acceleration impulse response
H_γ	sensitivity function
j	imaginary unit
k_0	acoustic wavenumber
k_c	convective wavenumber
k_f	flexural wavenumber of a plate
$\mathbf{k}$	wavenumber vector (k_x, k_y)
$\bar{\mathbf{k}}$	normalized wavenumber vector $(\bar{k}_x, \bar{k}_y)$
L	modal participation factor matrix
L_x	length of the plate

L_y	width of the plate
M	cut-off modal orders along x-axis
M_a	Much number
M_b	maximum mode number of plate along x-axis below the excitation frequency
N	cut-off modal orders along y-axis
N_0	number of response points
N_b	maximum mode number of plate along y-axis below the excitation frequency
N_f	number of discrete frequencies
N_i	number of excitation points
N_k	number of wavenumbers
$N_{k_{LW}}$	number of wavenumbers in the low-wavenumber domain
N_R	number of realizations
N_s	number of sensors
p	pressure
P	number of unique vector spacings
$P_{\max}$	maximum number of spacings
Q_r	scaling factor for r^{th} mode
R_{pp}	space-frequency correlation function of pressure field
$R_{\gamma\gamma}$	cross-correlation function of acceleration
Re	Reynolds number
Re_θ	momentum Reynolds number
$S_{\gamma\gamma}$	cross-spectrum of panel acceleration
$\mathbf{S}, \bar{\mathbf{S}}$	vector of cross-spectrum elements
Sh	Strouhal number
t	time
u_k	unscaled mode shape for k^{th} repeated root
u_τ	friction velocity
U	left singular matrix
U_c	convective velocity
U_e	boundary layer edge velocity
U_∞	free stream velocity
V	right singular matrix
$\mathbf{x}, \mathbf{x}', \tilde{\mathbf{x}}, \tilde{\tilde{\mathbf{x}}}$	points in (x, y, z)

Y	FRF matrix
(x, y, z)	rectangular or Cartesian coordinates
$*$	complex conjugate
$\dagger$	pseudo-inverse
α_x, α_y	exponential decay coefficients
δ	turbulent boundary layer thickness
δ^*	turbulent boundary layer displacement thickness
δk_x	streamwise wavenumber resolution
δk_y	spanwise wavenumber resolution
δ_x	spatial resolution along x-axis
δ_y	spatial resolution along y-axis
$\hbar$	FRF data
λ_b	flexural wavelength of a plate
π	Archimedes' constant
ρ	density
ρ_s	density of the plate
μ	mean value
μ_f	dynamic viscosity
ν	kinematic viscosity
ν_k	equivalent mode participation factor for k^{th} repeated root
ν_p	Poisson's ratio
γ	acceleration of plate
σ	singular value matrix
Σ_p	surface of plate
ϕ_{pp}	cross-spectrum of pressure field
ϕ_{pp}^e	estimated cross-spectrum of pressure field
ϕ_{pp}^r	reference cross-spectrum of pressure field
$\tilde{\phi}_{pp}, \bar{\phi}_{pp}$	normalized cross-spectrum of pressure field
$\Phi_{pp}, \bar{\Phi}_{pp}$	vector of cross-spectrum of wall pressure elements
φ	mode shape functions
ψ	modal force
Ψ_{pp}	auto-spectrum of pressure field

Ψ_s	vibration modal response
Ξ	mode shapes matrix
ξ	distance between two points along x-axis
η	distance between two points along y-axis
η_s	structural loss factor
τ	time lag
τ_w	wall shear stress
θ	random phase
ϑ	eigenvalue of FRF matrix
λ_b	flexural wavelength of plate
λ_r	system pole value of r^{th} mode
Ω	modal mass
Γ	coherence
ω	angular frequency

Chapter 1

Introduction

The interaction of fluid flows with structures generates noise and vibrations which has significant implications in many mechanical applications, including the vibration and noise produced in water transport pipelines, aircraft cabin noise, and in automobiles [29–31]. Different internal and external forces can cause a structure to vibrate and radiate noise. A turbulent boundary layer (TBL), which occurs when a fluid flows over a surface at a sufficient speed, can generate pressure fluctuations over the surface, subsequently imposing an unsteady load on the structure that leads to noise and vibrations. These flow-induced vibrations might lead to structural fatigue, flutter and aeroelastic instability, compromising the integrity and longevity of the structures. Moreover, the noise generated by these vibrations can propagate away from the structure, affecting the surrounding environment. This radiated noise can impact acoustic comfort in inhabited areas and reduce the overall environmental quality. For example, in aircraft, such noise can affect passenger comfort. Therefore, understanding how structures react to TBL excitations is crucial for developing effective design strategies. By gaining insight into fluid-structure interactions, engineers can devise methods to minimize flow-induced vibrations. This can lead to designs that enhance structural integrity, reduce maintenance costs, and improve acoustic comfort and environmental quality.

The development of turbulent flow on a semi-infinite flat plate has been shown in Figure 1.1. The no-slip condition at the wall, slows down a fluid particle very close to the wall. This means that any disturbance will push the particle away from the wall and cause it to collide with particles travelling at a higher speed. In the absence of significant viscous forces to damp these motions, collisions result in more collisions, and ultimately leading to the random disturbances that are characteristic of the turbulent boundary layer [98]. In this case, the TBL generates a wall pressure field (WPF) over the surface which results noise and vibrations.

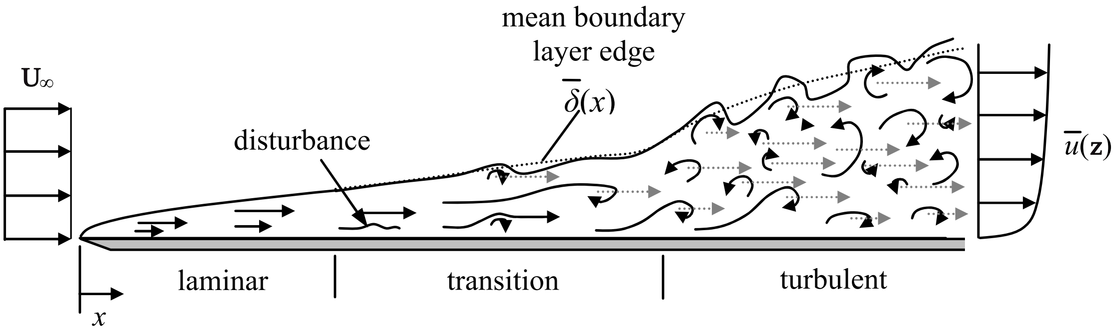

FIGURE 1.1: Illustration of the boundary layer development (not to scale) . Figure from [98].

Analytical expression of the WPF beneath of a TBL does not exist because of its random and complex nature of these loads. Many of the analyses performed by scientists and engineers are based on numerical simulations and empirical evidence from flow measurements [71, 92]. Usually, three approaches are used to evaluate the WPF [89].

1. In the first approach (unsteady approach), the time-resolved flow field is available and averaged quantities are derived posteriorly. In this approach, unsteady simulations such as Direct Numerical Simulations (DNS) or Large Eddy Simulation (LES) are used to predict the cross-spectrum density (CSD) of the WPF [24, 65, 163].

2. In the second approach, no time-resolved data is available, and instead, a statistical expression is derived using the Poisson's equation. Typically, Reynolds-averaged Nervier-Stokes Simulation (RANS) is used in this statistical method to calculate time-averaged turbulence statistics [41, 88, 142].

3. As part of the third approach, experimental data is used to formulate semi-empirical models. This approach combines experimental observations with theoretical insights to develop models that can predict the statistical properties of the WPF beneath a TBL. The foundation of semi-empirical models began with the pioneering work of researchers like Willmarth and Wooldridge [173], Bull [21], and Corcos [37], who conducted detailed measurements of the WPF.

Although the first and second approaches can simulate the TBL fluid flow, they are very costly to compute, especially if the fluid's compressibility is considered [65]. Consequently, researchers have given more attention to semi-empirical models, leading to the development of many models in the last 50 years, each with varying degrees of accuracy, aimed at predicting the WPF beneath a TBL [51, 110, 167, 171, 174].

Researchers have employed two approaches for measuring the WPF. The first one is the acoustic based approach (ABA) which involves using a microphone array to directly measure the sound waves created by a TBL. In this method, a network of microphones record the sound waves produced by the pressure fluctuations. To estimate the TBL WPF, the recorded sound signals are processed using techniques like Fourier transform, beamforming, or other signal processing methods to extract information about the WPF.

An alternative approach involves measuring the vibration responses of a structure that is excited by the WPF using an accelerometer array. The data from the accelerometers are then used to identify the fluctuating pressure that would cause the resulting vibrations of the structure.

1.1 Research Motivation

To accurately predict flow-induced noise and vibrations, an accurate estimation of the WPF is required. A significant portion of the TBL energy is primarily transmitted through pressure fluctuations at the convective wavenumber, $k_c = \omega/U_c$, where ω is the angular frequency and U_c being the velocity of convection or the average speed of eddies in the boundary layer. Figure 1.2 shows a schematic of the CSD of the TBL WPF, $\phi_{pp}(k, \omega)$, and vibration modal response of the structure, $\Psi_s(k, \omega)$. In this figure, the acoustic and flexural wavenumbers are denoted as $k_0 = \omega/c_0$ and $k_f = \omega/c_f$, respectively, where c_0, c_f are the sound speed and the bending wave speed, respectively. As shown in Figure 1.2, the CSD of the WPF can be mainly characterized by two distinct regions: the convective region and the sub-convective region. Vibration response of the structure can be mathematically determined by integrating the product of the WPF CSD function and modal response of the structure in the wavenumber domain [31].

While the peak energy in the TBL is concentrated around the convective wavenumber, it is recognized that in low Mach number flows, the primary source of structural vibration arises from the low-wavenumber components of the WPF [17, 32, 74]. The reason is that the structure acts as a filter, attenuating the excitation from the convective ridge of the TBL at frequencies well above the coincidence frequency (the frequency at which the bending wave speed in the structure and the convection speed are equal [114]). As a result, the vibration induced by the TBL is primarily governed by the low-wavenumber portion of the WPF [17, 32, 33, 74, 94, 126]. This highlights the importance of the low-wavenumber WPF in the prediction of flow-induced vibrations.

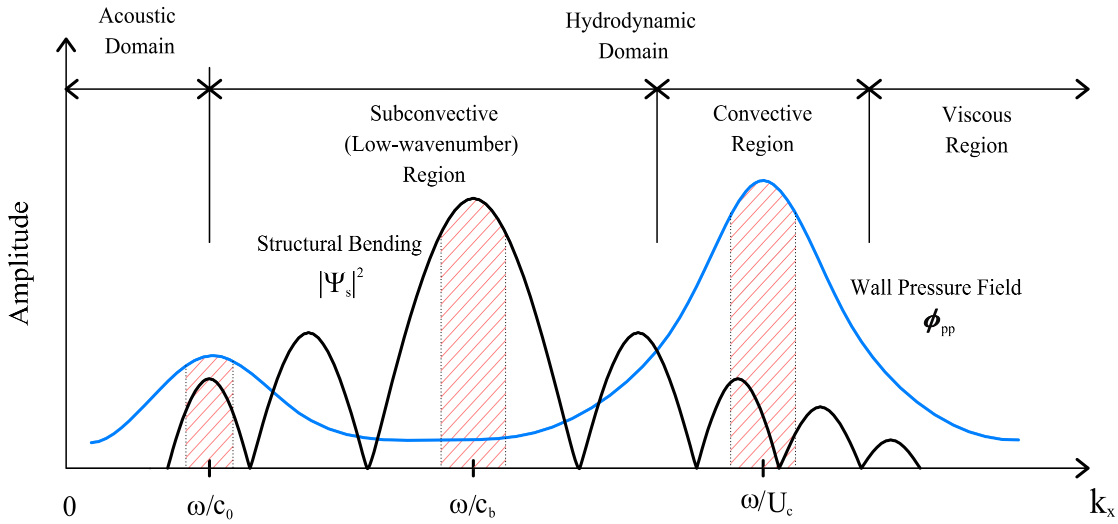

FIGURE 1.2: Schematic of the spatial matching of the wavenumber-frequency spectrum of the TBL WPF and vibration modal function when $U_c < c_f < c_0$ (not in scale). Figure from [2]

A variety of semi-empirical TBL models have been developed in the last 50 years [51, 110, 167, 171, 174]. Most of these studies have primarily focused on identifying the convective ridge. Despite the fact that most models are in good agreement when it comes to predicting the convective region, there is a significant discrepancy at subconvective region. Due to the low amplitudes of the WPF in the low-wavenumber domain compared to those at convective wavenumbers, they can easily be contaminated by convective wavenumbers and also background noise. Thus, it has been difficult to model and measure these levels of the TBL WPF. Moreover, most of the existing body of research on estimation of the TBL WPF focuses on the convective ridge and not on the low-wavenumber region despite of its importance. Therefore, ongoing research in this field is essential.

The broad and main aim of this thesis is to find a procedure that enable us to estimate the low-wavenumber WPF with good accuracy, not to develop a new model for WPF. To achieve this, both the ABA and vibration-based approach (VBA) have been examined to understand how they estimate the low-wavenumber domain of the WPF and to highlight their advantages and challenges.

1.2 Thesis Overview

In this section, we provide an overview of the remainder of this thesis. In Chapter 2, we begin with a detailed description of the TBL concept and then conduct a literature review of various TBL models developed by researchers. This chapter also discusses the vibration response of structures under TBL excitations and examines the impact of different models on structural response. Finally, we review the relevant literature on measuring and identifying the WPF using the ABA and VBA.

Chapter 3 highlights the challenges of estimating the low-wavenumber WPF in a TBL using a microphone array. A regularized Fourier-based approach is proposed to numerically study the estimation of the low-wavenumber WPF. Performance of the proposed method is initially evaluated by comparing the estimated WPF against a closed-form input TBL model. Effects of sensor spacing, co-array factor, and sensor distribution on the estimation of the low-wavenumber WPF levels are then investigated. To mimic experimental measurements a virtual acoustic experiment is proposed, involving the synthesis of snapshots of TBL-induced WPF.

The research of Chapter 3 was published in the Journal of Sound and Vibration [2] titled "On the challenges of estimating the low-wavenumber wall pressure field beneath a turbulent boundary layer using a microphone array". It was shown that to achieve accurate estimation of the WPF all the three factors should be considered. It was found that to obtain accurate results, in addition to the Nyquist criterion, one needs to use an irregular array pattern with the maximum possible co-array factor. It was also showed that reasonable estimation of the WPF in the convective region is much easier than that in the low-wavenumber domain and can be achieved with relatively small number of sensors. However, it has been shown that while the convective region can be identified with a relatively small number of realizations in experimental situations, a significant number of realizations is required to accurately estimate the low-wavenumber levels in the TBL pressure field.

In Chapter 4, we investigate the feasibility of estimating the low-wavenumber WPF by analyzing vibration data from a structure excited by a TBL. The proposed approach is based on the relationship between the TBL forcing function and structural vibrations in the wavenumber domain. By utilizing vibration data obtained from a structure excited by a TBL at a single frequency, and incorporating the sensitivity functions of the respective structure, it is possible to estimate the CSD of the pressure fluctuations in the wavenumber domain. To demonstrate the effectiveness of the proposed method, an analytical model of a simply-supported panel excited by a reference TBL model is employed. The vibration data of the panel is then used in an inverse method to identify the low-wavenumber levels of the pressure fluctuations, which are then compared to those of the reference TBL model.

The research in Chapter 4 was presented at the Inter-noise 20-23 August 2023 Chiba, Japan, and also included in the refereed conference proceedings as "H. Abtahi, M. Karimi, and L. Maxit. Numerical study on the estimation of the low-wavenumber wall pressure field using vibration data. INTER-NOISE and NOISE-CON Congress and Conference Proceedings. Vol. 268. No. 6. Institute of Noise Control Engineering, 2023." We also extended this work and investigated the performance of the proposed method through a parametric study and virtual experiments. The outcome of this investigation was presented in the Acoustic 4-8 December 2023 Conference in Sydney, Australia, and later on a more comprehensive version of this work was published in the Journal of Fluids and Structures [3] titled "Identification of low-wavenumber wall pressure field beneath a turbulent boundary layer using vibration data". It was found that, unlike the acoustic-based methods, where a relatively high number of sensors is required to respect the Nyquist criterion, a few sensors are sufficient to estimate the WPF in the low-wavenumber using the proposed vibration-based method. Moreover, it was shown that unlike the ABA where a substantial number of realizations is needed to accurately estimate the low-wavenumber levels in the TBL pressure field (due to contamination by the convective ridge), utilizing the structure in the VBA filters the convective region of the WPF, allowing for accurate estimation of the low-wavenumber WPF using a significantly smaller number of realizations.

In order to minimize the number of realizations required, an alternative approach based on the frequency band analysis, instead of a single frequency analysis, is proposed in Chapter 5. The outcome of this Chapter was presented in the Inter-noise 25-29 August

2024 Nantes, France, and also included in the refereed conference proceedings as "H. Abtahi, M. Karimi, and L. Maxit. A vibration-based method to estimate the low-wavenumber wall pressure field in a turbulent boundary layer. INTER-NOISE and NOISE-CON Congress and Conference Proceedings. Vol. 268. No. 6. Institute of Noise Control Engineering, 2024."

To identify the low-wavenumber components of the WPF using VBA (Chapters 4 and 5), it is necessary to calculate the sensitivity functions, which corresponds to the plate's response to a unit wall plane wave [115]. While this function can be computed analytically or numerically, it is challenging to experimentally obtain this function in practice. The procedure for calculating the sensitivity functions is discussed in Chapter 6. In this chapter, two methods for calculating the sensitivity functions—modal expansion (Section 6.1.1) and the reciprocity principle (Section 6.1.2)—have been examined and verified experimentally. An experiment was conducted in the Acoustics Lab at UTS Tech Lab to determine the sensitivity functions experimentally. For this purpose, a clamped plate was installed in the Acoustics Lab, and its vibrational response, excited by a Shaker Brüel & Kjær Type V406 M4-CE, was measured using a Polytec Type PSV-500-HV Xtra Laser Doppler Vibrometer (LDV). These data were then used to calculate the sensitivity functions in Section 6.1.1 using the modal expansion method and in Section 6.1.2 using the reciprocity principle method.

1.3 Contribution to Research

Below is a summary of the contributions of the research presented in this thesis:

For estimation of the WPF using the ABA, the main contribution of the study in Chapter 3 is to highlight the challenges of estimating the low-wavenumber WPF in a TBL using a microphone array. In particular,

- proposing a regularized Fourier-based approach to identify the low-wavenumber levels of the WPF,
- studying the effects of three array parameters, namely sensor spacing, co-array factor and sensor distribution on the performance of proposed method,

- studying the effectiveness of using a microphone array to estimate the WPF in an experimental condition using a virtual experiment,
- showing the number of realizations required for estimation of the WPF in the low-wavenumber domain,
- showing the number of realizations required for estimation of the WPF in the convective region,
- studying three different TBL models to investigate the effect of the convective ridge on the identification of the low-wavenumber domain WPF.

For estimation of the WPF using the VBA, the main contribution of the study in Chapters 4 and 5 is to estimate the low-wavenumber WPF in a TBL using an accelerometer array. In particular,

- proposing truncated generalized singular value decomposition method to identify the low-wavenumber levels of the WPF,
- studying the effect of sensor number and size of the plate on the accuracy of the WPF estimation in the low-wavenumber domain,
- studying the effectiveness of using an accelerometer array to estimate the WPF in an experimental condition using a virtual experiment,
- showing the minimum number of sensors and realizations required for estimation of the WPF in the low-wavenumber domain,
- showing the advantages of using the VBA in estimation of the WPF in the low-wavenumber domain compared to the ABA,
- proposing a frequency band method for estimating the WPF in the low-wavenumber domain.

For the calculation of the sensitivity functions, the main contribution of the study in Chapter 6 is to perform this calculation experimentally. In particular,

- studying two methods—modal expansion and the reciprocity principle—for calculating the sensitivity functions,

- extracting the modal parameters of a plate experimentally and using these parameters to calculate the sensitivity functions using the modal expansion method,
- experimentally calculating the sensitivity functions using the reciprocity principle and comparing the obtained results with those obtained from modal expansion method.

Chapter 2

Literature Review

To provide a comprehensive summary of our study, this literature review is comprised of three main sections. The first section, Section 2.1, reviews the TBL conception and its interaction with a structure. Then, different semi-empirical WPF models developed in the wavenumber domain have been reviewed. In Section 2.2, the vibration response of structures under the TBL excitations, as well as the effect of different models on the structural response, have been reviewed. Finally, the literature relevant to the research for measuring and estimation of the WPF using the ABA and VBA are reviewed. It is recognised from this review that there is an opportunity to investigate on estimation of the WPF in the low-wavenumber domain.

2.1 Turbulent Boundary Layer Wall Pressure Field

2.1.1 Turbulent Boundary Layer Conception

TBL is a complex and critical phenomenon in fluid mechanics with numerous research applications. Despite significant advances, the physics of turbulent flows remain challenging to fully comprehend. This section provides a brief overview of TBLs, highlighting key concepts and historical milestones.

The concept of the boundary layer was first introduced by Ludwig Prandtl in 1905 [146]. Prandtl's work bridged the gap between fluid mechanics and Euler's theory of inviscid flows, emphasizing the significance of fluid viscosity. According to Prandtl, the effects of viscosity cannot be ignored, no matter how small they may be, and this insight has profoundly influenced the field of fluid-structure interaction over the past century. Within the boundary layer, flow can be either laminar or turbulent depending on the effects of viscosity.

The transition from laminar to turbulent flow is predicted by a dimensionless parameter known as the Reynolds number, introduced by Osborne Reynolds in 1883 [150]. The Reynolds number represents the ratio of inertial forces, which accelerate fluid particles, to viscous forces, which dampen motion. When the Reynolds number increases, inertial forces dominate, causing small disturbances in the flow to grow, ultimately leading to chaotic turbulence.

Turbulence, however, may originate and propagate in a sufficiently complicated manner; brief explanations will be given below [98]. Within a TBL, fluid particles will fluctuate randomly and chaotically. These particles swirl and form irregular, rotating patches of fluid known as eddies. Eddies originate from disturbances near the wall, causing fluid particles to rotate and form small vortex filaments that roll along the wall. As these vortex filaments lift from the wall, they encounter higher velocity flows, stretching into shapes resembling horseshoes or hairpins. This vortex stretching process increases the kinetic energy of the vortices, transferring energy from the main flow to the turbulence. This process has been shown in Figure 2.1.

Secondary vortices with lower energy may form adjacent to the primary hairpin vortices. These vortices oscillate and interact with other eddies, eventually becoming unstable and breaking up. The remnants of these vortices form streamwise rolls, which lift other vortex filaments from the wall, perpetuating the turbulent process. Thus, turbulence is fundamentally characterized by rotation and the continuous transfer of energy through vortex interactions.

Understanding the intricacies of TBLs is essential for numerous engineering applications, including aerodynamics, hydrodynamics, and fluid-structure interactions. Continued research in this field is vital for advancing our knowledge and improving practical applications in engineering and technology.

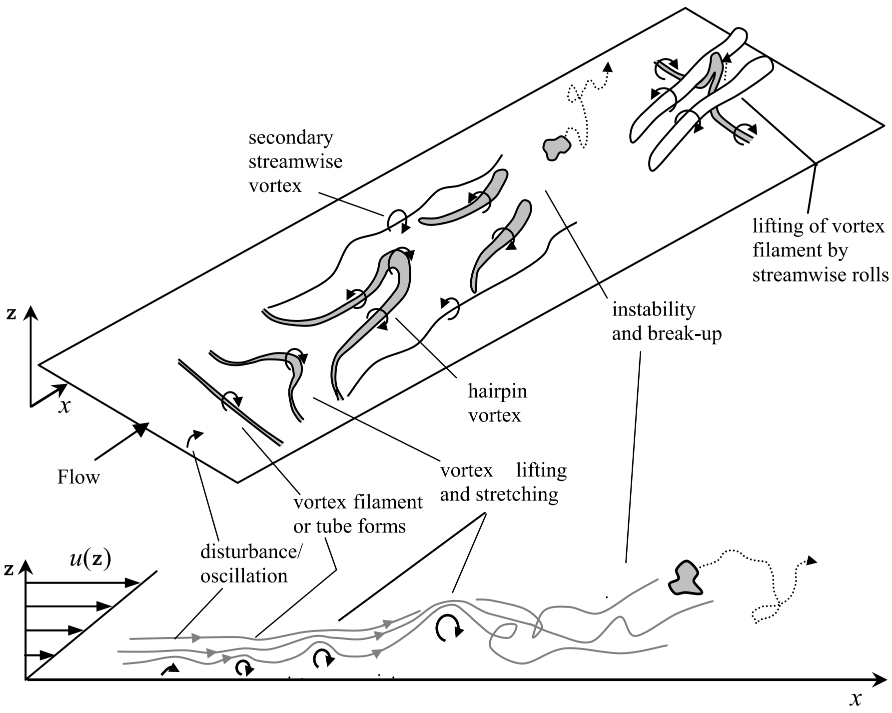

FIGURE 2.1: Schematic process of eddy formation in a turbulent boundary layer. Figure from [98].

2.1.2 Turbulent Boundary Layer Models

Due to the random nature of the pressure field, the typical methodology for analysing TBL excitation of structures is based on random analysis techniques. Thus, the CSD of WPF is considered as the essential quantity to calculate and evaluate the influence of the fluid flow. Currently, no analytical formula can accurately predict the WPF.

Over the past 50 years, researchers have developed various semi-empirical TBL models with differing levels of accuracy to estimate the WPF beneath a TBL [91, 104, 134]. These models fall into two categories: the auto-spectrum (or single point spectrum) models and the normalized CSD models. The auto-spectrum models quantify the energy of pressure fluctuations using mean square pressure fluctuations, while the normalized CSD models describe the pressure energy distribution based on wavelength.

Graham's formulation allows the CSD of WPF to be expressed independently as the auto-spectrum ($\Psi_{pp}(\omega)$) and the normalized CSD of the pressure field ($\tilde{\phi}_{pp}(k, \omega)$) [71, 92]. This approach enables the use of each normalized wavenumber-frequency spectrum with any auto-spectrum model as follows

$$\phi_{pp}(\mathbf{k},\omega) = \Psi_{pp}(\omega)\left(\frac{U_c}{\omega}\right)^2 \tilde{\phi}_{pp}(\mathbf{k},\omega), \tag{2.1}$$

where $\mathbf{k}$ is the wavevector with components k_x and k_y in the streamwise and spanwise directions in the (x, y) plane, respectively. This equation is valid when the wavenumber-frequency spectrum fulfills the following requirement [92]

$$\int_{-\infty}^{\infty}\int_{-\infty}^{\infty} \tilde{\phi}_{pp}(\mathbf{k},\omega)d\mathbf{k} = 1, \tag{2.2}$$

$$\int_{-\infty}^{\infty}\int_{-\infty}^{\infty} \phi_{pp}(\mathbf{k},\omega)d\mathbf{k} = \Psi_{pp}(\omega). \tag{2.3}$$

Subsection 2.1.2.1 provides an overview of several developments of semi-empirical models for calculating single-point wall pressure spectrum models. Most of the models have been developed in the last fifty years, and are briefly presented here.

2.1.2.1 Single-point Wall Pressure Spectrum Models

Single-point wall pressure spectrum models, or power spectra, describe how to distribute the mean-square fluctuating pressure with frequency. Essentially, it is how energies are sorted into frequencies. A variety of models have been developed for point spectrum prediction over the last 50 years [14, 15]. Hwang [91, 92] presented a summary of the last 50 years of semi-empirical study on the prediction of TBL wall pressure frequency spectrum.

The various length and velocity scales in the close vicinity of the wall mean that no single scaling leads to a satisfactory fit of experimental data at all relevant frequencies. Klebanoff [109], Laufer [112], and Townsend [165] showed that a TBL can be described using viscous wall layer and friction layer. The viscous wall layer is situated very close to the wall, where viscous effects dominate. Quantities in this region are defined using inner variables such as wall-shear stress ($\tau_w = \mu_f dU/dy$, where μ_f is the dynamic viscosity), friction velocity ($u_\tau = \sqrt{\tau_w/\rho}$, where ρ is the density), and kinematic viscosity (ν). Friction layer is situated further from wall. In this region, turbulent fluctuating motions prevail over viscous effects. Quantities in this region are defined using outer variables such as the free stream velocity (U_∞), dynamic pressure ($\frac{1}{2}\rho U_\infty^2$), boundary layer thickness (δ), and displacement thickness (δ^*).

For a boundary layer along a flat plate, the point spectrum can be scaled using inner and outer layer variables [4, 144]. The separation between these two regions occurs at the frequency where the point spectrum reaches its maximum value. The overlap of the two regions is known as the universal region. Figure 2.2 illustrates a typical wall pressure spectrum (auto-spectrum), highlighting which scaling variables are most effective across different frequency ranges.

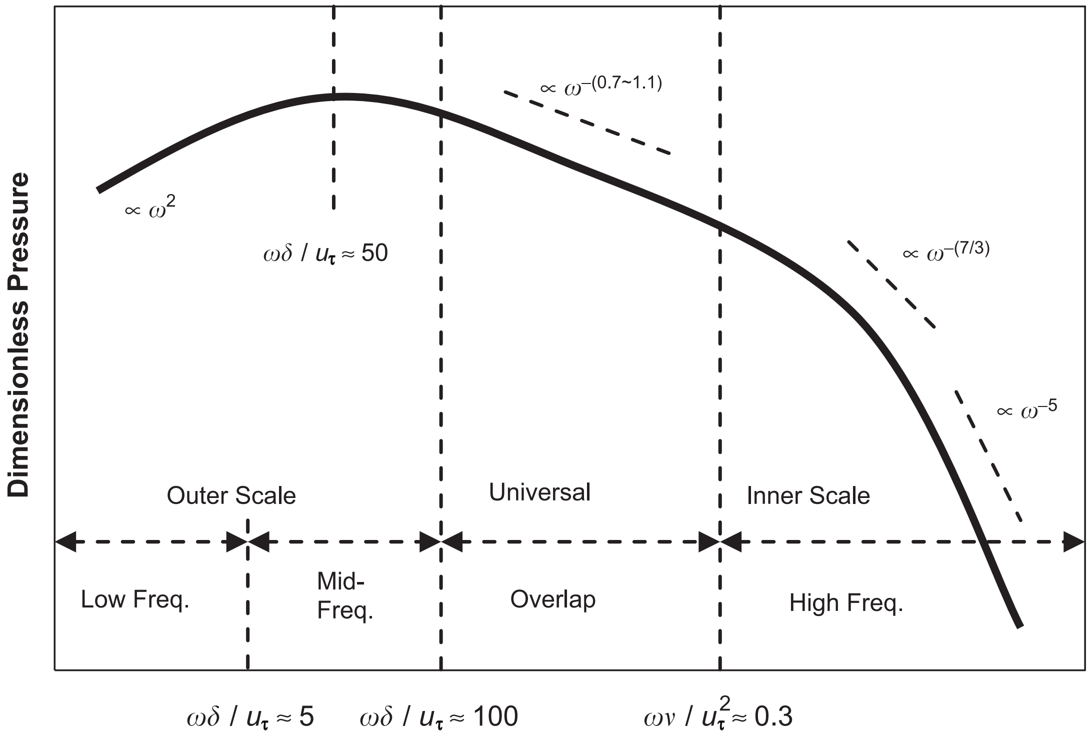

FIGURE 2.2: An overview of the spectral features for a TBL wall pressure spectrum at different frequencies. Figure from [92].

By using dimensionless frequencies, the spectrum is divided into four distinct regions [92]:

- Low-frequency region: For $\omega\delta/U_\infty \leq 0.03$ (or $\omega\delta/u_\tau \leq 5$), the spectrum varies as ω^2. In this region, flow structures in the outer layer dominate. Either q or τ_w can be used as the pressure scale, with δ/U_∞ as the time scale.

- Mid-frequency region: For $5 \leq \omega\delta/u_\tau \leq 100$, which includes the spectral peak at approximately $\omega\delta^*/U_\infty = 50$, τ_w is used as the pressure scale and δ/u_τ as the time scale.

- Overlap region: For $100 \leq \omega\delta/u_\tau \leq 0.3(u_\tau\delta/\nu)$, this region is present when the Reynolds number $u_\tau\delta/\nu > 333$. Both outer and inner-layer scaling can collapse the data in this range, with the spectrum varying approximately as ω^{-1}. However, studies by Goody [69] and Smol'yakov [161] suggest variations in the spectrum of $\omega^{-0.7}$ and $\omega^{-1.1}$, respectively.

- High-frequency region: For $0.3 \leq \omega\nu/u_\tau^2$, the high-frequency region is affected by viscosity and is typically based on inner-layer variables. Pressure scales are defined by τ_w and time scales by ν/u_τ^2.

In the low- and mid-frequency regions of the wall pressure spectrum, pressure fluctuations are caused by physical processes occurring mainly in the outer layer. In contrast, the higher frequency region reflects the physical behaviour occurring close to the wall.

According to Hwang [92], the following scaling laws can be applied for each region

- in the low-frequency region: $\Psi_{pp}(\omega)U_\infty/q^2\delta^* = f_1(\omega\delta^*/U_\infty) = \text{constant} \times (\omega\delta^*/U_\infty)^2$,
- in the mid-frequency region: $\Psi_{pp}(\omega)u^*/\tau_w^2\delta = f_2(\omega\delta/u_\tau)$,
- in the overlap region: $\omega\Psi_{pp}(\omega)\tau_w^2 = f_3 = \text{constant}$,
- in the high-frequency region: $\Psi_{pp}(\omega)u_\tau^2/\tau_w^2\nu = f_4(\omega\nu/u_\tau^2)$.

Spectral characteristics that are frequency-dependent suggest that an appropriate auto-spectra prediction model must rely on a wide range of scaling parameters. Below, we present solutions from multiple researchers based on their work.

Robertson [153] conducted one of the earliest studies on single-point wall-pressure spectrum models. He developed a formulation for the pressure spectrum based on Lowson's work [117] using supersonic measurements from NASA-Ames. However, his model underestimated spectral levels at low Strouhal numbers (Sh) and exhibited an excessive roll-off at high Strouhal numbers. Despite these shortcomings, Robertson's model provided a new formula that better represented experimental findings across a broader range of Mach numbers (M_a). For Mach numbers between 0.6 and 3.0, his calculated values showed good agreement with experimental data. Subsequently, Amiet [6] proposed an expression for the pressure spectrum based on measurements conducted by Willmarth and Roos [172] over a flat plate. His expression is valid for $0.1 < \omega\delta^*/U_\infty < 20$.

In a 1974 investigation of the vibration response of spacecraft shrouds to in-flight fluctuating pressures, Cockburn and Robertson [34] proposed a model for the auto-spectrum density of the WPF. Their experiments were conducted on a 15° cone-cylinder payload shroud at three different Mach numbers ($M_{a_1} = 0.7$, $M_{a_2} = 0.8$, $M_{a_3} = 2.0$). The data was obtained from an Atlas-Agena launch vehicle, which featured a standard payload shroud made of fiberglass skin with aluminum ring-frame stiffeners. The model had a diameter of 1.676 meters and a total length of 5.791 meters, with a cylindrical section length of 3.302 meters. While similar to the Robertson model [153], Cockburn and Robertson used a modified estimate for the characteristic frequency that accounted for the local thickness of the TBL.

In 1982, Kim and George [105] presented a mathematical formula by fitting a curve to experimental data from Brooks and Hodgson [19] and Yu and Joshi [176] on an airfoil. Their model is only valid for adverse pressure gradient conditions.

In 1982, Efimtsov [51] introduced his first model (Efimtsov 1) based on multiple wall pressure measurements on aircraft fuselage during flight tests. The Efimtsov 1 model is dependent on Reynolds (Re), Strouhal, and Mach numbers and is valid for $0.42 < M_a < 2.1$ and $0.5 \times 10^8 < Re < 4.85 \times 10^8$. These measurements evaluated pressure fields at several points on the fuselage for a fully developed boundary layer and zero pressure gradients. The Efimtsov 2 model [52] builds upon the original Efimtsov 1 model by integrating further data collected from low and high-speed wind tunnel experiments at TsAGI (Central Aerohydrodynamic Institute in Moscow, Russia). These measurements encompass a Mach number range of $0.015 < M_a < 4$ and Reynolds numbers from 6×10^2 to 1.5×10^5 [52].

In 1987, Chase [26] updated his initial model, which was published in 1980 [28]. The Chase frequency spectrum was obtained by integrating the wavenumber-frequency spectrum over the wavevector plane according to Eq. (2.3). According to Chase, the convective velocity ranges between $0.65U_\infty$ and $0.75U_\infty$. A more accurate method for measuring this value involves using the phase velocity derived from the cross-spectrum between two sensors aligned with the flow direction. Using this method and based on the free stream and convective velocity, a ratio of approximately $0.75 \leq U_c/U_\infty \leq 0.8$ was computed for aircraft flight data [106].

To account for compressibility effects, Laganelli and Wolfe [111] derived a model in 1993 based on experimental studies and an expansion of Robertson's model [153]. In 1994, Goodwin [68] developed a model using flight test data from three supersonic aircraft.

In 1998, Howe [84] extracted a single-point wall pressure spectrum model from Chase's model [28], which is applicable at high frequencies. This model is known as the Chase-Howe model [69]. Compared to the original Chase model, the updated Chase-Howe model incorporates fewer TBL variables, resulting in a simpler formulation.

In 2000, Smol'yakov introduced a new model that applies distinct scaling variables for different frequency ranges [161]. This model segments the spectrum into three regions: low-frequency, universal, and high-frequency. After a comprehensive examination of his mathematical formulation of the wavenumber-frequency spectrum and an extensive set of published data [92], Smol'yakov developed this model. He used the boundary layer momentum loss thickness (θ) as a dimensional factor in the Reynolds number, introducing the momentum Reynolds number as $Re_\theta = U_\infty \theta/\nu$. His equations are valid for $Re_\theta > 10^3$ ($Re > 5 \times 10^5$).

In 2004, Goody [69] modified Howe's [84] model based on 19 different experimental studies. Goody's relationship, valid for $1400 < Re_\theta < 23400$, yields higher levels at low frequencies and results in a faster decay at high frequencies. By adding various terms to the original formula, Goody better represented the spectrum across all frequencies.

In 2005, Rackl and Weston [148] compared measured flight data to predictions from Efimtsov's model, identifying two discrepancies. First, they observed a broadband spectral peak at a certain Strouhal number, attributed to specific frequency ranges that enhance the contribution of turbulent energies based on boundary layer thickness. Second, they noted a steeper roll-off at higher frequencies, where Efimtsov's model predicted a shallower negative slope compared to other models and flight data. To address these issues, they modified the updated Efimtsov model [52] to incorporate the broadband spectral peak appearing near the Strouhal number of $Sh = 2\pi f \delta^*/U_\infty = 0.6$. This requires converting the Efimtsov model to decibels, applying Rackl and Weston's factors, and converting the corrected model back into the original units. Their expressions include a function centered at 1000 Hz to adjust only the high-frequency slope.

In 2007, Rozenberg et al. [155] developed a model based on Goody's model but used displacement thickness instead of boundary layer thickness in their formulation. They analyzed spectral variations between adverse pressure gradient and zero pressure gradient boundary layers using numerical and experimental results. They fitted new parameters to their analysis based on data from six different adverse pressure gradient flow cases, opting to consider the maximum shear stress along the wall rather than the shear stress suggested by Simpson [160].

In 2012, Miller et al. [134] reviewed various models, including Graham's [71] formulations, to evaluate each model's appropriateness and accuracy for aircraft applications. Compared to experimental data, the spectrum at low frequencies rolled off similarly to the Goody model. Due to its mathematical simplicity, the Goody model was deemed the most suitable single-point wall-pressure spectrum model for aircraft applications.

In 2014, Catlett et al. [25] introduced an empirical model for the TBL WPF under an adverse pressure gradient. They used the Goody model with constants calibrated from measurements taken over the trailing edge region of an airfoil profile in a wind tunnel for various pressure gradient intensities.

Similarly, in 2016, Klabes et al. [108] developed another model based on the Goody model. They re-evaluated the exponents and constants in Goody's formula and proposed a new normalized relationship according to the local kinetic energy values. Additionally, in 2016, Hu and Herr [87] created a WPF model for zero, adverse, and favorable pressure gradient TBLs in a wind tunnel, applying the Goody model to scale new parameters.

Figure 2.3 depicts a comparison of auto-spectrum models developed by Cockburn & Robertson, Robertson, Efimtsov, Rack and Weston, Goody, Chase, Chase-Howe, and Smol'yakov at $M_a = 0.78$ [107]. The Cockburn & Robertson, Robertson, Efimtsov, Rack, and Weston models were derived from flight test data and wind tunnel model results at high Mach numbers and Reynolds numbers. These models exhibit a large plateau in the low-frequency domain with a pronounced roll-off at higher frequencies.

In contrast, the second group comprises the Goody, Smol'yakov, and Chase-Howe models, each offering distinct spectral shapes, especially at low frequencies. These models show an increase in spectral values as frequency rises, peaking in the mid-frequency range before declining at higher frequencies.

The Chase model falls between these two groups. Like the Robertson & Robertson-Cockburn and Weston & Efimtsov-Rackl models, it features a substantial plateau in the low-frequency range. However, its predicted spectrum peaks at higher frequencies before rolling off similarly to the Goody, Smol'yakov, and Chase-Howe models. Each model exhibits unique characteristics and shapes tailored to fit specific measurements, highlighting differences in data quality and model design.

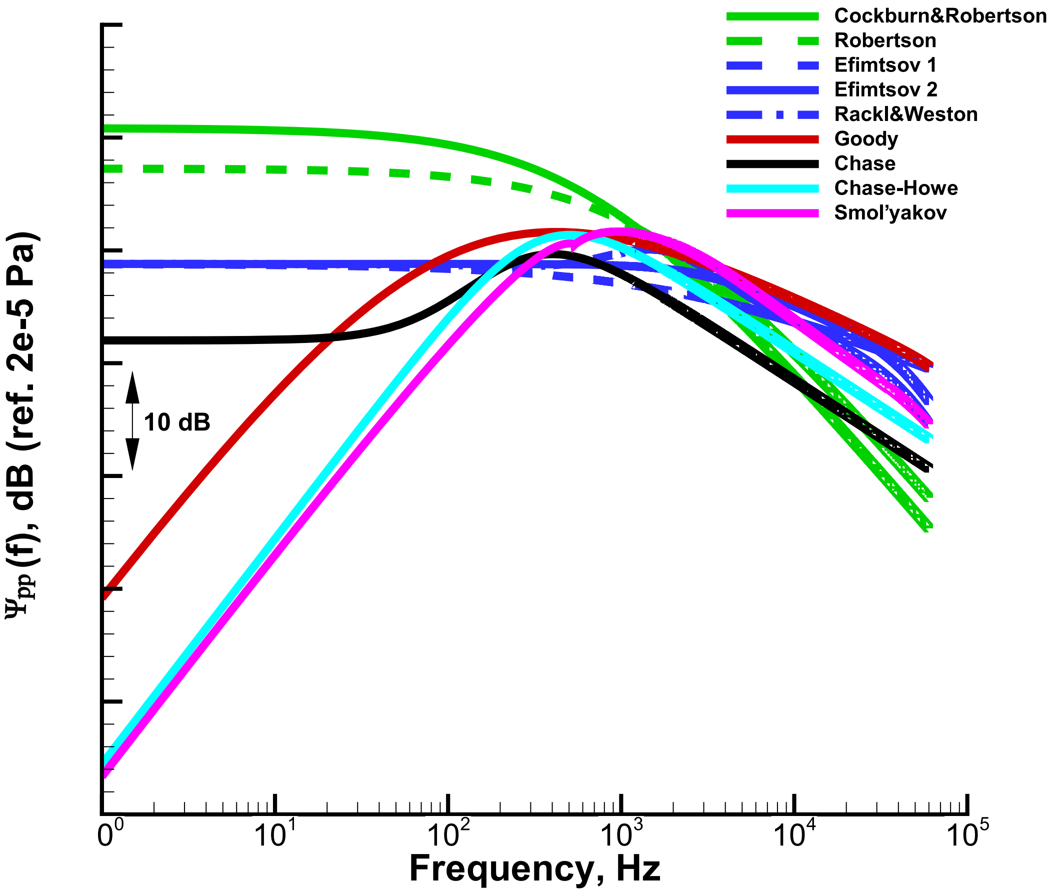

FIGURE 2.3: Comparison of auto-spectra models at $M_a = 0.78$. Figure from [107].

2.1.2.2 Normalized Wavenumber-Frequency Spectrum Models

Signal processing typically uses recorded data in the time domain to calculate correlation functions. These data are derived as a result of observing two signals with a space (or time) lag. This process eliminates non-recurring contents while periodically recurring contents are filtered. The aim of correlation functions is to indicate how two signals are related, which in turn provides insight into their relationship [107]. The CSD can be calculated by a Fourier transform of correlation function with respect to time. Additionally, the spatial Fourier transform of the CSD can be used to generate a wavenumber-frequency spectrum $\phi_{pp}(k_x, k_y, \omega)$ for each frequency [53].

Along with the auto-correlation empirical models, various cross-correlation empirical models are developed by researchers. In this section, we review the available wavenumber-frequency models for the TBL.

Figure 2.4 illustrates the wavenumber-frequency spectrum at a constant frequency, highlighting all distinct regions. The spectrum in Figure 2.4 is classified into the following regions [22]:

- Supersonic region (not shown), $k < \omega/c = (k_0)$;
- Sonic or acoustic region, $k \approx \omega/c$;
- Subconvective region, $\omega/c < k < \omega/U_c$;
- Convective region, centered around $k = \omega/U_c$;
- Viscous region, $k \gg \omega/U_c$.

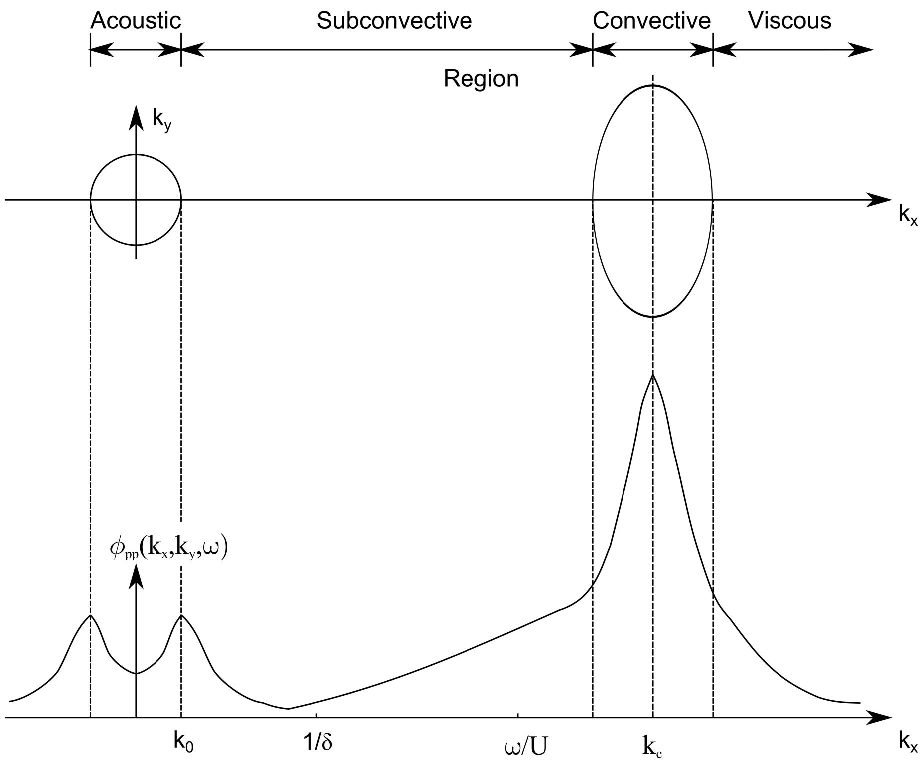

FIGURE 2.4: Schematic of the characteristic region for wavenumber-spectrum of $\phi_{pp}(k_x, k_y, \omega)$. Figure from [85].

Bull demonstrated in [22] that the standard shape of the spectrum beneath the TBL is primarily determined by pressure-field components associated with the phase velocity $\omega/k = U_c$. This zone, known as the wavenumber-spectrum convective ridge (centered around $k_\omega = \omega/U_c$)), is where the primary source of TBL energy is concentrated. Acoustic radiation is defined as $k_0 = \omega/c_0$. It occurs due to elements with phase velocities equal to or greater than the speed of sound in fluids.

Graham [71] observed that, although the subconvective region is important for low-Mach fluid flow applications, it holds less significance in high-Mach contexts, such as those encountered in aircraft. In these situations, the convective region—containing most of the TBL energy—becomes a primary factor in inducing vibrations in aircraft structures. The viscous region, on the other hand, is characterized by the occurrence of small-scale turbulence [133].

When examining various modeling approaches, it is evident that the core of the convective region, where energy primarily accumulates, exhibits a greater width in cross-flow directions compared to in-flow directions. This difference arises from variations in coherence length across each direction [107]. Additionally, Smol'yakov highlights in [162] that wavenumber-frequency models generally fall into two main types.

The first type includes "convertible" models, which allow for the transformation between an analytically derived wavenumber-frequency perspective of the spectrum and a cross-spectrum format, and vice versa, through interactive Fourier transformations. Smol'yakov explains that this convertibility enables the application of various techniques to assess structural vibrations and flow-induced noise. In contrast, the second type encompasses models that do not share this advantageous property.

In 1964, Corcos [38] introduced his model by fitting a curve to the narrow-band spatial correlation between wall pressures. The Corcos model is widely utilized in scientific research. According to his hypothesis, the coherence loss between two spatially separated points is the product of coherence loss in the streamwise direction and the spanwise direction. In this model, the coefficients α_x and α_y represent the decay rates in the flow and cross-flow directions, respectively. The Corcos model does not account for the acoustic region.

Graham [70], along with measurements by Willmarth and Woolridge [173], estimated α_x and α_y to be 0.1 and 0.77, respectively. Blake [14, 15] further suggested that $\alpha_x = 0.32$ and $\alpha_y = 0.7$ are suitable for aircraft boundary layers, while $\alpha_x = 0.116$ and $\alpha_z = 0.70$ are appropriate for smooth walls.

A significant drawback of the Corcos model lies in its formulation of coherence length. As the frequency (ω) approaches zero, the model suggests that coherence length increases without bound. In contrast, experimental data indicate that coherence length remains finite at low frequencies due to the finite thickness of the TBL, which prevents unlimited growth of coherence length. Analyzing this data, Blake [14] concluded that the Corcos model lacks predictive power at low-wavenumbers because it ignores the finite size of the TBL. Recent studies by Finnveden et al. [61], Cohen [36], and Hu and Herr [87] have demonstrated that the correlation length coefficients do not remain constant across all frequencies. Additionally, the Corcos model does not account for the compressibility of the fluid. The Corcos model in the wavenumber-frequency domain is comprehensively detailed in [28]. Figure 2.5 illustrates 2D and 3D plots of the Corcos model at 2000 Hz.

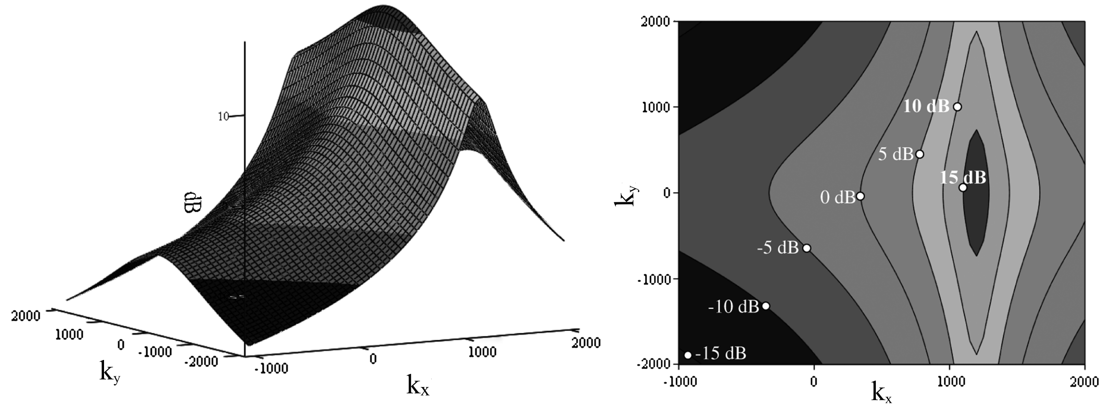

FIGURE 2.5: 2D and 3D plots of the Corcos wavenumber-frequency for 15 m/s at 2000 Hz. Figure from [134].

In 1968, Cockburn and Jolly [35] enhanced the Corcos model by adding a boundary layer thickness factor $\epsilon_{\delta*}$, addressing the boundary layer's finite thickness overlooked by Corcos. This modification improves coherence length predictions, particularly in the low-frequency range. In 1982, Efimtsov [51] introduced a cross-correlation model based on Corcos' approach, but unlike Corcos, Efimtsov included the boundary layer thickness when calculating coherence length, utilizing different correlation lengths α_x and α_y. Efimtsov's results are preferred over Blake's recommendations because they are based on an extensive series of measurements on aircraft across a Mach number range of $0.41 < M_a < 2.1$, whereas Blake's recommendations are derived from a more limited data set reported by Bhat [13]. Bhat observed shorter correlation lengths than those associated with the "smooth wall" parameters $\alpha_y = 0.77$ and $\alpha_x = 0.1$, attributing this to factors such as misalignment between the x-axis and the flow direction and surface roughness, which led Blake to use the rough-wall parameter $\alpha_x = 0.32$. However, the differences between Efimtsov's results and Bhat's findings might be fully explained by flow misalignment and another unconsidered factor: the decrease in correlation lengths with Sh, which would impact the lower frequencies in Bhat's data. Consequently, Efimtsov's expressions should be considered more reliable. While this model improves upon Corcos's, it still tends to overestimate the spectrum at low-wavenumbers.

Chase's initial model [28], developed in 1980, offered better low-wavenumber domain predictions compared to Corcos' model, which tended to overestimate experimental data. Figure 2.6 displays 2D and 3D plots of the Chase 1 model at 2000 Hz. At $k_x = k_y = 0$, Chase's first model introduces a discontinuity that reduces acoustic levels. It also fails to account for the supersonic region ($|k_x| < \omega/c_0$) and does not accurately reproduce features of experimental results in the low-wavenumber domain ($\omega/c_0 < k_x \leq \omega/U_c$) [14]. To address this, Chase applied Kraichnan-Phillips's theorem to the low-wavenumber domain, aiming to develop a more accurate model that includes the acoustic domain [26]. In 2005, Finnveden et al. [61] further modified the Chase model by examining the vibration responses of structures excited by a TBL.

Building on Lighthill's acoustic analogy and assuming that the velocity source terms followed the general Corcos form, Ffowcs [171] derived an expression for the CSD of WPF that included several unknown constants and functions requiring experimental determination. Hwang and Geib [93] later proposed a simplified version of this expression by disregarding the effects of compressibility and assuming specific forms for the remaining unknown functions.

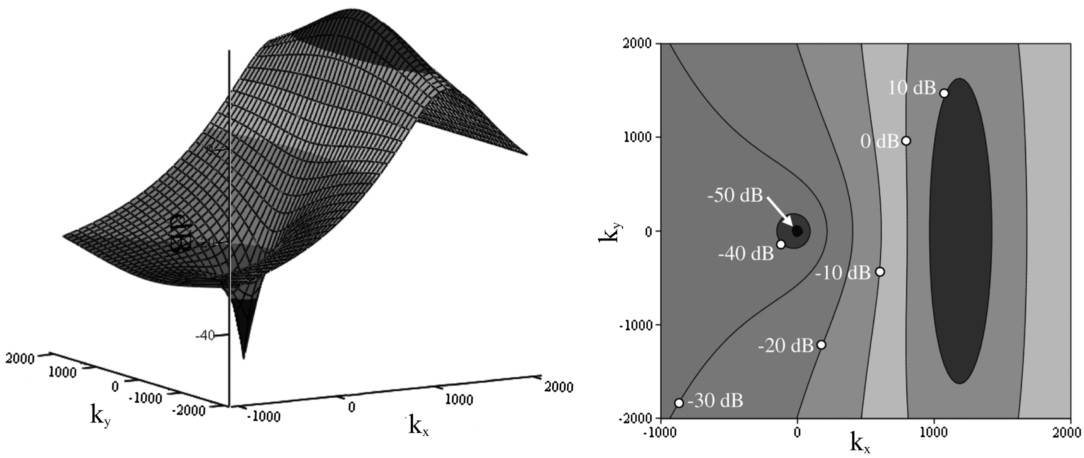

FIGURE 2.6: 2D and 3D plots of the Chase 1 wavenumber-frequency for 15 m/s at 2000 Hz. Figure from [134].

In 1990, Mellen [131] developed an elliptical model for the CSD of WPF with $\alpha_x = 0.10$ and $\alpha_y = 0.77$. Instead of the distribution of rhombic coherence zones in the Corcos model, which makes little physical sense, the Mellen model simulates a distribution of elliptical coherence zones. The shape of the ellipse is controlled by the ratio α_x/α_y. An illustration of the 2D and 3D plots of the Mellen model at 2000 Hz are shown in Figure 2.7.

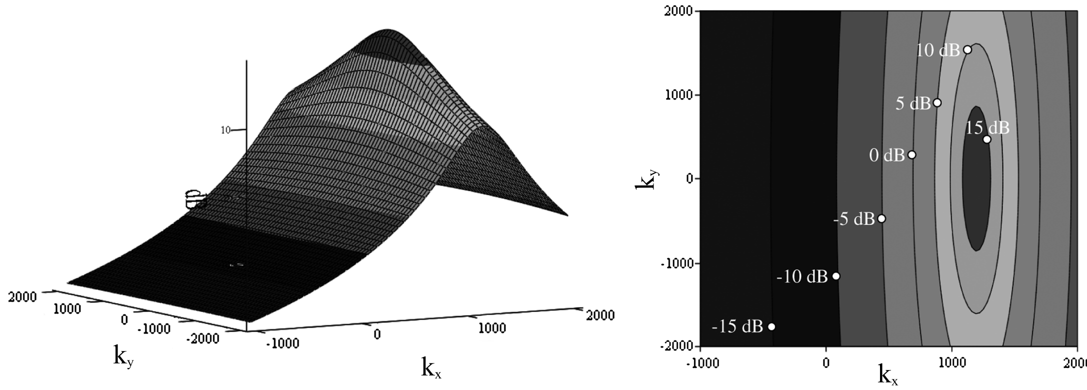

FIGURE 2.7: 2D and 3D plots of the Mellen wavenumber-frequency for 15 m/s at 2000 Hz. Figure from [134].

In 1991, Smol'yakov and Tkachenko [167] investigated spatial correlations of WPF within a TBL without a pressure gradient. They analyzed how these correlations varied with spatial separation and boundary layer thickness, deriving a formula by fitting exponential curves to their experimental results. The measurements took place in a closed-section wind tunnel with a free-stream velocity of $U_\infty = 40$ m/s. Figure 2.8 illustrates the 2D and 3D plots of the Smol'yakov model at 2000 Hz. They found that the low-level low-wavenumber components of WPF in their model showed an improvement compared to the Corcos model but were still higher than the experimental data. To correct this, they adjusted the model by adding a correction factor to align it more closely with the experimental data without significantly affecting the convective peak values. The Smol'yakov and Tkachenko model produced a convective ridge with a quasi-elliptical shape, rather than the rhombic shape, which was more realistic and consistent with observations.

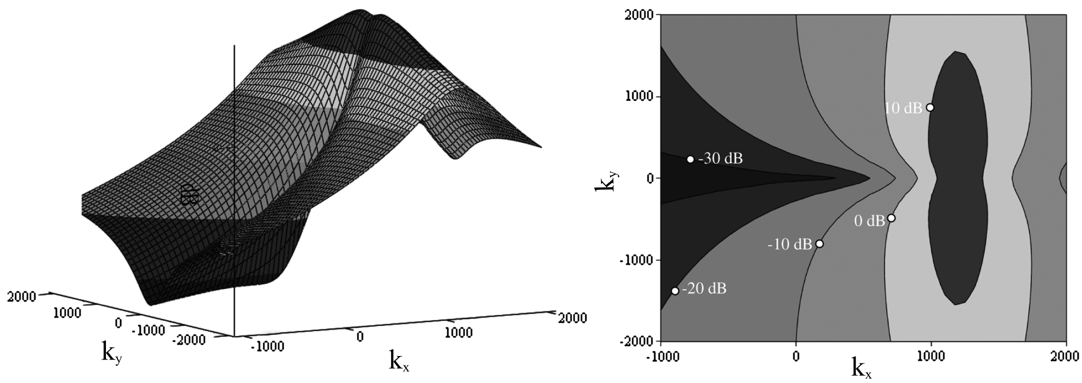

FIGURE 2.8: 2D and 3D plots of the Smol'yakov wavenumber-frequency for 15 m/s at 2000 Hz. Figure from [134].

In 2006, Smol'yakov introduced a new model for calculating wavenumber-frequency spectra as described in [162]. This model builds upon the earlier work of Smol'yakov and Tkachenko [167], using a similar method for calculating the cross-spectrum. Unlike previous models, this new model accounts for the fluid's viscosity, making it dependent on the Reynolds number. Ignoring viscosity causes the coherence length to drop to zero as frequency increases, due to the limiting effect of viscous forces on the minimum vortex size. This model utilizes an auto-spectrum that explicitly accounts for viscosity, and it assumes that the ratio of convective velocity to free-stream velocity varies according to the dimensionless frequency $\omega\delta^*/U_\infty$. The model also incorporates coherence length as a key parameter.

Figure 2.9 compares the shapes of different models at $k_y = 0$ to highlight the location of the convective ridge, where most energy is concentrated. The plots reveal that all models exhibit a strong peak at $k_x = \omega/U_c$, $k_y = 0$. If the boundary layer were convected at speed U_c, all energy would collect there [71].

The models can be divided into two main categories. The first category includes models centered around the Corcos model, including the Efimtsov and Jolly models, which are based on the Corcos model's principles of cross-flow direction and flow separation.

The second category includes models developed by Chase and Smol'yakov, which seek to more accurately represent wavenumber regions distant from the convective ridge. These models incorporate combined multidimensional wavenumbers for both flow and cross-flow directions, producing a more elliptical shape that better reflects reality. In the peak zone, differences can exceed 7 dB, and they can reach over 30 dB further from the convective ridge. Compared to rhombic models, elliptical models offer a more realistic representation in areas away from the convective ridge [107].

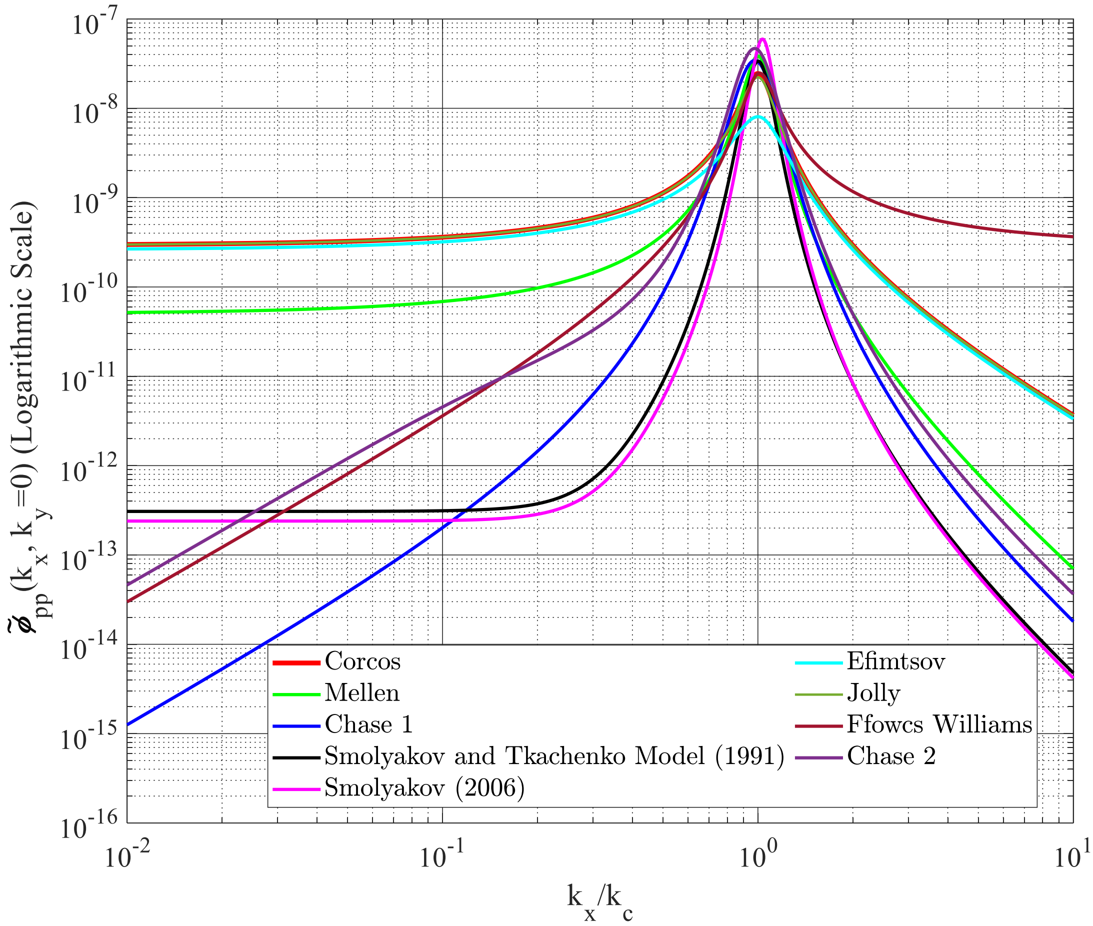

FIGURE 2.9: Comparison of wavenumber-frequency spectra models $\phi_{pp}(\mathbf{k}, f)$ (dB, ref. 1 $Pa^2.Hz^{-1}$) at $k_y = 0$ for 15 m/s at 2000 Hz. k_x and k_y represent the streamwise and spanwise wavenumbers, respectively, and k_c is the convective wavenumber. Goody model is used for the auto-spectrum density.

2.2 Vibration Response of Structures Under TBL Excitation

To gain a better understanding of how a TBL interacts with a structure, as well as how different models of WPF with varying accuracy in the low-wavenumber domain can impact the vibrational response of a structure, this section reviews researches on the vibrational response of structures under TBL excitations. It also highlights the importance of accurate estimation of WPF in the low-wavenumber domain.

The structural response to a random pressure field necessitates the application of random analysis techniques, which have been extensively covered in numerous articles and publications discussing the mathematics of random variables. The vibration responses of structures under the influence of stationary random processes, such as random WPF beneath a TBL, are particularly relevant for naval applications. Notably, Paez [139] provided an insightful overview of the history of random vibration up to 1958, a milestone year in the field marked by Crandall's seminal proceedings [40], which is considered the starting point of modern probabilistic structural dynamics.

Since then, standard text books on random vibration analysis techniques have been published, including works by Bendat and Piersol [11], Newland [136], and Elishakoff [54]. These books serve as fundamental resources for introducing random load distribution concepts. Regarding TBL excitation, various analytical, numerical, and experimental methods have been employed [30, 46, 74, 100, 103, 116, 125, 130, 175] to investigate the vibration response of planar structures excited by a TBL.

There are several approaches available for determining frequency response functions (FRFs), including the use of finite element (FE) models or analytical models. The dynamic behavior of a structure can be characterized by either a modal expansion technique or a wave-based approach. The modal expansion method is especially effective for low-frequency excitation, where a few dominant modes typically influence the peak responses. As a result, the overall frequency response function can be efficiently expressed as a combination of these individual modal responses [89]. On the other hand, a wave method may be preferable, as it interprets the resonance response predicted by the modal expansion method as the coincident superposition of traveling waves with opposite wave-number vectors, described as incident and reflected waves [58].

Powell [145] introduced the idea of the joint acceptance function to clarify the interaction between the forcing function and the structural modes. Wilby [169] expanded on this concept to investigate the response of simple panels subjected to TBL excitation. During this time, significant research focused on the response of flat plates to TBL, with key contributions from Dyer [50], Maidanik [121], Ribner [151], Maestrello [119, 120], White [168], and Davies [45]. It has been shown that FRFs can be calculated using a modal expansion method, which involves summing the responses of individual modes. In certain cases, FRFs assume an infinite plate model. Strawderman [164] reviewed models of plate vibration induced by turbulent flow, using theories related to both finite and infinite thin plates. The infinite plate model is particularly advantageous for its simplicity in the mathematical development of estimating the power input from the TBL.

In some cases, FRFs are based on the assumption of an infinite plate. Strawderman [164] reviewed models of turbulent-flow-induced plate vibration using theories of both finite and infinite thin plates. The infinite plate model is particularly useful due to its simplicity in the mathematical developments for estimating the power injected by the TBL.

For both finite and infinite structures, representing vibration behavior in the wavenumber domain is beneficial. This approach offers two significant advantages. First, it improves the analytical manageability of the problem and provides complete or partial closed-form solutions, which can significantly reduce computational effort. Second, wavevector-frequency analysis allows for a physical interpretation of the problem, particularly regarding the system's filtering effect. It also shows how certain system characteristics are distributed across wavevector and frequency variables, indicating the rate at which these characteristics change with respect to distance and time [127]. This method was first applied to predict sound radiation from standard geometries like flat, baffled surfaces, as well as spherical and cylindrical shells. Foundational works by Junger and Feit [99], Fahy [58], Skelton and James [95], and William [170] have detailed this approach.

In this approach, the vibro-acoustic response can be interpreted as the outcome of passing the excitation spectrum through a three-dimensional filter (involving frequency and two wavenumber components). This filter is characterized by a sensitivity function that depends solely on the geometrical and mechanical properties of the structure [127]. This function corresponds to the plate's response to a unit wall plane wave [124]. Maury et al. [127, 128] formulated the vibroacoustic response of a panel excited by either an incident dynamic acoustic field or a fully developed turbulent layer analytically. Their work led to the standard representation in the wavenumber domain, as the coupling evaluation is achieved by integrating the product of the sensitivity function and the TBL wavevector spectrum over the wavenumber domain. Fundamental aspects of fluid-loading in vibrating structures are also summarized by Blake [15] and Howe [84].

A critical aspect of this approach is the necessary accuracy for both the excitation model and the wavenumber-frequency sensitivity function of the structure, as well as their relationship. For some infinite structures, where the sensitivity function is precisely known, the accuracy of the excitation model fully determines the accuracy of the calculated system response. However, for finite and complex structures, the accuracy of numerical approximations for the sensitivity function depends on the validity of the model's simplifying assumptions and the quality of the approximation method [127]. Recent studies by Marchetto et al. [124, 125] estimated the sensitivity functions of a simply supported plate using the reciprocity principle and examined the vibrational response of surfaces under a diffuse acoustic field (DAF) and a TBL excitation.

2.2.1 Fluid-Structure Interaction in Wavenumber Domain

Visualizing the spectral contents of both the excitation and the sensitivity function on a graph offers a clear interpretation of the spectral distribution of the system's response. The acoustic wavenumbers and convection wavenumbers are dependent on the angular frequency ω, and they may coincident with each other [114]. Generally, we can say that at low frequency, the convective peak will locate near the $k_x = 0$, and it will coincident with the acoustic domain. In this case, distinguishing the acoustic peak from the convective ridge is difficult. By increasing the frequency, the radius of the acoustic region will increase and also the wavenumber related to the convective ridge will move away from the $k_x = 0$. Accordingly, the acoustic peak can be distinguished from the convective ridge at high frequency [31]. The region between convective region and acoustic domain is called sub-convective domain (see Figure 2.4). Typically, the wavenumber-frequency spectrum of the WPF is characterized by three distinct regions: the convective region, the sub-convective region, and acoustic domain.

The interaction between fluid and structure, alongside the wavenumber-frequency spectrum of WPF, is influenced by the flexural waves (k_f) propagating along the interface of the structure and fluid. The ability of flexural waves to match with the surrounding fluids depends on whether these waves are subsonic (slower than the fluid wave speed) or supersonic (faster than the fluid wave speed). Depending on the excitation frequency, these waves can match with either the acoustic or hydrodynamic waves of the fluid. Hydrodynamic coincidence occurs at the angular frequency ω_c when $k_c = k_f$, while acoustic coincidence occurs at ω_0 when $k_0 = k_f$ [89].

A typical wavenumber-frequency diagram for the surface pressure spectrum $\phi(\mathbf{k}, \omega)$ of a subsonic flow is depicted in Figure 2.10. Flexural waves exhibit dispersion, meaning that their wave speeds increase with frequency. For problems associated with low-speed flows ($M_a \approx 0.1$), convected wavenumbers k_c can be up to two orders of magnitude greater than corresponding acoustical k_0 and structural k_f wavenumbers, as illustrated graphically in Figure 2.10 [89].

For finite panels, the discontinuities at the boundaries cause a superposition of traveling waves with opposing free bending wave vectors, known as standing waves. These standing waves occur at natural or specific frequencies ω_{mn} (associated with discrete wavenumbers k_{mn}), such as $k_f = k_{\text{resonance}}$. Since the panel is finite in both the streamwise and spanwise directions, the standing waves form a two-dimensional regular pattern in wavenumber space. At a given frequency ω, the resonant modes lie on a circle with a radius of k_f. When the wavenumbers of a vibration mode closely align with k_c or k_0, the Fourier transform in space or wavenumber of the structural mode peaks around these wavenumbers, making it more likely to absorb energy from the flow for that particular mode of vibration. This phenomenon, known as panel acceptance, is often referred to as 'wavenumber coincidence' [89].

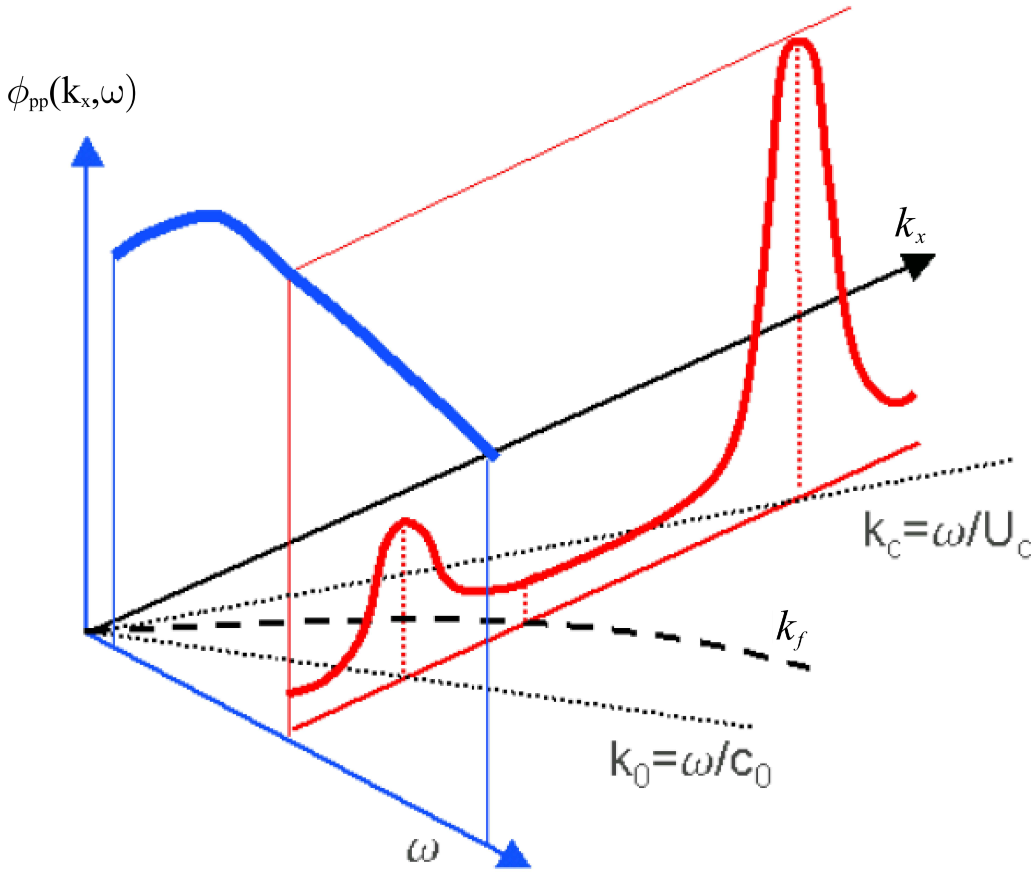

FIGURE 2.10: A schematic wavenumber-frequency diagram of a TBL WPF for a subsonic flow. The standard wavenumber of resonance, $k_{\text{resonance}}$, is acquired at the interface between waves propagating at the free wavenumber, k_f. Figure from [89]

The spatial matching schematic of the wavenumber-frequency spectrum of the TBL WPF, denoted as $\phi_{pp}(k_x, \omega)$, and vibration modal response of the structure, denoted as $\Psi_s(k_x, \omega)$ in a scenario where the fluid's flow velocity equals or exceeds the velocity of structural waves, is shown in Figure 2.11. As discussed in Section 2.2, the vibration response of the structure can be mathematically determined by integrating the product of WPF regions and modal response of the structures in the wavenumber domain [31]. Two main sources of structural vibration are highlighted in shaded areas. In this scenario, the convective wavenumbers in the flow align with the wavenumbers of the bending waves, resulting in hydrodynamic coincidence [114]. This phenomenon is typically observed in high Mach number flows, such as those over cars [31]. Consequently, the vibration of the structure is predominantly induced by TBL excitation at convective wavenumbers.

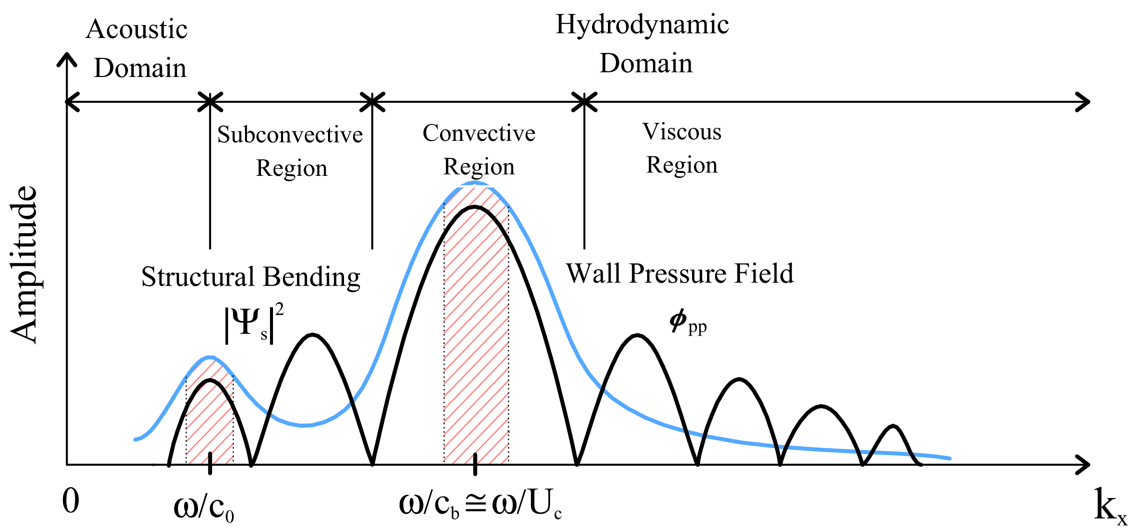

FIGURE 2.11: Schematic of the spatial matching of the wavenumber-frequency spectrum of the TBL WPF and vibration modal function when $U_c \approx c_f < c_0$ (not in scale).

The convective wavenumbers, however, are too high in low Mach number flows associated with structures excited by heavy fluids to match the bending waves of the underlying structure and therefore do not cause significant vibration in these systems [17, 32, 74]. The reason is that the structure acts as a filter, attenuating the excitation from the convective ridge of the TBL at frequencies well above the coincidence frequency. This behaviour is shown graphically in Figure 1.2. In this figure three primary sources of structural vibration are illustrated (shaded areas). These three major parts are responsible for the final vibration data. The first one is the interaction between the amplitude peak of the acoustic spectrum and the corresponding wavenumber in the acoustic domain of the modal function shape. Two other regions are the interaction of convective and modal shape peak with the corresponding wavenumber level of the WPF in the hydrodynamic domain. Vibration response can be approximated by adding these three parts. However, in this situation, structural wavelength occurs in the sub-convective region of the wall pressure spectrum, and the vibration induced by the TBL is mainly dominated by this domain of WPF [94].

This was confirmed by Hambric et al. [74] and Hwang and Maidanik [94], who investigated the vibration response of a baffled flat rectangular plate with various boundary conditions under a low-speed TBL flow excitation. The study revealed that a plate with simply supported or clamped boundary conditions significantly filters out the contribution of the TBL convective ridge to its vibrational response and at high frequencies, where the flexural wavenumber of the plate was lower than the convective wavenumber, the response of the plate with these boundary conditions was mostly due to the wall pressure energy in the low-wavenumber region. Consequently, apart from the low level of wall pressure spectrum beneath an attached TBL in the sub-convective region, these low-wavenumber pressure levels are responsible for structure-born sounds and vibrations in many applications. This highlights the importance of the low-wavenumber WPF in the prediction of flow-induced vibrations.

Theoretically, for a homogeneous incompressible flow over a plane surface, the conservation of mass dictates that the wavenumber spectrum value at $k_x = k_y = 0$ must be exactly zero [22]. Additional considerations based on the pressure Poisson equation suggest that the spectrum should increase as k^2 at low-wavenumbers, a characteristic included in the Chase model [28]. Chase later accounted for acoustic contributions at low-wavenumbers, which altered this result [26]. Nonetheless, if the boundary layer thickness δ is sufficiently large, the Chase model also predicts a wavenumber-white plateau in the intermediate low-wavenumber range, approximately $\delta^{-1} < k_x < 0.1k_c$ (see [118]).

However, experimental measurements [17, 47] have shown that the low-wavenumber values do not vary with κ^2 and tend to support the idea of an approximately plateau. Additionally, because of growing the boundary layer flows over a flat surface, the pressure field near the wall is not completely homogeneous, so this assumption is not valid in real flows, and as a result, other factors may contribute to the low-wavenumber results.

2.2.2 Effect of Different Models on Vibration Response of Structures

The correct spectral values for the subconvective region are still being debated. Therefore, there is a need for further development of precise measurement methods and numerical simulations for identification of the WPF. Historically, the levels of low-wavenumber components of the WPF have been challenging to model and measure due to their low magnitude relative to convective wavenumber pressures and the lack of experimental validation. As shown in Figure 2.9, while different models generally agree on predicting the convective ridge region, there is often significant uncertainty at wavenumbers below the convective ridge. As expected, these differences can lead to different responses for a system simulated by each model.

Based on the Corcos and Chase models, Figure 2.12 shows the acceleration power specteral density of a plate with simply supported boundary conditions subjected to TBL fluctuations [31]. According to this figure, there is a reasonable similarity between the curves around the hydrodynamic coincidence frequency of $f_c = 65$ Hz, but at other frequencies, large differences are observed, with the Corcos model yielding results that are 10 dB higher than those obtained using the Chase model. The reason is that the Corcos wavenumber levels in sub-convective and super-convective regions are much higher than those in Chase model. It is well-known that the Corcos model significantly overestimates levels in the subconvective region, which primarily affects the panel's response at frequencies higher than the hydrodynamic coincidence frequency. However, there is still ongoing debate regarding the correct spectral values, particularly in the subconvective region. This uncertainty justifies the ongoing efforts to develop more accurate measurement devices and numerical simulations for WPF.

Moreover, Hambric and Lysak [73] demonstrated that although both the Corcos and Mellen models can be used for conditions where flexural wavenumber is approximately equal to convective wavenumber ($k_f \approx k_c$), the Corcos model overestimates vibrations for lower k_f/k_c ratios. The overestimates worsen with decreasing k_f/k_c ratio. Based on their numerical comparison, applying the Mellen model with Smolyakov's convection velocities and length scales agree well with the measurements and improves low-frequency accuracy [31].

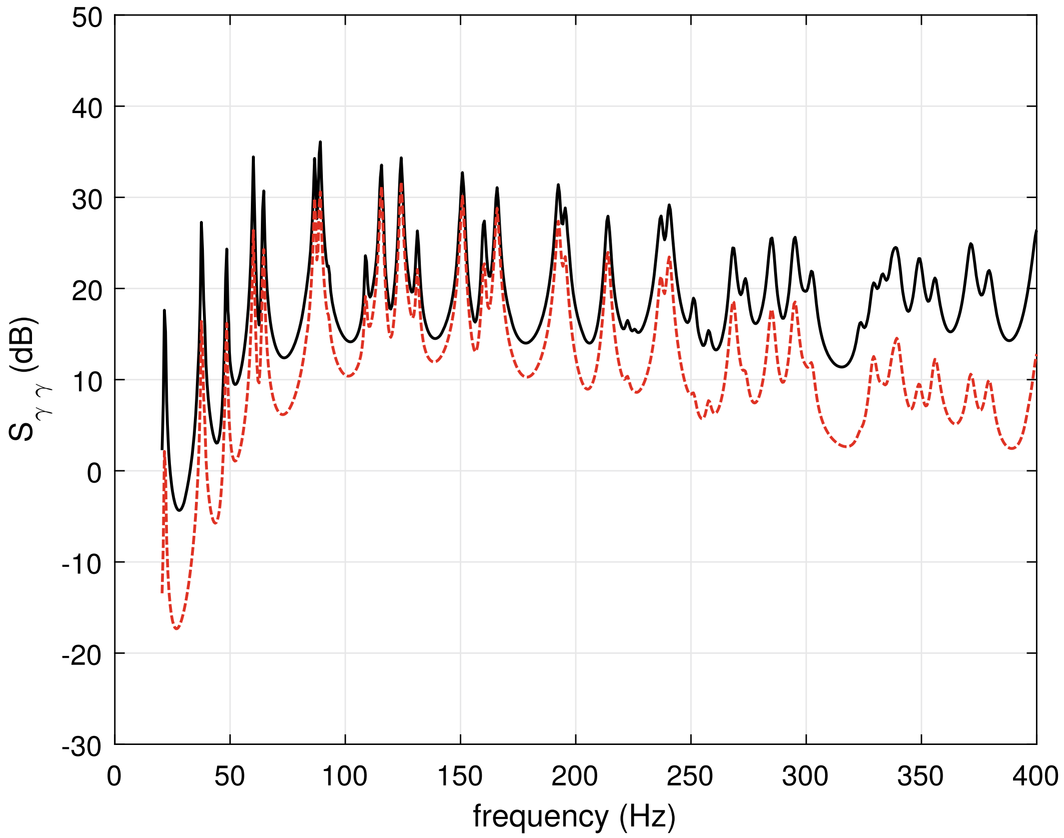

FIGURE 2.12: The acceleration power spectral densities of a simply-supported plate excited by a TBL load simulated using wavenumber-frequency spectra models, with Corcos shown in solid lines and Chase in dashed lines. Figure from [31].

2.3 Methods for Measuring the WPF beneath a TBL

Despite technological advances, measuring wall-pressure fluctuations remains challenging, even for single-point measurements. One of the main challenges has to do with the small turbulent wavelengths that must be resolved by the sensors [31]. Below, we review two approaches, ABA and VBA, for measuring the WPF.

2.3.1 Acoustic-based Approach

Microphone arrays are typically used to measure the WPF. They directly capture the sound waves generated by the WPF. To estimate the WPF, microphones are usually placed near a rigid wall exposed to turbulent flow, recording the sound waves produced by the pressure fluctuations. However, this approach has limitations related to spatial resolution, which is constrained by microphone spacing and configuration. Reducing the spacing between microphones can enhance resolution but often requires more sensors, increasing both cost and setup complexity. Conversely, increasing the distance between sensors may result in the failure to capture all samples of incoming sound waves, leading to a reduction in the resolution of pressure fluctuations. Furthermore, the data recorded in this approach can easily be contaminated by background noise.

There are various ways to measure two-point cross-spectral pressure. One straightforward method used by Panton and Robert [140] is to utilize two microphones and then increase the distance between them along a line. This concept had been further expanded to the point that an array of sensors was used for the first time by Maidanik [122] and was further developed by Blake and Chase [16] and Farabee and Geib [62]. In this approach, the microphones are spaced regularly at specific intervals in a linear streamwise array. Using a linear streamwise equidistant array with intervals of d, they could measure pressure fluctuations around $k_x = \pi/d$ by analyzing alternate microphone outputs. These mode arrays were then used to calculate spectral levels in sonic and subsonic regions by selecting suitable frequencies [31]. Another example of this approach is Abraham and Keith [1] who utilized a linear array of evenly spaced flush-mounted pressure sensors to directly measure the streamwise wavenumber-frequency spectra of the WPF in an acoustically quiet tunnel.

While microphones can record the pressure magnitude of the WPF, spatial aliasing can introduce noise into the measurement [43]. This issue arises due to the finite size of practical sensors and the process of signal averaging over a sensor's surface, which inherently limits the precision of WPF measurements at high frequencies [86]. Consequently, using larger sensors results in reduced resolution for high-frequency pressure fluctuations. Corcos [39] was a pioneer in exploring the relationship between sensor size and the corresponding spectral attenuation based on theoretical foundations. More recently, Hu [86] introduced a correction model to address high-frequency attenuation associated with sensor size when measuring WPF beneath the TBL.

Aliasing occurs in any array where sensor spacing cannot resolve the smallest turbulent scales [31]. The results of using a large number of sensors were presented by Manoha [123] and Bermer [18] to alleviate the aliasing effect. For example, wavelengths of acoustic waves for a flow with a convective velocity of $U_c = 34$ m/s are typically ten times larger than those of the most powerful hydrodynamic waves [31]. Therefore, based on the fluid velocity and frequency of interest, there is a requirement to use many sensors. In order to comprehensively capture the spatial characteristics of the two-point cross-spectrum of the WPF, which can subsequently undergo Fourier transformation to generate the wavenumber-frequency spectrum of wall pressure, an alternative methodology was introduced [7, 156]. In this technique, transducers were deployed in an array spanning the diameter of a disk, arranged along a line that can be rotated to various angular positions. The technique of using large arrays and small sensors has enabled investigators to create clear maps illustrating the convective ridge and acoustic cone [8]. For example, on a wall embedded under a TBL, Arguillat et al. [8] mounted 63 pressure microphones with different sizes across an antenna disk that could be rotated to different positions. They rotate the disk in various positions to calculate the two-point cross-spectrum characteristic of TBL flow. Then they calculated the wavenumber frequency spectrum of the WPF by measuring the spatial dependence of that computed cross-spectrum. By transforming data that comes from space-frequency measurements into wavenumber-frequency spectra, original post-processing has been implemented to separate the acoustic and the aerodynamic effects. A schematic of the test channel mounted on the outlet of the wind tunnel and the measured wavenumber-frequency spectrum is shown in Figure 2.13.

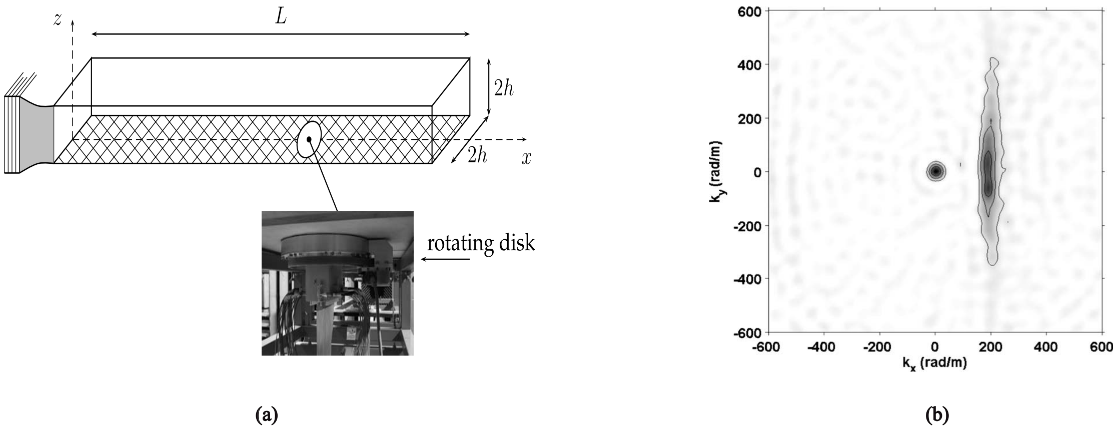

FIGURE 2.13: (a) Test channel mounted on the outlet of the wind tunnel and (b) measured spectrum at $f = 1000$ Hz in the wavenumber domain. Figure from [8].

It should be noted that a periodic arrangement of microphones is not the best choice since it causes redundant distances between sensors [81]. The number of sensors would be greatly increased if wavenumber aliasing were to be avoided by following the Shannon-Nyquist criterion. This criterion states that the distance between two close sensors should be kept smaller than half of the minimum effective wavelength in the TBL flow

[31]. Various techniques have been proposed to optimize array efficiency. One of the most common techniques is using an array with a spiral shape [49]. The advantage of using a non-equidistant array was studied by Haxter and Spehr [81] in 2014. They evaluated the efficiency of equidistant and non-equidistant array patterns in detecting a single source in the wavenumber domain. Figure 2.14 illustrates these two types of patterns. In the array on the left, the transducers are equidistantly spaced $\Delta x = \Delta y = 0.1$m, but in the array on the right, the transducers are not equidistantly spaced. They showed that opposed to the non-equidistant spaced array pattern, the equidistant array has amplitudes on the side lobes identical to that of the main lobe. In other words, the non-equidistant spacing of the transducers has the capability to transfer aliasing effects at a greater wavenumber than in the equidistant array. Wavenumber spectrum from the wind tunnel test were shown in Figure 2.15 for $f = 1480$ Hz and $f = 2454$ Hz. The convective region is dominant in both frequencies, but the acoustic region is more evident at lower frequencies. In addition to Nyquist criterion and array pattern, the co-array size plays an important role in the array performance [31]. Co-array describes the number of different cases where the distance between every pair of sensors is unique [166]. As an example in [166], for a square array with 64 sensors, the maximum possible number of separation with one pair of sensors is 4033 which 225 of them are only unique. More recently, Schram et al. [158] applied a similar procedure to Ref. [81] and used 64 microphones on a rotatable disk to minimize the number of rotation angles and acquisition time while providing a relatively uniform sampling of the co-array plane.

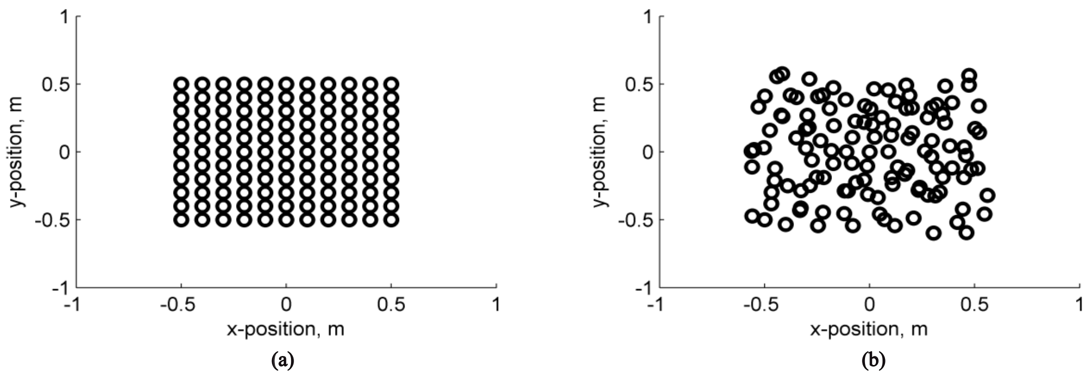

FIGURE 2.14: (a) equidistant transducer distribution and (b)non- equidistant transducer distribution. Figure from [81].

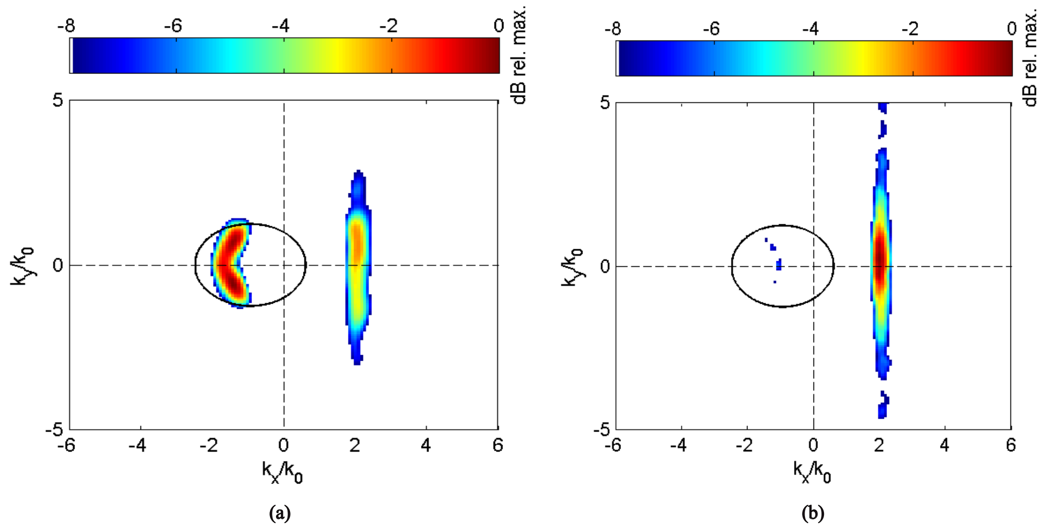

FIGURE 2.15: Wavenumber spectrum from the wind tunnel test at (a) $f = 1480$ Hz and (b) $f = 2454$ Hz. Figure from [81].

Measuring the wavenumber spectra is difficult, especially in the sub-convective and acoustic domains. In an array, the size of the main lobe is inversely proportional to the diameter; as an example, the corresponding disk diameter to an acoustic wavelength of frequency 1.4 kHz is approximately 25 cm [31]. Therefore, using directly the Fourier transform of the measured cross-correlations to resolve the acoustic section information of the fluid flow with the wavenumber spectrum below say 2 kHz will be very difficult [31].

To address these issues, advanced signal processing techniques have been developed to extract the WPF information [31, 177]. This enables the direct measurement of pressure fluctuations, offering detailed information about the pressure field's characteristics [82]. One widely used signal processing technique is beamforming, which combines microphone outputs to form a directed or focused sensitivity beam. This enhances the desired signal while suppressing interference and noise from other directions. Various beamforming techniques are discussed in [102, 132, 157].

Another method often used to boost an array's low-frequency resolution is deconvolution, which is developed to compute the inverse of the ill-posed of the array's point spread function (PSF). Since wavenumber-frequency spectrums are positive quantities by definition, one can use the DAMAS algorithm (introduced by Brooks et al. [20]) or its variants effectively since they are developed based on a deconvolution algorithm with a positive preconditioning value.

The first attempt at implementing the deconvolution method to estimate WPF was made by Ehrenfield and Koop [53] in 2008. Figure 2.16 illustrates the experimental setup used to measure the wavenumber-frequency spectrum. They measured the WPF beneath a compressible TBL at a high subsonic Mach number of $M_a = 0.85$ using a sparse array of 48 pressure transducers (Figure 2.16 (a)). They applied the infinite beamforming technique and DAMAS2 deconvolution algorithm to deconvolve the wavenumber-frequency spectrum from the surface pressure array data. They only detect the domains associated with convective peak and acoustic peak in their studies. The contour plot of the beamforming output map at $f = 1172$ Hz is illustrated in Figure 2.16 (b). The wavenumber spectrum in Figure 2.18 indicates the presence of acoustic waves and convective ridge within the wavenumber spectrum. Those sources propagating at speeds equal to or higher than the speed of sound are positioned in an elliptical acoustic domain in the two plots. The results indicate that convective fluctuations dominate at higher frequencies, while acoustic fluctuations prevail at lower frequencies. They also demonstrated that the cross-spectral density of homogeneous pressure fields depends only on the sensor separation vector and not on the absolute coordinates of each sensor. In other words, the repetition of a large number of the same separation in an equidistant transducer array has a side effect on determining a wide range of scales. Typically, the non-equidistant transducer arrays (co-array) are designed to optimize the number and distribution of separation vectors. Their results showed that the acoustic noise is particularly dominant in the lower frequencies.

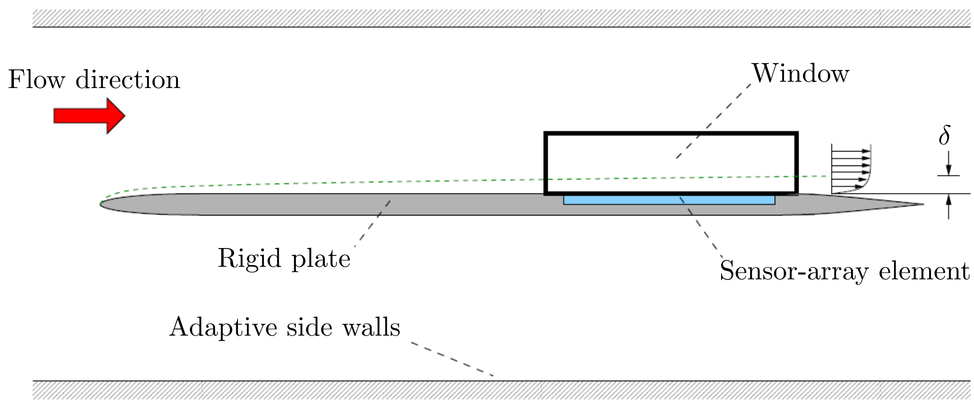

FIGURE 2.16: Sketch of the experimental setup: side view of the plate in the test section. Figure from [53].

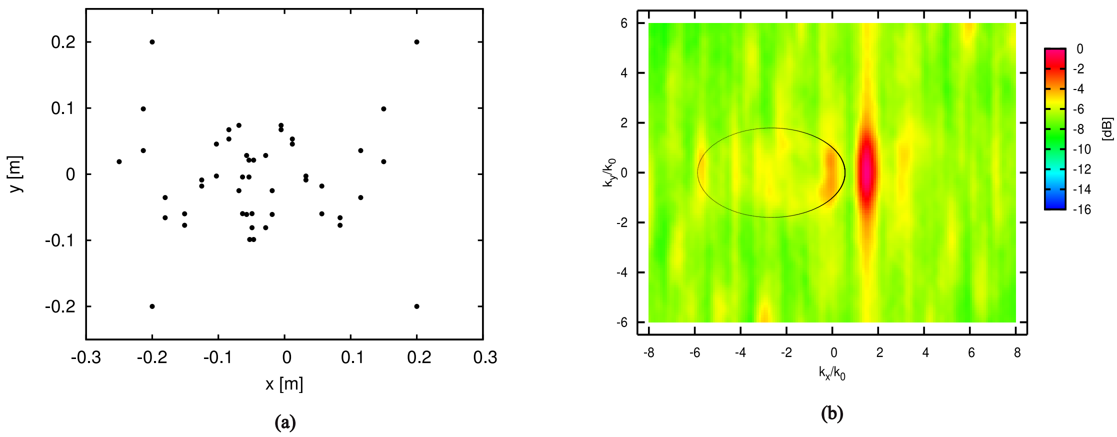

FIGURE 2.17: (a) Layout of the sensor array with 48 sensor positions and (b) beamforming output map at $f = 1172$ Hz. Figure from [53].

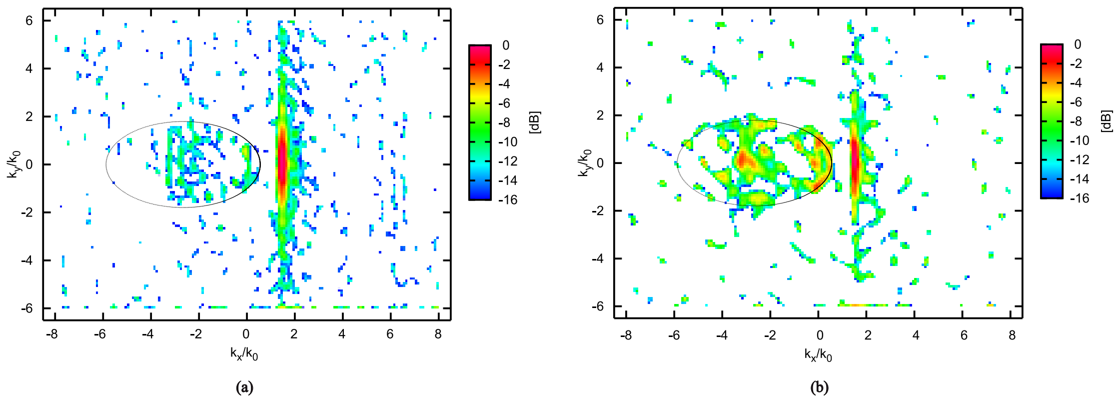

FIGURE 2.18: Wavenumber-frequency spectrum for (a) $f = 1758$ Hz and (b) $f = 1172$ Hz. Figure from [53].

In 2017, Haxter et al [80], conducted a study that built upon the work of Ehrefried and Koop [53] by using the same microphone array arrangement to obtain the phase velocity of TBL pressure fluctuations at high subsonic Mach number from wind tunnel data affected by strong background noise. They used a method called CLEAN-SC to remove the dominant existing acoustic signals and their coherent parts in the beamforming map, which improved the accuracy of their results. Additionally, as shown in Figure 2.19, Prigent et al. [147] used beamforming and DAMAS deconvolution techniques to process a synthetic field consisting of a diffuse acoustic field and the Corcos WPF model. To estimate the WPF, they utilized an aligned microphone array with a rotating configuration. Although the approach has limitations, including noisy data, it can highlight a new path for a much better analysis of the sub-convective and acoustic region of WPF.

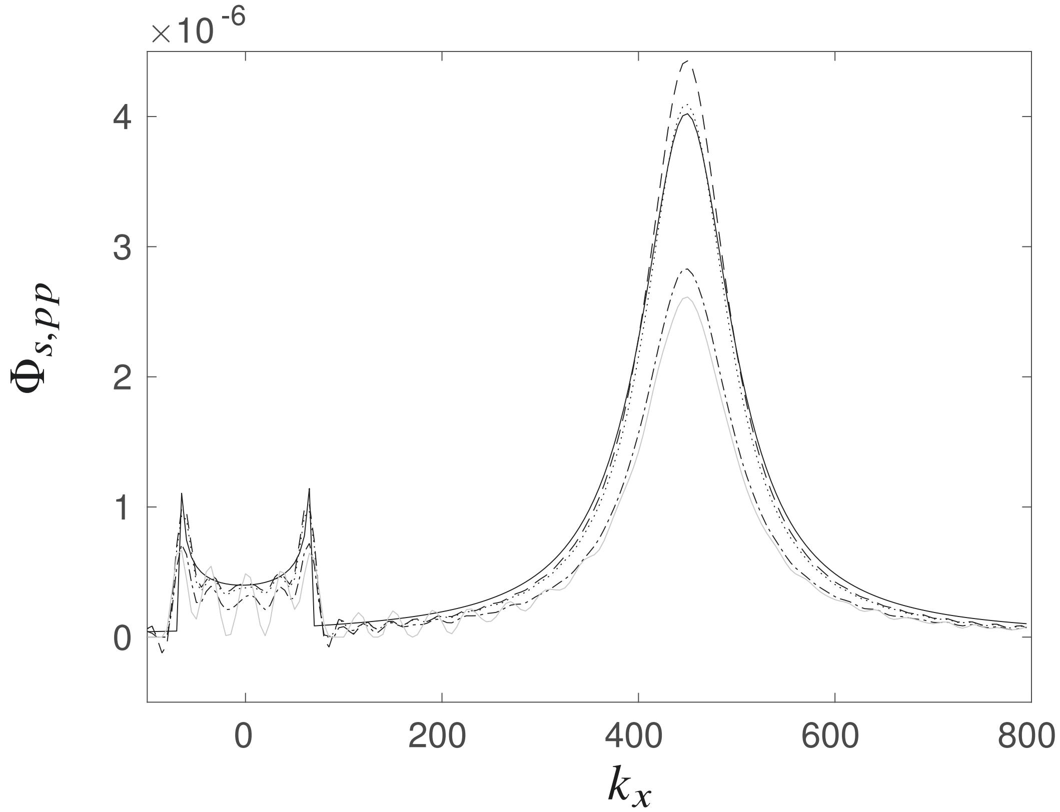

FIGURE 2.19: Examination of DAMAS2 algorithm in the estimation of WPF at $k_y = 0$. Figure from [147].

In order to assess the structural vibrations induced by a high-speed flow, Zhao et al. [177, 178] proposed and developed an improved technique for the prediction of the WPF. They used a conventional phased array technique to specify the wavenumbers of the WPF and noise. The concept is introduced with an integrated expression for WPF in a variety of situations. Then, a modified subsection approaching method is used to separate the pressure fluctuations from the noise. An array design with variable spacing is proposed in order to improve the precision of the count calculations for pressure fluctuation separations. To improve the low-frequency wave number resolution, they used a newly proposed method named the accelerated focusing method (AFM).

In this study, the researchers used the beamforming algorithm to plot the wavenumber spectrum maps for different array patterns at $f = 5000$ Hz and compared the results to the theoretical wave number of the pressure fluctuations and noise. They showed that the circular arrays have a higher wavenumber resolution. However, it is essential for the circular array design to account for the side lobe of the wavenumber graph. By using a multiple-spiral array, they demonstrated that beam boundaries can be shown clearly, which is helpful for recognizing correlations. To provide evidence of the validity of the proposed method, they conducted a wind tunnel test.

In order to investigate the characteristics of flow-induced WPF, Zhao and Lei [179] conducted measurements in a hyper-sonic wind tunnel. They measured the wall pressure variations using a linear sensor array and used a beamforming algorithm to identify spatial correlations of the pressure fluctuations. Their research focused on the significant characteristics of convective and acoustic modes for WPF arising from laminar flow, transitions, and fully developed turbulence.

Recently, Damani et al. utilized a Kevlar-covered acoustic resonator-based cavity sensor for capturing the low-wavenumber components of WPF beneath a TBL flow [42]. These sensors possess an innate ability to filter the convective pressure fluctuations owing to their physical dimensions. Their investigation primarily focused on streamwise wavenumber-frequency spectrum outcomes, presuming the flow to be temporally stationary and spatially homogeneous in the flow direction. They noted that the spatial averaging characteristics of these sensors are not uniformly distributed across the surface area. However, the membrane-like characteristics of the Kevlar scrim indicate a gradual decrease in sensitivity towards the edges of the sensors, posing a challenge in optimizing these sensors for sub-convective pressure measurements [44]. Recognizing the limitations of Kevlar-covered sensors, Damani et al. pursued an alternative approach by employing multiple-neck Helmholtz resonator-based sensors [44]. These sensors offer a more precise and predictable response to grazing flow and acoustics, providing an enhanced method for measurement. They investigated a measurement technique utilizing large sensors and a large array. The discrepancies between their predictions and the measured data were suspected to stem from differences between the true spatial sensitivity of the sensor and its modeled form, as well as variations in sensor dynamic response in the presence of grazing flow. Comparisons with existing wall pressure models, they revealed that pressure levels in the low-wavenumber domain are about 45 dB lower than the convective pressures.

2.3.2 Vibration-based Approach

Another approach for evaluation of the low-wavenumber WPF is based on measuring the vibroacoustic responses of a structure excited by a TBL and then using the measured data to reconstruct the low-wavenumber WPF from an inverse method. This approach takes advantage of the structure's wavenumber filtering capabilities, reducing contamination of the low-wavenumber domain by the convective region as it occurs in the acoustic approaches. Another benefit of this approach is that it is non-intrusive as the accelerometers can be placed on the side of the structure opposite to the one excited by the fluid flow, therefore not impacting the turbulent flow. Consequently, there is no need to drill holes in the structure to have flush-mounted sensors as required by the ABA.

Jameson pioneered the use of a vibration-based approach to measure the amplitude of the WPF in the low-wavenumber domain [97]. Employing a carefully designed rectangular clamped plate, he minimized contributions from the convective peak of the TBL pressure, ensuring that the low-wavenumber components of the WPF matched the wavenumber of the plate's bending waves. Jameson made the assumption that the spectral density in the low-wavenumber frequency domain is symmetric (i.e. in k_x, k_y, and ω). He utilized the individual modes of the clamped plate to create a theoretical framework for the average power within each mode. Subsequently, he employed the accelerometer output as an indicator of modal response to estimate the level of the low-wavenumber spectral components in the TBL wall pressure. In 1977, Martin and Leehey employed a flexible membrane excited by a turbulent airflow as a spatial filter to capture the wavenumber components of the WPF, specifically focusing on ranges far below the convective region but above the acoustic region [126]. In their experiment, they used a non-contact optical sensor to monitor the displacement response at the center of the membrane. They assumed that the WPF in the low-wavenumber range is uniformly flat. By applying spatial Fourier transformation to the observed mode shape, they effectively translated the modal response to the wavenumber domain. Subsequently, they computed the low-wavenumber components of unsteady surface pressure based on the spatial-wavenumber response of the structure and its resonance characteristics. Finally, they compared the measured displacement response with data from modal analysis of the membrane. Comparing the estimated low-wavenumber WPF in the Martin and Leehey's work to those obtained by Blake and Chase in the same wind tunnel [16] and Jameson using an acoustic-based approach [96], it was observed that the Blake's estimation exceeded the magnitude of the Martin and Leehey's estimated WPF in the low-wavenumber domain. Whereas, the estimated low-wavenumber WPF by Martin and Leehey surpassed that of Jameson's.

These studies laid the foundation for subsequent experiments. For instance, Boness et al. [17] and Evans et al. [56] estimated the TBL surface pressure levels at low-wavenumbers for both smooth and rough surfaces. To minimize the effect of background noise on the measurement data, they used a reservoir of water to drive flow through the pipe instead of using a water circulating pump. In Figure 2.20, two views of the experimental test section and the flow measurement layout used by Bonness et al. [17] are shown. They used an accelerometer array mounted on external surface of a water pipe, and then the measured vibration of the pipe due to the internal WPF excitation was used in an iterative inverse method to identify the WPF. A flush-mounted wall pressure sensor array consists of two lines of sensors, with one array parallel to the flow and the other array perpendicular to the flow. The modes of the cylinder act similarly to Martin's and Leehey's membranes by reacting to fluctuating boundary layer pressures at finite frequencies. In order to compute the modal force, they assumed a constant pressure spectrum level in the low-wavenumber range around the modal wavenumber. An analytical formulation for the modal force as a function of the TBL wavevector-frequency spectrum and the computed sensitivity functions (obtained from experimental modal analysis) were used. This was then used to compute the frequency response function for each individual mode. Next, the low-wavenumber TBL pressure levels were fine-tuned to align the computed vibration data with the measured data. Finally, the measured low-wavenumber pressure data was compared with findings from other studies. The low-wavenumber pressure data measured in this study were compared with those calculated from TBL models by Smol'yakov, Chase, and Corcos (Figure 2.21). The results for the smooth pipe indicated that the measured data fell between the predicted results from the TBL models by Chase [27] and Smolyakov [162], registering a few decibels below the lower bounds reported in related measurements in air by Farabee and Geib [59] and Martin and Leehey [126]. However, the pressure levels for fully rough conditions exhibited a 13 dB increase in low-wavenumber wall pressure compared to a hydraulically smooth surface.

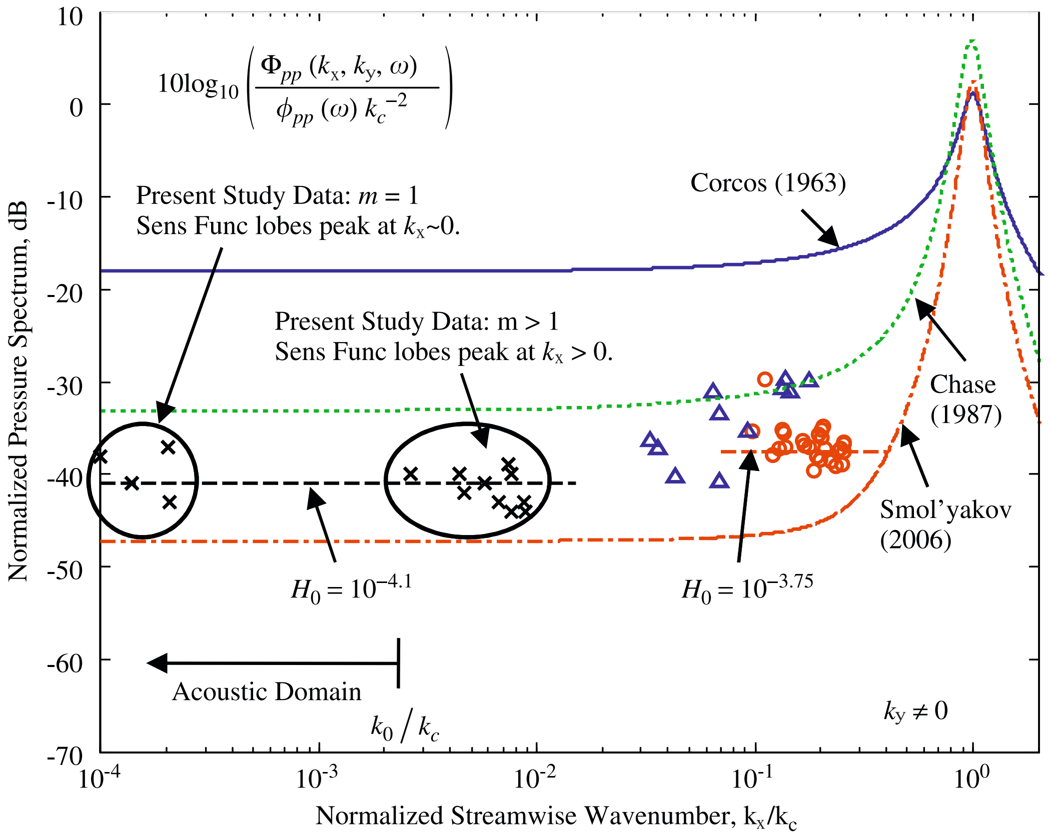

FIGURE 2.20: Experimental test-section and flow measurement layout: (a) reference noise sensors and accelerometer array and (b) reference noise sensors and pressure sensor array. Figure from [17].

In 2014 Lecoq et al. [114] utilized the Force Analysis Technique (FAT) to localize the acoustic components of DAF along with convective peak of turbulent wall pressure numerically. To estimate the excitation, they initially computed the plate's displacement field and then incorporated it into the equation of motion, with spatial derivatives calculated using a finite difference method. Introducing some noise to the displacement to simulate experimental conditions, they demonstrated that the FAT method could effectively localize the acoustic region of the excitation. Moreover, Leclere et al. [113] recently compared results obtained from acoustic-based and vibration-based approaches for separating and analyzing TBL and acoustic contributions. They utilized a beamforming technique to pinpoint the convective zone and acoustic peak.

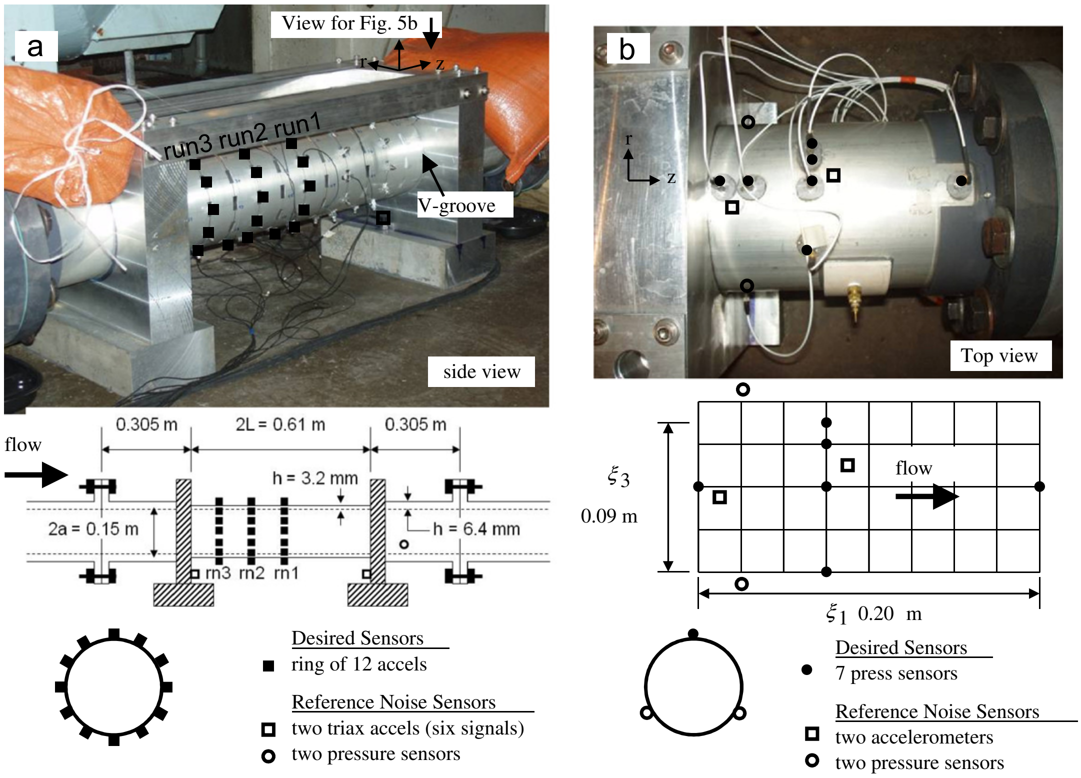

FIGURE 2.21: Measured low-wavenumber pressure spectrum levels as a function of non-dimensional wavenumber: $\times$ present study, Δ Farabee and Geib data; $\circ$ Martin and Leehey data. Figure from [17].

2.4 Summary

The literature review, as discussed in Section 2.1, highlights the existence of numerous semi-empirical models aimed at simulating the WPF beneath a TBL. In scenarios involving structures exposed to high-speed flows, the convective region of the WPF beneath a TBL significantly influences their vibration characteristics. However, as inferred from the review from Section 2.2, structures experiencing low Mach number flows tend to filter out the convective domain of WPF. In such cases, WPF excitation necessitates considering both hydrodynamic and acoustic contributions, with the primary cause of vibration being attributed to the acoustic domain and low-wavenumber components (or sub-convective domain) of the WPF. However, due to the challenge in modeling and measuring the low levels of low-wavenumber components relative to the convective wavenumber pressures, along with a lack of experimental verifications, accurately capturing these levels poses significant difficulties. Consequently, there is substantial variation among the WPF models presented by researchers in the low-wavenumber region, indicating a need for further investigation. Through the methods outlined in Section

2.3, an effective approach to estimating the low-wavenumber components of WPF can be established. This research project aims to address this gap, presenting a numerical investigation into the estimation of WPF in the low-wavenumber domain in subsequent chapters.

Chapter 3

Estimation of the Low-wavenumber WPF beneath a TBL using a Microphone Array

This chapter highlights the challenges of using an array of microphones for estimating the low-wavenumber region of TBL WPF. Most previous studies have primarily focused on identifying the convective ridge and acoustic peak. Moreover, the importance of the low-wavenumber domain in the vibration of structures subjected to turbulent flow as well as the significant discrepancies between different existing TBL models for this region are the main motivations for this work. The analytical formulation is detailed in Section 3.1, where it is assumed that a microphone array is flush-mounted on a rigid surface over which a TBL flows. A regularized Fourier-based approach (RFBA) is proposed to numerically study the estimation of the low-wavenumber WPF. This approach relies on the inverse Fourier transform (IFT) expression that links the CSD of the pressure in both physical and wavenumber spaces. The discretization of the integral in this expression is achieved using the rectangular rule, which results in a linear matrix system. An adapted regularization technique is then used to invert this system and estimate a stable solution. To assess the capability of the RFBA in estimating the low-wavenumber components of the WPF, numerical simulations of a TBL excitation are conducted, and the WPF estimated by the RFBA using a microphone array is compared with the reference WPF of a closed-form input TBL model. Considering this process, the effect of number of sensors, array pattern, co-array factor and data averaging on the estimated WPF are examined. The findings are presented in Section 3.2. Initially, the equidistant cross-array pattern (3.2.1.1) is analyzed to estimate the low-wavenumber WPF and examine the impact of the Nyquist criterion on the WPF estimation in this domain. Next, the non-equidistant cross-array pattern (3.2.1.2) is evaluated to explore the effect of the co-array on the WPF estimation in the low-wavenumber range. Finally, an irregular array pattern (3.2.1.3) is considered to assess the influence of sensor distribution on the WPF estimation in the low-wavenumber domain. Moreover, to mimic experimental measurements, a virtual acoustic experiment is proposed, involving the synthesis of snapshots of the TBL-induced WPF (3.2.2). These snapshots are generated by employing so-called uncorrelated wall plane wave (UWPW) technique [129]. Performance of the RFBA on estimating the WPF in the low-wavenumber domain is evaluated based on this virtual experiment. Finally, this chapter concludes with a summary of the findings in Section 3.3. It is demonstrated that although with relatively small number of snapshots the convective region can be identified, a significant number of snapshots is required to well estimate the TBL low-wavenumber region.

This chapter is based on the article "On the challenges of estimating the low-wavenumber wall pressure field beneath a turbulent boundary layer using a microphone array", published in the *Journal of Sound and Vibration* [2].

3.1 The Regularized Fourier-Based Approach

This section covers the theoretical formulation of the regularized Fourier-based approach to estimate the WPF in the wavenumber domain using pressure measurements obtained from microphones. Figure 3.1 shows a network of N_s flush-mounted microphones that are installed on a rigid surface. They are distributed within a rectangular area measuring $a \times b$. The position of each microphone is determined by the coordinates $\mathbf{x}_i$, denoted as (x_i, y_i) for $i \in \{1, N_s\}$. The sensors are used for recording the WPF beneath a TBL. The TBL is assumed to be homogeneous, stationary and fully developed over the surface. The x-axis is considered parallel to fluid flow with a constant free stream velocity of U_∞.

The wavenumber-frequency spectrum $\phi_{pp}(k_x, k_y, \omega)$ of the wall pressure $p(x, y, t)$ can be expressed as follows [53]

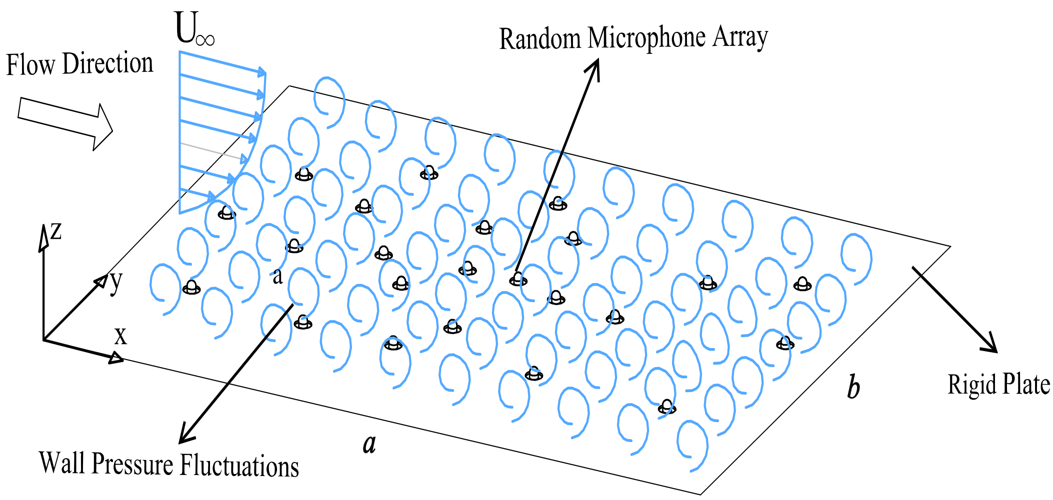

FIGURE 3.1: Schematic representation of a microphone array mounted within a rectangular area with dimensions a in length and b in width to measure wall pressure fluctuations from the TBL.

$$\phi_{pp}(k_x, k_y, \omega) = \frac{1}{4\pi^2} \int_{-\infty}^{\infty} \int_{-\infty}^{\infty} R_{pp}(\xi, \eta, \omega) e^{-\mathrm{j}(k_x \xi + k_y \eta)} \,\mathrm{d}\xi \mathrm{d}\eta, \tag{3.1}$$

where (ξ, η) are the distances between two points in the (x, y) plane, ω is the angular frequency, $\mathrm{j} = \sqrt{-1}$ is the imaginary unit, and k_x, k_y are wavenumber components in the streamwise and spanwise direction, respectively. $R_{pp}(\xi, \eta, \omega)$ is the temporal Fourier transform of the space-time correlation function of wall pressure given by [53]

$$R_{pp}(\xi, \eta, \omega) = \frac{1}{2\pi} \int_{-\infty}^{\infty} G_{pp}(\xi, \eta, \tau) e^{\mathrm{j}\omega\tau} \,\mathrm{d}t, \tag{3.2}$$

$$G_{pp}(\xi, \eta, \tau) = \langle p(x, y, t)\, p(x + \xi, y + \eta, t + \tau) \rangle, \tag{3.3}$$

where the angle bracket $\langle \cdots \rangle$ denotes the mathematical expectation. The IFT of the Eq. (3.1) can be used to determine how the wavenumber spectrum $\phi_{pp}(k_x, k_y, \omega)$ relates to $R_{pp}(\xi, \eta, \omega)$

$$R_{pp}(\xi, \eta, \omega) = \int_{-\infty}^{\infty} \int_{-\infty}^{\infty} \phi_{pp}(k_x, k_y, \omega) e^{\mathrm{j}(k_x \xi + k_y \eta)} \,\mathrm{d}k_x \mathrm{d}k_y. \tag{3.4}$$

By employing a rectangular integration method over a truncated wavenumber domain, one can approximate $R_{pp}(\omega)$ between two points $\mathbf{x}_i$ and $\mathbf{x}_j$ as follows

$$R_{pp}(\xi_{i,j}, \eta_{i,j}, \omega) \approx \sum_{l=1}^{N_k} \phi_{pp}(k_{x,l}, k_{y,l}, \omega)\, e^{\mathrm{j}(k_{x,l}\xi_{i,j} + k_{y,l}\eta_{i,j})}\, \delta k_x \delta k_y, \tag{3.5}$$

where $(\xi_{i,j}, \eta_{i,j}) = (x_i - x_j, y_i - y_j)$ with $i, j = 1, 2, \ldots, N_s$ and $\delta k_x, \delta k_y$ are the wavenumber resolutions in the streamwise and spanwise directions, respectively, and $N_k = N_{k_x} \times N_{k_y}$ corresponds to the total number of grid points in the truncated wavenumber space, and each vector index l is assigned uniquely to a grid point $(k_{x,l}, k_{y,l})$. A cut-off wavenumber is defined to take into account the convective contributions of the TBL WPF (see Section 3.2). Eq. (3.5) can be represented in matrix notation as follows

$$\mathbf{S}_{pp} = \mathbf{Q}\Phi_{pp}, \tag{3.6}$$

where $\mathbf{S}_{pp}$ is a vector consisting of the cross-spectrum elements and Φ_{pp} is a vector consisting of the unknown WPF components in the truncated wavenumber space as follows

$$\mathbf{S}_{pp} = \begin{bmatrix} R_{pp}(\xi_{1,1}, \eta_{1,1}, \omega) \\ R_{pp}(\xi_{1,2}, \eta_{1,2}, \omega) \\ \vdots \\ R_{pp}(\xi_{i,j}, \eta_{i,j}, \omega) \\ \vdots \\ R_{pp}(\xi_{N_s,N_s-1}, \eta_{N_s,N_s-1}, \omega) \\ R_{pp}(\xi_{N_s,N_s}, \eta_{N_s,N_s}, \omega) \end{bmatrix}_{N_s^2 \times 1}, \boldsymbol{\Phi}_{\mathbf{pp}} = \begin{bmatrix} \phi_{pp}(k_{x,1}, k_{y,1}, \omega) \\ \phi_{pp}(k_{x,1}, k_{y,2}, \omega) \\ \vdots \\ \phi_{pp}(k_{x,l}, k_{y,l}, \omega) \\ \vdots \\ \phi_{pp}(k_{x,N_{k_x}}, k_{y,N_{k_y}-1}, \omega) \\ \phi_{pp}(k_{x,N_{k_x}}, k_{y,N_{k_y}}, \omega) \end{bmatrix}_{N_k \times 1} \tag{3.7}$$

The components of $\boldsymbol{\Phi}_{\mathbf{pp}}$ are organized such that the first N_{k_y} components correspond to $\phi_{pp}(k_{x,1}, k_{y,l}, \omega)$ with $l \in \{1, N_{k_y}\}$, the next N_{k_y} components correspond to $\phi_{pp}(k_{x,2}, k_{y,l}, \omega)$ with $l \in \{1, N_{k_y}\}$, and so on. Also, for a microphone array with N_s sensors, the elements of $\mathbf{S}_{pp}$ can be measured for the discrete separations of sensors, $(\xi_{i,j}, \eta_{i,j})$, which the first N_s components correspond to $R_{pp}(\xi_{1,j}, \eta_{1,j}, \omega)$ with $j \in \{1, N_s\}$, the next N_s components correspond to $(\xi_{2,j}, \eta_{2,j}, \omega)$ with $j \in \{1, N_s\}$, and so on. Besides, $\mathbf{Q}$ is the matrix with the following elements

$$\mathbf{Q} = \delta k_x \delta k_y \begin{bmatrix} e^{\mathrm{j}(k_{x,1}\xi_{1,1}+k_{y,1}\eta_{1,1})} & e^{\mathrm{j}(k_{x,1}\xi_{1,1}+k_{y,2}\eta_{1,1})} & \cdots & \cdots & e^{\mathrm{j}(k_{x,N_{k_x}}\xi_{1,1}+k_{y,N_{k_y}}\eta_{1,1})} \\ e^{\mathrm{j}(k_{x,1}\xi_{1,2}+k_{y,1}\eta_{1,2})} & \ddots & & & \vdots \\ \vdots & & e^{\mathrm{j}(k_{x,l}\xi_{i,j}+k_{y,l}\eta_{i,j})} & & \vdots \\ \vdots & & & \ddots & e^{\mathrm{j}(k_{x,N_{k_x}}\xi_{N_s,N_s-1}+k_{y,N_{k_y}}\eta_{N_s,N_s-1})} \\ e^{\mathrm{j}(k_{x,1}\xi_{N_s,N_s}+k_{y,1}\eta_{N_s,N_s})} & \cdots & \cdots & & e^{\mathrm{j}(k_{x,N_{k_x}}\xi_{N_s,N_s}+k_{y,N_{k_y}}\eta_{N_s,N_s})} \end{bmatrix}_{N_s^2 \times N_k} . \tag{3.8}$$

Considering Eq. (3.6), we arrive at N_s^2 equations for the N_k unknown coefficients. In most cases, the number of unknowns N_k exceeds the number of equations N_s^2. Eq. (3.6) is therefore an under-determined system and the system of equations has no unique solution. Using the Moore-Penrose inverse of matrix $\mathbf{Q}$ can yield a solution with minimal 2-norm, but the problem posed by Eq. (3.4) is equivalent to a first-kind Fredholm integral equation that is known to be ill-conditioned [76]. Hence, the inversion method derived from the discretization of the Riemann integral formula leads to a severely ill-conditioned linear system (i.e., Eq. (3.6)) with many tiny singular values. This means applying the Moore-Penrose inversion using singular value decomposition (SVD) generates inadequate results. Since matrix $\mathbf{Q}$ can contain small rounding errors due to computer calculation and vector $\mathbf{S}_{pp}$ can contain errors induced by measurement in practice, the ill-conditioning of $\mathbf{Q}$ can greatly amplify these errors, resulting in erroneous results. However, adapted regularization techniques can produce useful stabilized solutions [12, 23, 76]. The goal of regularization theory is to provide proper side constraints with optimal weights so that the regularized solution is a good approximation of the unknown solution.

There are several types of inverse algorithms that differ primarily in what kind of regularization for reconstruction process is used and how the regularization parameter is computed [76]. Some of the most common methods include:

- Tikhonov regularization: This method adds a small regularization term to the matrix, which helps to stabilize the solution and reduce the sensitivity to small perturbations in the input data [64].
- Pseudoinverse: The Moore-Penrose pseudoinverse is a generalization of the inverse matrix that can be used for non-square matrices. It can be calculated using the SVD or the QR decomposition [67].

- Truncated SVD: This method uses the SVD to decompose the matrix into its singular values and singular vectors. It then truncates the singular values below a certain threshold, effectively reducing the rank of the matrix and making it less ill-posed [67].

- Conjugate Gradient Method: It is an iterative method that solves a system of linear equations. It can be used to find an approximate inverse of a matrix [137].

- Ridge Regression: It is a variation of linear regression, It can be used to find an approximate inverse of a matrix [78].

Moreover, there are several methods for determining the optimal value of the regularization parameter in an inverse problem, including:

- Cross-validation [78]: This is one of the most widely used methods. It involves dividing the data into a training set and a validation set, and using the training set to determine the regularization parameter. The performance of the model is then evaluated on the validation set for each value of the regularization parameter, and the value that results in the best performance is chosen as the optimal value.

- L-curve method [75]: The L-curve is a plot of the solution norm versus the data misfit norm, where the solution norm represents the smoothness of the solution and the data misfit norm represents the fit to the data. The L-curve method consists in finding the corner of the L-curve, which is the point on the L-curve where the curvature changes. The regularization parameter that corresponds to the corner of the L-curve is chosen as the optimal value.

- Generalized cross-validation (GCV) [66]: This method is an extension of cross-validation that takes into account the degrees of freedom of the solution. GCV uses an estimate of the degrees of freedom to adjust the cross-validation score, and it is particularly useful when the data is noisy.

- Bayesian methods [63]: This method involves using a prior probability distribution on the solution to determine the regularization parameter. The prior distribution is used to encode prior knowledge or assumptions about the solution, and the regularization parameter is chosen to balance the fit to the data with the prior distribution.

- Discrepancy principle [55]: This method involves choosing the regularization parameter such that the solution is close to the data, but not too close. The regularization parameter is chosen to be the smallest value such that the solution and the data differ by a certain level of noise.

- Morozov discrepancy principle [135]: This method is similar to the discrepancy principle, but it allows for the presence of noise in the data. The regularization parameter is chosen to be the smallest value such that the solution and the data differ by a certain level of noise, taking into account the noise in the data.

These methods are not always mutually exclusive and can be combined in a complementary way. The choice of the method depends on the specific characteristics of the problem and the data, and it is usually based on the assumptions made about the data, the noise and the prior information available. Different regularization techniques described in [76] were applied to Eq. (3.6) to evaluate the WPF in the low-wavenumber domain. The truncated generalized singular value decomposition (TGSVD) method with minimising the first derivative 2-norm of the solution was found to be the most appropriate [76, 154]. The regularization parameter is determined from the corner of the discrete L-curve produced by the TGSVD method [77]. For the numerical applications presented herein, the Matlab package developed by C. Hansen for the analysis and solution of discrete ill-posed problems [76] was utilized (See Appendix A).

3.2 Results and Discussion

To evaluate the WPF in the low-wavenumber domain, the procedure described in Section 3.1 is employed, and the results obtained by the RFBA are examined.

According to the Graham formulation [70, 71], the CSD of the WPF can be computed using various models for ASD of the pressure field, $\Psi_{pp}(\omega)$, and the normalized CSD of the pressure field, $\tilde{\phi}_{pp}(k, \omega)$, independently from each other as Eq. (2.1).

Among various semi-empirical models developed for simulation of ASD of the WPF, many works showed that the Goody model is more compatible with experimental data compared to other models [92, 134]. Thus, the Goody model [69] is used in this work to assess the ASD function of the WPF in Eq. (2.1),

$$\Psi_{pp}(\omega) = \frac{3\tau_\omega^2 \delta \left(\frac{\omega\delta}{U_e}\right)^2}{U_e \left(0.5 + \left(\frac{\omega\delta}{U_e}\right)^{0.75}\right)^{3.7} \left(1.1 R_T^{-0.57} \left(\frac{\omega\delta}{U_e}\right)\right)^7}, \tag{3.9}$$

where $R_T = U_\tau^2 \delta / U_e \nu$ and U_e is the boundary layer edge velocity. It is worth mentioning that $\Psi_{pp}(\omega)$ represents a one-sided radial frequency spectrum. Therefore, to transform it into a cyclic frequency spectrum density $\Psi_{pp}(f)$, it is multiplied by 2π.

For the normalized CSD function, various semi-empirical models have been developed [134]. The Corcos model is by far the most popular model since it considers homogeneity across the surface, and this assumption leads to a cross spectrum model dependent only on the separation distances [38]. Thus, the Corcos model has two separate relationships for representing the in-flow and cross-flow directions of the WPF [38]. Even though separability is convenient analytically, it is not a realistic assumption. Other researchers recognized this issue and proposed a simple change to the Corcos model. For example, Mellen proposed an elliptical coherence zone, which is different from the Corcos model with the rhombic coherence zone [31]. It is well known that Corcos model overpredicts the amplitude of the low-wavenumber domain, whereas the Mellen model provides more realistic predictions of the low-wavenumber levels. This has been confirmed by comparing the vibration responses of a plate excited by a TBL modelled by the Corcos/Mellen models with experimental data [100]. Therefore, in this study, the normalized CSD function was obtained using the Mellen model [131] as follows

$$\tilde{\phi}_{pp}(k_x, k_y, \omega) = \frac{2\pi \left(\alpha_x \alpha_y\right)^2 k_c^3}{\left(\left(\alpha_x \alpha_y k_c\right)^2 + \left(\alpha_x k_y\right)^2 + \alpha_y^2 \left(k_x - k_c\right)^2\right)^{3/2}}, \tag{3.10}$$

where $\alpha_x = 0.1$ and $\alpha_y = 0.77$. Also, the convection velocity U_c is approximated as follows [21, 74]

$$U_c \approx U_\infty \left(0.59 + 0.3 e^{-0.89\delta^* \omega / U_\infty}\right), \tag{3.11}$$

where δ^* is the TBL displacement thickness.

For all the subsequent numerical analyses, a wavenumber resolution of $\delta k_x = \delta k_y = 4$ m^{-1} is considered and the results are presented at frequency of 1000 Hz.

Furthermore, in order to assess the effectiveness of the proposed method for estimating the WPF in the low-wavenumber domain, we have defined the low-wavenumber domain as the region within the flexural wavenumber ($-k_f \leq k_x, k_y \leq k_f$) of a steel plate with a 1 mm thickness. The plate's properties include a Young's modulus of 210 Gpa, a density of 7800 (kg m^{-3}), and a Poisson's ratio of 0.3, resulting in a flexural wavenumber of $k_f = 63.26$ m^{-1}. The low-wavenumber region is indicated with the square area in Figure 3.2 where the CSD function of the reference TBL using the Goody and truncated Mellen models is plotted. In Section 3.2.1 and 3.2.2 we employ the RFBA to estimate the WPF in the low-wavenumber domain and the results are compared with those simulated using the theoretical WPF formula based on the Goody and truncated Mellen models as shown in Figure 3.2.

A turbulent flow with an air flow speed of $U_\infty = 50$ m s^{-1} is assumed flowing over the rigid surface, see Figure 3.1. The values of air density and the kinematic viscosity are set to 1.225 kg m^{-3} and 1.5111×10^{-5} m^2 s^{-1}, respectively. It is assumed that the TBL is homogeneous, stationary and fully developed over the panel surface. The TBL parameters used for this analysis are given in Table 3.1.

The simulations are performed in Matlab on a desktop computer with 32 GB of RAM and four physical cores. To employ Eq. (3.5), one needs to truncate the wavenumber domain. It is necessary to note that the range of the considered wavenumber domain should be large enough to be able to include the significant contribution of the CSD function. Hence, a cut-off wavenumber of $1.2k_c$ was used in both the streamwise and spanwise directions to take into account the convective contributions of the TBL WPF, where $k_c = \omega/U_c$ is the convective wavenumber. It is noteworthy to mention that converge studies have been done for the selection of the cut-off wavenumber and wavenumber resolution to ensure that the input TBL is accurately modelled.

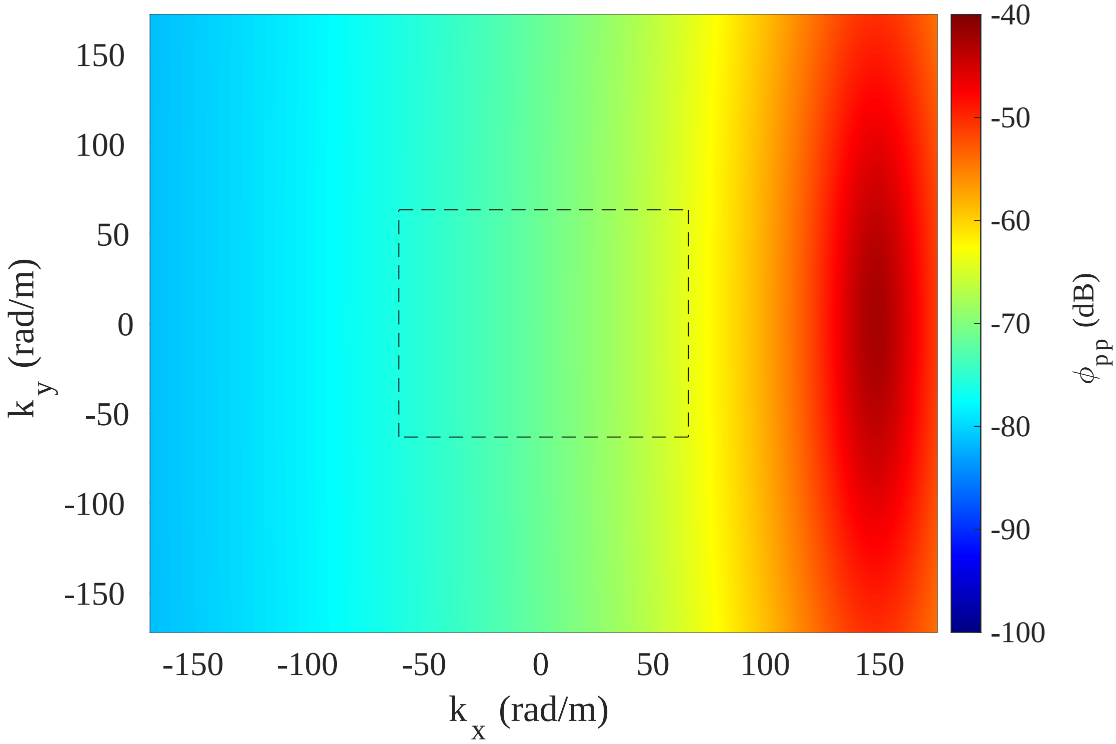

FIGURE 3.2: Contour plots of the Goody+Mellen wavenumber-frequency WPF model $\phi_{pp}(\mathbf{k}, f)$ (dB, ref. 1 $\text{Pa}^2.\text{Hz}^{-1}$) for a flow speed of 50 m/s at 1000 Hz.

TABLE 3.1: TBL parameters for a air flow with speed of 50 m/s.

Parameter	Value
TBL thickness δ (mm)	5.77
TBL displacement thickness δ^* (mm)	0.729
Wall shear stress τ_w (pa)	5.989

3.2.1 Effect of Microphone Array Parameters on the Estimated TBL Wall Pressure Field

In this section, the effects of array parameters namely number of sensors, co-array factor and sensor distribution on the performance of the RFBA are examined. The array size is kept constant in all subsequent calculations.

3.2.1.1 Effect of Sensor Spacing

Before processing the array data for signal analysis, the initial step involves establishing the relative position of sensors, which is crucial in array creation. In this process, special attention must be given to avoid spatial aliasing. Spatial aliasing arises as a result of spatially under-sampling the aperture of the array. To avoid aliasing in time domain signal processing, it is essential to sample the signal at a rate of at least twice the highest frequency. This sampling rate, known as the Nyquist rate [138], can also be applied in spatial domain signal processing by ensuring that the sampling interval does not exceed one-half wavelength [166]

$$k_{\mathrm{sample}} = 2k_{\mathrm{max}} = \frac{2\pi}{\Delta x}. \tag{3.12}$$

This equation indicates a direct relationship between the Nyquist waveform frequency and the sampling interval Δx. This interval, as determined by the Nyquist principle, sets a limit on the maximum distance that can exist between microphone positions. As mentioned above, a criterion of 1.2 times of the convective wavenumber is considered for the highest waveform frequency in measuring the pressure with a microphone array. This criterion is taken into account in Eq. (3.12), so the minimum distance between the microphone positions is obtained as $\Delta x = \pi/k_{\mathrm{max}}$. If this criterion is not fulfilled, then the aliasing can be observed in the low-wavenumber domain, which is the region of interest.

In this section, an equidistant cross-array pattern with the fixed size of $a = 455$ mm and $b = 375$ mm is assumed to demonstrate the aliasing phenomenon and the effects of sensor spacing on the estimated TBL WPF. The study considers a minimum of 16 sensors, with the number of sensors increased by 4 until the maximum of 68 sensors is reached (as shown in Figure B.1). Figure 3.3 presents the results for only four selected cases, namely those with 16, 32, 48, and 68 sensors. As an additional feature, Figures 3.3 (c), (g), (k), and (o) demonstrate all possible vector spacings between all pairs of sensors, along with the co-array factors corresponding to each case study. In the upcoming section (Section 3.2.1.2), the impact of this parameter will be discussed. Figures 3.3 (b), (f), (j), and (n) show the color map and Figures 3.3 (d), (h), (l), and (p) show the corresponding cross-section view of the estimated WPF obtained by RFBA, respectively, for different number of sensors of cross-array pattern. The color maps in the Figure 3.3 include a rectangular area which is surrounded by flexural wavenumber of the assumed plate and denoting the range of low-wavenumber domain which needs to be evaluated ($-k_f \leq k_x, k_y \leq k_f$). This range is shown in the cross-section view of the results with the red dashed-line.

To quantify the performance of the proposed method in the estimation of the TBL WPF, the mean absolute error (MAE) of the estimated WPF in the low-wavenumber domain is calculated for each case with respect to the reference input TBL model based on the Goody and Mellen Models [69, 131] in the corresponding low-wavenumber domain. The MAE is computed in decibels rather than absolute values because the WPF amplitude in the low-wavenumber domain is significantly low, and a logarithmic scale provides a more meaningful comparison. The following formula is used to compute the MAE of the estimated WPF in the low-wavenumber domain

$$\mathrm{MAE} = \frac{1}{N_{k_{LW}}} \sum_{l=1}^{N_{k_{LW}}} |10\mathbf{log}_{10}\phi^{\mathrm{e}}_{pp}(k_{x,l}, k_{y,l}, \omega) - 10\mathbf{log}_{10}\phi^{\mathrm{r}}_{pp}(k_{x,l}, k_{y,l}, \omega)|, \tag{3.13}$$

where $N_{k_{LW}}$ corresponds to the total number of grid points in the low-wavenumber domain. $\phi^{\mathrm{e}}_{pp}(k_{x,l}, k_{y,l}, \omega)$ and $\phi^{\mathrm{r}}_{pp}(k_{x,l}, k_{y,l}, \omega)$ are the estimated and reference wavenumber-frequency spectrum of the WPF, respectively. It can be observed from Figure 3.3 that by increasing the number of sensors, the estimated WPF is improved, and it gradually converges towards the reference input TBL model (see, Figure 3.2).

It is clear from Figures 3.3 (f) and (h) that RFBA struggle to provide reasonable estimation of the WPF due to the presence of aliasing phenomenon when $N_s < 48$. For the given array size, the aliasing effect is mitigated by increasing the number of sensors to 48. This is consistent with Nyquist criterion, as for the considered array size, according to Eq. (3.12) at least 24 sensors are required along the x-axis and 20 sensors along the y-axis to satisfy the Nyquist criterion and avoid aliasing effect. Assuming that the number of sensors is the same in both the streamwise and spanwise directions, the minimum number of sensors required to satisfy the criterion is $N_s = 48$ which is what we observed in Figures 3.3 (j) and (i). An interactive plot demonstrating the impact of increasing the number of sensors on reducing the aliasing effect is shown in Figure B.1 of the Appendix B.

As illustrated by Figures 3.3 (j) and (n) and their corresponding MAEs, the accuracy of estimated results is improved by increasing the number of sensors from 16 to 48, but adding more sensors does not significantly enhance the estimated WPF in the low-wavenumber domain(see Figures 3.3 (j) and (n)). This suggests that respecting the Nyquist criterion alone is not sufficient for obtaining accurate estimation of the low-wavenumber WPF. However, this does not hold true for the convective region. Figure 3.3 (h) shows that estimation of the convective region is much easier than the low-wavenumber domain as it has the highest amplitude in the domain. Moreover, a good estimation of this region is achieved using only 24 sensors which does not satisfy the Nyquist criterion (see Figure B.1) and the estimated result in this region is quite accurate when the Nyquist criterion is fulfilled. Therefore, unlike the low-wavenumber region, accurate estimation of the convective region is possible by fulfilling only the Nyquist criterion.

Figures 3.3 (c), (g), (k), and (o) also show that the co-array factor F is always below 0.4 for all the sensor spacing using the equidistant cross array. The effect of this parameter is examined in the following section.

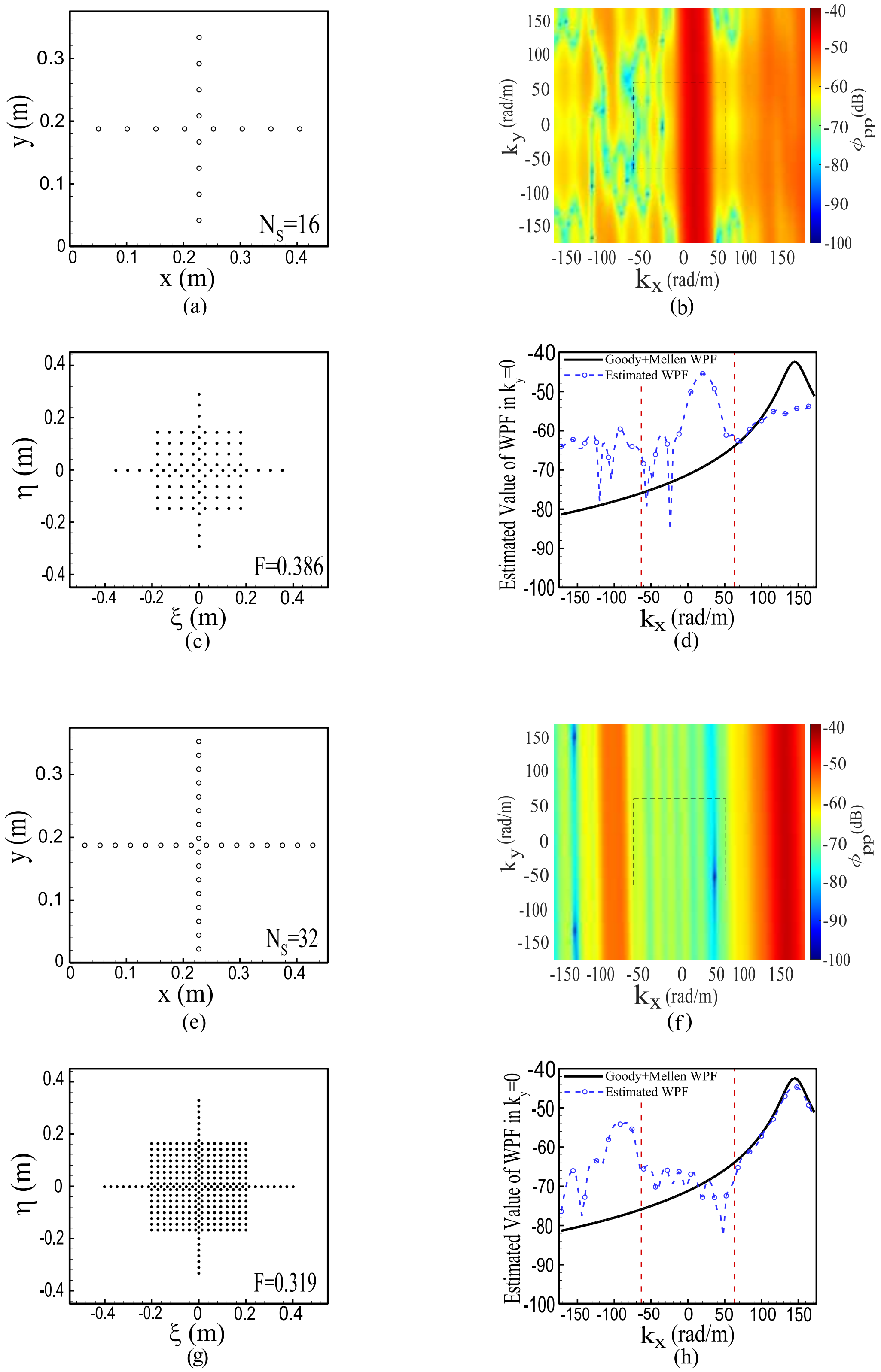

y (m)
x (m)
N_s=16
(a)
k_y (rad/m)
k_x (rad/m)
φ_pp (dB)
(b)
η (m)
ξ (m)
F=0.386
(c)
Goody+Mellen WPF
Estimated WPF
Estimated Value of WPF in k_y=0
k_x (rad/m)
(d)
y (m)
x (m)
N_s=32
(e)
k_y (rad/m)
k_x (rad/m)
φ_pp (dB)
(f)
η (m)
ξ (m)
F=0.319
(g)
Goody+Mellen WPF
Estimated WPF
Estimated Value of WPF in k_y=0
k_x (rad/m)
(h)

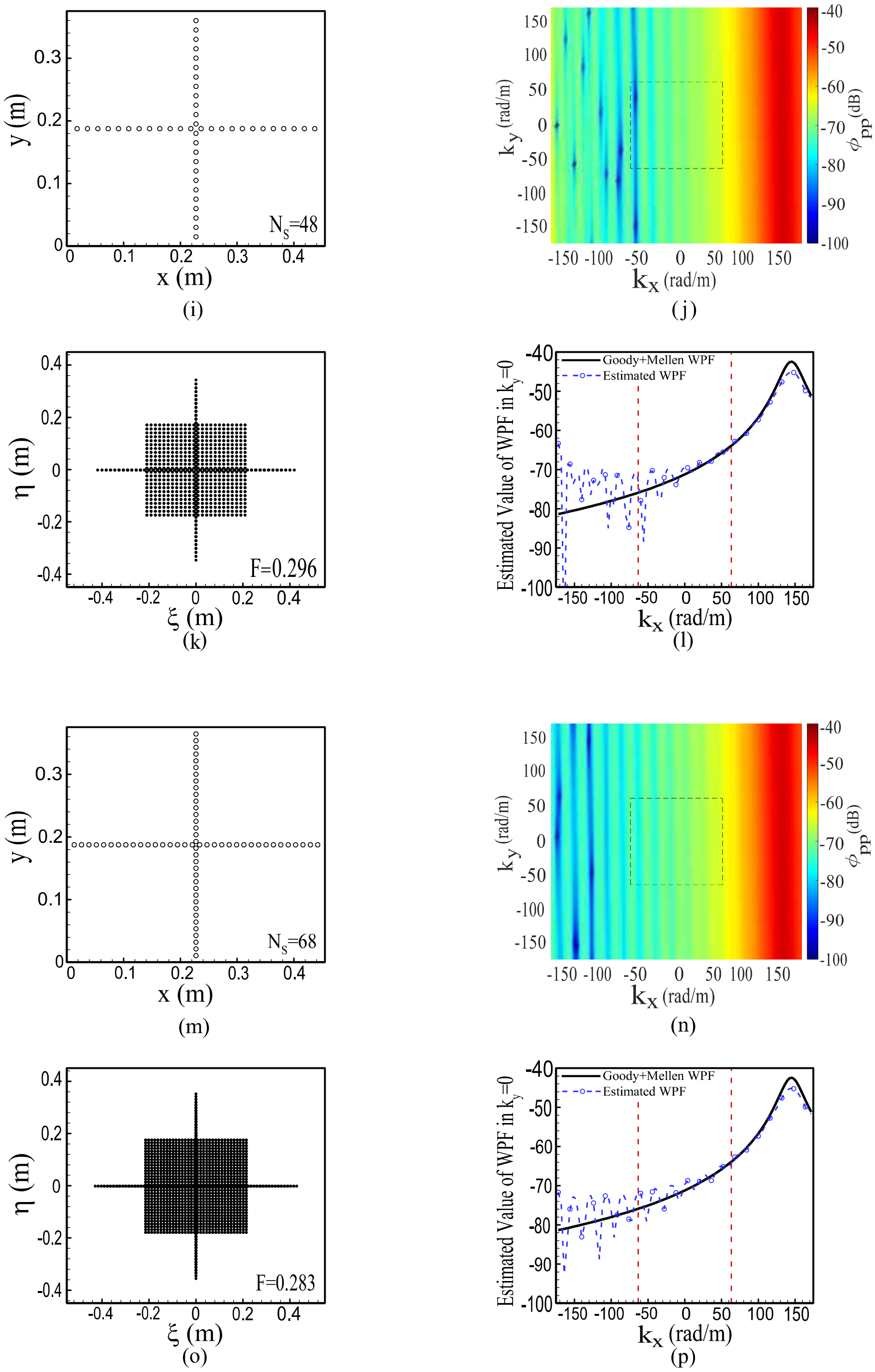

FIGURE 3.3: Comparison of the estimated WPF $\phi_{pp}(\mathbf{k}, f)$ (dB, ref. 1 Pa^2.Hz^{-1}) using RFBA for equidistant cross-array pattern with 16 (a-d), 32 (e-h), 48 (i-l), and 68 (m-p) sensors, respectively. Equidistant cross arrays for each case are shown in (a), (e), (i), and (m) and associated set of distinct vector spacings between sensors are presented in (c), (g), (k), and (o). Co-array factor (F) are displayed for each case and MAEs calculated between the reference input TBL model and the estimated low-wavenumber WPF shown in (b), (f), (j), and (n) are 13.48 dB, 5.67 dB, 1.81 dB, and 1.49 dB, respectively. 2D wavenumber-frequency spectra for $k_y = 0$ are plotted against longitudinal wavenumber in (d), (h), (l), and (p).

3.2.1.2 Effect of Co-array Factor

In terms of array performance, in addition to the minimum distance between sensors, the size of co-array is an important factor to be considered. Co-array describes the number of different distances between every pair of sensors in the array [31]. Given an array of N_s sensors whose locations are given by

$$\mathbf{x}_m, \quad m = 1, 2, \ldots, N_s. \tag{3.14}$$

The associated set of vector spacing between all pairs of elements in the array can be expressed as

$$\mathbf{X}_p = \mathbf{x}_m - \mathbf{x}_n, \quad m = 1, 2, \ldots, N_s, \quad n = 1, 2, \ldots, N_s. \tag{3.15}$$

The set of points $\mathbf{X}_p$ is called the co-array of the array $\mathbf{x}_m$ [79]. To evaluate the efficiency of the different periodic array pattern with respect to aperiodic ones, the F factor is introduced below, which show the ratio of the actual number of unique vector spacings of an array, P, to the corresponding maximum number of spacings, $P_{\max}$

$$F = \frac{P}{P_{\max}} \leq 1. \tag{3.16}$$

Since there are N_s^2 vectors, and N_s of these are zero, the maximum possible unique vector spacings in an array consisting of N_s sensors can be calculated as follow

$$P_{\max} = N_s^2 - (N_s - 1). \tag{3.17}$$

An optimal array maximizes the number of unique vector spacings, resulting in $F = 1$. The low value of F means that there will be a large number of duplicate distances between the sensors, which usually can be seen in the periodic pattern. For instance, in Figures 3.3 (c), (g), (k) and (o), the F factor decreases with an increase in the number of sensors. This indicates that when more sensors are added in a cross-array pattern at equal distances, the size of P will not increase as much as $P_{\max}$ (Eq. (3.17)) due to the repetitive occurrence of the same distances. Thus, it can be inferred that improper sensor positioning can lower the F factor. This is one of the reasons why an accurate

WPF estimate in the low-wavenumber domain cannot be obtained by equidistant cross array pattern even with 68 sensors (see Figures 3.3 (n) and (p)).

To maximize the co-array size while using a fixed number of sensors, it is generally preferable to opt for a non-equidistant arrangement of the array. This will result in a relatively low level of secondary lobes on the estimated WPF, which appear due to the aliasing effect [166]. In the following, the effect of the non-equidistant cross-array pattern on estimation of the WPF is studied.

To maximize F factor in the cross-array pattern, the position of sensors are arranged non-equidistantly on the two cross lines, and the same study as above (Section 3.2.1.1) has been carried out again. Figure 3.4 presents the results with the same number of sensors as studied in Section 3.2.1.1. Similar to the equidistant-array pattern, the convective region is the first region where the estimated WPF converges to the reference model. However, in the non-equidistant array pattern, only 16 sensors are required to identify this region (Figures 3.4 (b) and (d)), whereas in the equidistant array pattern, it takes at least 24 sensors (see Figure B.1). Moreover, the estimated WPF obtained by the RFBA in each case (Figures 3.4 (b), (f), (j), and (n)) is more accurate than corresponding case in the equidistant cross-array pattern (Figures 3.3 (b), (f), (j), and (n)), which is evident by the lower MAE for the non-equidistant array. As it can be seen from Figures 3.4 (f) and (h), in this case the aliasing effect is less profound for the array with 32 sensors when compared to the corresponding case shown in Figures 3.3 (f) and (h). Consequently, this improvement results in a decrease in the MAE from 5.07 dB to 3.03 dB.

In the Appendix B, readers can access an interactive plot (Figure B.2) that showcases how WPF estimation in the low-wavenumber domain is affected by 14 arrays of non-equidistant cross-array patterns. The plot includes the results for different arrays from 16 to 68 sensors, with increments of 4.

Comparing the results presented in Figures 3.3 and 3.4, it can be concluded that respecting the Nyquist criterion and the maximum co-array factor can result in a better estimation of the WPF. In the next section, it is demonstrated that in addition to sensor spacing and co-array factor, sensor distribution plays a key role in accurate estimation of the TBL WPF. Effect of this factor has been investigated using a random array pattern in the following section.

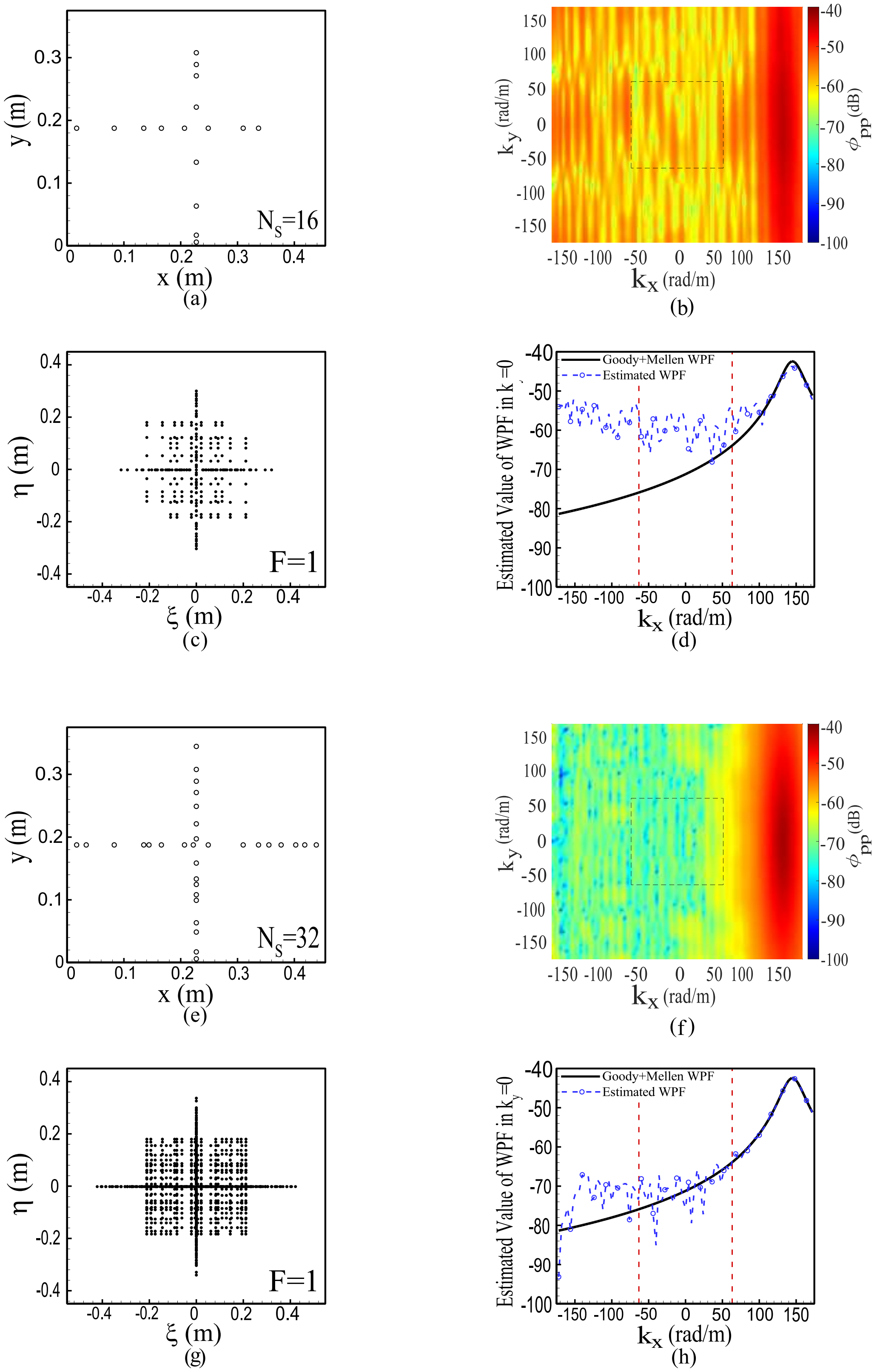

y (m)
x (m)
N_S=16
(a)
k_y (rad/m)
k_x (rad/m)
φ_PP (dB)
(b)
η (m)
ξ (m)
F=1
(c)
Estimated Value of WPF in k_y=0
Goody+Mellen WPF
Estimated WPF
k_x (rad/m)
(d)
y (m)
x (m)
N_S=32
(e)
k_y (rad/m)
k_x (rad/m)
φ_PP (dB)
(f)
η (m)
ξ (m)
F=1
(g)
Estimated Value of WPF in k_y=0
Goody+Mellen WPF
Estimated WPF
k_x (rad/m)
(h)

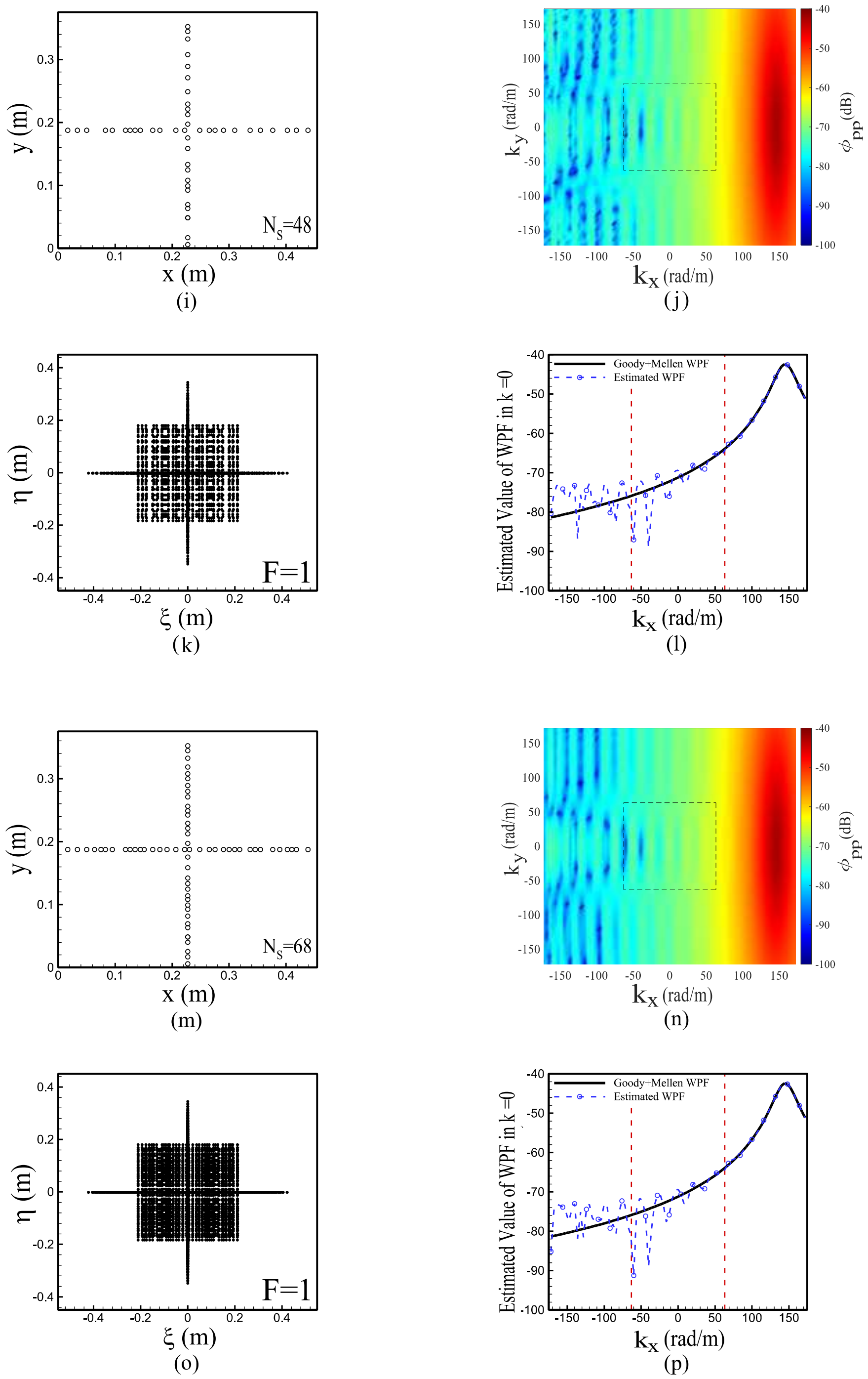

FIGURE 3.4: Comparison of the estimated WPF $\phi_{pp}(\mathbf{k}, f)$ (dB, ref. 1 Pa^2.Hz^{-1}) using RFBA for non-equidistant cross-array pattern with 16 (a-d), 32 (e-h), 48 (i-l), and 68 (m-p) sensors, respectively. Non-equidistant cross arrays for each case are shown in (a), (e), (i), and (m) and associated set of distinct vector spacings between sensors are presented in (c), (g), (k), and (o). Co-array factor (F) are displayed for each case and MAEs calculated between the reference input TBL model and the estimated low-wavenumber WPF shown in (b), (f), (j) and (n) are 10.63 dB, 3.03 dB, 1.45 dB, and 1.31 dB, respectively. 2D wavenumber-frequency spectra for $k_y = 0$ are plotted against longitudinal wavenumber in (d), (h), (l) and (p).

3.2.1.3 Effect of Sensor Distribution

As discussed above, the half-wavelength criterion is the main constraint of regular array patterns. Failure to meet this criterion, results in spatial aliasing, which produces secondary lobes on the estimated WPF as it was illustrated in Figures 3.3 (b) and (f). It is possible to diminish these secondary lobes by removing all periodicities from the microphone array. This results in a class of arrays known as irregular or aperiodic arrays [166].

In order to design an irregular array, a random process can be used to determine sensor locations. Another option would be to use an algorithm that ensures a certain degree of irregularity in sensor positions. The latter should be used whenever a sensor location can be specified and controlled because a knowledge-based sensor location approach outperforms a random algorithm [166]. In this work, the second approach is employed for distributing the sensors and creating a random-array pattern. Figure 3.5 shows the estimated WPF using the RFBA for four random array patterns with the number of sensors of 16, 32, 48, and 68. For additional visualization, an interactive plot (Figure B.3) containing 14 random array patterns with sensors ranging from 16 to 68 in increments of 4 is available in the Appendix B. All the configurations meet the Nyquist criterion and have the maximum possible co-array factor (i.e. $F = 1$). For example, for the first irregular array of 16 sensors, the sensor arrangement was designed such that at least one pair of sensors satisfied the Nyquist criterion in both the streamwise and spanwise directions. Following this, in each subsequent step, four new sensors were added to the previous arrangement in such a way that at least one existing sensor could meet the minimum distance required by the Nyquist criterion for each new sensor. This process was repeated up to the fourteenth array of 68 sensors. Also, the position of sensors was chosen in a manner that the F factor was always maximi and equal to 1. The obtained results in Figure 3.5 show that using the irregular array with above conditions will avoid spatial aliasing and also generate a more coherent vector spacing separation of ξ and η which lead to the better estimation of the WPF compared with the regular array patterns.

Figure 3.5 shows that using the irregular array the estimated WPF converges to the reference WPF much faster than that using the regular array. For example, Figures 3.5 (j) and (l) show that applying RFBA to a random array with 48 sensors provides excellent estimations of the WPF in the low-wavenumber domain with a mean absolute error of less than 1 dB. Moreover, RFBA provides an accurate result in the entire considered wavenumber domain using 68 sensors (shown in Figures 3.5 (n) and (p)). Therefore, employing a random array pattern while adhering to the Nyquist criterion and optimizing the co-array factor yields improved the WPF estimations in comparison to the other array patterns investigated in Sections 3.2.1.1 and 3.2.1.2. In Section 3.2.1, we used a closed-from semi-empirical TBL model for computing the CSM. However, in practice, only limited number of samples/snapshots of the WPF is available. To investigate the impact of this factor on the proposed RFBA method, we introduce a virtual acoustic experiment, which we examine in detail in the subsequent section.

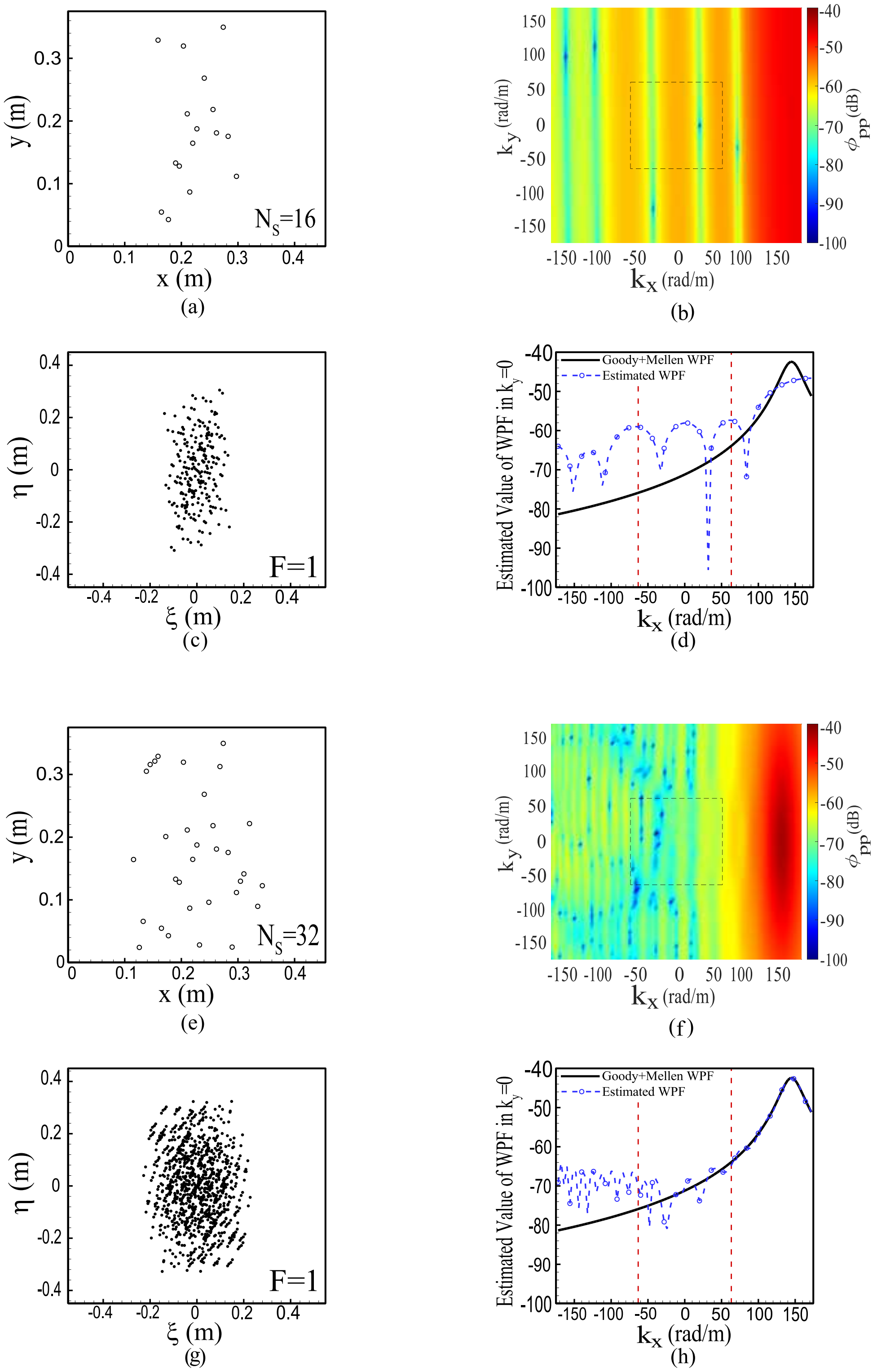

y (m)
x (m)
N_S=16
(a)
k_y (rad/m)
k_x (rad/m)
φ_pp (dB)
(b)
η (m)
ξ (m)
F=1
(c)
Goody+Mellen WPF
Estimated WPF
Estimated Value of WPF in k_y=0
k_x (rad/m)
(d)
y (m)
x (m)
N_S=32
(e)
k_y (rad/m)
k_x (rad/m)
φ_pp (dB)
(f)
η (m)
ξ (m)
F=1
(g)
Goody+Mellen WPF
Estimated WPF
Estimated Value of WPF in k_y=0
k_x (rad/m)
(h)

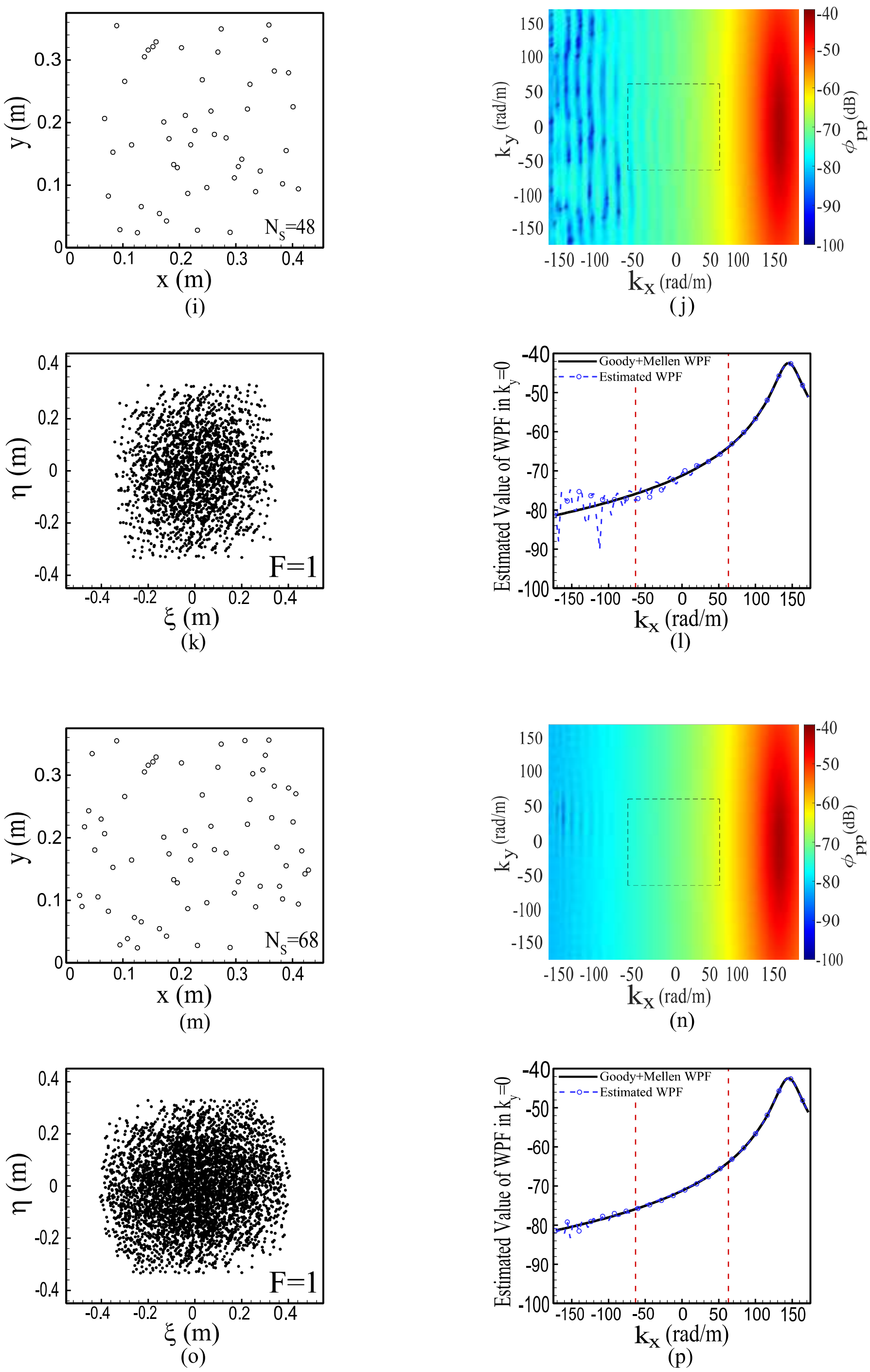

FIGURE 3.5: Comparison of the estimated WPF $\phi_{pp}(\mathbf{k}, f)$ (dB, ref. 1 Pa^2.Hz^{-1}) using RFBA for irregular-array pattern with 16 (a-d), 32 (e-h), 48 (i-l), and 68 (m-p) sensors, respectively. Irregular arrays for each case are shown in (a), (e), (i), and (m) and associated set of distinct vector spacings between sensors are presented in (c), (g), (k), and (o). Co-array factor (F) are displayed for each case and MAEs calculated between the reference input TBL model and the estimated low-wavenumber WPF shown in (b), (f), (j), and (n) are 10.08 dB, 2.68 dB, 0.61 dB, and 0.09 dB, respectively. 2D wavenumber-frequency spectra for $k_y = 0$ are plotted against longitudinal wavenumber in (d), (h), (l), and (p).

3.2.2 Virtual Acoustic Experiments

In the previous sections, the CSM was calculated from a closed-from semi-empirical TBL model. It was then utilized to investigate the effects of sensor spacing, co-array factor and sensor distribution on the performance of the RFBA in estimation of the WPF in the low-wavenumber domain. However, the theoretical TBL models cannot realistically simulate an experimental situation. Since the TBL pressure fluctuation is a random process, if several records of these pressure fluctuations are taken under the same experimental conditions, they would not be identical due to the random nature of the excitation. Each outcome of an experiment, in the case of a random process, is called a sample function. If n experiments are conducted, all the n possible outcomes of a random process constitute what is known as the ensemble of the process.

In this section, this process is simulated using a virtual acoustic experiment where different deterministic realizations of the TBL pressure fluctuations are computed, and the CSM is then estimated from ensemble average of these realizations.

3.2.2.1 Wall Pressure Field Snapshots using the UWPW Technique

Simulation of random TBL with deterministic loading is the main concept of the UWPW technique [129]. This approach mimics experimental conditions and calculates the WPF underneath of a TBL by ensemble averaging of the different realization of wall pressure at each frequency. The pressure beneath the TBL for the rth realization can be represented by a set of UWPWs at the qth sensor of the array pattern as follows [100, 101, 129]

$$p^r(\mathbf{x}^q, \omega) = \sum_{l=1}^{N_k} \sqrt{\frac{\phi_{pp}(k_{x,l}, k_{y,l}, \omega)\delta k_x \delta k_y}{4\pi^2}} e^{\mathrm{j}(k_{x,l}x^q + k_{y,l}y^q + \theta_l^r)}, \tag{3.18}$$

where θ is a random phase uniformly distributed in $[0, 2\pi]$. Similar to Eq. (3.5), N_k corresponds to the total number of grid points in the truncated wavenumber space. It is important to note that a cut-off wavenumber of $1.2k_c$ was employed in both the streamwise and spanwise directions to consider the convective contributions of the TBL WPF. As an illustration, Figure 3.6 displays the representation of four realizations of the surface pressure filed at a frequency of 1000 Hz and a flow velocity of 50 m/s. These realizations are employed in ensemble averaging of different realizations to compute the

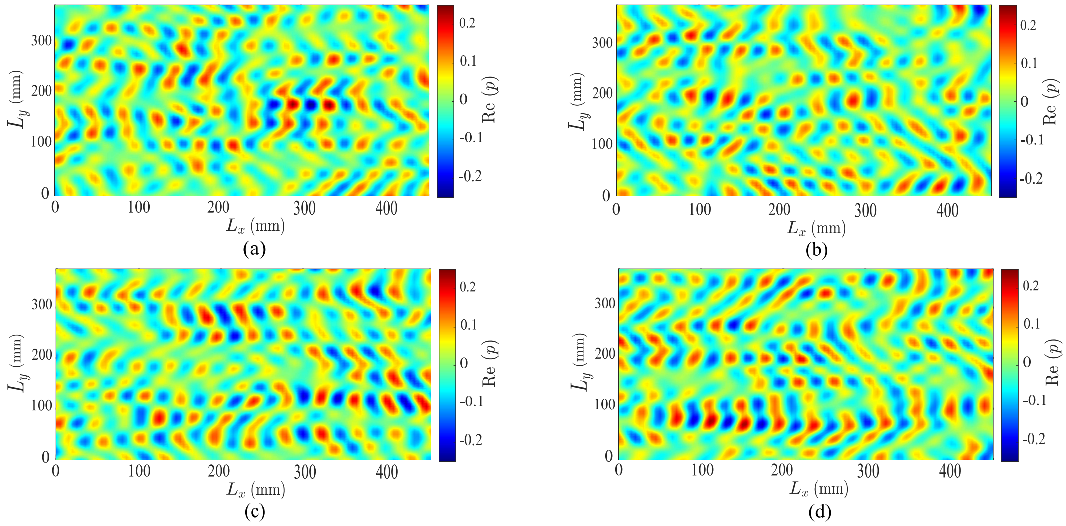

FIGURE 3.6: (a)-(d): Four different realizations of the WPF synthesized by the UWPW technique using the Goody and truncated Mellen models for a flow speed of 50 m/s at 1000 Hz.

CSM of the WPF. Figure 3.7 shows a flowchart describing the implementation of the UWPW technique in the virtual acoustic experiment for estimation of the WPF in the low-wavenumber domain.

Herein, three patterns (equidistant-cross array, non-equidistant-cross array, and irregular array) with 68 sensors are analyzed, and the impact of varying the number of realizations on estimating the WPF in the low-wavenumber domain using the RFBA is evaluated. The Appendix B contains an interactive plot showcasing 19 case studies for the three array patterns, highlighting the impact of varying numbers of realizations on estimation

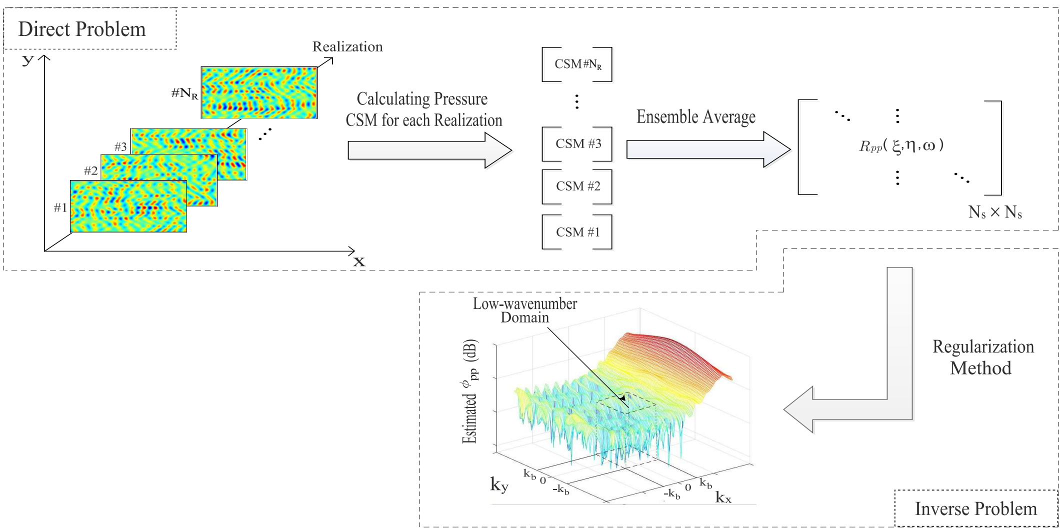

FIGURE 3.7: Simulation process in the virtual acoustic experiments using the UWPW technique.

of the WPF in the low-wavenumber domain (see Figure B.4). Besides, for each array pattern, the MAE (as defined in Eq. (3.13)) is shown to help quantifying the accuracy of the estimated WPF for different realizations. Figure 3.8 only shows some selected results for four different number of realizations. The obtained results shown in Figures 3.8 (f1) and (i1), indicate that a relatively small number of realizations is sufficient to identify the convective zone of the WPF in this virtual experiment and the random array pattern exhibits a better performance compared with the other two arrays shown in Figures 3.8 (d1), (g1), (e1) and (h1). However, for the estimation of the WPF in the low-wavenumber domain, a considerable number of realizations is necessary. For example, Figure 3.8 (f2) shows that after 50000 realizations, the estimated results has a MAE of approximately 4.5 dB. Moreover, increasing the number of realizations from 50000 to 200000 reduces the MAE by only 1 dB (see Figure 3.8 (l2)). This can be attributed to the fact that in the virtual experiment an approximate CSM is used which struggles to realise the pressure fluctuations in this region due to their low amplitudes compared to the convective region. Moreover, the MAE values for three different patterns indicate that the irregular-array pattern performs better than the equidistant and non-equidistant cross array patterns when evaluating the WPF in the low-wavenumber domain.

To analyze the WPF synthesized with Eq. (3.18), the coherence obtained from the WPF of N_r realizations are compared with the coherence obtained from the Mellen+Goody model's analytical formula in Figure 3.9. By using N_r realizations, the coherence between point $\mathbf{x}$ and $\mathbf{x}'$ can be estimated as follows

$$\Gamma(\mathbf{x}, \mathbf{x}', \omega) = \frac{\left| E\left[p^r(\mathbf{x}, \omega)\overline{p^r(\mathbf{x}', \omega)}\right]_{r\in\{1,\ldots N_r\}} \right|}{\sqrt{E\left[|p^r(\mathbf{x}, \omega)|^2\right]_{r\in\{1,\ldots N_r\}} E\left[|p^r(\mathbf{x}', \omega)|^2\right]_{r\in\{1,\ldots N_r\}}}}, \tag{3.19}$$

where $p^r(\mathbf{x}, \omega)$ is given by Eq. (3.18).

Figure 3.9 shows the results of Eq. (3.19) for $N_r = 50, 500, 5000$, and 50000 when applied to the 34 equidistant sensors positioned in the streamwise direction. It can be observed that a relatively small number of realizations is sufficient to estimate the coherence of the WPF between closely spaced sensors, which plays a vital role in calculating the convective peak in the WPF. However, there are significant discrepancies between the estimated coherence and the analytical one for sensors that are spaced far apart. By increasing the number of realizations, the estimated coherence for sensors with larger spatial separation approaches the analytically calculated coherence, which is crucial for accurate WPF estimation in the low-wavenumber range. This behaviour clarifies why a large number of realizations is necessary to estimate the WPF in the low-wavenumber range.

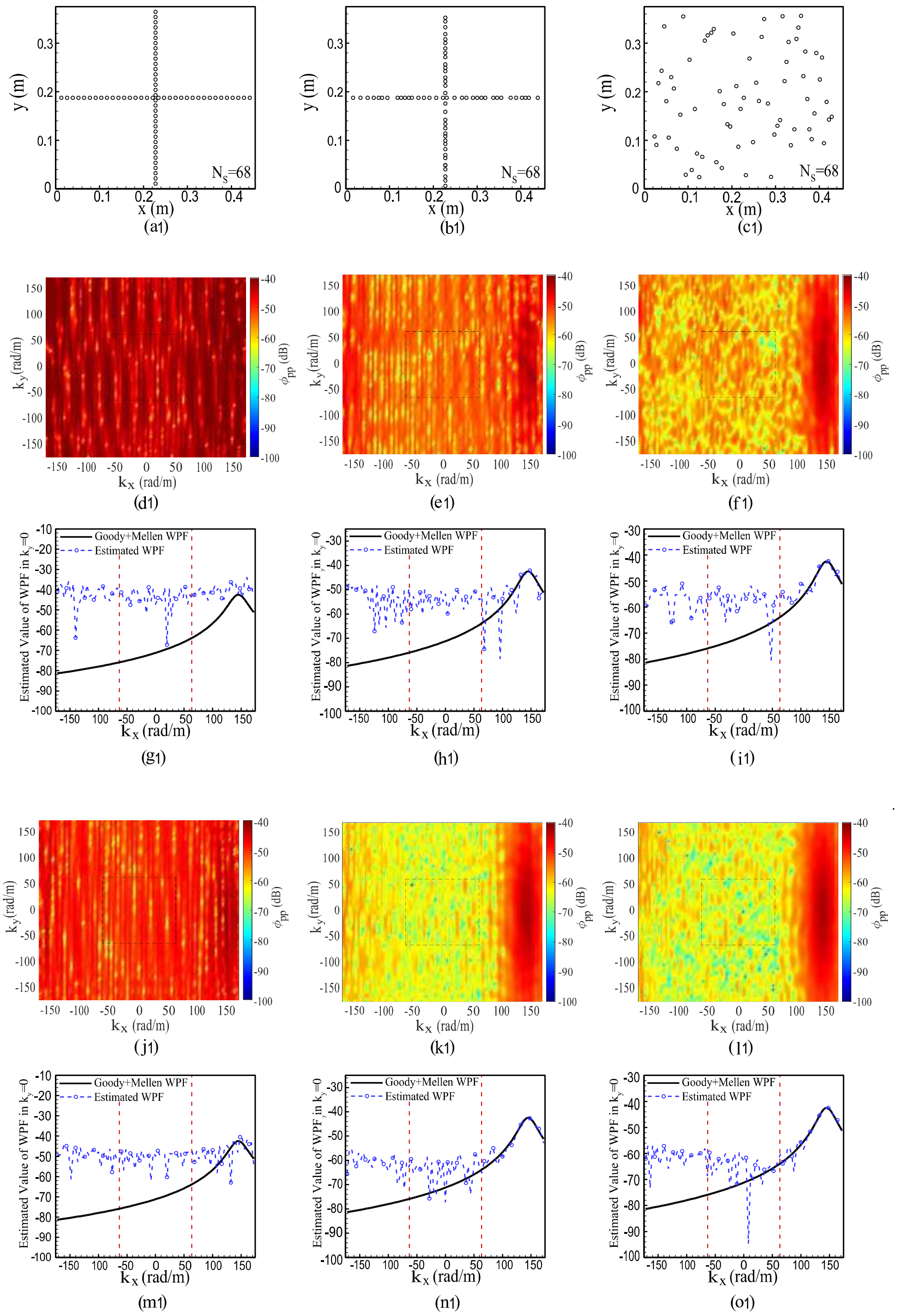

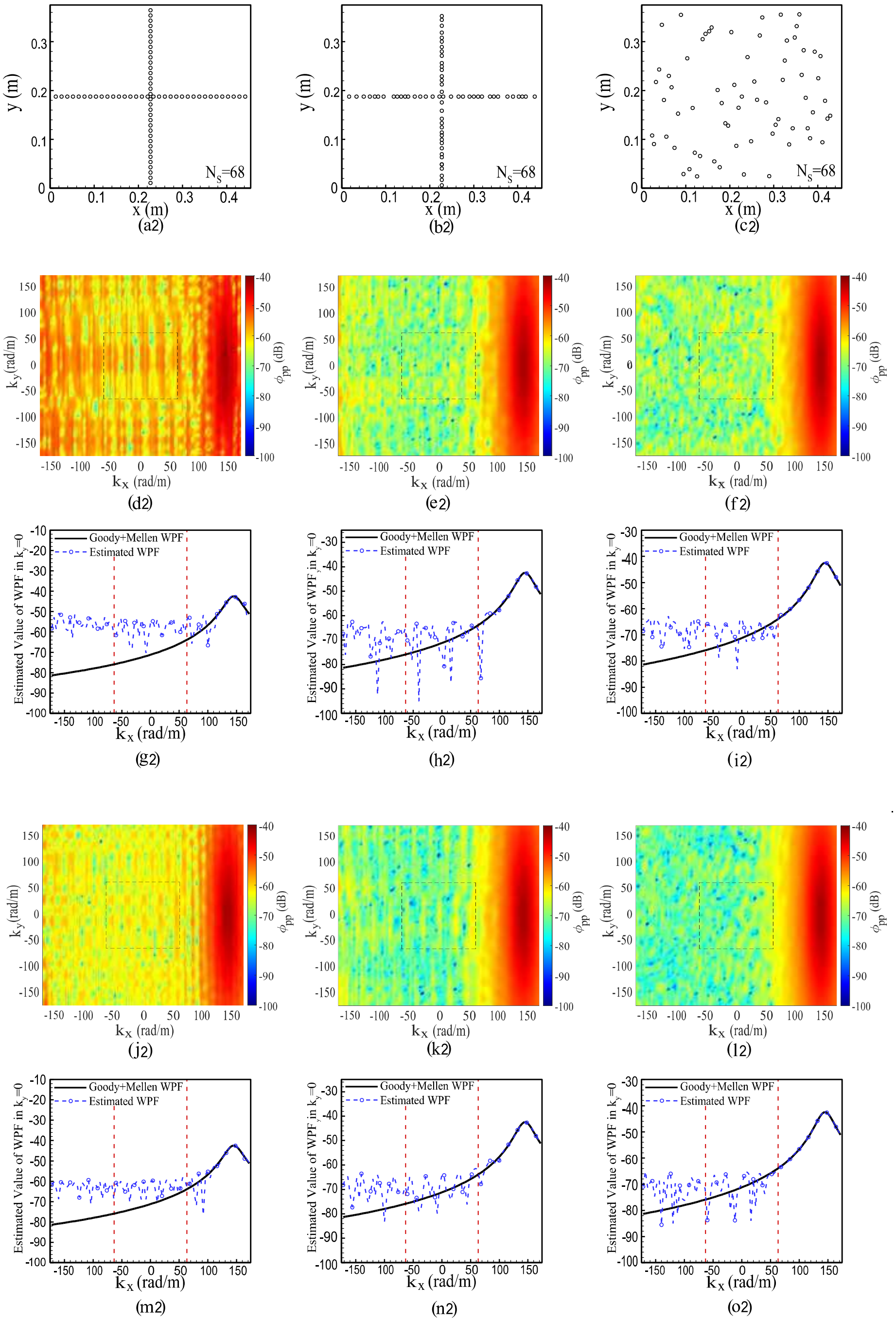

FIGURE 3.8: Comparison of the estimated WPF $\phi_{pp}(\mathbf{k}, f)$ (dB, ref. 1 Pa^2.Hz^{-1}) using the UWPW technique for three different array patterns, each comprising 68 sensors shown in (a1)-(c1) and (a2)-(c2) for 500 realizations (d1-i1), 5000 realizations (j1-o1), 50000 realizations (d2-i2), and 200000 realizations (j2-o2). The color maps depicting the estimated WPF are presented in (d1), (e1), (f1), (j1), (k1), (l1), (d2), (e2), (f2), (j2), (k2), and (l2), with respective MAEs between the reference input TBL model and the estimated low-wavenumber WPF of 26.86 dB, 16.20 dB, 12.90 dB, 20.12 dB, 8.01 dB, 7.48 dB, 10.80 dB, 4.65 dB, 4.55 dB, 8.37 dB, 4.22 dB, and 3.39 dB. The cross-section view of the estimated low-wavenumber WPF are illustrated in (g1), (h1), (i1), (m1), (n1), (o1), (g2), (h2), (i2), (m2), (n2), and (o2).

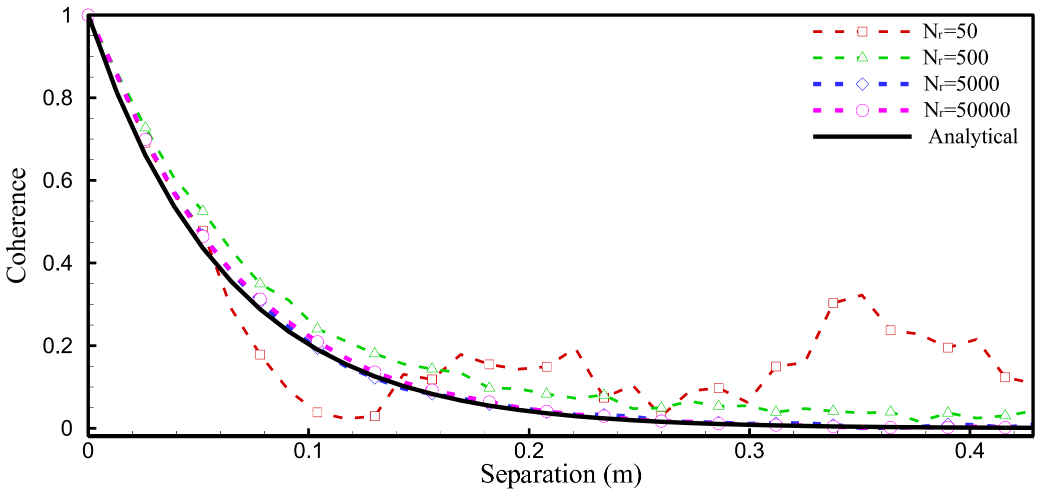

FIGURE 3.9: The TBL pressure filed coherence as a function of the spatial separation in the streamwise direction. Solid line, analytical formula of the Mellen+Goody model; dashed lines, numerical estimation considering 50, 500, 5000 and 50000 realizations.

3.2.2.2 Effect of Number of Realizations

In this section, the impact of the number of realizations on the estimation of the WPF in the low-wavenumber domain is examined. Figure 3.10 presents a comparison of the MAE values for the estimated WPF as a function of frequency, using the irregular array pattern with 68 sensors shown in Figure 3.8 (c2). To apply the acoustic approach for estimating the WPF in the low-wavenumber domain, a minimum frequency of $f = 400$ Hz is chosen. This selection ensures that the convective wavenumber of the TBL excitation remains far from the flexural wavenumber of the panel (for more details, refer to Section 4.2).

The MAE values are plotted for various numbers of realizations. The findings indicate that, as the number of realizations increases, the MAE values decrease. Moreover, the graph in Figure 3.10 shows that the MAE increases at higher frequencies, indicating lower accuracy in estimating the WPF in the low-wavenumber domain. This observation underscores the challenges the ABA faces in estimating the low-wavenumber domain at high frequencies.

3.2.2.3 Effect of the Convective Ridge on the Estimation of the Low-wavenumber WPF

In previous Sections, we exclusively utilized the Mellen model as the input TBL model. Since the levels of the WPF between the convective peak and the low-wavenumber

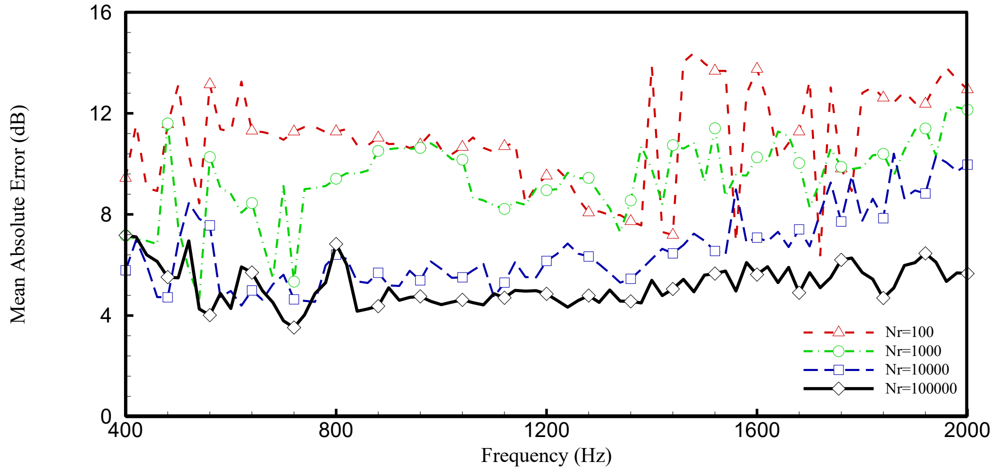

FIGURE 3.10: Comparison of MAE for the estimated WPF in the low-wavenumber domain as a function of frequency. The results showcase the impact of the number realization on the accuracy of the estimated WPF for the irregular array pattern with 68 sensors.

domain are different for different semi-empirical models (see Figure 2.9), in this section we investigate how this difference will affect the estimated low-wavenumber WPF. Hence, we have implemented two additional models: the Chase model [28, 71] and the Corcos model [38, 71], as input TBL models. As can be seen from Figure 2.9, among the three models of Chase, Corcos, and Mellen, the levels of the low-wavenumber WPF are the highest for Corcos model and the lowest for Chase model while they are somewhere in between for the Mellen model. The disparities between the convective peak level and the mean value of the WPF within the low-wavenumber domain are approximately 19 dB, 27 dB and 33 dB for the Corcos, Mellen and Chase models, respectively. In both the Corcos and Chase models, the convective peak occurs at a similar level as observed in the Mellen model [71].

For the estimation of the WPF, we employed a random array pattern with 68 sensors, as shown in Figure 3.8 (c1). We calculated the MAE for the three TBL models with different numbers of realizations, and the results are summarized in Table 3.2. The findings indicate that when using the Corcos model, fewer realizations are required for an accurate estimation of the WPF within the low-wavenumber domain. In fact, with just 50,000 realizations, we can achieve the WPF estimation with a MAE of approximately 2 dB. This number of realizations is significantly fewer than what is needed for the Mellen model (nearly 1,000,000 realizations) to reach the same level of accuracy. This can be attributed to the fact that the difference between the convective peak and the low-wavenumber levels in the Corcos model is smaller than that in the Mellen model.

Table 3.2: MAE of the low-wavenumber WPF for multiple numbers of realizations using three closed-form semi-empirical models as reference input TBL models.

Semi-empirical models	**Number of Realizations**							
	500	**5,000**	**50,000**	**200,000**	**500,000**	**700,000**	**1,000,000**	**2,000,000**
MAE (dB) - Corcos Model	6.19	3.39	2.18	1.36	0.60	0.51	0.48	0.32
MAE (dB) - Mellen Model	12.90	7.48	4.55	3.39	2.72	2.61	2.19	2.03
MAE (dB) - Chase Model	26.06	20.31	15.97	13.87	11.27	11.14	10.59	9.34

Therefore, the low-wavenumber components of the WPF are less contaminated by the convective ridge. Consequently, a lower number of realizations is necessary to attain an accurate estimation of the WPF within the low-wavenumber domain.

This has been further confirmed by the results for the Chase model where its MAE exceeds that of the Mellen model. For example, when using the Chase model, to achieve the WPF estimation with approximately 9 dB error, almost 2,000,000 realizations are required. Since the disparity in the WPF levels between the convective peak and the low-wavenumber domain is the highest for the Chase model among the considered models, the low-wavenumber components of the WPF are mostly masked by the large-amplitude components of the WPF in the convective ridge. This is one of the main challenges of measuring the low-wavenumber pressure fluctuations using a microphone array in real-world scenarios as the difference between the convective peak and low-wavenumber levels of the WPF is not known. This means it is not clear how many snapshots of the measured signal is required to achieve an accurate estimation of the low-wavenumber region.

It should be noted that in this virtual experiment the effect of data sampling and using an approximate CSM on the estimation of the TBL pressure field is demonstrated which is only one aspect of a real experiment. However, other common sources of error including instrumental, environmental, procedural, and human errors exist in practice. These errors can be either random or systematic, impeding the accurate estimation of the WPF in the low-wavenumber domain.

3.3 Summary

In this work, the efficacy of using a microphone array on the estimation of the TBL WPF in the low-wavenumber domain was studied. A regularized Fourier-based approach was proposed to identify the low-wavenumber levels of the WPF. Effects of three array parameters, namely sensor spacing, co-array factor and sensor distribution on the performance of each method were examined. It was shown that to achieve accurate estimation of the WPF all the three factors should be considered. It was found that to obtain accurate results, in addition to the Nyquist criterion, one needs to use an irregular array pattern with the maximum possible co-array factor ($F = 1$). It was also observed that reasonable estimation of the WPF in the convective region is much easier than that in the low-wavenumber domain and can be achieved with relatively small number of sensors.

Moreover, the effectiveness of using a microphone array to estimate the WPF in an experimental condition was evaluated using a virtual experiment where the CSM was approximated by an ensemble average of different realization of the WPF generated by the UWPW technique. This mimics an experimental measurement where many samples are collected from the random TBL pressure fluctuations. It was illustrated that increasing the number of realizations results in more accurate estimation of the wall pressure spectrum. Although, with relatively small number of realizations the convective region can be identified, a significant number of realizations is required to well estimate the low-wavenumber levels in the TBL pressure field.

To investigate the effect of the convective ridge on the identification of the low-wavenumber domain WPF, three different TBL models were used individually as input reference models. It was observed that the difference between the convective peak and the low-wavenumber levels significantly affects the accuracy of the low-wavenumber WPF estimation. In other words, the greater this difference, the higher the number of realizations. This happens because the convective ridge obscures the low-wavenumber components of the TBL WPF. This underscores a key issue when trying to capture the low-wavenumber pressure fluctuations using a microphone array in real-world scenarios, as the exact difference between the convective peak and the low-wavenumber levels is unknown in practice. As a result, it remains unclear how many snapshots of the recorded signal are required to achieve an accurate estimation of the low-wavenumber region.

Moreover, this highlights the challenges in estimation of this region in the experiments where not only a limited number of data samples can be recorded but also other sources of error and uncertainty exist, such as background noise and the influence of microphone instrumentation (particularly if not flush-mounted), which may contaminate the WPF or affect the TBL.

Chapter 4

Estimation of the Low-wavenumber WPF beneath a TBL using an Accelerometer Array: Single Frequency Analysis

In most of the previous studies using vibration-based approaches, it was assumed that the WPF level in the low-wavenumber domain is constant. Furthermore, once the low-wavenumber WPF was estimated, there was no reference WPF to ensure that obtained results were accurate. This highlights the necessity for further study not only to improve the process of identification of the low-wavenumber WPF but also to verify its effectiveness before employing it in practice. This is only possible if the estimated WPF could be benchmarked against a known input TBL WPF in the low-wavenumber domain. Thus, this chapter presents the the feasibility of estimating the low-wavenumber WPF by analyzing vibration data from a structure excited by a TBL.

The methodology for estimating the WPF is outlined in Section 4.1, where an accelerometer array assumed to be mounted on an elastic plate that is excited by a TBL WPF crossing over it. The proposed approach is based on the relationship between the TBL forcing function and structural vibrations in the wavenumber domain. By utilizing vibration data obtained from a structure excited by a TBL and incorporating the sensitivity functions of the respective structure, it is possible to estimate the cross-spectrum density of the pressure fluctuations in the wavenumber domain. To demonstrate the effectiveness of the proposed method, an analytical model of a simply-supported panel excited by a reference TBL model is employed. The proposed method is then implemented in a numerical study to verify the estimated WPF against an input reference TBL WPF modeled by semi-empirical models. The findings are presented in Section 4.2, where the results obtained using the closed-form semi-empirical TBL model and virtual vibration experiment are compared. The solution procedure, along with the estimated WPF in the low-wavenumber domain, is discussed in Section 4.2.1. This subsection examines the effect of number of sensors and plate dimensions on the estimation of the WPF in the low-wavenumber domain. This analysis is conducted while considering a closed form semi-empirical TBL model as the input exciting force. Next, the process for virtual experiments is detailed in Section 4.2.2, and the impact of the number of realizations/snapshots needed for a reliable estimation of the low-wavenumber WPF is investigated. Finally, this chapter concludes with a summary of the findings in Section 4.3.

This chapter is based on the article “Identification of low-wavenumber wall pressure field beneath a turbulent boundary layer using vibration data”, published in the *Journal of Fluids and Structures* [3].

4.1 Methodology

This section is divided into three subsections. In Section 4.1.1, we introduce an inverse vibration approach employed to estimate the TBL WPF in the low-wavenumber domain based on vibration data from the excited panel. This section describes the relation between the CSD of the WPF expressed in the wavenumber domain and the CSD of the panel acceleration at various points. The accuracy of the proposed method is evaluated through comparison with reference results. The CSD of the TBL WPF is simulated in two different ways. The first way, discussed in Section 4.1.2, involves using closed-form semi-empirical models as an input forcing function. This analysis enables us to examine the impact of various parameters on the performance of the proposed method. The second way, outlined in Section 4.1.3, involves simulating the input force using different realizations/snapshots. To simulate an experiment, various realizations of the WPF will be generated using the UWPW technique [129]. This approach allows for an investigation

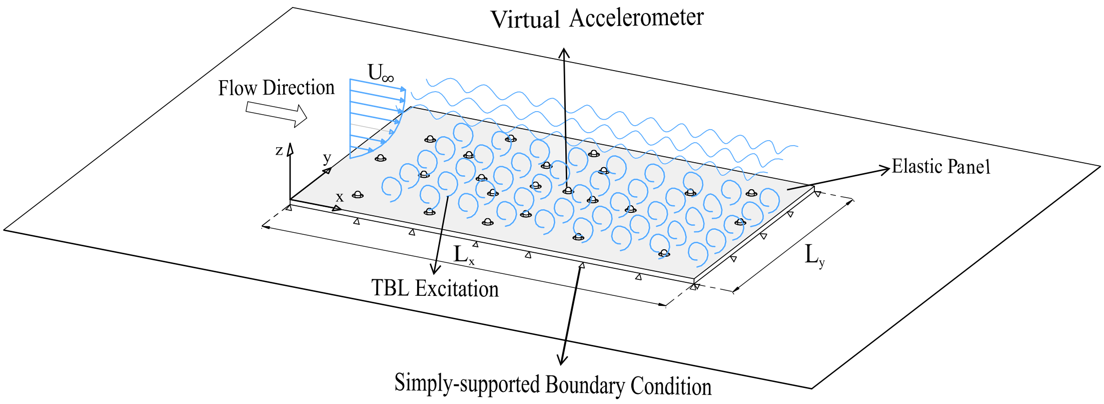

FIGURE 4.1: Schematic of a random accelerometer array mounted on an elastic simply-supported panel to measure acceleration response of the panel excited by wall pressure fluctuations beneath the turbulent boundary layer.

into the influence of the number of snapshots required for reliable estimation of the low-wavenumber WPF.

4.1.1 Inverse Vibration Method

In this section, an inverse vibration method is proposed to estimate the TBL WPF in the low-wavenumber domain from vibration data. Let us consider a flat panel excited by a TBL. We assume that the TBL is homogeneous, stationary, and fully developed across the panel surface, and that the vibration of the panel does not influence the WPF. Figure 4.1 illustrates the considered system for the numerical applications presented in this chapter: the panel is rectangular and simply-supported on its four edges. An array of N_s virtual accelerometers is mounted on the panel to measure the vibrations. The x-axis is considered parallel to the streamwise direction, and the free stream velocity is denoted by U_∞. The panel has the density of ρ_s, length of L_x and width of L_y, and bending stiffness of $D = Eh^3/(12(1-\nu_p^2))$, where h is the panel thickness, E is the Young's modulus and ν_p is Poisson's ratio. The Kirchhoff theory is considered here to represent the motions of the considered thin panel, and to calculate the acceleration of the panel [149].

The panel acceleration at point $\mathbf{x}$, $\gamma(\mathbf{x}, t)$ induced by the WPF, can be expressed as the convolution product [127]

$$\gamma(\mathbf{x}, t) = \iint_{\sum_p} \int_{-\infty}^{\infty} h_\gamma(\mathbf{x}, \tilde{\mathbf{x}}, t-\tau) p(\tilde{\mathbf{x}}, \tau) \, \mathrm{d}\tau \mathrm{d}\tilde{\mathbf{x}}, \tag{4.1}$$

where $p(\tilde{\mathbf{x}}, \tau)$ is the WPF exerted on the surface of the panel $\sum_p$, and $h_\gamma(\mathbf{x}, \tilde{\mathbf{x}}, t)$ is the acceleration impulse response at point $\mathbf{x}$ due to a normal unit force at point $\tilde{\mathbf{x}}$.

Due to the random nature of the turbulent flow, the panel response can be described by the cross-correlation function of the acceleration between two points $\mathbf{x}$ and $\mathbf{x}'$, denoted as $R_{\gamma\gamma}$. Assuming a stationary and ergodic random process, $R_{\gamma\gamma}$ can be expressed as follows

$$R_{\gamma\gamma}(\mathbf{x}, \mathbf{x}', t) = \int_{-\infty}^{\infty} \gamma(\mathbf{x}, t)\gamma(\mathbf{x}', t+\tau) \, \mathrm{d}\tau. \tag{4.2}$$

By substituting Eq. (4.1) into Eq. (4.2) and performing a temporal Fourier transform on the cross-correlation function of the panel acceleration, the space-frequency spectrum of the panel acceleration, $S_{\gamma\gamma}(\mathbf{x}, \mathbf{x}', \omega)$, can be computed as follows [127]

$$S_{\gamma\gamma}(\mathbf{x}, \mathbf{x}', \omega) = \iint_{\sum_p} \iint_{\sum_p} H_\gamma(\mathbf{x}, \tilde{\mathbf{x}}, \omega) S_{pp}(\tilde{\mathbf{x}}, \tilde{\tilde{\mathbf{x}}}, \omega) H_\gamma^*(\mathbf{x}', \tilde{\tilde{\mathbf{x}}}, \omega) \, \mathrm{d}\tilde{\mathbf{x}} \mathrm{d}\tilde{\tilde{\mathbf{x}}}, \tag{4.3}$$

where $H_\gamma(\mathbf{x}, \tilde{\mathbf{x}}, \omega)$ is the acceleration at point $\mathbf{x}$ for a normal force at point $\tilde{\mathbf{x}}$, $S_{pp}(\tilde{\mathbf{x}}, \tilde{\tilde{\mathbf{x}}}, \omega)$ is the temporal Fourier transform of the cross-correlation function of the WPF, and the asterisk denotes the complex conjugate. The space-frequency spectrum of $S_{pp}(\tilde{\mathbf{x}}, \tilde{\tilde{\mathbf{x}}}, \omega)$, can be expressed as follows by applying the inverse Fourier transform to the CSD function of TBL pressure in the wavenumber domain, $\phi_{pp}(\mathbf{k}, \omega)$,

$$S_{pp}(\tilde{\mathbf{x}}, \tilde{\tilde{\mathbf{x}}}, \omega) = \frac{1}{4\pi^2} \iint_{-\infty}^{\infty} \phi_{pp}(\mathbf{k}, \omega) e^{\mathrm{j}\mathbf{k}(\tilde{\tilde{\mathbf{x}}} - \tilde{\mathbf{x}})} \, \mathrm{d}\mathbf{k}, \tag{4.4}$$

where $\mathbf{k}$ is the wavevector with components k_x and k_y in the streamwise and spanwise directions in the (x, y) plane, respectively. By substituting Eq. (4.4) into Eq. (4.3) and rearranging the terms, one obtains

$$S_{\gamma\gamma}(\mathbf{x}, \mathbf{x}', \omega) = \frac{1}{4\pi^2} \iint_{-\infty}^{\infty} H_\gamma(\mathbf{x}, \mathbf{k}, \omega) \phi_{pp}(\mathbf{k}, \omega) H_\gamma^*(\mathbf{x}', \mathbf{k}, \omega) \, \mathrm{d}\mathbf{k}, \tag{4.5}$$

where

$$H_{\gamma}(\mathbf{x},\mathbf{k},\omega) = \iint_{\sum_p} H_{\gamma}(\mathbf{x},\tilde{\mathbf{x}},\omega)e^{-\mathrm{j}\mathbf{k}\tilde{\mathbf{x}}}\,\mathrm{d}\tilde{\mathbf{x}}. \tag{4.6}$$

$H_{\gamma}(\mathbf{x},\mathbf{k},\omega)$ characterizes the vibration behavior of the panel and is called sensitivity function. Eq. (4.6) indicates that $H_{\gamma}(\mathbf{x},\mathbf{k},\omega)$ is the acceleration at point $\mathbf{x}$ when the panel is excited by a unit wall plane wave of wavevector $\mathbf{k}$.

The sensitivity function $H_{\gamma}(\mathbf{x},\mathbf{k},\omega)$ for a simply-supported rectangular panel corresponding to the acceleration at point $\mathbf{x}$ when the panel is excited by a unit wall plane wave is given by

$$H_{\gamma}(\mathbf{x},\mathbf{k},\omega) = -\omega^2 \sum_{m=1}^{M}\sum_{n=1}^{N} \frac{\psi_{mn}(\mathbf{k})\varphi_{mn}(\mathbf{x})}{\Omega(\omega_{mn}^2 - \omega^2 + \mathrm{j}\eta_s\omega\omega_{mn})}, \tag{4.7}$$

where $\Omega = \rho_s h L_x L_y/4$ is the modal mass, η_s is the structural loss factor, and M, N are the cut-off modal orders in the x and y directions, respectively. For a flat rectangular panel with simply-supported boundary conditions, ω_{mn} and $\varphi_{mn}(\mathbf{x})$ are respectively the modal frequency and mode shapes of the panel given by [103, 149]

$$\omega_{mn} = \sqrt{\frac{D}{\rho_s h}}\left(\left(\frac{m\pi}{L_x}\right)^2 + \left(\frac{n\pi}{L_y}\right)^2\right), \tag{4.8}$$

$$\varphi_{mn}(\mathbf{x}) = \sin\left(\frac{m\pi x}{L_x}\right)\sin\left(\frac{n\pi x}{L_y}\right). \tag{4.9}$$

The modal forces ψ_{mn} are calculated by integration over the panel surface A as follows

$$\psi_{mn}(k_x,k_y) = \int_A \varphi_{mn}(x,y)e^{\mathrm{j}(k_x x + k_y y)}\,\mathrm{d}A = I_m^x(k_x)I_n^y(k_y), \tag{4.10}$$

and

$$I_s^r|(r,s) = (x,m)\vee(y,n) = \begin{Bmatrix} \left(\frac{s\pi}{L_r}\right)\frac{(-1)^s e^{\mathrm{j}(k_r L_r)}-1}{k_r^2-\left(\frac{s\pi}{L_r}\right)^2} & k_r \neq \frac{s\pi}{L_r} \\ \frac{1}{2}\mathrm{j}L_r & \text{otherwise} \end{Bmatrix}. \tag{4.11}$$

Let us consider N_s accelerometers mounted on the panel surface excited by a TBL, see Figure 4.1. The position of each accelerometer is determined by the coordinates $\mathbf{x}_i$, denoted as (x_i, y_i) for $i \in \{1, N_s\}$. By truncating and sampling the wavenumber space, and employing the rectangular rule to approximate the integration in Eq. (4.5), one can compute the CSD of panel acceleration between two points $\mathbf{x}_i$ and $\mathbf{x}_j$ as follows

$$S_{\gamma\gamma}(\mathbf{x}_i, \mathbf{x}_j, \omega) = \frac{1}{4\pi^2} \sum_{l=1}^{N_k} H_\gamma(\mathbf{x}_i, \mathbf{k}_l, \omega) \phi_{pp}(\mathbf{k}_l, \omega) H_\gamma^*(\mathbf{x}_j, \mathbf{k}_l, \omega) \, \delta k_x \delta k_y, \tag{4.12}$$

where δk_x and δk_y denote the resolutions of the wavenumber domain in the streamwise and spanwise directions, respectively. The total number of points in the wavenumber space is denoted by $N_k = N_{k_x} \times N_{k_y}$, where N_{k_x} and N_{k_y} indicate the number of points considered in sampling the wavenumber space along the x and y axes, respectively. The wavevector at a discrete point l is represented by $\mathbf{k}_l = (k_{x,l}, k_{y,l})$.

For the given array of N_s sensors, we define the CSD of the panel acceleration between each $N_s \times N_s$ combination of sensors as $S_{\gamma\gamma}(\mathbf{x}_i, \mathbf{x}_j, \omega)$, where $i, j \in \{1, N_s\}$. Then, all computed CSD of accelerations are stored in a vector denoted as $\mathbf{S}_\gamma$, referred to as the acceleration CSD vector. The components of $\mathbf{S}_\gamma$ are organized such that the first N_s components correspond to $S_{\gamma\gamma}(\mathbf{x}_1, \mathbf{x}_j, \omega)$ with $j \in \{1, N_s\}$, the next N_s components correspond to $S_{\gamma\gamma}(\mathbf{x}_2, \mathbf{x}_j, \omega)$ with $j \in \{1, N_s\}$, and so on:

$$\mathbf{S}_\gamma = \begin{bmatrix} S_{\gamma\gamma}(\mathbf{x}_1, \mathbf{x}_1, \omega) \\ S_{\gamma\gamma}(\mathbf{x}_1, \mathbf{x}_2, \omega) \\ \vdots \\ S_{\gamma\gamma}(\mathbf{x}_i, \mathbf{x}_j, \omega) \\ \vdots \\ S_{\gamma\gamma}(\mathbf{x}_{N_s}, \mathbf{x}_{N_s-1}, \omega) \\ S_{\gamma\gamma}(\mathbf{x}_{N_s}, \mathbf{x}_{N_s}, \omega) \end{bmatrix}_{N_s^2 \times 1}. \tag{4.13}$$

As the CSD of the panel acceleration between different sensors can be estimated by Eq. (4.12), we can then write it in the following compact format

$$\mathbf{S}_\gamma = \mathbf{Q} \mathbf{\Phi}_{\mathbf{pp}}, \tag{4.14}$$

where $\mathbf{\Phi_{pp}}$ is a vector consisting of the unknown WPF components in the truncated wavenumber space as follows

$$\mathbf{\Phi_{pp}} = \begin{bmatrix} \phi_{pp}(k_{x,1}, k_{y,1}, \omega) \\ \phi_{pp}(k_{x,1}, k_{y,2}, \omega) \\ \vdots \\ \phi_{pp}(k_{x,l}, k_{y,l}, \omega) \\ \vdots \\ \phi_{pp}(k_{x,N_{kx}}, k_{y,N_{ky}-1}, \omega) \\ \phi_{pp}(k_{x,N_{kx}}, k_{y,N_{ky}}, \omega) \end{bmatrix}_{N_k \times 1} . \tag{4.15}$$

The components of $\mathbf{\Phi_{pp}}$ are organized such that the first N_{k_y} components correspond to $\phi_{pp}(k_{x,1}, k_{y,l}, \omega)$ with $l \in \{1, N_{k_y}\}$, the next N_{k_y} components correspond to $\phi_{pp}(k_{x,2}, k_{y,l}, \omega)$ with $l \in \{1, N_{k_y}\}$, and so on. Besides, $\mathbf{Q}$ is a matrix with the following elements

$$\mathbf{Q} = \frac{\delta k_x \delta k_y}{4\pi^2} \begin{bmatrix} H_\gamma(\mathbf{x}_1, \mathbf{k}_1, \omega) H_\gamma^*(\mathbf{x}_1, \mathbf{k}_1, \omega) & H_\gamma(\mathbf{x}_1, \mathbf{k}_2, \omega) H_\gamma^*(\mathbf{x}_1, \mathbf{k}_2, \omega) & \cdots & \cdots & H_\gamma(\mathbf{x}_1, \mathbf{k}_{N_k}, \omega) H_\gamma^*(\mathbf{x}_1, \mathbf{k}_{N_k}, \omega) \\ H_\gamma(\mathbf{x}_1, \mathbf{k}_1, \omega) H_\gamma^*(\mathbf{x}_2, \mathbf{k}_1, \omega) & \ddots & & & \vdots \\ \vdots & & H_\gamma(\mathbf{x}_i, \mathbf{k}_l, \omega) H_\gamma^*(\mathbf{x}_j, \mathbf{k}_l, \omega) & & \vdots \\ \vdots & & & \ddots & H_\gamma(\mathbf{x}_{N_s}, \mathbf{k}_{N_k}, \omega) H_\gamma^*(\mathbf{x}_{N_s-1}, \mathbf{k}_{N_k}, \omega) \\ H_\gamma(\mathbf{x}_{N_s}, \mathbf{k}_1, \omega) H_\gamma^*(\mathbf{x}_{N_s}, \mathbf{k}_1, \omega) & \cdots & \cdots & & H_\gamma(\mathbf{x}_{N_s}, \mathbf{k}_{N_k}, \omega) H_\gamma^*(\mathbf{x}_{N_s}, \mathbf{k}_{N_k}, \omega) \end{bmatrix}_{N_s^2 \times N_k} . \tag{4.16}$$

The $\mathbf{Q}$ matrix and $\mathbf{S}_\gamma$ in Eq. (4.14) can be computed using Eqs. (4.7) and (4.12), respectively. The elements of matrix $\mathbf{Q}$ can be acquired through experiments or numerical simulations. At a specific excitation frequency, the vector $\mathbf{S}_\gamma$ can also be calculated based on the panel vibration response to the TBL forcing function. According to Eq. (4.14), we arrive at N_s^2 equations for the $N_x \times N_y$ unknown coefficients. In most cases, the number of unknowns $N_x \times N_y$ exceeds the number of equations N_s^2. Eq. (4.14) is therefore an under-determined system, and it has no unique solution. Moreover, $\mathbf{Q}$ in Eq. (4.14) is a non-square matrix, and standard inversion cannot be applied to the matrix. Hence, the goal is to find an approximate solution of $\phi_{pp}(\mathbf{k}, \omega)$ that minimizes the residuals of the Eq. (4.14). For this purpose, a regularization technique can be used as a pseudo-inverse method to estimate the WPF in the low-wavenumber domain [76]. Consequently, the wall pressure CSD vector for that particular frequency can be approximated as follows

$$\mathbf{\Phi_{pp}} = [\mathbf{Q}]^{\dagger}\mathbf{S}_{\gamma}, \tag{4.17}$$

where † denotes the pseudo-inverse.

Performance of the proposed method can be numerically evaluated by benchmarking the estimated WPF against a reference input WPF. This can be done by exciting the panel through a known forcing function and applying Eq. (4.17) to the computed vibration response. Therefore, modeling the reference TBL forcing function is very important in the performance evaluation of the proposed method. In Sections 4.1.2 and 4.1.3, we have described two ways of simulating the reference TBL forcing functions, which allow us to study the efficacy of the proposed method in both ideal and practical situations.

4.1.2 Closed-form CSD of the Wall Pressure Field

In this subsection, we have detailed the process of simulating the reference TBL forcing function using the closed-form semi-empirical models. The CSD of the WPF in Eq. (4.5) can be determined as per Graham formulation [70, 71] by utilizing different models for auto-spectral density (ASD) of the pressure field, $\Psi_{pp}(\omega)$, and the normalized CSD of the pressure field, $\tilde{\phi}_{pp}(k, \omega)$, independently, as stated in Eq. (2.1)

As in Chapter 3, this chapter employs the Goody model, presented in Eq. (3.9), and the Mellen model, presented in Eq. (3.10), to evaluate the ASD function of the WPF and the normalized CSD function in Eq. (2.1), respectively.

In order to calculate the panel acceleration using the closed-form semi-empirical models in Eq. (4.12), a truncated number of wavenumbers in the x and y directions need to be defined. When defining the cut-off wavenumbers in these directions, it is important to ensure that the range of considered wavenumbers is large enough to be able to include the significant contribution of the CSD function. For this study, a cut-off wavenumber of $1.2k_c$ was used in both directions to account for the convective contributions of the WPF of the TBL simulated using the Goody+Mellen model. It is noteworthy mentioning that a convergence study has been performed to select the cut-off wavenumber and identify the wavenumber resolution in the wavenumber domain to ensure that the input TBL is accurately modeled and the estimated wall pressure field is converged.

4.1.3 Realizations of the Wall Pressure Field

A closed-form formula for the TBL WPF does not exist in practice, and only a limited number of snapshots/samples is available. Therefore, we have introduced a second procedure in this subsection, which involves a virtual model specifically designed for conducting vibration experiments. To do this, a random TBL is simulated with deterministic loading using the UWPW technique [129], which mimics experimental situations. This virtual experiment synthesizes TBL wall pressure and then uses this deterministic forcing function to calculate the acceleration response of a panel using the ensemble average of different realizations of wall pressure. The pressure beneath the TBL for the rth realization can be represented by a set of UWPWs at point (x_M, y_M) of the panel, as shown in Eq. (3.18).

Using the modal expansion method (as described in Section 4.1.1 for evaluation of the sensitivity functions), the acceleration response of a panel at point (x_M, y_M) at a given frequency of ω induced by the wall pressure (Eq. (3.18)) corresponding to the rth realization at each sensor position can be obtained by [129],

$$\gamma^r(x_M, y_M, \omega) = -\omega^2 \sum_{m=1}^{M} \sum_{n=1}^{N} \frac{F^r_{mn}(\omega)\varphi_{mn}(x_M, y_M)}{\Omega(\omega^2_{mn} - \omega^2 + \mathrm{j}\eta_s\omega\omega_{mn})}, \tag{4.18}$$

where the modal forces are given by

$$F^r_{mn} = \sum_{l=1}^{N_k} \sqrt{\frac{\phi_{pp}(k_{x,l}, k_{y,l}, \omega)\delta k_x \delta k_y}{4\pi^2}} e^{\mathrm{j}\theta^r_l} \psi_{mn}(k_{x,l}, k_{y,l}). \tag{4.19}$$

In the following section, we assess the results obtained from employing the proposed approach to estimate the WPF in the low-wavenumber domain.

4.2 Results and Discussion

This section uses the formulation outlined in Section 4.1 to evaluate the WPF in the low-wavenumber domain. This study investigates a rectangular steel panel with a simply-supported boundary condition that is excited by a TBL. Table 4.1 presents the panel's dimensions and material properties. Figure 4.1 shows a turbulent airflow with a free flow velocity of 50 m/s moving over the panel. The air density and the kinematic viscosity values are set to 1.225 kg/m^3 and 1.5111×10^{-5}m^2/s, respectively. The TBL parameters for the panel are given in Table 4.2.

TABLE 4.1: Dimensions and material properties of the panel

Parameter	Value
Young's modulus E (Gpa)	210
Poisson's ratio ν_p	0.3
Density ρ_s (kg/m^3)	7800
Length L_x (mm)	455
Width L_y (mm)	375
Thickness h (mm)	1
Damping loss factor η_s	0.01
Flexural Wavenumber k_f $(1/m)$	89.46

Moreover, selecting the wavenumber resolution is pivotal in the WPF calculations, necessitating a balance between computational costs and accuracy. As $\mathbf{Q}$ is dependent on the wavenumber resolution, in this study, we adjust the wavenumber resolution at each frequency to ensure a constant size for matrix $\mathbf{Q}$ across all frequencies. To ensure that the computed CSD of the panel acceleration by the virtual accelerometers in both techniques incorporates all major modes, in this study, we employed $M = N = 50$ in calculating $\mathbf{S}_\gamma(\omega)$ according to Eqs. (4.7) and (4.12). However, for computing the $H_\gamma(\mathbf{x}, \mathbf{k}, \omega)$ in Eq. (4.16), we only consider the modes number of M and N within the frequency range $[0, 1.3\omega]$, as in practice, only the resonant modes in a given frequency band can be reasonably estimated. Furthermore, in order to effectively utilize the structure's wavenumber filtering abilities for estimating the low-wavenumber domain of the WPF through the panel's vibration response, it is essential that the excitation frequency be well above the coincidence frequency. This condition ensures that the convective wavenumber of the TBL excitation remains far from the flexural wavenumber of the panel. The flexural wavenumber k_f of a panel is given by [72]

$$k_f = \sqrt[4]{\frac{12\rho_s(1-\nu_p^2)}{Eh^2}}\sqrt{\omega}. \tag{4.20}$$

TABLE 4.2: TBL parameters for air flow with speed of 50 m/s

Parameter	Value
TBL thickness δ (mm)	5.77
TBL displacement thickness δ^* (mm)	0.729
Wall shear stress τ_w (pa)	5.989

It is important to note that the low-wavenumber domain investigated in this study is defined within the range of the panel's flexural wavenumber ($-k_f \leq k_x, k_y \leq k_f$).

Figure 4.2 illustrates the flexural wavenumber of the plate and the convective wavenumber of the TBL as a function of frequency. The figure demonstrates that the coincidence frequency (the frequency at which the bending wave speed in the structure and the convection speed are equal [114]) occurs around $f \approx 200$ Hz. Consequently, to apply the vibration approach for estimating the WPF in the low-wavenumber domain, a minimum frequency of $f = 400$ Hz is chosen. This condition ensures that the convective wavenumber of the TBL excitation remains far from the flexural wavenumber of the panel. Hence, the convective domain is filtered out by the structure (see Figure 1.2), and this allows us to overcome the main challenge of estimating the low-wavenumber components of the WPF using an acoustic method [2].

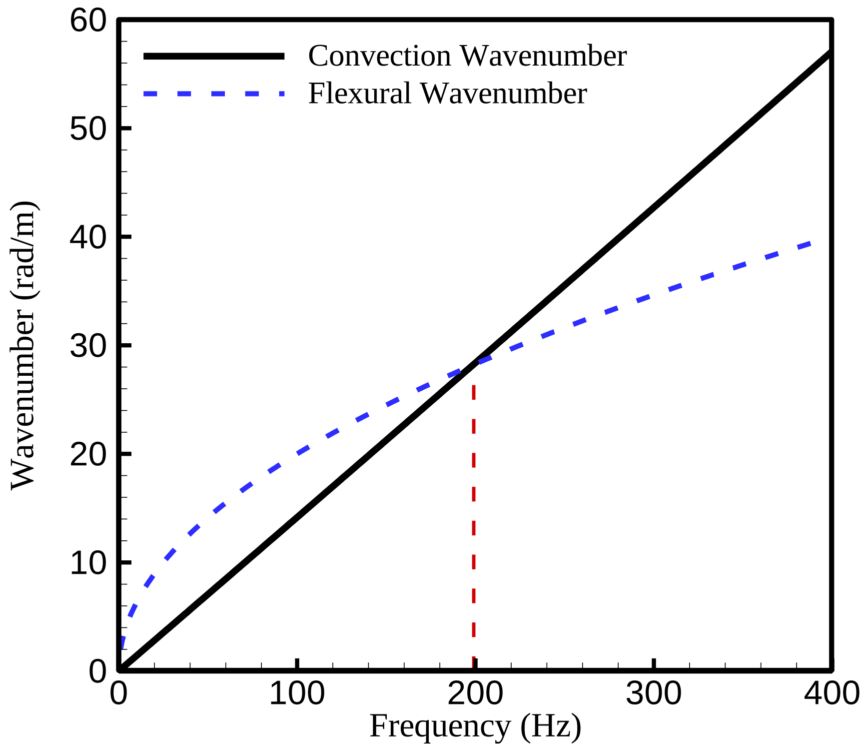

FIGURE 4.2: Flexural and convective wavenumbers as a function of frequency.

Figure 4.3 illustrates the flowchart outlining the three-step procedure employed in this work for estimating the WPF in the low-wavenumber domain. In the first step, the CSD of the panel acceleration is calculated. Here, we have initially simulated the TBL forcing function using both the closed-form semi-empirical models (Subsection 4.1.2) and the UWPW technique (Subsection 4.1.3). The former employs Eqs. (4.7) and

(4.12) to compute the CSD of the panel accelerations at the sensor positions. This technique provides a theoretical framework for estimating the WPF in an ideal situation and is particularly useful for parametric study and gaining insights into the fundamental behavior of the proposed method (see Section 4.2.1). However, by utilizing the virtual experiment model (see Section 4.2.2), it is possible to have a more realistic assessment of the efficiency of using an accelerometer array to estimate the low-wavenumber WPF in real-world situations. To achieve this, Eq. (3.18) simulates the TBL forcing function using the UWPW technique, and the panel accelerations at the sensor positions are computed using Eq. (4.18). In the second step, components of matrix $\mathbf{Q}$ are computed by substituting the sensitivity function of the simply-supported panel (Eq. (4.7)) into Eq. (4.16). In the final step, the regularization technique is applied to Eq. (4.17) to estimate the low-wavenumber components of the WPF.

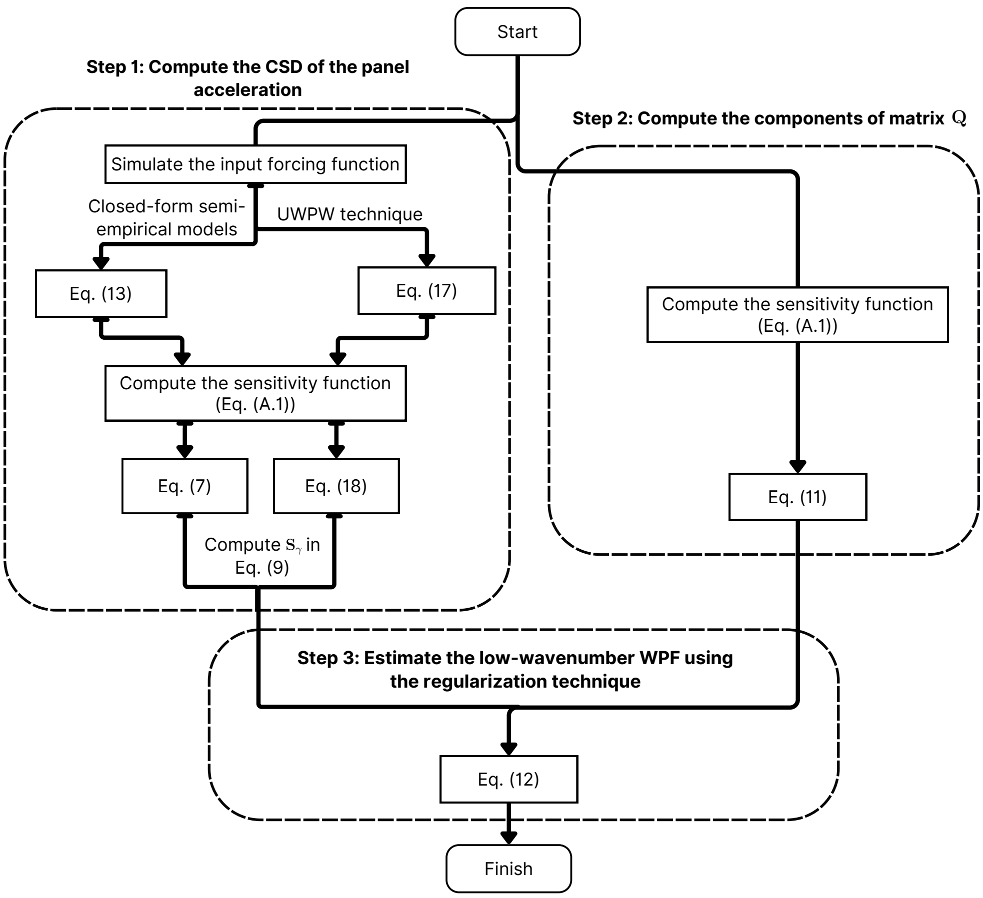

FIGURE 4.3: Flowchart illustrating the procedure for estimating the low-wavenumber WPF.

4.2.1 WPF Estimation Using a Closed-form Semi-empirical TBL Model

The initial step in measuring the acceleration response of the panel excited by a TBL involves arranging sensors. However, practical limitations prevent using a large number of accelerometers. This raises the question of how many sensors are needed to obtain a reasonable estimation of the WPF in the low-wavenumber domain. In this work, we employ a random array of sensors as shown in Figure 4.4 Each sensor is numbered to highlight the sensors' location for estimating the WPF in the low-wavenumber domain. For example, when it is stated that 10 or 20 sensors are used in the array, it simply means the sensors from 1 to 10 or 1 to 20 are selected from the 34 sensors shown in Figure 4.4. In the upcoming subsections, we examine the impact of the number of sensors on the estimation of WPF in the low-wavenumber domain using two numerical methods: 1) the Moore-Penrose pseudo-inverse method [10] and 2) the TGSVD method [76].

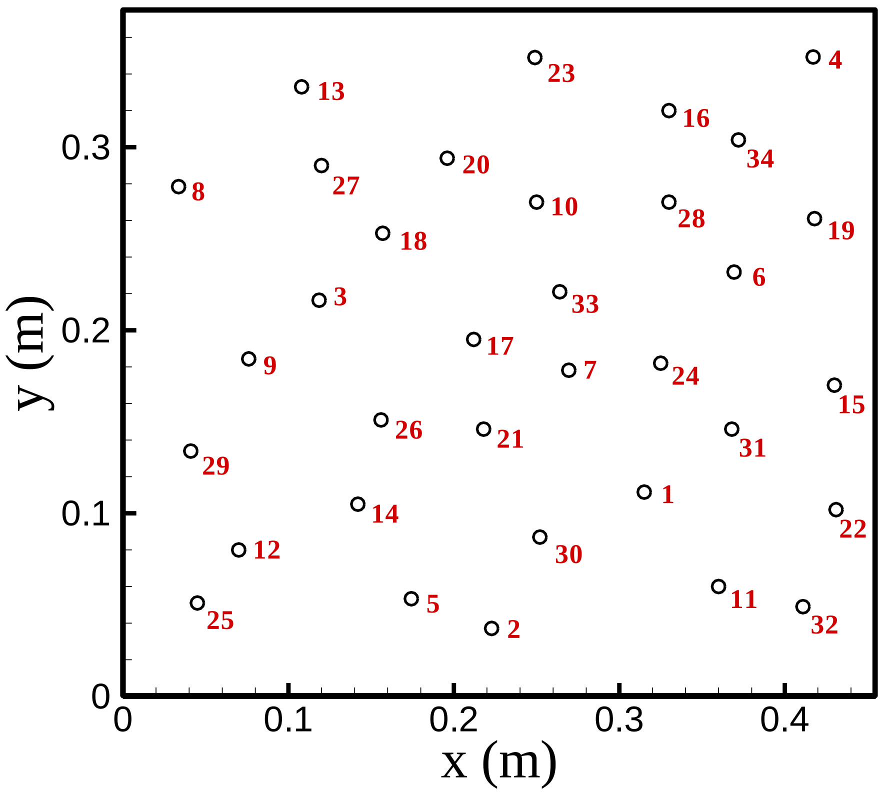

FIGURE 4.4: An irregular array pattern with 34 sensors; x-axis in streamwise and y-axis in spanwise directions.

4.2.1.1 Moore-Penrose Pseudo-inverse Method

To estimate the TBL WPF, Eq. (4.17) needs to be solved. As a first attempt, the Moore-Penrose pseudo-inverse method [10] is employed to estimate the WPF using all singular values (SVs) of matrix $\mathbf{Q}$. This technique is particularly useful for inverting non-square or singular matrices, which do not have a standard inverse. To study the effect of the number of sensors on the estimation of the TBL WPF, the MAE of the estimated WPF in the low-wavenumber domain is calculated for different number of sensors with respect to the corresponding domain of the reference input TBL model simulated using the Goody and Mellen Models. Eq. (3.13) is used to compute the MAE of the estimated WPF in the low-wavenumber domain.

It should be noted that unlike the acoustic-based approach, where the co-array factor and sensor locations were crucial for estimating the WPF in the low-wavenumber domain [2], our investigation (results are not shown here) showed that in the vibration-based approach the estimation of WPF in the low-wavenumber domain is almost independent from the sensor positions and co-array factor.

Figure 4.5 depicts the MAE of the estimated WPF in the low-wavenumber domain as a function of the number of sensors at some selected frequencies. For the results in Figure 4.5, the WPF is evaluated by applying the Moore-Penrose pseudo-inverse method to obtain the inverse of the matrix $\mathbf{Q}$ in Eq. (4.17) using all SVs of matrix $\mathbf{Q}$. In the case of a rectangular plate, two mode numbers are necessary in both the x-direction and the y-direction to label each vibration mode. Upon examining the mode numbers and referring to Figure 4.5, it is found that for a given frequency of excitation, as the number of sensors approaches the sum of maximum mode number of the plate along x and y directions below the excitation frequency ($M_b + N_b$), a notable increase in the MAE is manifested. The vertical dashed lines show this sum for each frequency. This observation leads to the conclusion that to avoid a dramatic increase in MAE while using the Moore-Penrose pseudo-inverse with all SVs, the maximum number of sensors should be limited to the $M_b + N_b$ at the excitation frequency. However, the condition number for the matrix norm of $\mathbf{Q}$ in Eq. (4.17) is very large, classifying it as severely ill-conditioned [76]. This condition implies that even a small perturbation in the input data can lead to a significant impact on the solution, rendering the equation without a unique solution [76]. Consequently, as the number of sensors increases, the condition number also increases, making the system more susceptible to numerical errors. This effect explains why, beyond a certain sensor count, the MAE starts increasing despite the expectation of improved accuracy with additional data. This suggests that numerical instability, rather than physical limitations, is the primary reason for the observed trend.

Moreover, as can be seen from Figure 4.5, the MAE is still large even when the above threshold is considered. This suggests that an alternative approach must be explored to achieve a more accurate estimation of the WPF in the low-wavenumber domain.

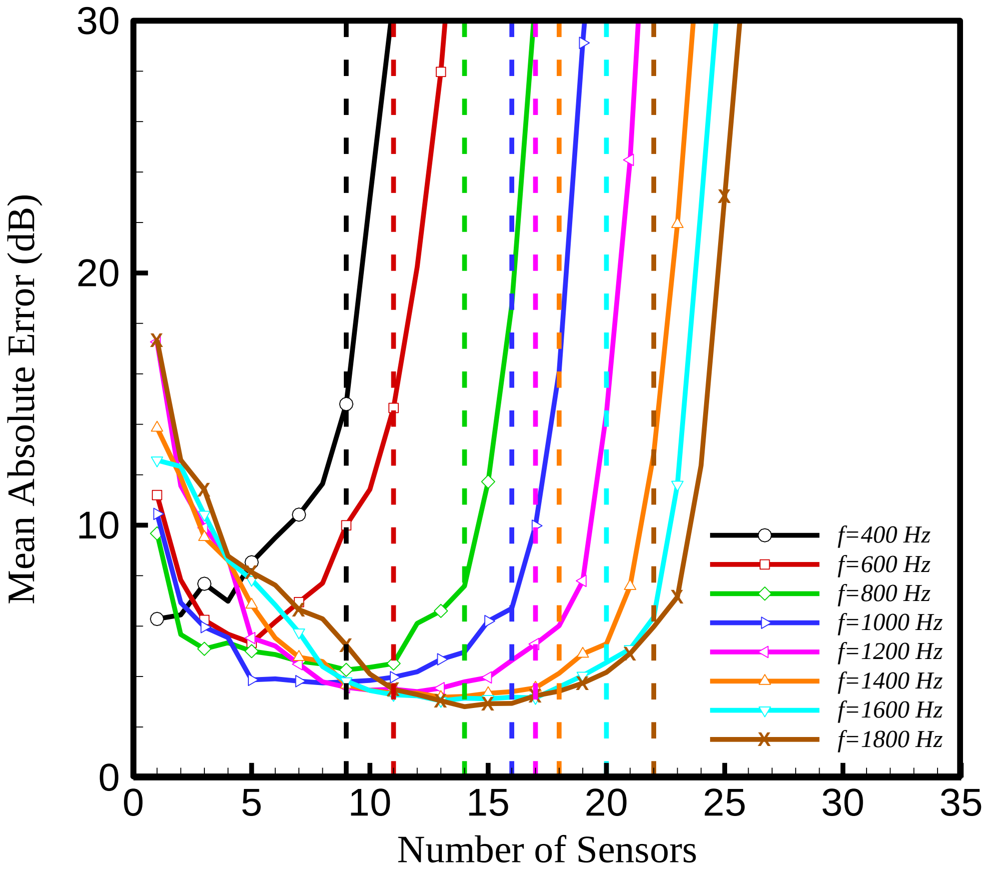

FIGURE 4.5: MAE for the estimated WPF in the low-wavenumber domain as a function of number of sensors at some selected frequencies using the Moore-Penrose Pseudo-inverse method.

4.2.1.2 Truncated Generalized Singular Value Decomposition Method

To improve the accuracy of the WPF estimation in the low-wavenumber domain, numerical regularization methods have been used for computing stabilized solutions for discrete ill-posed problems. The goal of regularization theory is to provide appropriate side constraints with optimal weights so that the regularized solution is a suitable approximation of the unknown desired solution. These methods filter out contributions to the solution that correspond to small singular values, but there is no specific procedure that can solve every individual problem [76].

We used various regularization techniques described in [76] to compute the WPF through Eq. (4.17). The truncated generalized singular value decomposition (TGSVD) method was found to be more effective in estimating the WPF in the low-wavenumber domain by minimizing the first derivative 2-norm of the solution [76]. The regularization parameter for truncating the generalized singular value problem is determined using the corner method, considering a minimum of 4 sensors for the array arrangement. This method employs an adaptive pruning algorithm to identify the corner of a discrete L-curve generated by the TGSVD method [77]. For the numerical applications presented herein, the Matlab package developed by [76] for the analysis and solution of discrete ill-posed problems was utilized (see Appendix C).

Similar to Figure 4.5, Figure 4.6 illustrates the MAE as a function of sensor numbers at selected frequencies using the TGSVD method. Based on the observations made earlier in Figure 4.5 concerning the relationship between the mode numbers and the number of SVs used for the inversion of matrix $\mathbf{Q}$, it is essential to restrict the number of SVs to the sum of maximum mode number of the plate along x and y directions bellow each frequency of excitation $(M_b + N_b)$ when a higher number of SVs can be employed for the WPF estimation. It is worth mentioning that for an array with N_s sensors, N_s^2 CSD can be computed. Thus, the number of SVs in matrix $\mathbf{Q}$ is equivalent to N_s^2. Using this observation, we set a preconditioning for determining the regularization parameter using the corner method: if the number of sensors in the array arrangement is lower than $M_b + N_b$ at the exciting frequency, all SVs are used for regularization parameter determination. However, if the number of sensors exceeds $M_b + N_b$, the regularization parameter is determined using the first $(M_b + N_b)^2$ SVs. The results depicted in Figure 4.6 reveal that the utilization of the TGSVD method consistently yields lower MAE at each frequency when compared to Figure 4.5, even for $N_s \leq (M_b + N_b)$. Additionally, this figure highlights that the calculated MAE is lower at higher frequencies compared to the corresponding MAE values at lower frequencies. This suggests that as we move further away from the coincidence frequency, the panel's vibration is dominated by the low-wavenumber components of the WPF, resulting in a more precise estimation of the

WPF. Furthermore, for frequencies beyond 1000 Hz, the MAE remains below 1 dB when utilizing only 5 sensors, and increasing the number of sensors does not result in a substantial enhancement in the estimation of the low-wavenumber WPF. Consequently, in contrast to the acoustic-based approach [2], employing a relatively small number of sensors in the vibration-based method is sufficient for accurate estimation of the WPF in the low-wavenumber domain.

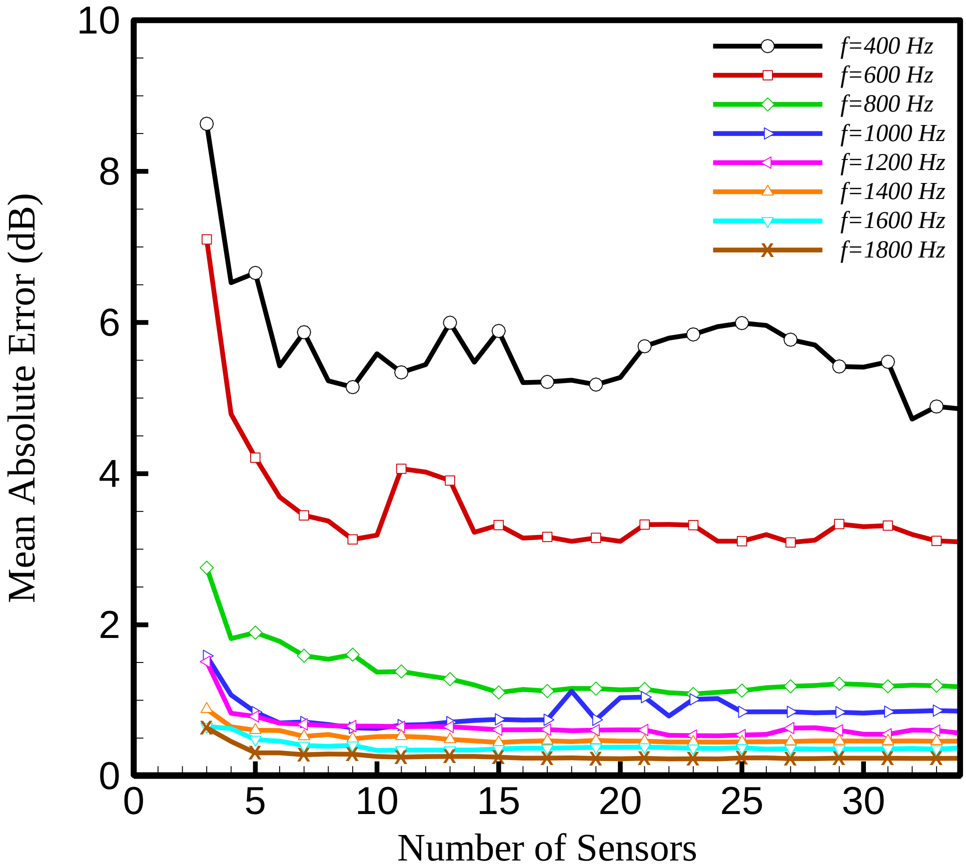

FIGURE 4.6: MAE for the estimated WPF in the low-wavenumber domain as a function of sensor number at some selected frequencies using the truncated generalized singular value decomposition method.

In what follows, we showcase the results of the WPF estimation in the low-wavenumber domain and the corresponding MAE calculations using the TGSVD method. The outlined procedure from the preceding subsections is applied at two selected frequencies: 1400 Hz (non-resonance frequency) and 1511 Hz (resonance frequency). We use a wavenumber resolution of $\delta k_x = \delta k_y = 5.6$ m^{-1} for the resonance frequency, and a resolution of 6.1 m^{-1} for non-resonant frequencies. Figure 4.7 (a), (b) illustrate the CSD of the TBL WPF generated using the Goody+Mellen model as the reference input at 1400 Hz and 1511 Hz, respectively. The targeted low-wavenumber domain is represented by a rectangular area in Figure 4.7 (a), (b).

Figure 4.7 (c)-(f) present the estimated WPF obtained by applying the TGSVD method to the CSM of acceleration data collected from an irregular arrangement of 10 sensors mounted on the TBL-excited panel at resonance and non-resonance frequencies. Figure 4.7(c),(d) present a color map of the estimated WPF. Figure 4.7(e),(f) provide cross-sectional views of both the reference and estimated WPF at $k_y = 0$, with two red-dashed lines indicating the boundaries of the low-wavenumber domain. Additionally, the calculated MAEs between the reference input WPF and estimated WPF in the low-wavenumber domain for $f = 1400$ Hz and $f = 1511$ Hz are 0.52 dB and 0.32 dB, respectively. The results depicted in Figure 4.7 (c)-(f) demonstrate that by following the procedure outlined in Section 4.1 and utilizing an irregular array consisting of 10 sensors, it is possible to accurately estimate the WPF in the low-wavenumber domain, with an MAE below 1 dB. It can also be observed that when the excitation frequency is sufficiently distant from the coincidence frequency, the panel filters the convective region of the WPF. Hence, the panel vibration is mostly due to the low-wavenumber domain of the WPF. As a result, the proposed method could estimate the WPF within the low-wavenumber domain accurately, while the WPF outside of this domain cannot be effectively estimated.

4.2.1.3 Improving the Accuracy of Low-wavenumber WPF Estimation at Low Frequencies

As shown in Figure 4.6, the calculated MAE within the low-wavenumber domain of the WPF at lower frequencies ($f = 400$ Hz and $f = 600$ Hz) is higher compared to that at higher frequencies due to the proximity to the coincidence frequency. To enhance the accuracy of the estimated WPF within the low-wavenumber domain for these particular frequencies, we explored the impact of modifying the panel's dimensions, as illustrated in Figure 4.8. This involves considering a scaling ratio (SR) for the panel, where the L_x and L_y dimensions of the panel were multiplied by the SR value, and the positions of the sensors were adjusted or scaled accordingly. All other parameters were kept constant during this investigation. It is important to note that this modification does not affect the flexural wavenumber of the panel (as per Eq. (4.20)), ensuring that the targeted low-wavenumber domain for estimation remains unchanged. As observed in Figure 4.8, increasing the SR results in enhanced estimations of the WPF and a subsequent reduction in the MAE. To provide rationale for this observation, Figure 4.9 illustrates the

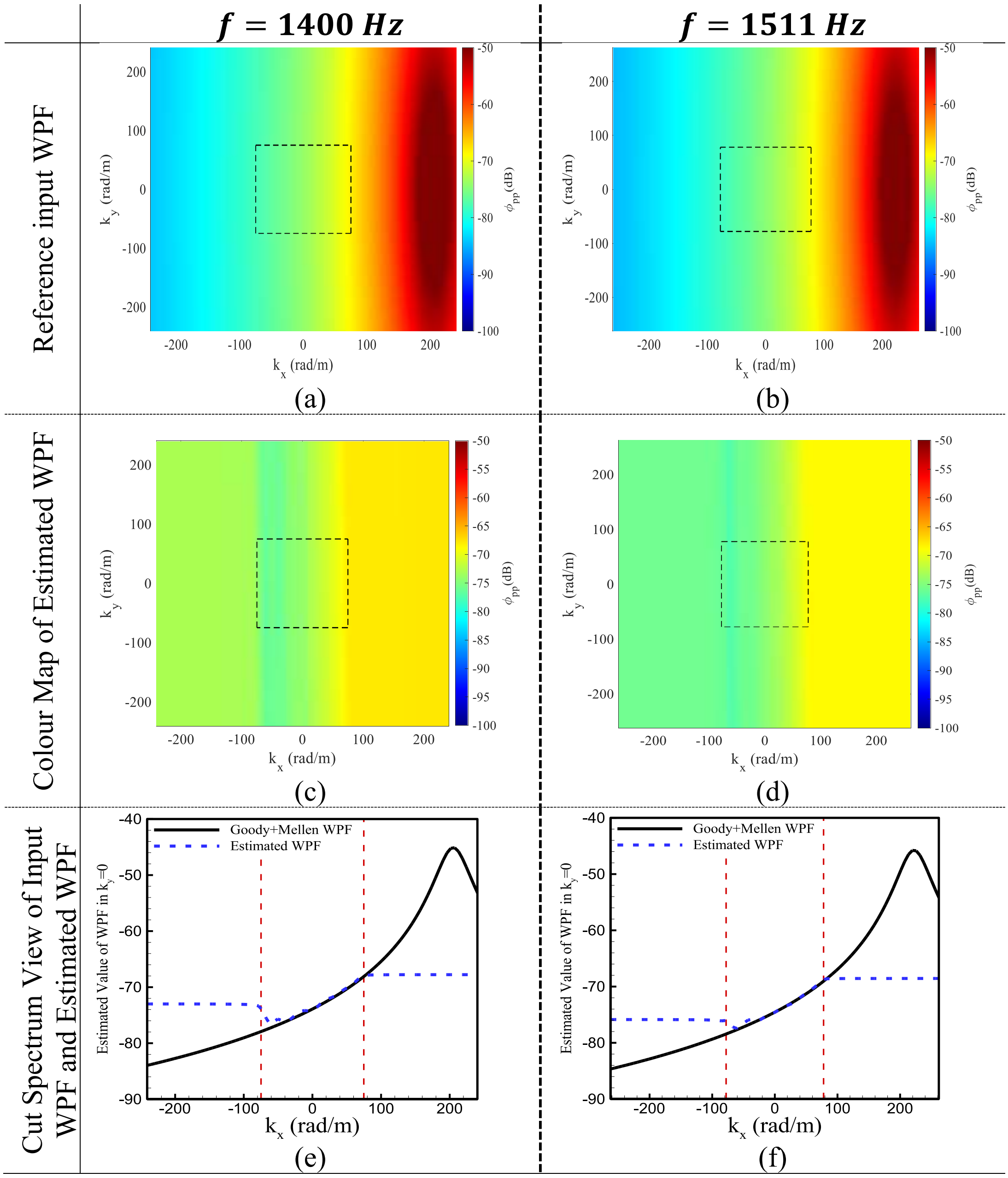

FIGURE 4.7: Evaluation of the proposed method on the estimation of the WPF $\phi_{pp}(\mathbf{k}, f)$ (dB, ref. 1 Pa^2.Hz^{-1}) in the low-wavenumber domain at 1400 Hz (left column) and 1511 Hz (right column) using a random array pattern with 10 sensors. Reference input CSDs of the WPF for each frequency are shown in (a) and (b), and map view of the estimated WPF are presented in (c) and (d). 2D wavenumber-frequency spectra for $k_y = 0$ are plotted against longitudinal wavenumber in (e) and (f). MAEs calculated between the reference input CSD and estimated WPF in the low-wavenumber domain for $f = 1400$ Hz and $f = 1511$ Hz are 0.52 dB and 0.32 dB, respectively.

MAE against $\beta = \mathrm{SR}\sqrt{A}/\lambda_b$ across multiple low frequencies (close to the coincidence frequency). Here, A represents the surface area of the original plate ($L_x \times L_y$), and $\lambda_b = 2\pi/k_f$ denotes the flexural wavelength of the plate at the excitation frequency. This ratio signifies the number of wavelengths present in the plate at each frequency.

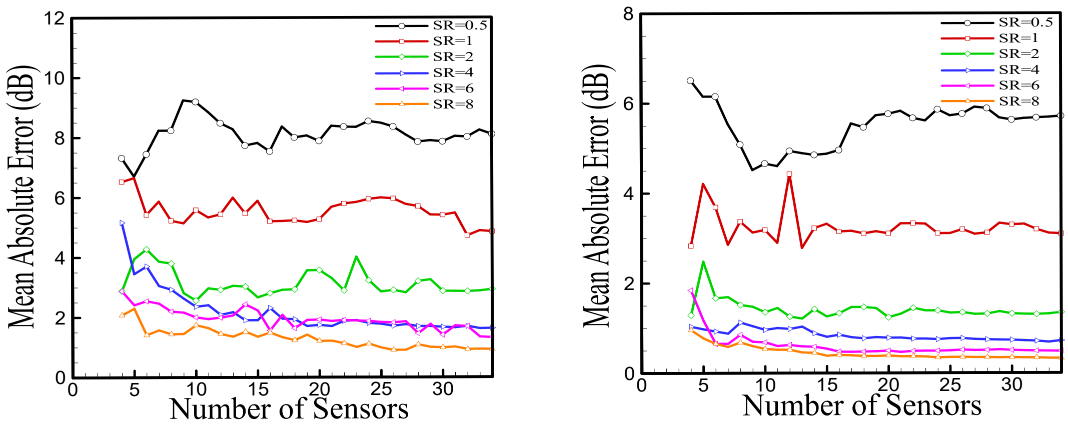

(a) (b)

FIGURE 4.8: Comparison of the MAE for the estimated WPF in the low-wavenumber domain at (a) 400 Hz and (b) 600 Hz as a function of number of sensors for different scaling ratio values.

As it can be seen from Figure 4.9, with a low number of flexural wavelengths ($\beta \leq 5$), the magnitude of MAE is notable. However, with an increase in β, the MAE decreases across the selected frequencies. Particularly at high β values, the MAE converges to a level below 1 dB. This trend implies that employing larger panels with $\beta > 5$, which accommodate a greater number of flexural wavelengths of the plate, leads to improved the WPF estimations at low-frequencies.

4.2.2 Virtual Vibration Experiments

In Subsection 4.2.1, we used a closed-form formula for the CSD function of the WPF and employed the vibration of a panel excited by the forcing function based on this WPF to estimate the input WPF through an inverse method. A parametric study was then carried out to better understand the effect of each system's parameter on the WPF estimation. However, in practice, such a closed-form WPF does not exist. Even when multiple records of the pressure fluctuations are obtained under the same experimental conditions, they would not be identical due to the random nature of excitation. Each outcome of an experiment involving random processes is known as a sample function, and the collective set of potential outcomes is referred to as the ensemble of the process. In order to have a more realistic assessment of the effectiveness of the proposed method for estimating the WPF, a virtual vibration experiment is conducted. This involves simulating the WPF using various deterministic realizations of TBL pressure fluctuations, and then estimating the CSM through ensemble averaging of these realizations.

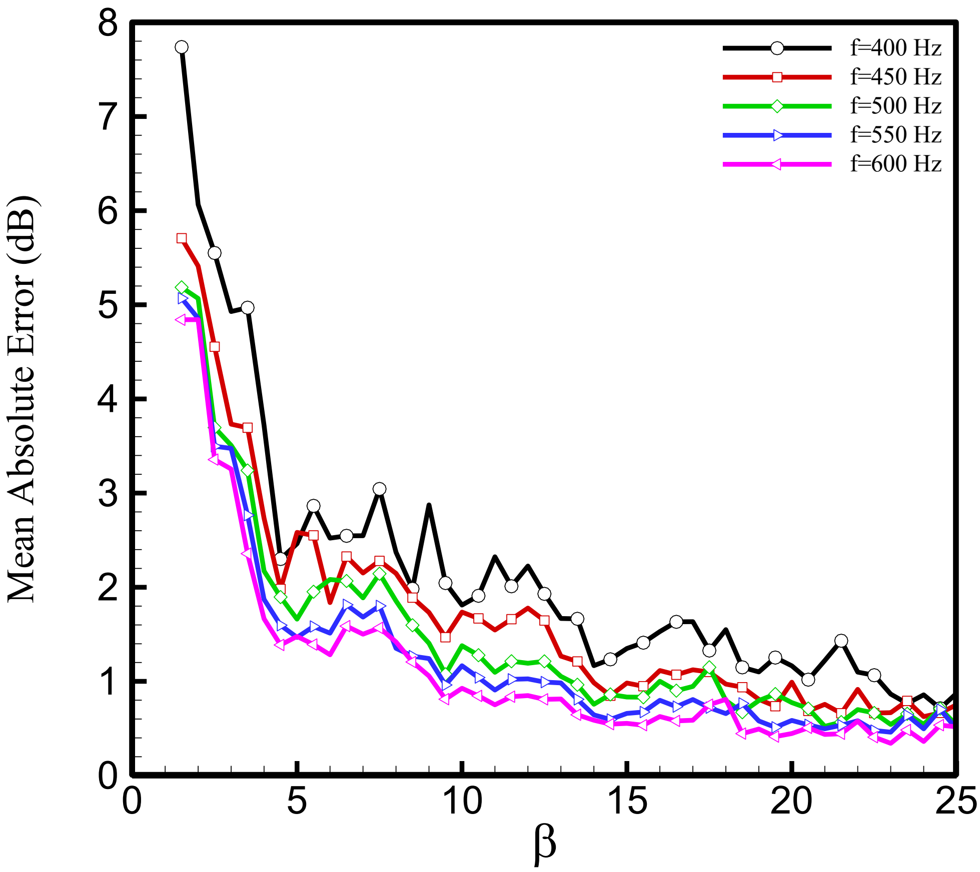

FIGURE 4.9: Comparison of the MAE for the estimated WPF in the low-wavenumber domain at low frequencies as a function of $\beta = \mathrm{SR}\sqrt{A}/\lambda_b$.

To achieve this, the UWPW technique [129] described in Section 4.1.3 is employed for simulating the WPF.

By employing multiple realizations, the acceleration response of the panel can be computed using Eq. (4.18) for each realization. As an illustration, Figure 4.10 displays two realizations of the surface pressure field at frequencies of 1400 Hz and 1511 Hz, accompanied by their corresponding panel displacements. Different number of realizations is used in the ensemble averaging process to calculate the CSM of panel accelerations at the sensor positions. Subsequently, the CSM of the panel acceleration can be obtained by ensemble averaging of the calculated CSD of acceleration between different pairs of sensors across all realizations. Figure 4.11 shows a flowchart describing the implementation of the UWPW technique in the virtual vibration experiment for estimation of the WPF in the low-wavenumber domain. This approach allows simulation and estimation of the WPF in a realistic manner.

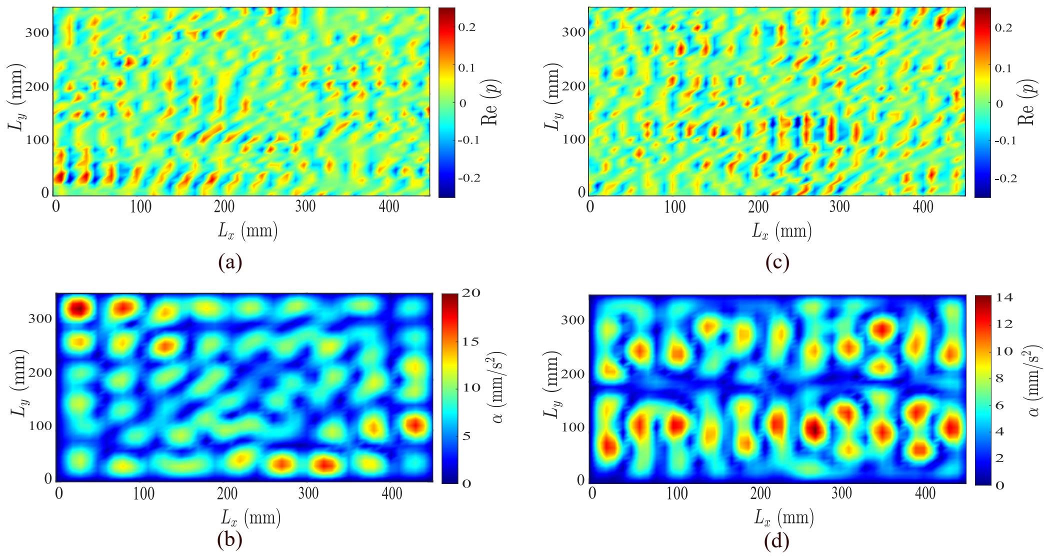

FIGURE 4.10: Two realizations of the WPF at (a) 1400 Hz and (c) 1511 Hz using the truncated Mellen and Goody models for a flow speed of 50 m/s, accompanied by the corresponding panel displacement in (b) and (d).

In following subsection, we study the effect of the number of realizations as a function of the excitation frequency and number of sensors (Subsection 4.2.2.1) using the virtual vibration approach on the estimation of the WPF in the low-wavenumber domain.

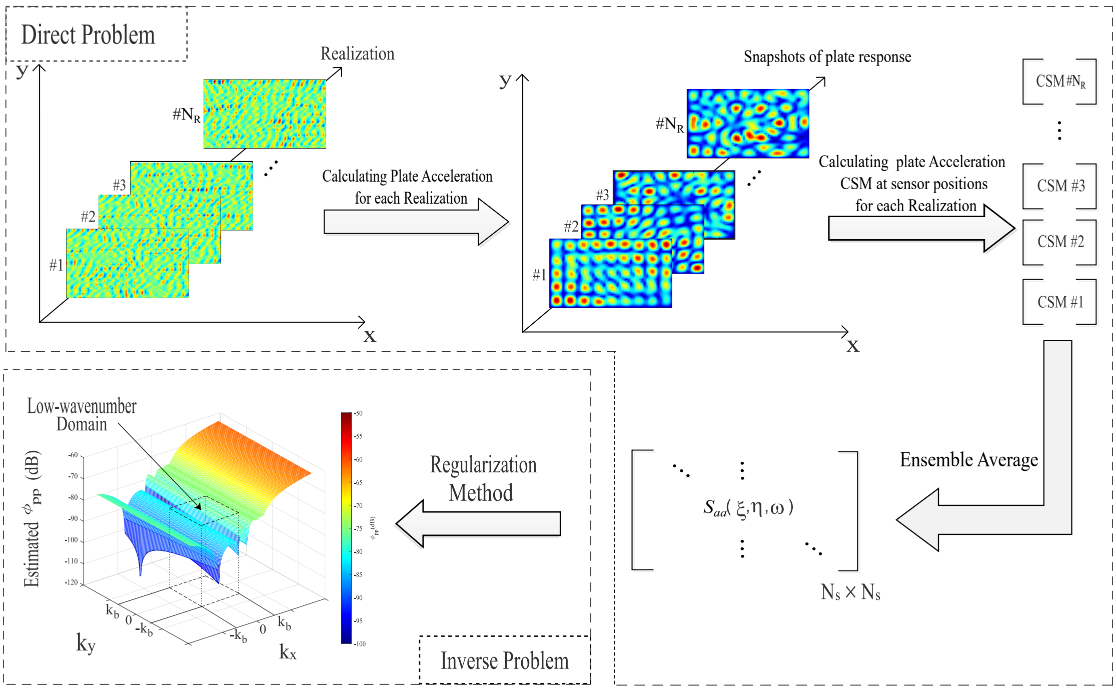

FIGURE 4.11: Simulation process in the virtual vibration experiments using the UWPW technique.

4.2.2.1 Effect of Number of Realizations

In this section, the impact of the number of realizations on the estimation of the WPF in the low-wavenumber domain is examined. Figure 4.12 presents a comparison of the MAE values for the estimated WPF as a function of frequency using an irregular array pattern with numbers of sensors: $N_s = 5$, $N_s = 10$, and $N_s = 15$. In this figure, "Ref. TBL" represents the MAE computed using the closed-form formula. The MAE values are plotted for various numbers of realizations. The findings indicate that with an increase in the number of realizations, the MAE values converge towards the ideal case (Ref. TBL). Furthermore, the graph in Figure 4.12 illustrates that MAE decreases at higher frequencies, indicating greater accuracy in estimating the WPF in the low-wavenumber domain. This observation underscores that the accuracy of the estimated WPF improves as the frequency of excitation deviates further from the coincidence frequency, whether it's at resonance or non-resonance frequencies.

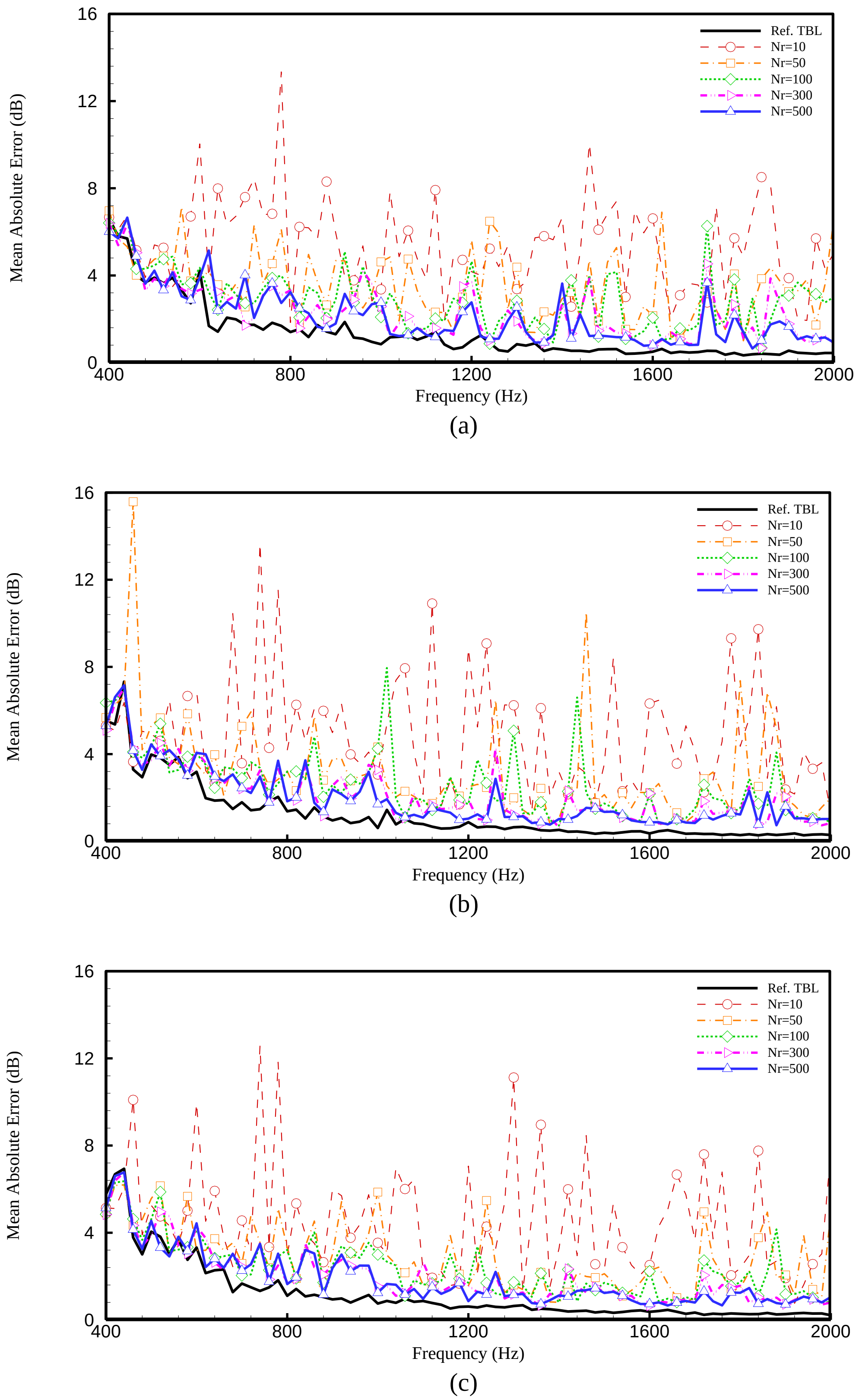

FIGURE 4.12: Comparison of MAE for the estimated WPF in the low-wavenumber domain as a function of frequency. The results showcase the impact of the number realization on the accuracy of the estimated WPF for (a) $N_s = 5$, (b) $N_s = 10$, and (c) $N_s = 15$.

In Figure 4.13, the impact of the number of sensors on the estimation of the WPF in the low-wavenumber domain is examined at two frequencies: 1) the non-resonance frequency of $f = 1400$ Hz and 2) the resonance frequency of $f = 1511$ Hz. In this figure, the MAE is plotted as a function of the number of sensors for the selected frequencies for different number of realizations. These MAE values are compared with those obtained using the reference input TBL excitation (Ref. TBL). The results indicate that as the number of realizations increases, the MAE values approach the reference case. It is observed that to achieve an accurate estimation of the WPF at these two selected frequencies with MAE below 2 dB, more than 300 realizations are required. Furthermore, it is observed that when a high number of realizations is used, increasing the number of sensors does not result in a significant improvement in the estimated WPF.

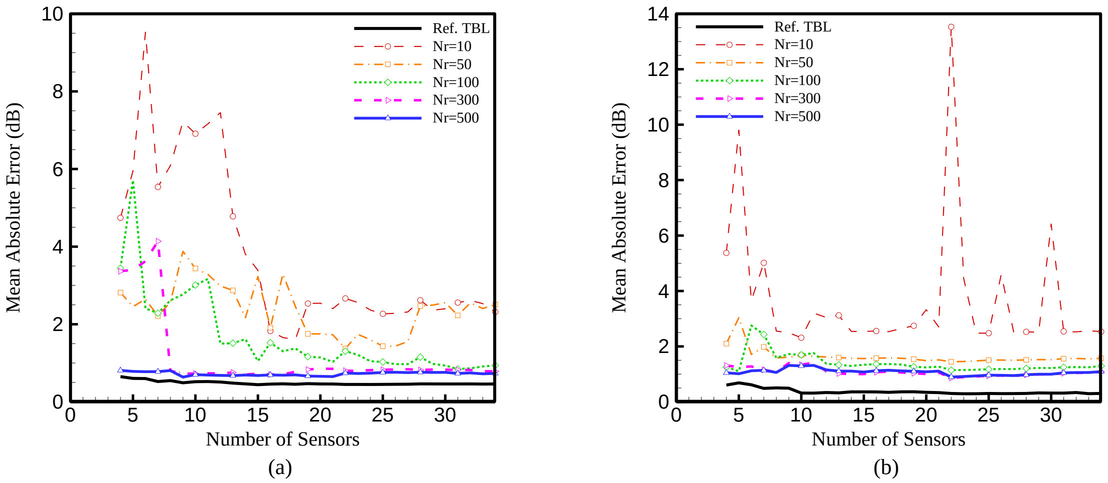

FIGURE 4.13: Comparison of MAE for the estimated WPF in the low-wavenumber domain as a function of number of sensors. The results showcase the impact of the number realization on accuracy of the estimated WPF for (a) $f = 1400$ Hz and (b) $f = 1511$ Hz.

The color-maps and cross-section views at $k_y = 0$ of the estimated WPF in the low-wavenumber domain at $f = 1400$ Hz and $f = 1511$ Hz using different number of realizations are demonstrated in Figure 4.14 and Figure 4.15, respectively. The MAE between the input reference WPF (Figure 4.7 (a), (b)) and the estimated WPF in the low-wavenumber domain is included for each case to assess the accuracy of the estimations.

Based on the results displayed in Figure 4.14 and Figure 4.15, it can be seen that with only ten realizations ($N_r = 10$), the MAE exceeds 5 dB at the non-resonance frequency, while at the resonance frequency, it is approximately 2 dB. However, as the number of realizations increases to $N_r = 100$, the estimated WPF improves at both frequencies, with the MAE dropping to 3 dB at the non-resonance frequency and 1.69 dB at the resonance frequency. Further increasing the number of realizations results in even more accurate estimations, bringing the estimated WPF closer to the reference WPF. Notably, for $N_r \geq 300$, the estimated WPF exhibits high accuracy, with an MAE of approximately 1 dB. When comparing Figure 4.7 (f) with Figure 4.15 (b), (d), and (f), slight discrepancies between the estimated WPF and the reference become apparent, especially in the lower end of the low-wavenumber domain. These differences could be attributed to the number of realizations used to estimate the CSM. They can be alleviated by increasing the number of realizations. Additionally, this observation corresponds with the findings presented in Figure 4.12, indicating that regardless of whether the excitation is at resonance or non-resonance frequency, the accuracy of the estimated WPF at each number of realizations generally improves as the frequency of excitation deviates further from the coincidence frequency.

Furthermore, upon comparing the results obtained by Abtahi et al. [2] with the above findings, it can be inferred that, unlike the acoustic-based approach where a substantial number of realizations is needed to accurately estimate the low-wavenumber levels in the TBL pressure field (due to contamination by the convective ridge), utilizing the vibration-based approach filters the convective region of the WPF, allowing for accurate estimation of the low-wavenumber WPF using a significantly smaller number of realizations.

4.2.2.2 Repeatability Study of the Virtual Vibration Experiment

The utilization of a random procedure in the UWPW technique to generate the phase in Eq. (4.19) introduces variability in the CSM of the acceleration data obtained for each realization of the panel. This variability has the potential to impact the MAE value of the estimated WPF in the low-wavenumber domain. To assess the influence of this factor on the WPF estimation, we considered four different numbers of realizations: $N_r = 50$, $N_r = 100$, $N_r = 200$, and $N_r = 300$. We calculated the vibration response of the panel

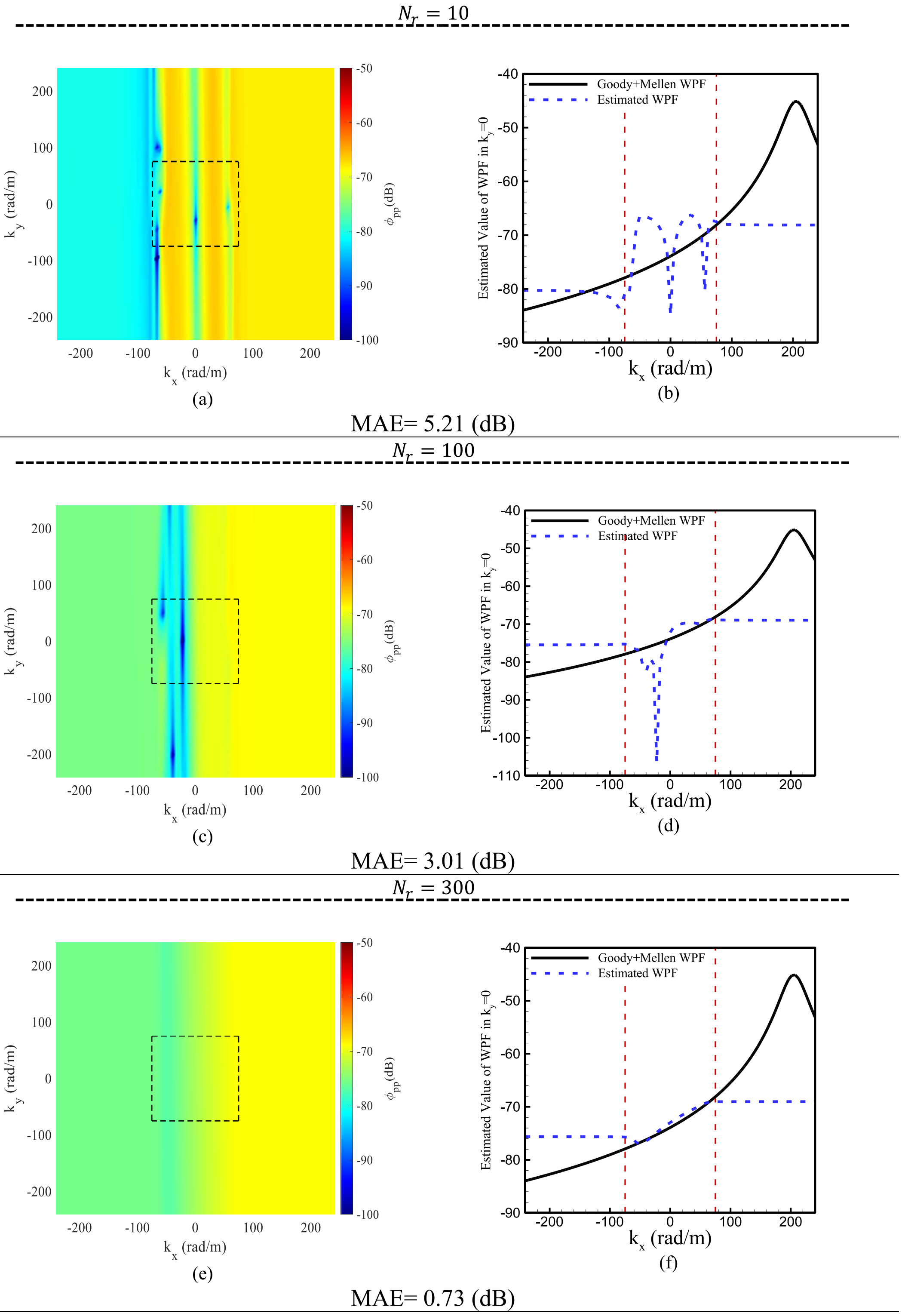

FIGURE 4.14: The estimated WPF $\phi_{pp}(\mathbf{k}, f)$ (dB, ref. 1 Pa^2.Hz^{-1}) at $f = 1400$ Hz for an irregular array pattern with 10 sensors for different numbers of realizations. The left column shows the color maps of the estimated WPF, while the right column displays the 2D wavenumber-frequency spectra for $k_y = 0$. The MAE for each case is displayed in decibels (dB).

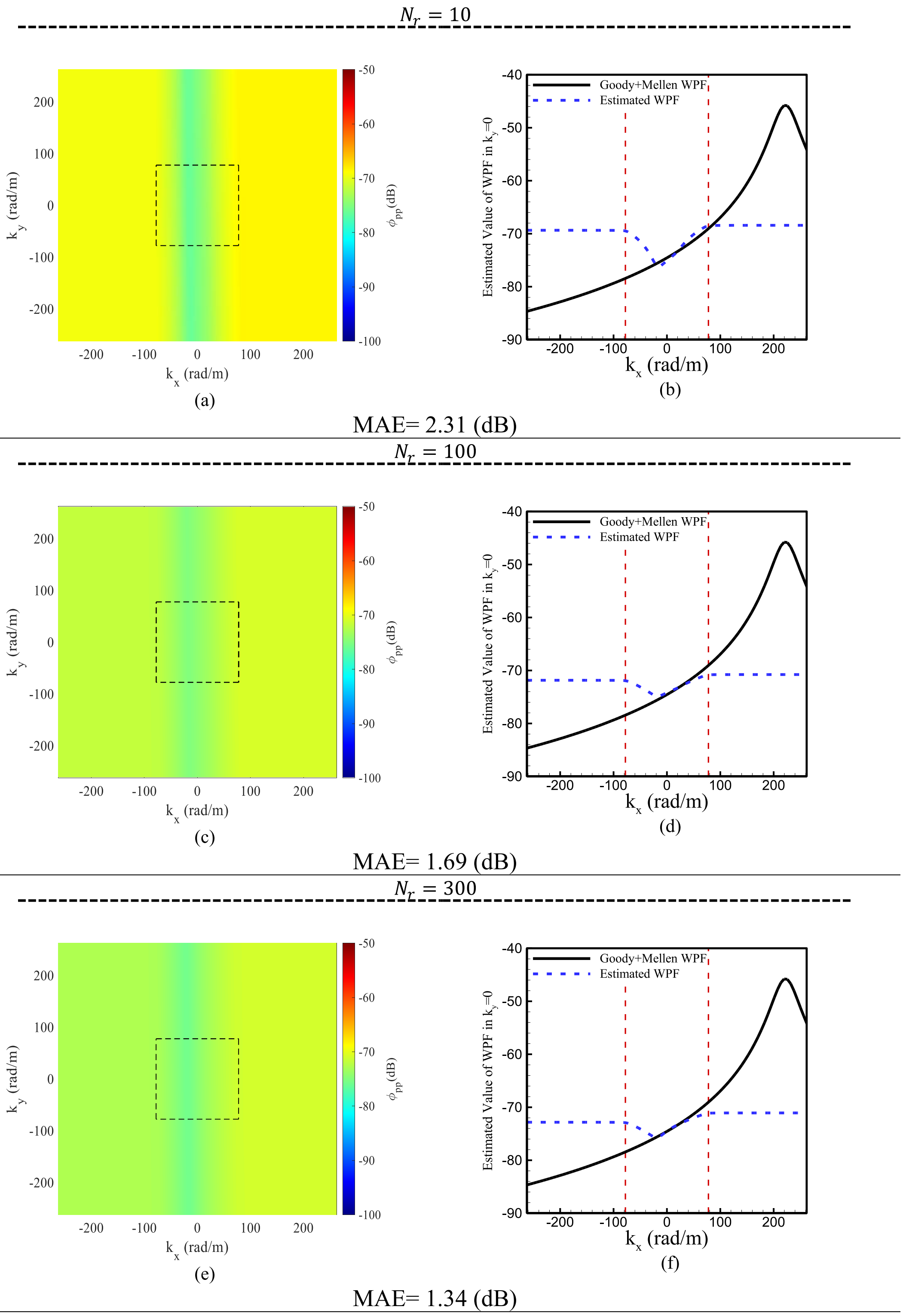

FIGURE 4.15: The estimated WPF $\phi_{pp}(\mathbf{k}, f)$ (dB, ref. 1 Pa^2.Hz^{-1}) at $f = 1511$ Hz for an irregular array pattern with 10 sensors for different numbers of realizations. The left column shows the color maps of the estimated WPF, while the right column displays the 2D wavenumber-frequency spectra for $k_y = 0$. The MAE for each case is displayed in decibels (dB).

at $f = 1400$ Hz and generated probability density function (PDF) graphs based on 100 data samples collected for three irregular arrays with $N_s = 5$, $N_s = 10$, and $N_s = 15$, as shown in Figure 4.4. Figure 4.16 displays the PDF graphs for these scenarios with mean value μ of the collected samples. In the context of an experiment, this could be regarded as a repeatability study that measures the variation in the estimated output data under the same conditions.

This figure illustrates that the probability of encountering higher MAE values is significantly higher for the case with $N_s = 5$ and $N_r = 50$ compared to the other cases. However, as the number of sensors and realizations increase, the mean value μ of the samples decreases. This reduction indicates an improvement in the accuracy of the estimated WPF in the low-wavenumber domain. Additionally, the results presented in Figure 4.16 underscore the robustness of employing the TGSVD method in the vibration-based approach, especially when a substantial number of realizations and a sufficiently high number of sensors are employed for the estimation of the WPF in the low-wavenumber domain. For instance, with $N_s = 15$ and $N_r = 300$, the majority of the calculated MAEs among 100 samples exhibit an accuracy below 1 dB, emphasizing the stability of the method.

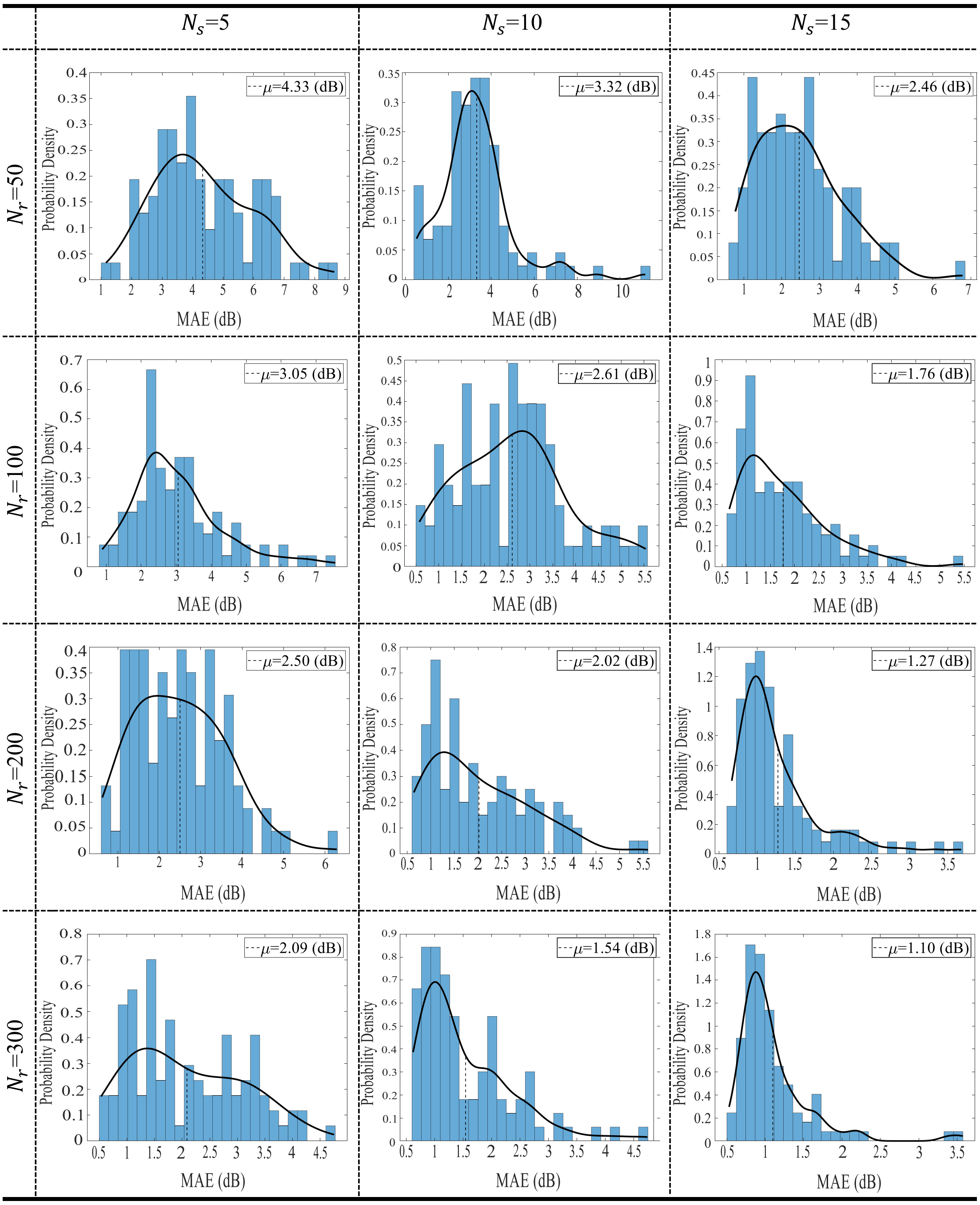

FIGURE 4.16: The probability density function graphs showing the distribution of 100 samples obtained for different numbers of realizations at three irregular numbers of sensors.

4.3 Summary

In this study, an inverse vibration method for the estimation of the TBL WPF in the low-wavenumber domain was proposed. To demonstrate the efficacy of the method, an analytical model of an elastic simply-supported panel subjected to a TBL excitation was considered. Acceleration data acquired from the panel was then employed to estimate the WPF in the low-wavenumber domain. A parametric study was initially carried out using a closed-form TBL forcing function to show the effects of number of vibration sensors and size of the panel on the accuracy of the WPF estimation in the low-wavenumber domain. It was found that, unlike the acoustic-based methods, where a relatively high number of sensors is required to respect the Nyquist criterion, a few sensors are sufficient to estimate the WPF in the low-wavenumber using the proposed vibration-based method. Moreover, the error of the WPF estimation in the low-wavenumber domain at low frequencies (close to the coincidence frequency) can be substantially reduced by increasing only the size of the panel without changing other parameters. This allows accurate estimation of the WPF over a wider frequency range.

Moreover, to quantify the potential effectiveness of the proposed method in practice, virtual experiments were conducted using the UWPW technique, where the CSM was approximated through an ensemble average of various realizations of the panel's acceleration induced by the WPF. This simulated a practical scenario where limited samples are available and can be collected from vibration measurements of the panel. It was realized that a few hundred snapshots were required for accurately estimating the WPF in the low-wavenumber domain. Additionally, to evaluate the repeatability of the proposed procedure in real experiments for estimating the WPF in the low-wavenumber domain, we considered different sets of realizations using the UWPW technique across various numbers of sensors. The obtained results demonstrated the effective and accurate performance of the proposed regularization method when a substantial number of realizations and an ample number of sensors were employed for the estimating WPF in the low-wavenumber domain.

Nevertheless, it is important to note that this investigation was under the assumptions of having a homogeneous, stationary, and fully developed TBL with zero pressure gradient across the plate. Additionally, it was assumed that panel vibrations do not affect the WPF and that the random TBL force is ergodic. These simplifications underscore the difficulties in estimating this region in experiments, where not only homogeneity in the TBL and ergodic randomness may not hold true, but also various sources of error and uncertainties, including background noise, instrumental and human errors, exist.

Chapter 5

Estimation of the Low-wavenumber WPF beneath a TBL using an Accelerometer Array: Frequency Band Analysis

In Chapter 4, we explored the estimation of the WPF in the low-wavenumber domain using single-frequency analysis. We demonstrated that, to achieve an accurate estimation of the WPF with an MAE below 2 dB at frequencies well above the coincidence frequency, more than 300 realizations are necessary.

However, collecting more than 300 samples of experimental data under identical conditions to estimate the WPF in real-world scenarios could be a cumbersome and time-consuming task. In order to maintain the accuracy of the estimated WPF while minimizing the number of realizations required, we propose a frequency band method in this chapter, instead of the single frequency analysis. This method aims to reduce the required number of realizations by leveraging computed acceleration data across multiple discrete frequencies. However, when utilizing the frequency band method, we need to make the assumptions that the ASD of the WPF is known in advance, and the low-wavenumber components of the WPF remain independent of frequency within a narrow frequency range (frequency band).

Section 5.1 outlines the methodology for estimating the WPF using multiple discrete frequencies. In this approach, an accelerometer array is assumed to be mounted on an elastic plate that is excited by a TBL WPF. Similar to Chapter 4, the method is based on the relationship between the TBL forcing function and structural vibrations in the wavenumber domain. By using vibration data obtained from a TBL-excited structure at multiple frequencies and incorporating the sensitivity functions of the respective structure, the cross-spectrum density of the pressure fluctuations in the wavenumber domain can be estimated. To demonstrate the method's effectiveness, an analytical model of a simply-supported panel excited by a reference TBL model is used. The proposed method is then tested in a numerical study to verify the estimated WPF against an input reference TBL WPF modeled by a semi-empirical model. The findings are presented in Section 5.2, where the results from the virtual vibration experiment are compared. The chapter concludes with a summary of the findings in Section 5.3.

This chapter is based on the article "A vibration-based method to estimate the low-wavenumber wall pressure field in a turbulent boundary layer", which will be presented in the *Inter-Noise 2024*.

5.1 Analytical Formulation

In this section, we have detailed the process of estimating the WPF in the low-wavenumber domain through the utilization of the frequency band method. In this method, the cross-spectrum matrix (CSM) calculated for different frequencies within the frequency band of $[\omega_{\text{min}} - \omega_{\text{max}}]$ is utilized to estimate the WPF in the low-wavenumber domain. Prior to implementing this method, it is assumed that the ASD of the WPF ($\bar{\Psi}_{pp}(\omega)$) has been experimentally measured using a microphone array. Therefore, estimating the normalized CSD of the WPF is sufficient for the WPF estimation.

In Figure 5.1, the schematic diagram of the system under consideration is presented. In the upcoming subsection, the frequency band approach is introduced for the estimation of the WPF in the low-wavenumber domain.

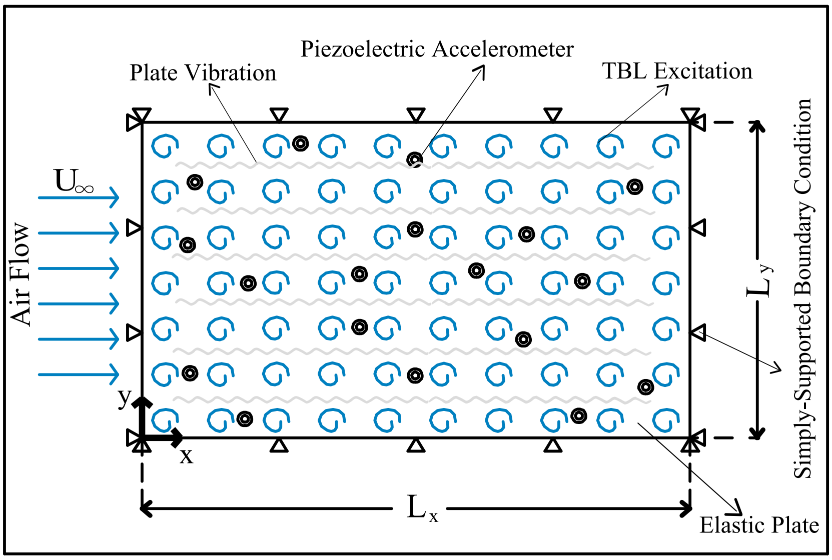

FIGURE 5.1: A Schematic diagram depicting the random array of accelerometers mounted on an elastic plate to record the plate's acceleration response to TBL-induced wall pressure fluctuations.

5.1.1 Frequency Band Analysis

In this section, we have detailed the process of estimating the WPF in the low-wavenumber domain through the utilization of the frequency band approach. The space-frequency spectrum of the plate acceleration, $S_{\gamma\gamma}(\mathbf{x}, \mathbf{x}', \omega)$, excited by the WPF can be expressed by Eq. (4.5). Using a rectangular rule to approximate the integration of Eq. (4.5) by truncating and sampling the wavenumber space, one can compute the CSD of plate acceleration between two points $\mathbf{x}_i$ and $\mathbf{x}_j$ using Eq. (4.12).

Moreover, the CSD of the WPF as indicated in Eq. (4.5) can be calculated according to Graham's method [70, 71] expressed in Eq. (2.1) by employing various models for the ASD of the pressure field, $\Psi_{pp}(\omega)$, and the normalized CSD of the pressure field, $\bar{\phi}_{pp}(\mathbf{k}, \omega)$, separately. Normalizing the wavenumber values in the CSD of the WPF with respect to $k_c = \frac{\omega}{U_c}$, the Graham's formulation can be expressed to the following equation

$$\phi_{pp}(\bar{\mathbf{k}}, \omega) = \Psi_{pp}(\omega)\bar{\phi}_{pp}(\bar{\mathbf{k}}), \tag{5.1}$$

where $\bar{\mathbf{k}}$ is the normalized wavenumber (i.e. $\bar{\mathbf{k}} = \frac{\mathbf{k}}{k_c}$). Introducing Eq. (5.1) in Eq. (4.12) leads to the following equation for the CSD of the plate acceleration

$$S_{\gamma\gamma}(\mathbf{x}_i, \mathbf{x}_j, \omega) = \frac{1}{4\pi^2} \sum_{l=1}^{N_{\bar{\mathbf{k}}_l}} H_\gamma(\mathbf{x}_i, \frac{\omega \bar{\mathbf{k}}_l}{U_c}, \omega) \Psi_{pp}(\omega) \bar{\phi}_{pp}(\bar{\mathbf{k}}_l) H^*_\gamma(\mathbf{x}_j, \frac{\omega \bar{\mathbf{k}}_l}{U_c}, \omega)\, \delta\bar{k}_x \delta\bar{k}_y. \tag{5.2}$$

We define the CSD for the plate acceleration between every combination of sensors in an array of N_s sensors as $S_{\gamma\gamma}(\mathbf{x}_i, \mathbf{x}_j, \omega)$, where $i, j \in \{1, N_s\}$. These computed CSDs are then stored in a vector denoted as $\bar{\mathbf{S}}_\gamma$, known as the acceleration CSD vector. The elements of $\bar{\mathbf{S}}_\gamma$ are arranged such that the first N_s components correspond to $S_{\gamma\gamma}(\mathbf{x}_1, \mathbf{x}_j, \omega)$ with $j \in \{1, N_s\}$, the subsequent N_s components correspond to $S_{\gamma\gamma}(\mathbf{x}_2, \mathbf{x}_j, \omega)$ with $j \in \{1, N_s\}$, and so on:

$$\bar{\mathbf{S}}_\gamma(\omega) = \begin{bmatrix} S_{\gamma\gamma}(\mathbf{x}_1, \mathbf{x}_1, \omega) \\ S_{\gamma\gamma}(\mathbf{x}_1, \mathbf{x}_2, \omega) \\ \vdots \\ S_{\gamma\gamma}(\mathbf{x}_i, \mathbf{x}_j, \omega) \\ \vdots \\ S_{\gamma\gamma}(\mathbf{x}_{N_s}, \mathbf{x}_{N_s-1}, \omega) \\ S_{\gamma\gamma}(\mathbf{x}_{N_s}, \mathbf{x}_{N_s}, \omega) \end{bmatrix}_{N_s^2 \times 1}. \tag{5.3}$$

Given that the CSD of the plate acceleration between various sensors can be approximated using Eq. (5.2), we can express it in a more concise form as follows

$$\bar{\mathbf{S}}_\gamma(\omega) = \bar{\mathbf{Q}}(\omega) \bar{\Phi}_{pp}(\omega), \tag{5.4}$$

where $\bar{\Phi}_{pp}$ is a vector consisting of the unknown components of the normalized CSD of the WPF, presented as a function of the normalized wavenumbers as follows

$$\bar{\mathbf{\Phi}}_{\mathbf{pp}}(\omega) = \begin{bmatrix} \bar{\phi}_{pp}(\bar{k}_{x,1}, \bar{k}_{y,1}, \omega) \\ \bar{\phi}_{pp}(\bar{k}_{x,1}, \bar{k}_{y,2}, \omega) \\ \vdots \\ \bar{\phi}_{pp}(\bar{k}_{x,l}, \bar{k}_{y,l}, \omega) \\ \vdots \\ \bar{\phi}_{pp}(\bar{k}_{x,N_{k_x}}, \bar{k}_{y,N_{k_y}-1}, \omega) \\ \bar{\phi}_{pp}(\bar{k}_{x,N_{k_x}}, \bar{k}_{y,N_{k_y}}, \omega) \end{bmatrix}_{N_k \times 1}. \tag{5.5}$$

The elements of $\bar{\mathbf{\Phi}}_{\mathbf{pp}}$ are arranged in such a way that the initial N_{k_y} components correspond to $\bar{\phi}_{pp}(\bar{k}_{x,1}, \bar{k}_{y,l}, \omega)$ with $l \in \{1, N_{k_y}\}$, the subsequent N_{k_y} components correspond to $\bar{\phi}_{pp}(\bar{k}_{x,2}, \bar{k}_{y,l}, \omega)$ with $l \in \{1, N_{k_y}\}$, and so forth. Additionally, $\bar{\mathbf{Q}}$ represents an excitation-response matrix with the following elements

$$\bar{\mathbf{Q}} = \frac{\Psi_{pp}(\omega)\delta\bar{k}_x\delta\bar{k}_y}{4\pi^2} \begin{bmatrix} H_\gamma(\mathbf{x}_1, \frac{\omega\bar{\mathbf{k}}_1}{U_c}, \omega)H_\gamma^*(\mathbf{x}_1, \frac{\omega\bar{\mathbf{k}}_1}{U_c}, \omega) & \cdots & H_\gamma(\mathbf{x}_1, \frac{\omega\bar{\mathbf{k}}_{N_{\bar{\mathbf{k}}}}}{U_c}, \omega)H_\gamma^*(\mathbf{x}_1, \frac{\omega\bar{\mathbf{k}}_{N_{\bar{\mathbf{k}}}}}{U_c}, \omega) \\ H_\gamma(\mathbf{x}_1, \frac{\omega\bar{\mathbf{k}}_1}{U_c}, \omega)H_\gamma^*(\mathbf{x}_2, \frac{\omega\bar{\mathbf{k}}_1}{U_c}, \omega) & & \vdots \\ \vdots & H_\gamma(\mathbf{x}_i, \frac{\omega\bar{\mathbf{k}}_l}{U_c}, \omega)H_\gamma^*(\mathbf{x}_j, \frac{\omega\bar{\mathbf{k}}_l}{U_c}, \omega) & \vdots \\ \vdots & & H_\gamma(\mathbf{x}_{N_s}, \frac{\omega\bar{\mathbf{k}}_{N_{\bar{\mathbf{k}}}}}{U_c}, \omega)H_\gamma^*(\mathbf{x}_{N_s-1}, \frac{\omega\bar{\mathbf{k}}_{N_{\bar{\mathbf{k}}}}}{U_c}, \omega) \\ H_\gamma(\mathbf{x}_{N_s}, \frac{\omega\bar{\mathbf{k}}_1}{U_c}, \omega)H_\gamma^*(\mathbf{x}_{N_s}, \frac{\omega\bar{\mathbf{k}}_1}{U_c}, \omega) & \cdots & H_\gamma(\mathbf{x}_{N_s}, \frac{\omega\bar{\mathbf{k}}_{N_{\bar{\mathbf{k}}}}}{U_c}, \omega)H_\gamma^*(\mathbf{x}_{N_s}, \frac{\omega\bar{\mathbf{k}}_{N_{\bar{\mathbf{k}}}}}{U_c}, \omega) \end{bmatrix}_{N_s^2 \times N_{\bar{\mathbf{k}}}} . \tag{5.6}$$

For a particular excitation frequency, the calculation of the vector $\bar{\mathbf{S}}_\gamma$ relies on the plate's vibrational response to the TBL forcing function. According to the this procedure, we end up with N_s^2 equations for the $N_{k_x} \times N_{k_y}$ unknown coefficients outlined in Eq. (5.4). Typically, the number of unknowns $N_{k_x} \times N_{k_y}$ surpasses the number of equations N_s^2. Consequently, Eq. (5.4) represents an under-determined system and the system of equations has no unique solution. Also, matrix $\bar{\mathbf{Q}}$ in Eq. (5.6) is not a square matrix, and therefore, standard matrix inversion methods cannot be directly applied to it for computing the $\bar{\mathbf{\Phi}}_{\mathbf{pp}}$.

The normalized domain corresponds to low-wavenumber domain is $\bar{k}_{x,LW}, \bar{k}_{y,LW} \in [\frac{-U_c k_f}{\omega}, \frac{U_c k_f}{\omega}]$. Since $k_f \propto \sqrt{\omega}$, normalized low-wavenumber domain is proportional to $\bar{k}_{x,LW}, \bar{k}_{y,LW} \propto \frac{1}{\sqrt{\omega}}$. This signifies that as the excitation frequency increases, the extent of the low-wavenumber domain diminishes. Therefore, to define a fixed low-wavenumber domain using this method, the low-wavenumber domain corresponding to $\omega_{\min}$ within the frequency band is chosen as the target domain for estimation. This selection encompasses the low-wavenumber domain linked to the higher frequency in the given frequency band.

The vector $\bar{\mathbf{S}}_\gamma$ and matrix $\bar{\mathbf{Q}}$ in Eq. (5.4) are frequency-dependent. Given the assumption made by Martin and Leehey [126] and Bonness et al. [17] in their studies, one could posit that the frequency-independent nature of $\bar{\Phi}_{pp}$ holds true within the low-wavenumber domain across a small frequency band (i.e. $[\omega_{\min} - \omega_{\max}]$). Therefore, by taking into account N_f discrete frequencies within the frequency band, $\bar{\Phi}(\omega_i) \approx \bar{\Phi}_{pp}^{[\omega_{\min}, \omega_{\max}]}$, where $i \in \{1, N_f\}$. Utilizing the results of $\bar{\mathbf{S}}_\gamma(\omega_i)$ and $\bar{\mathbf{Q}}(\omega_i)$ at different frequencies, we can derive the following set of equations

$$\begin{bmatrix} \bar{\mathbf{S}}_\gamma(\omega_1) \\ \bar{\mathbf{S}}_\gamma(\omega_2) \\ \vdots \\ \bar{\mathbf{S}}_\gamma(\omega_{N_f}) \end{bmatrix} = \bar{\Phi}_{pp}^{[\omega_{\min},\omega_{\max}]} \begin{bmatrix} \bar{\mathbf{Q}}(\omega_1) \\ \bar{\mathbf{Q}}(\omega_2) \\ \vdots \\ \bar{\mathbf{Q}}(\omega_{N_f}) \end{bmatrix}. \tag{5.7}$$

If the number of frequencies is such that $N_s^2 \times N_f$ is larger than the size of $N_{k_x} \times N_{k_y}$, then the system will be overdetermined, and the matrix $\bar{\mathbf{Q}}$ that needs to be inverted will be better conditioned. The objective is to seek an approximate solution for $\bar{\phi}_{pp}^{[\omega_{\min},\omega_{\max}]}$ within the low-wavenumber domain, aiming to minimize the residuals of the Eq. (5.4). To achieve this, a regularization technique can be employed to estimate the WPF in the low-wavenumber domain, as suggested in [76].

5.1.2 Virtual Vibration Experiments

The performance of the proposed approach can be assessed numerically by comparing the estimated WPF with a known reference input WPF. This evaluation involves exciting the plate with a predetermined forcing function and applying Eq. (5.7) to the resulting vibration response. In this study, a virtual model is utilized to simulate the TBL excitation. To achieve this, the TBL excitation force is simulated through deterministic loading, employing the UWPW technique as described in [129]. This technique aims to replicate experimental scenarios by synthesizing TBL wall pressure. Subsequently, the deterministic forcing function is utilized to compute the plate's acceleration response, utilizing the ensemble average of various realizations of wall pressure. The pressure beneath the TBL for the rth realization is characterized by a series of UWPWs at a specific point (x_M, y_M) on the plate, as detailed in [100, 101, 129].

$$p^r(x_M, y_M, \omega) = \sum_{l=1}^{N_k} \sqrt{\frac{\bar{\phi}_{pp}(\bar{k}_{x,l}, \bar{k}_{y,l}, \omega)\delta\bar{k}_x\delta\bar{k}_y}{4\pi^2}} e^{\mathrm{j}(\bar{k}_{x,l}x_M + \bar{k}_{y,l}y_M + \theta_l^r)}, \tag{5.8}$$

Then, utilizing the modal expansion technique, the acceleration response of a plate at the specified point (x_M, y_M) for a given frequency ω, caused by the wall pressure (Eq. (5.8)), corresponding to the rth realization at each sensor location, can be computed using Eq. (4.18). The modal forces in Eq. (4.18) can be obtained by [129]

$$F^r_{mn} = \sum_{l=1}^{N_{\mathbf{k}}} \sqrt{\frac{\bar{\phi}_{pp}(\bar{k}_{x,l}, \bar{k}_{y,l}, \omega)\delta\bar{k}_x\delta\bar{k}_y}{4\pi^2}} e^{\mathrm{j}\theta^r_l} \psi_{mn}(\bar{k}_{x,l}, \bar{k}_{y,l}). \tag{5.9}$$

Using Eq. (4.18), the CSD of acceleration between two points of $\mathbf{x}_i$ and $\mathbf{x}_j$ using the UWPW technique can be computed as follows

$$S_{\gamma\gamma}(\mathbf{x}_i, \mathbf{x}_j, \omega) = \frac{1}{N_r} \sum_{r=1}^{N_r} \gamma^r(x_i, y_i, \omega)\gamma^{*r}(x_j, y_j, \omega), \tag{5.10}$$

where N_r is number of realizations. In the following section, we assess the results obtained from employing the proposed method to estimate the WPF in the low-wavenumber domain.

5.2 Results and Discussion

This section utilizes the analytical formulations described in Section 5.1 to assess the WPF within the low-wavenumber range. To demonstrate the effectiveness of the suggested approach, we analyze the performance using the identical plate characteristics and TBL properties as studied in Chapter 4.

This study employs the Goody model to evaluate the ASD function of the WPF, and the Mellen model for the normalized CSD function. Eq. (5.8) serves for simulating the input TBL forcing function. To simulate the TBL, Eq. (4.12) needs a truncated number of wavenumbers in both the x and y directions. For this study, a cut-off wavenumber of $1.2k_c$ was chosen in both directions to accommodate the convective contributions of the TBL's WPF. Additionally, the wavenumber resolutions used for the WPF calculations should strike a balance: not too small to avoid increasing computational costs, yet not too large to skip the main WPF values. In this study, the wavenumber resolution is fixed at $\delta k_x = \delta k_y = 5.6$ m^{-1} for all examined frequencies.

In order to guarantee that the calculated CSD of the plate acceleration, measured by the virtual accelerometers, encompasses all significant modes, we opted to use $M = N = 50$ when computing $\bar{\mathbf{S}}_\gamma(\omega)$ in Eq. (4.12) through Eq. (5.10). However, when calculating the $\bar{\mathbf{Q}}$ matrix as expressed in Eq. (5.6), we limit our consideration to the modes M

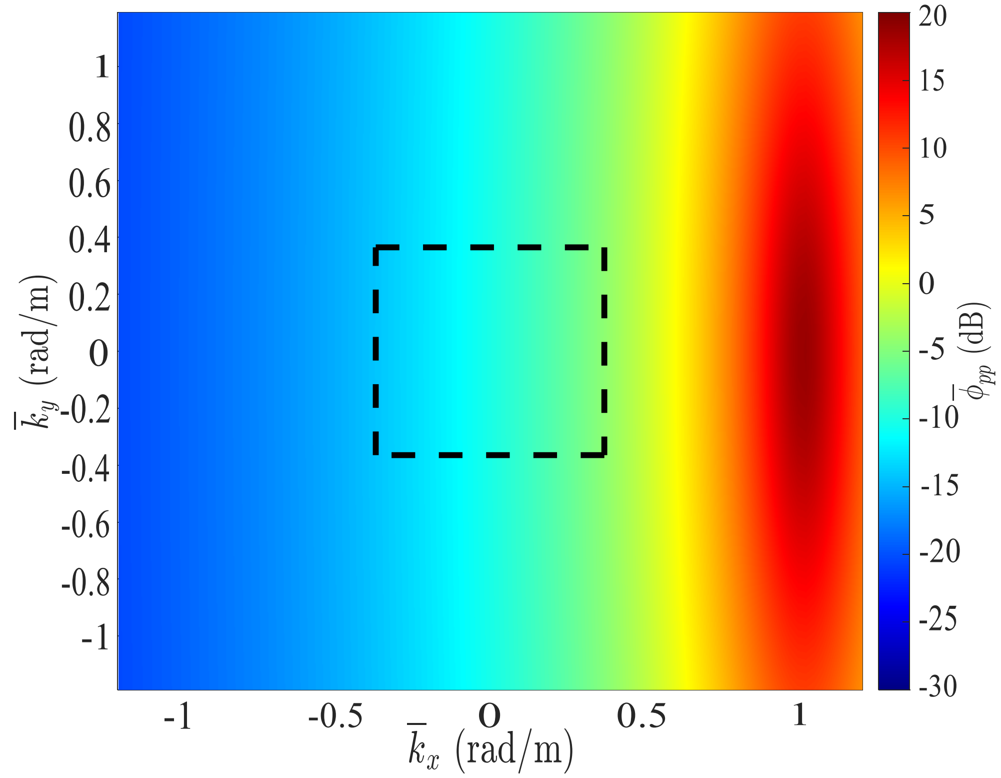

FIGURE 5.2: Contour plots of the Mellen wavenumber-frequency model $\bar{\phi}_{pp}(\bar{\mathbf{k}}, f)$ (dB, ref. 1 $\mathrm{Pa}^2.\mathrm{Hz}^{-1}$) for a flow speed of 50 m/s at 1400 Hz.

and N within the frequency range $[0, 1.3\omega_{\max}]$. This choice is made as in practice, only resonant modes within a given frequency band can be reasonably estimated.

Figure 5.2 depicts the normalized CSD of a TBL WPF based on the Mellen model in the normalized wavenumber domain for the reference TBL at $f = 1400$ Hz. It's crucial to emphasize that the rectangular area shown in this figure indicates the low-wavenumber domain under investigation in this study.

To compute the TBL WPF, Eq. (5.7) must be resolved. However, this equation falls under the category of ill-posed problems, meaning that even small perturbations in the input data can greatly impact the solution. Same as Chapter 4, the TGSVD technique is employed here to estimate the WPF within the low-wavenumber domain. This is achieved by minimizing the 2-norm of the first derivative of the solution, as described in [76]. The regularization parameter, crucial for truncating the generalized singular value problem, is determined using the corner method. This technique utilizes an adaptive pruning algorithm to pinpoint the corner of a discrete L-curve produced by the TGSVD method [77].

This study assumes an irregular array of accelerometer to estimate the low-wavenumber WPF. The sensors arrangement remains consistent with that outlined in Chapter 4.

In this study, we consider the frequency band of $f = [1400 - 1475]$ Hz to estimate the WPF in the low-wavenumber domain, and subsequently compare the findings with those obtained using a single frequency of $f = 1400$ Hz in Chapter 4. This method involves leveraging the CSM computed for various frequencies and employing these data to estimate the WPF. To transform the underdetermined system of equations in Eq. (5.7) into an overdetermined system, a minimum of $N_f = 76$ frequency steps is required. Consequently, a frequency step of $df = 1$ Hz is adopted in this example to over-determine the system of equations.

To evaluate the effectiveness of the proposed method in estimating the TBL WPF, we calculate the MAE of the estimated WPF in the low-wavenumber domain relative to the reference input TBL model, which is based on the Mellen model (Figure 5.2). The MAE of the estimated WPF in the low-wavenumber domain is computed using the following formula

$$\mathrm{MAE} = \frac{1}{N_{k_{LW}}} \sum_{l=1}^{N_{k_{LW}}} \left[10\mathbf{log}_{10} \left(\bar{\phi}_{pp}^{[\omega_{\min},\omega_{\max}]}(\bar{\mathbf{k}}_l) \right)_e - 10\mathbf{log}_{10} \left(\bar{\phi}_{pp}^{[\omega_{\min},\omega_{\max}]}(\bar{\mathbf{k}}_l) \right)_r \right], \quad \text{(dB)} \tag{5.11}$$

where $\left(\bar{\phi}_{pp}^{[\omega_{\min},\omega_{\max}]}(\bar{\mathbf{k}}_l) \right)_e$ and $\left(\bar{\phi}_{pp}^{[\omega_{\min},\omega_{\max}]}(\bar{\mathbf{k}}_l) \right)_r$ are the estimated and reference wavenumber-frequency spectrum of the WPF in the frequency band, respectively, and $N_{k_{LW}}$ corresponds to the total number of grid points in the low-wavenumber domain. Figures 5.3 (a), (c), and (e) illustrate the color maps of the estimated normalized WPF using Eq. (5.7) across the frequency range of $[1400 - 1475]$ Hz for varying numbers of realizations. Figure 5.3 (b), (d), and (f) illustrate the cross-sectional views of both the reference and estimated WPF at $\bar{k}_y = 0$. Two red-dashed lines in the figure represent the boundaries of the low-wavenumber domain. Moreover, the MAE values in decibels (dB) are presented for each case. The results shown in Figure 5.3 reveals that utilizing a group of closely spaced frequencies instead of a single frequency [3] reduces the required number of realizations to obtain a certain level of accuracy of the estimated WPF. For instance, when using the frequency band method, the MAE for $N_r = 5$ decreases from almost 5 dB (obtained for the single frequency method in Chapter 4) to 1.66 dB, indicating a good improvement. Moreover, doubling the number of realizations to $N_r = 10$ further reduces the MAE to 1.12 dB, indicating a reasonable level of accuracy in estimating the WPF.

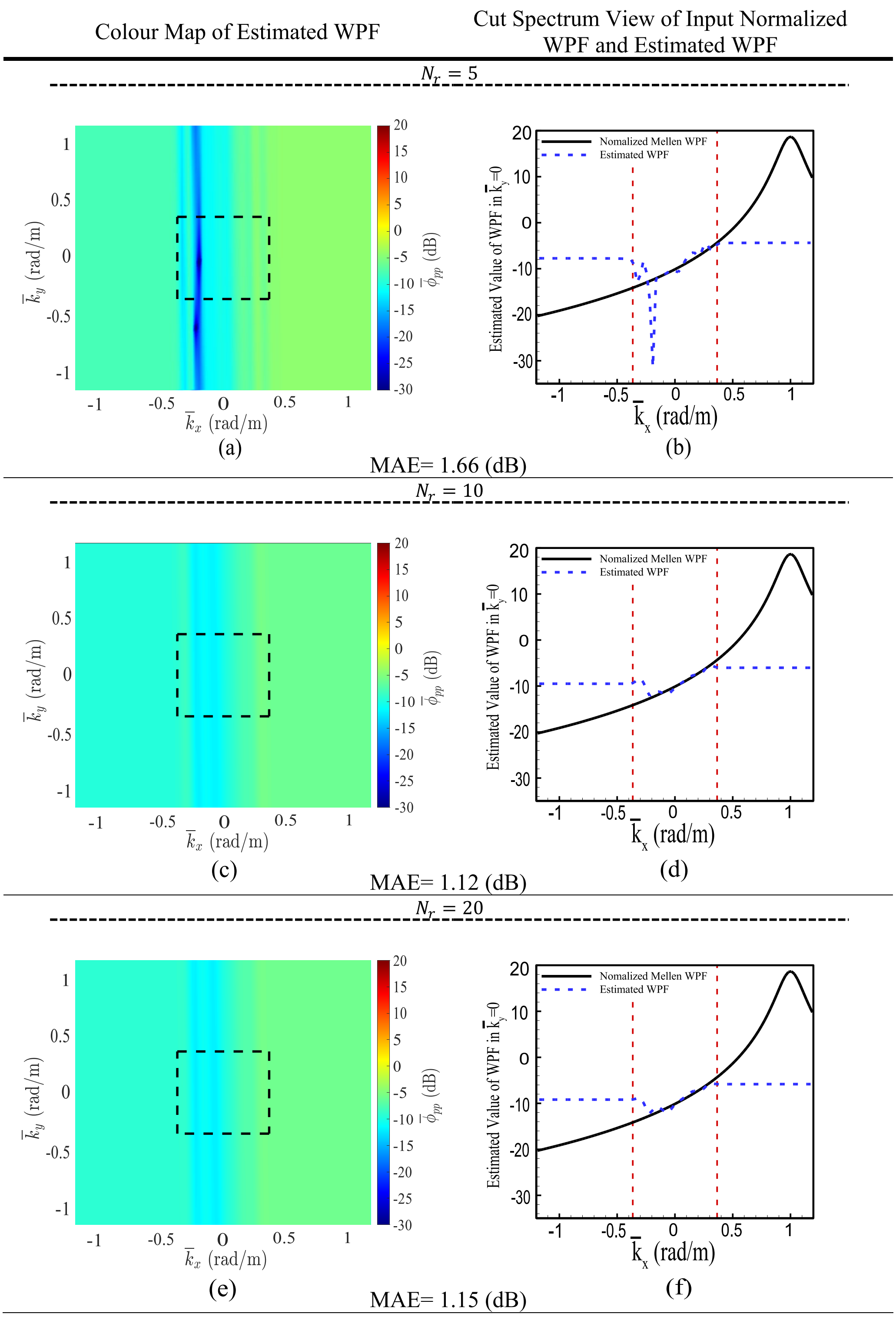

FIGURE 5.3: The estimated normalized WPF $\bar{\phi}_{pp}(\bar{\mathbf{k}}, f)$ (dB, ref. 1 Pa^2.Hz^{-1}) in frequency band of $[1400 - 1475]$ Hz for an irregular array pattern with 10 sensors, shown for different numbers of realizations. The left-hand plots depict the color maps, while the right-hand plots display the 2D wavenumber-frequency spectra for $\bar{k}_y = 0$. The MAE for each case is displayed in decibels (dB).

Figure 5.4 compares the MAE as a function of the number of sensors for different number of realizations, depicted separately for (a) a single frequency of $f = 1400$ Hz (Chapter 4) and (b) a frequency band of $f = [1400 - 1475]$ HZ. These MAE values are compared with those obtained using the reference input TBL excitation (Ref. TBL). The findings demonstrate that for accurate estimation of the low-wavenumber WPF at a single frequency of $f = 1400$ Hz with an MAE below 2 dB, over 300 realizations are necessary. In contrast, employing the frequency band method requires only 20 realizations to effectively estimate the WPF in the low-wavenumber domain. Moreover, it is evident that increasing the number of sensors does not yield substantial enhancements in the estimated WPF when a sufficient number of realizations are utilized in both scenarios. However, it is worth mentioning that in employing frequency band method, we have made two assumptions: (1) the ASD of the WPF is available beforehand through experimental measurements or computational fluid dynamics simulation, and (2) the WPF in the low-wavenumber domain is frequency independent within the small frequency range under consideration for implementing the proposed methodology.

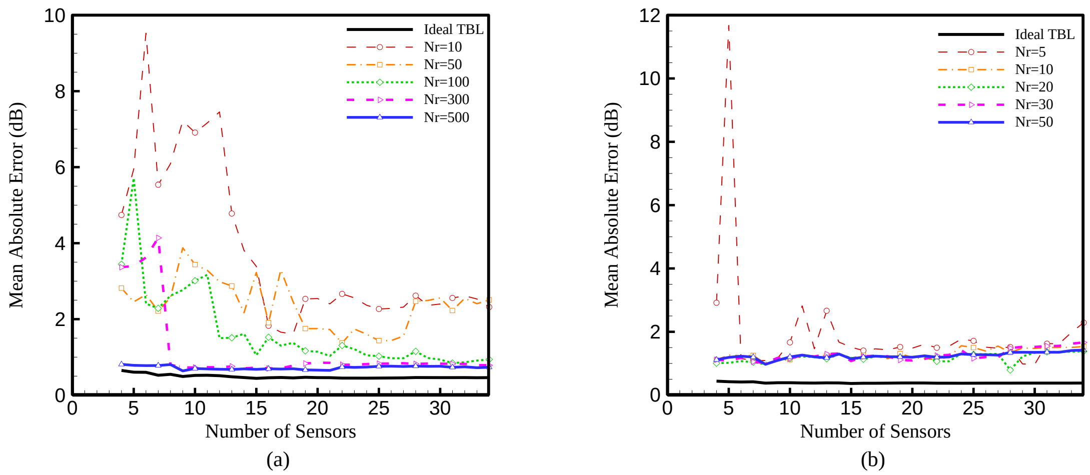

FIGURE 5.4: The comparison of MAE for the estimated WPF in the low-wavenumber domain as a function of number of sensors. The results highlight the impact of the number realization on accuracy of the estimated WPF for (a) single frequency of $f = 1400$ Hz [3] and (b) frequency band of $f = [1400 - 1475]$ Hz.

5.3 Summary

This chapter investigated the effectiveness of using a vibration-based method at multiple discrete frequencies for estimating the WPF in the low-wavenumber domain. The frequency band formulation with the assumption that the low-wavenumber WPF does not vary within the frequency band of interest was applied to identify the low-wavenumber levels of the WPF. It was found that few number of realizations is enough to accurately estimate the WPF in the low-wavenumber region using the frequency band method. This is advantageous in practice as only a few data samples need to be recorded at each frequency. Furthermore, it was observed that due to the filtering properties of the plate, the proposed method is limited to estimating the WPF within the low-wavenumber domain, and the WPF outside of this domain cannot be estimated accurately.

Chapter 6

Experimental Identification of Plate's Sensitivity Functions

As discussed in Chapters 4 and 5, identifying the WPF using the VBA requires the calculation of the $\mathbf{Q}$ and $\bar{\mathbf{Q}}$ matrices via Eqs. (4.16) and (5.6), respectively. To compute these matrices, we must determine the sensitivity functions of the plate under study.

As described in Chapter 4, the sensitivity function $H_\gamma(\mathbf{x}, \mathbf{k}, \omega)$ for a panel corresponds to the acceleration at point $\mathbf{x}$ when the panel is excited by a unit wall plane wave with the wavenumber $\mathbf{k}$. In Chapter 4, it was shown that Eq. (4.7) can be used to evaluate the sensitivity function in the wavenumber domain. To obtain the sensitivity function using this equation, the modal properties of the structure under study, such as modal shapes, natural frequencies, and structural loss factors, are required. A simply-supported plate was used in Chapters 4 and 5 to evaluate the sensitivity functions because analytical formulations for the modal frequencies and mode shapes of a simply-supported plate are available.

While sensitivity functions can be computed analytically or numerically for a given structure, it is challenging to experimentally obtain them in practice, which is required for estimating the low-wavenumber WPF using the VBA. Therefore, this chapter is dedicated to experimental evaluation of the sensitivity functions for a steel palte using two methods: modal expansion and the reciprocity principle.

Initially, the modal expansion method, discussed in Section 6.1.1, is employed. This method requires the modal properties of the steel plate to calculate the sensitivity functions. However, accurate measurement of all modal frequencies and mode shapes of the plate is challenging in practice. As an alternative, the reciprocity principle method is explored in Section 6.1.2 for computing the sensitivity functions. The results from these two methods are then compared and verified.

6.1 Experimental Setup

In this section, we evaluate the sensitivity functions of a plate experimentally. The experimental setup used for calculation of the sensitivity functions in this section is shown in Figure 6.1. The experiment considers a steel plate with dimensions of 980.1 mm $\times$ 965.5 mm and a thickness of 2.44 mm, as depicted in Figure 6.1 (a). The testing was conducted using measurement equipment from the UTS Acoustics Lab, as listed in Table 6.1. Excitation was applied using Shaker B&K Type V406 M4-CE (Figure 6.1 (b)), while the response was recorded and analyzed using Polytec Type PSV-500-HV Xtra Laser Doppler Vibrometer (Figure 6.1 (d)).

Table 6.1: The equipment used in the vibration measurements

Equipment Name	**Description**
Laser Doppler Vibrometer	Polytec Type PSV-500-HV Xtra S/N: (1) 299160
Vibration Shaker	Brüel & Kjær Type V406 M4-CE S/N: (1) 472991/21
Vibration Transducer	DJB Type AF/100/10 S/N: (1) 9120002 (2) 9120003
Linear Power Amplifier	Brüel & Kjær Type LDS LPA 100 S/N: (1) B0100E1A17K0033

The rectangular steel plate used in the experiment is shown in Figure 6.2. This plate was drilled at 40 points and bolted to a frame which was attached to a thick concrete wall at 38 points. To prevent obstruction of the laser beam by the shaker and its hanger, the shaker was positioned to excite the plate from one side, while the scanning LDV measured the plate vibrations from the opposite side. A force transducer is placed at the shaker's excitation point to measure the applied forces. Two corner holes were left open (highlighted in grey in Figure 6.2) to allow for the passage of cables connecting the shaker to the LDV. The diameters of the holes are 10 mm (shown in blue) and 12.5 mm

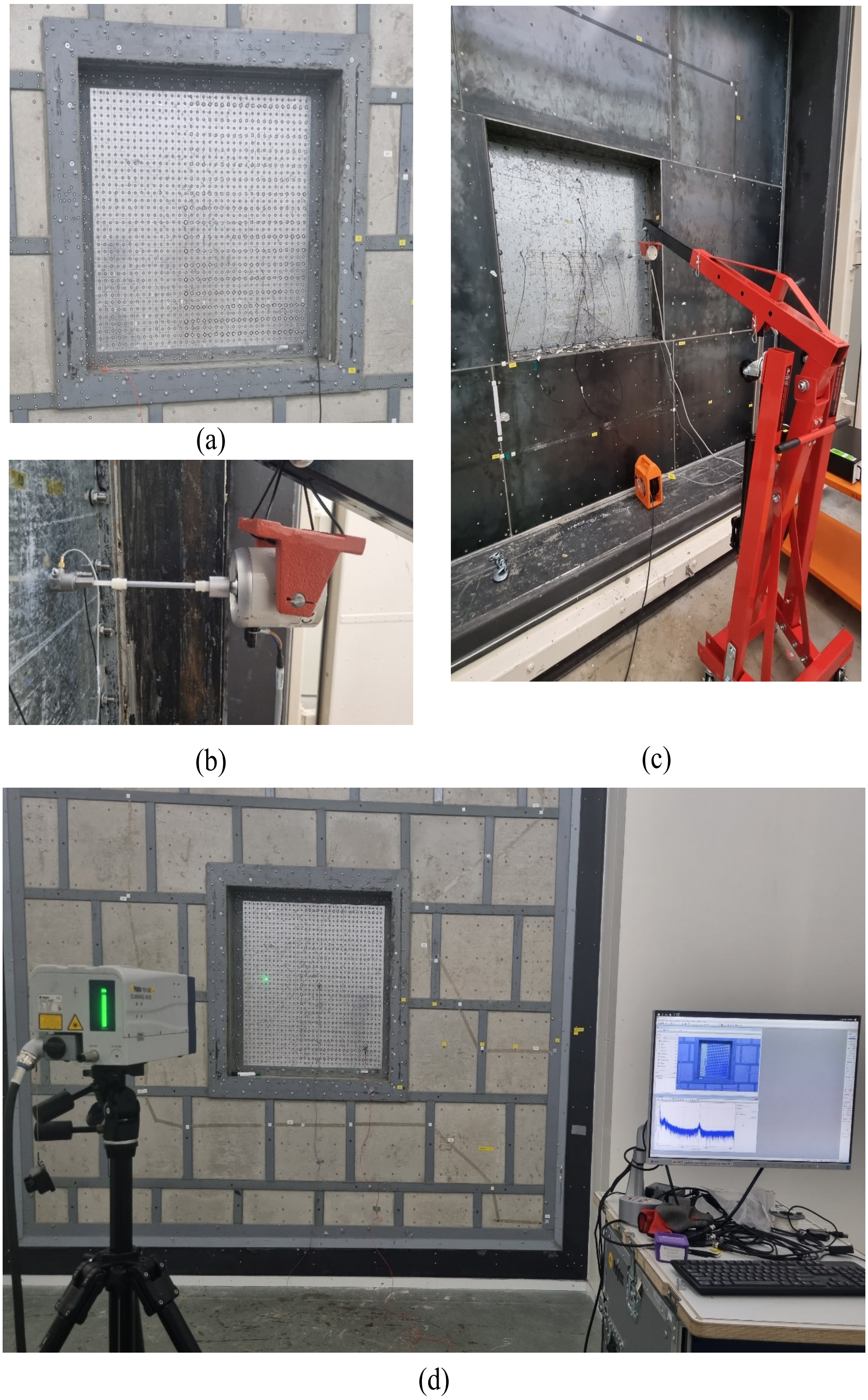

FIGURE 6.1: Experimental setup used for calculation of the sensitivity functions. (a) A rectangular steel plate bolted to a carbon steel frame and attached to a concrete wall, (b) The shaker used for excitation of the plate, (c) The hydraulic folding engine crane used for hanging the shaker, and (d) the scanning laser Doppler vibrometer.

(shown in purple) in the figure. The sensitivity functions have been computed at 15 points. The coordinates of these points are presented in Table 6.2. The location and order of these points are also indicated by red circles and numbers, respectively, in the Figure 6.2. Table 6.3 presents the panel's geometrical and mechanical properties.

TABLE 6.2: Coordinates of 15 points on the plate used for calculation of the sensitivity functions

Point Number	1	2	3	4	5	6	7	8	9	10	11	12	13	14	15
x (mm)	856.4	732.7	609.2	492.2	372.7	250.5	140	489	488	487	486	486	486	485	484
y (mm)	485	485	485	486	484	482	484	869.5	769.5	669.5	569.5	391.5	293	193	94.5

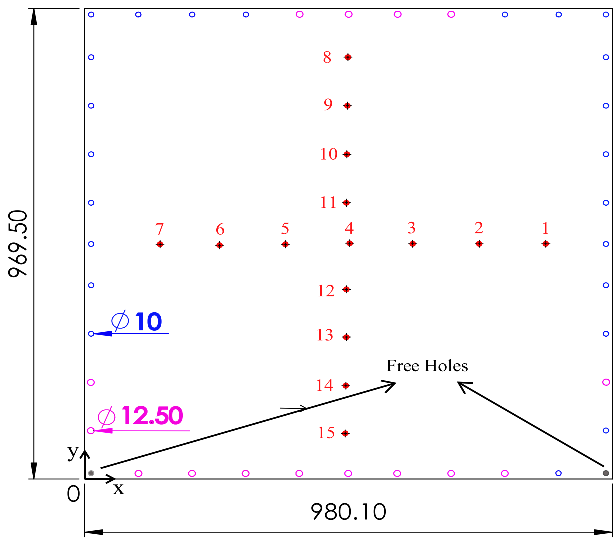

FIGURE 6.2: Schematic of the rectangular plate used in the experiment, showing 15 measurement points, whose locations and order are indicated by red circles and numbers. The plate was bolted to a frame attached to a thick concrete wall at the blue holes (10 mm diameter) and purple holes (12.5 mm diameter). The two grey holes were left open.

TABLE 6.3: Dimensions and material properties of the panel

Parameter	Value
Young's modulus E (Gpa)	210
Density ρ_s (kg/m^3)	7721
Length L_x (mm)	980.1
Width L_y (mm)	969.5
Thickness h (mm)	2.44

In this chapter, two methods for acquiring the sensitivity functions have been evaluated. The first method involves obtaining the damped natural frequencies and mode shapes of the plate, followed by using Eq. (4.7) to calculate the sensitivity functions. The alternative method, based on the reciprocity principle, involves exciting the plate at specific points and using the plate's response to compute the sensitivity functions at those points. In the subsequent sections, both methods, modal expansion and the reciprocity principle, are employed to compute the sensitivity functions of the plate experimentally, and the results are compared.

6.1.1 Modal Expansion Method

In this section, our aim is to compute the sensitivity functions of the plate using the procedure explained in Chapter 4. The relationship for calculating the sensitivity function is derived from Eq. (4.7), which expresses the sensitivity function as a function of the plate's modal properties. To obtain the sensitivity functions using Eq. (4.7), it is necessary to determine the modal mass (Ω_{mn}), structural loss factor (η_s), modal frequencies (ω_{mn}), modal shapes (φ_{mn}), and modal forces (ψ_{mn}). The accurate determination of these parameters is critical for ensuring the reliability of the sensitivity function calculations. The modal mass, Ω_{mn}, in Eq. (4.7) can be calculated as:

$$\Omega_{mn} = \rho_s h \int_A \varphi_{mn}^2(x, y)\, \mathrm{d}A. \tag{6.1}$$

Additionally, the modal forces ψ_{mn} are calculated using the Fourier transform via Eq. (4.10) as follows:

$$\psi_{mn}(k_x, k_y) = \int_A \varphi_{mn}(x, y) e^{\mathrm{j}(k_x x + k_y y)}\, \mathrm{d}A. \tag{6.2}$$

Here, we will determine the modal parameters of the plate using enhanced Frequency Response Function (eFRF) which is obtained from Complex Mode Indicator Function (CMIF) [5, 83, 141, 143, 159]. In summary, the modal parameters can be identified through the following five steps. For more details, please refer to Appendix D.

1. **CMIF Curves**: In the first step, the eigenvalues of the normal matrix are plotted as CMIF curves on a logarithmic magnitude scale as a function of frequency. The number of curves corresponds to the number of reference points, which represent either excitation or measurement locations in the modal test. For example, in a Single Input Multiple Output (SIMO) configuration, where there is only one

excitation point (reference), one CMIF curve is generated. If two references are used, such as in a Multiple Input Multiple Output (MIMO) configuration, two CMIF curves will be produced. The value of each peak's eigenvector, equivalent to the modal participation factor, is obtained in this step. Peaks in the CMIF plot indicate the presence of vibration modes and their approximate frequencies. However, not all peaks represent modes; errors such as noise, leakage, nonlinearity, and cross eigenvalue effects can create false peaks. For example, leakage errors can be minimized by including several spectral lines of data in the singular value decomposition calculation. Cross eigenvalue effects occur when two modes contribute equally at a specific frequency, causing their eigenvalue curves to cross [159].

2. **eFRF**: The CMIF method is able to distinguish closed and also coupled modes. Then, these identified peaks are used as initial estimate of natural frequencies to create eFRF for each mode. The eFRF method is employed as second step to identify natural frequencies and scale an equivalent single Degree of Freedom (DOF) characteristic linked to each peak observed in the CMIF [5, 143].

3. **RFP Method**: In the third step, the rational fraction polynomial (RFP) method performs multiple reference curve fitting using the modal participation factors to estimate modal frequencies and damping for the previously detected peaks. The estimated frequency is the damped natural frequency, where the maximum magnitude of the singular value occurs. The frequencies and damping of all modes are then listed in a spreadsheet [159].

4. **Modal Residues**: Once the modal frequencies and damping are estimated, modal residues (magnitudes and phases) can be determined in the fourth step, using the modal participation factors [159].

5. **Mode Shapes**: In the fifth step, after curve fitting is completed, mode shapes are computed based on the relative strengths of the modal participation factors for each reference and the largest participation factor for each mode [159].

Due to the close resemblance of the plate's geometry to that of a symmetrical square plate, it's possible that the plate exhibits repeated roots or closely coupled modes. These nuances cannot be accurately resolved using a single reference curve fitting method. To address this, when two repeated roots are present, it's necessary to utilize at least two references or responses (rows or columns) of the Frequency Response Function (FRF) matrix to identify the modal parameters (refer to Appendix D).

In this experimental setup, the plate was excited at 15 points specified in Table 6.2 using a shaker, while response measurements were taken at 400 points for each excitation. The spatial resolution was set to $\delta x = \delta y \approx 50$ mm for the scanned grid points. Measurements were conducted over a frequency range from 0 to 1600 Hz with a resolution of 0.5 Hz. Each signal was recorded for a duration of four seconds, resulting in a total of 3200 FFT lines. The Burst Chirp waveform type was used for the shaker excitation, with the amplitude set to 0.1 and the burst length to 50%.

Figure 6.3 shows the coherence between each excitation and corresponding vibration for the frequency range of 0 to 1000 Hz. The coherence between force and vibration measures the correlation or degree of linear relationship between the force applied to a plate (excitation) and the resulting vibration response of the plate at excitation points. This high coherence indicates that the force is effectively transmitting energy to the structure, and the structure is responding to the force input in a predictable and consistent manner. It is often desirable to have high coherence between force and vibration signals, especially in structural testing and modal analysis, as it ensures that the measured responses accurately reflect the applied excitation and can provide reliable insights into the dynamic behavior of the structure. As it can be seen for wide range of frequencies the coherence is close to 1, which means that the vibration response of the structure at those frequencies is directly and strongly influenced by the applied force. In other words, the measured vibrations closely follow the force input, indicating a high level of consistency or synchronization between the two signals.

Figure 6.4 illustrates the average FRF spectrum obtained across all 400 measurement points for each excitation force, spanning frequencies from 0 to 1000 Hz.

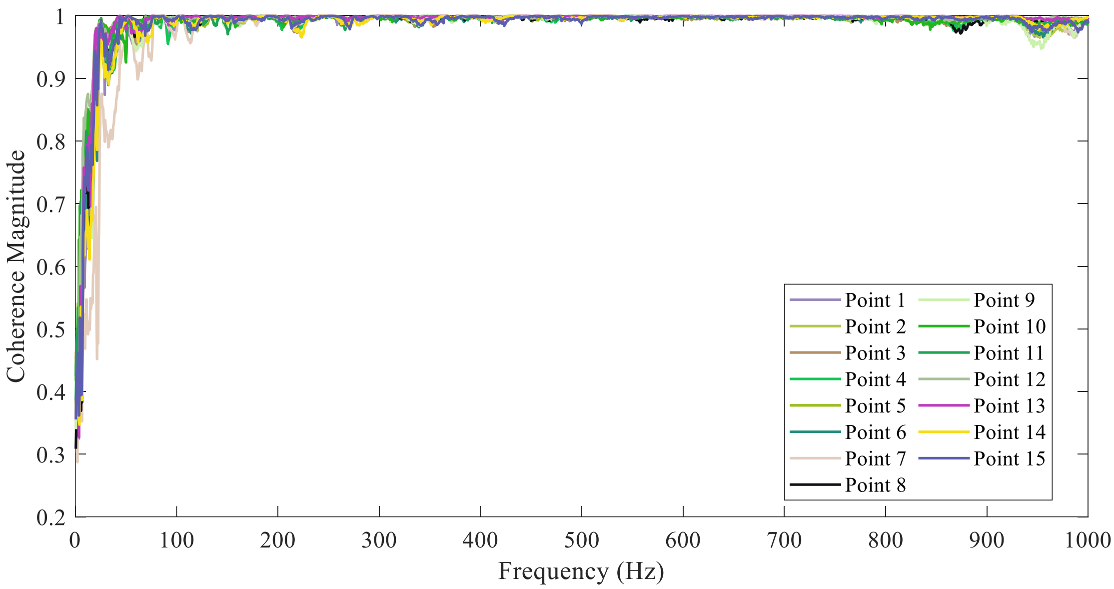

FIGURE 6.3: Coherence between between each excitation force and and corresponding vibration

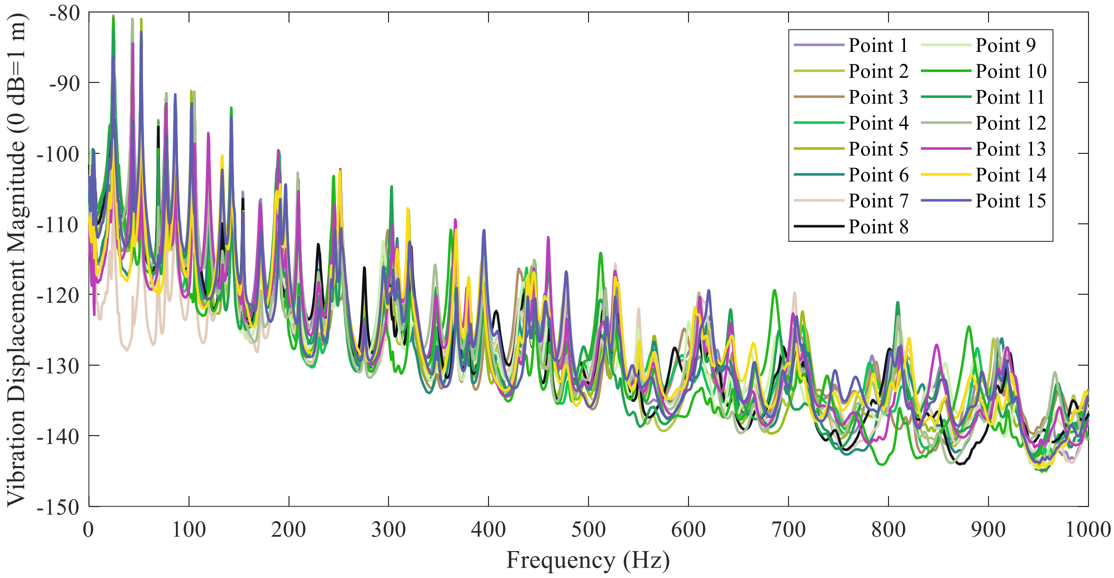

FIGURE 6.4: Average spectrum of vibration displacement for each excitation.

With the FRF matrix available, we can now move on to estimating the modal parameters. Due to the 15 points of excitation and 400 measurement points for each excitation, the size of the FRF matrix at each frequency is 400×15. Figure 6.5 illustrates the CMIF derived from the SVD of the FRF matrix. The peaks identified from the CMIF are utilized for the initial estimation of natural frequencies. This initial estimation is crucial for generating the eFRF for each mode according to Eq. (D.8). The eFRF is a weighted average of all measured FRFs, where the left and right singular vectors used as discrete modal filters. Following the determination of eFRF, the RFP method is applied to the eFRF functions to estimate modal parameters. This is done by curve fitting the FRF. The FRF can be expressed in either rational (polynomial) fraction or partial fraction form. In both approaches, all modal parameters (frequency, damping, and modal coefficient) for all modes are estimated simultaneously (for more detail refer to Appendix D).

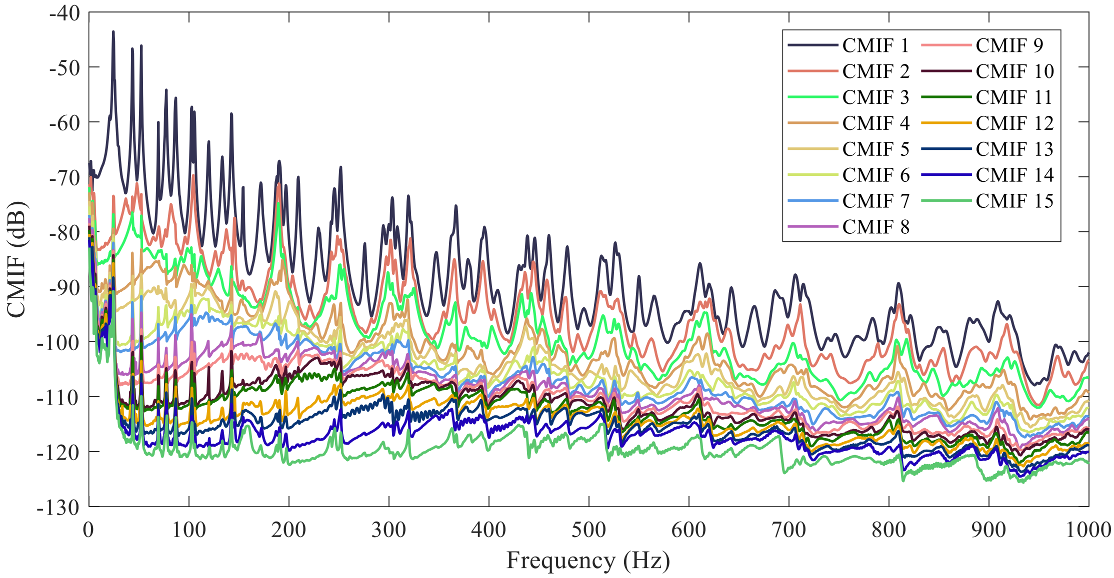

FIGURE 6.5: CMIF function (dB, ref. 1 Hz^2) from multiple-input multiple-output measurements.

Using the modal properties obtained from the aforementioned results, we can extract the natural mode shapes of the plate from the FRF response using Eq. (D.7). Figure 6.6 illustrates the first 24 natural frequencies of the plate, along with the corresponding structural loss factors and mode shapes.

As observed, due to the large dimensions of the plate, the first 18 mode shapes occur at frequencies below 200 Hz. To calculate the sensitivity functions at higher frequencies, a greater number of mode shapes are required. Extracting mode shapes at the higher frequencies necessitates measuring the vibrational response of the plate at more points. In this experiment, 400 points (20×20) were considered for measuring the vibration response of the plate. Applying the modal properties and mode shapes shown in Figure 6.6 to Eq. 4.7, one can calculate the sensitivity functions using the modal expansion method.

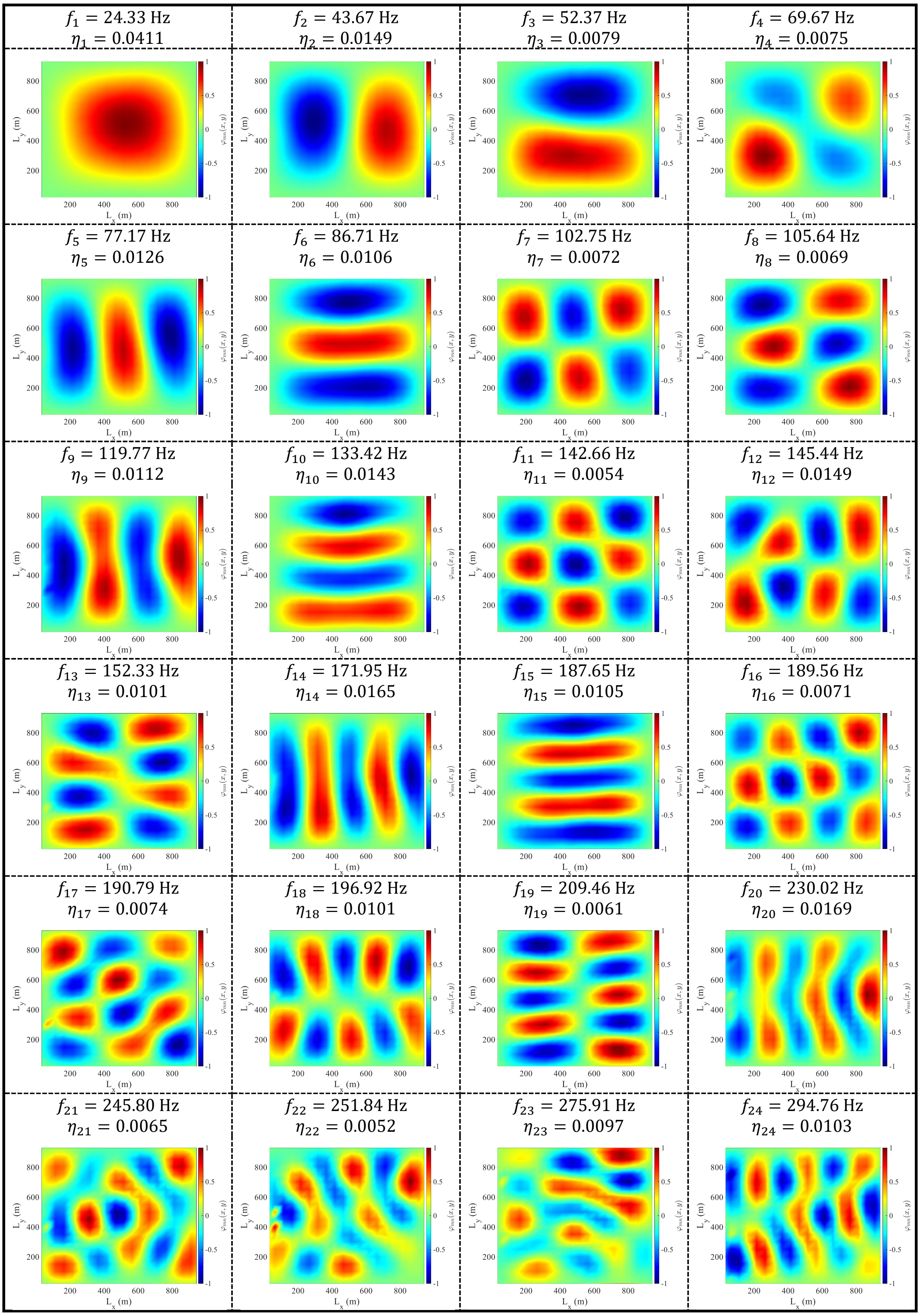

FIGURE 6.6: The first 24 mode shapes of the plate with corresponding damped natural frequencies and structural loss factor.

6.1.2 Reciprocity Principle Method

As evident, computing the sensitivity functions using the modal expansion method necessitates numerous mode shapes and modal frequencies, which can be challenging to obtain for complex structures. To extract mode shapes of the plate at high frequencies, measuring the vibrational response at more locations across the plate is essential. However, increasing the density of measurement points significantly prolongs the experiment runtime. As an alternative approach, the reciprocity principle method can be utilized, which circumvents the limitations associated with the modal expansion method.

As explained in Chapter 4, the sensitivity function $H_\gamma(\mathbf{x}, \mathbf{k}, \omega)$ for a panel represents the acceleration at point $\mathbf{x}$ when the panel is excited by a unit wall plane wave. The direct form of the sensitivity function is given by:

$$H_\gamma(\mathbf{x}, \mathbf{k}, \omega) = \iint_{\sum_p} H_{\gamma/F_n}(\tilde{\mathbf{x}}, \mathbf{x}, \omega) e^{-\mathrm{j}\mathbf{k}\tilde{\mathbf{x}}}, \mathrm{d}\tilde{\mathbf{x}}. \tag{6.3}$$

The right-hand side of Eq. (6.3) can be interpreted as the space-wavenumber transform of $H_\gamma(\tilde{\mathbf{x}}, \mathbf{x}, \omega)$ with respect to the spatial variable $\tilde{\mathbf{x}}$. The points $\tilde{\mathbf{x}}$ become observation points on the panel surface $\sum_p$, meaning that the space-wavenumber transform is performed over the panel's vibration acceleration field. In this form, the sensitivity function is calculated by integrating the frequency response functions between point $\mathbf{x}$ and all points on the panel surface $\tilde{\mathbf{x}}$ [124].

A simpler alternative involves using the reciprocity principle [124]. This principle states that the ratio of the panel's normal acceleration at point $\mathbf{x}$ to the normal force applied at point $\tilde{\mathbf{x}}$ is equal to the ratio of the normal acceleration at point $\tilde{\mathbf{x}}$ to the normal force applied at point $\mathbf{x}$ as follows

$$H_{\gamma/F_n}(\mathbf{x}, \tilde{\mathbf{x}}, \omega) = H_{\gamma/F_n}(\tilde{\mathbf{x}}, \mathbf{x}, \omega). \tag{6.4}$$

Consequently, the sensitivity functions $H_\gamma(\mathbf{x}, \mathbf{k}, \omega)$ can be determined by exciting the panel with a normal force at point $\mathbf{x}$ and performing a space-wavenumber transform of the transfer function between the panel's vibration acceleration response and the force function spectrum, as illustrated in Figure 6.7.

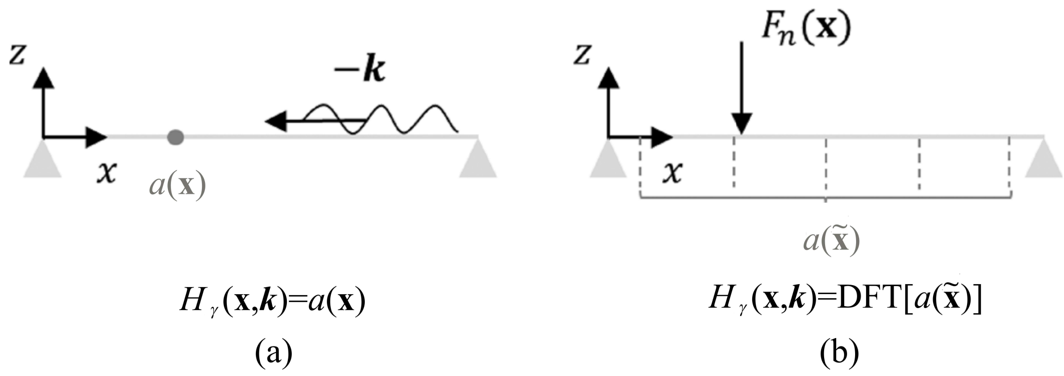

FIGURE 6.7: Schematic view of the sensitivity functions calculation using (a) direct interpretation of the sensitivity functions and (b) corresponding reciprocal interpretation. Figure from [124].

A scanning laser vibrometer can be used to measure the spatial vibratory response of the panel. The reciprocity principle leverages the fundamental idea that the response at a point due to a unit load applied at another point is the same as the response at the second point due to a unit load applied at the first point. This method simplifies the calculation process by avoiding the need for extensive modal analysis. Instead of identifying all the individual mode shapes and natural frequencies, which can be complex and computationally intensive, the reciprocity principle provides a more straightforward approach. By applying known forces and measuring responses, the sensitivity function can be accurately determined with fewer computational resources.

In this section, we follow this procedure to calculate the sensitivity functions using experimental data. Practically, the acceleration field must be measured on a regular grid of points, typically using a scanning laser vibrometer. The space-wavenumber transform is then approximated by a discrete Fourier transform. To prevent aliasing effects, the spatial resolution between grid points should be chosen to accurately represent the spatial variations of the acceleration field. For a homogeneous isotropic thin panel, the spatial resolution ($\delta\mathbf{x}$) should be no more than a quarter of the natural flexural wavelength (λ_b) of the panel at the highest frequency of interest. For more complex panels, a preliminary study should be conducted to determine the appropriate spatial resolution, potentially using a numerical model of the panel or a trial-and-error approach [124].

As noted in Section 6.1.1, measurements were taken over a frequency range from 0 to 1600 Hz with a resolution of 0.5 Hz. To implement the methodology described in this section, the plate acceleration field was calculated on a uniform mesh of 20×20 points in the x and y directions. This setup provides a spatial resolution of approximately

$\delta_x \approx \delta_y \approx 5$ cm. This resolution ensures at least four points per flexural wavelength of the plate, making the responses valid for frequencies up to 586 Hz [124].

The highest wavenumbers $k_x^{\max}$ and $k_y^{\max}$ that can be resolved in the x and y directions, respectively, are determined by [124]

$$k_x^{\max} = k_y^{\max} = \frac{\pi}{\delta_x} = \frac{\pi}{\delta_y} \approx 63 \quad \mathrm{m}^{-1}. \tag{6.5}$$

The sensitivity functions have been calculated at the 15 points specified in Table 6.2. To achieve this, a shaker with an amplifier was used to excite the plate at each point, and for each excitation, the LDV was used to scan the plate and measure its acceleration response. A transducer was connected to the shaker to measure the magnitude of input force. The discrete Fourier transform is then applied to the measured vibrational transfer function between the panel acceleration field and source magnitude to obtain the sensitivity function at each point. In the next section, the sensitivity functions will be computed using the reciprocity principle, and the results obtained will be compared with those obtained with modal expansion method.

6.2 Results and Discussion

In this section, the sensitivity functions are calculated and compared using two methods: the modal expansion method (Section 6.1.1) and the reciprocity principle method (Section 6.1.2). Figure 6.8 shows the squared absolute value of sensitivity functions at two resonance frequencies of $f = 52$ Hz and $f = 172$ Hz, at the 15 points specified in Table 6.2. Comparing the results shown in Figure 6.8 demonstrates that the computed sensitivity functions obtained from the reciprocity principle method are very similar to those obtained from the modal expansion method.

Additionally, Figures 6.9 and 6.10 illustrates the squared absolute value of the sensitivity functions of the plate at 15 point locations calculated as a function of frequency for $k_y = 0$ and $k_x = 0$, respectively. In both figures, the results obtained using the modal expansion and reciprocity principle method are presented and compared. The dispersion curves for the acoustic wave number k_0 and the plate bending wave number k_f are also displayed in both figures. Both figures show that the calculated sensitivity functions around the

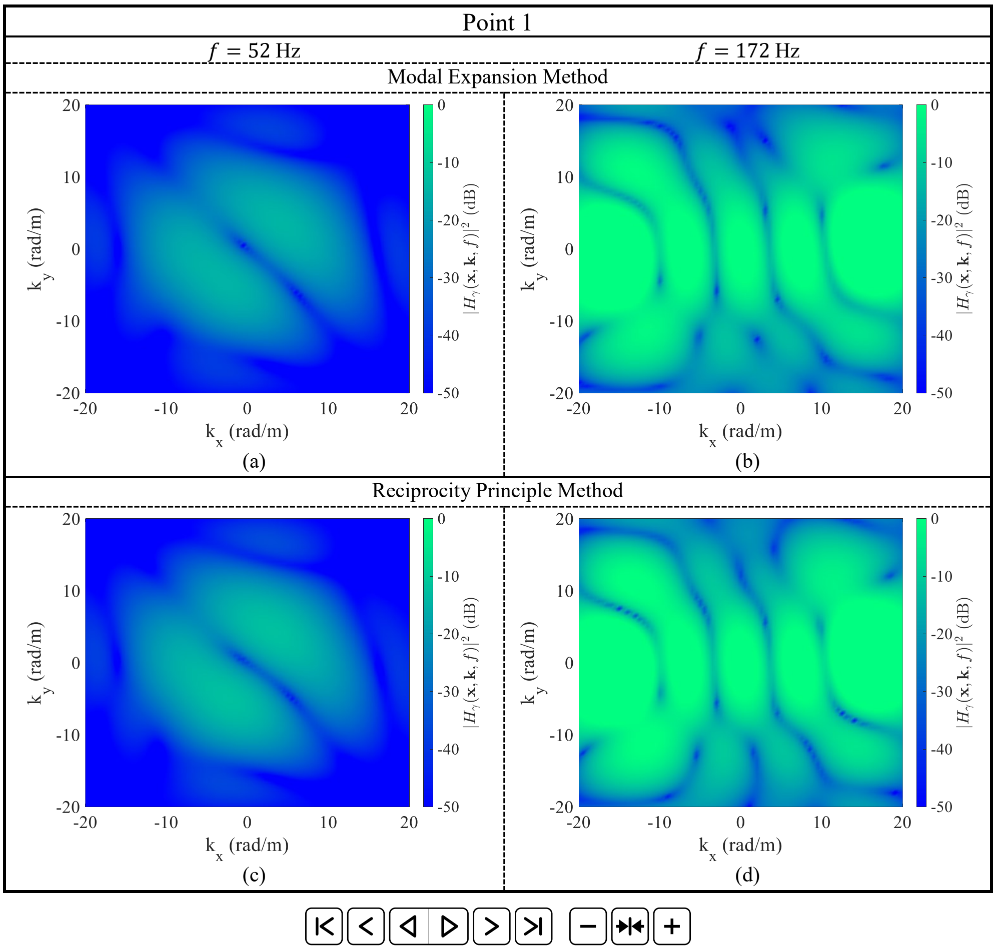

FIGURE 6.8: Interactive plots of squared absolute value of the sensitivity functions $|H_\gamma(\mathbf{x},\mathbf{k}, f)|^2$ (dB, ref. 1 $m^2.s^{-4}.Hz^{-1}$) at 15 points specified in Table 6.2 using (a),(b) modal expansion method and (c),(d) reciprocity principle method at two resonance frequencies of 52 Hz and 172 Hz.

natural frequency of the plate have higher intensity compared to other frequencies. As shown, the results from both methods are in very good agreement, particularly at low frequencies. However, the slight discrepancies observed at higher frequencies can be attributed to inaccuracies in the extracted modal properties at those frequencies. This is because, at higher frequencies, the natural mode shapes of the plate exhibit more complex patterns, with multiple peaks and valleys, which demand finer spatial resolution to capture accurately. Accurately representing the displacement variation in these modes requires a higher density of measurement points. In this study, the number of measurement points was insufficient to resolve these detailed features, including the peaks, valleys, and the curvature of the displacement between them at higher frequencies. Consequently, this limitation results in inaccuracies in the extracted mode shapes at higher frequencies.

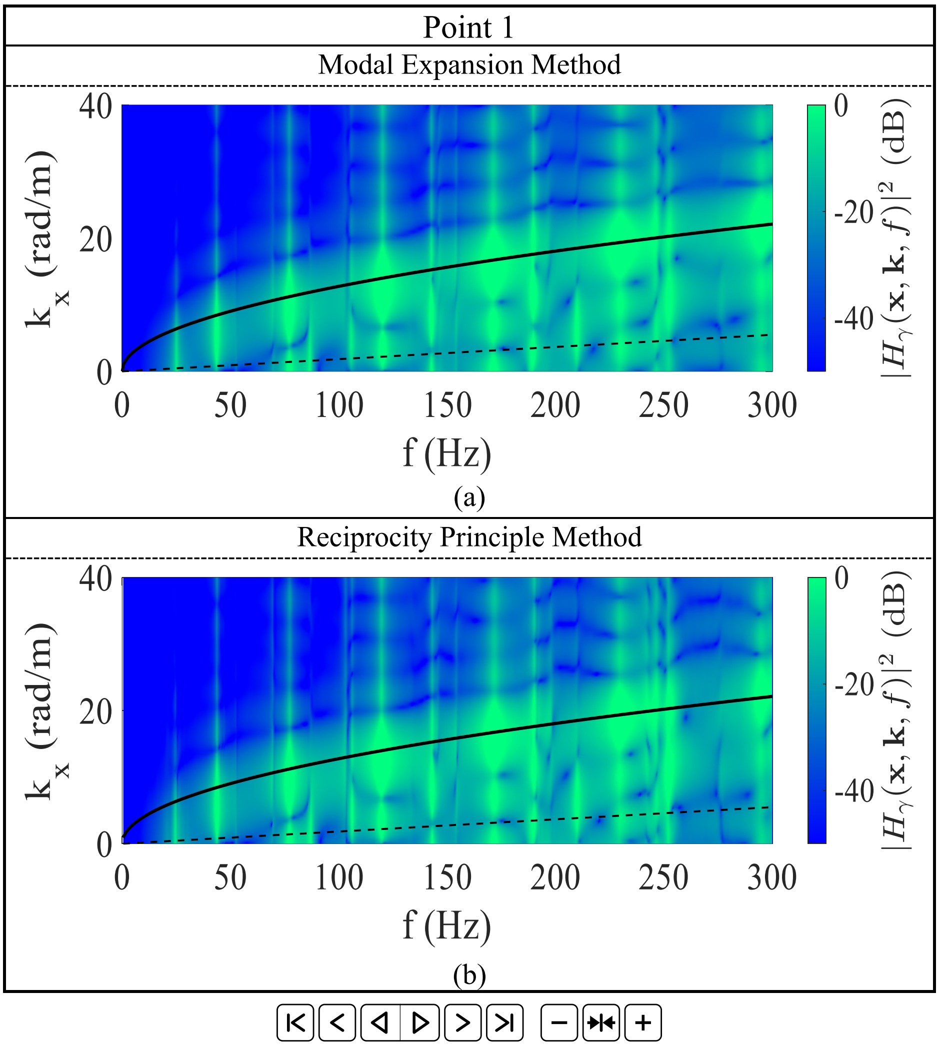

FIGURE 6.9: Interactive plots of squared absolute value of the sensitivity functions $|H_\gamma(\mathbf{x},\mathbf{k},f)|^2$ (dB, ref. 1 m^2.s^{-4}.Hz^{-1}) at 15 points specified in Table 6.2 using (a) modal expansion method and (b) reciprocity principle method as a function of frequency along $k_x \geq 0$ for $k_y = 0$. Solid line: flexural wavenumber k_f according to the Eq. (4.20). Dashed line: acoustic wavenumber of $k_0 = \omega/c_0$.

To further compare the accuracy of the computed sensitivity functions using the modal expansion and reciprocity principle methods, the CSD responses of the plate between point 1 and other points, when the plate is excited by a TBL WPF, are plotted in Figure 6.11. Herein, the Goody-Mellen model is considered for the TBL excitation force. Additionally, the TBL parameters specified in Table 3.1 are used for the simulation of the input TBL model. As can be seen, the computed CSDs from both the modal expansion and reciprocity principle methods match very well, especially at low frequencies. However, as the frequency increases, small differences between the results emerge. This highlights the importance of accurately extracting the modal properties of the plate for precise sensitivity functions calculation through the modal expansion method.

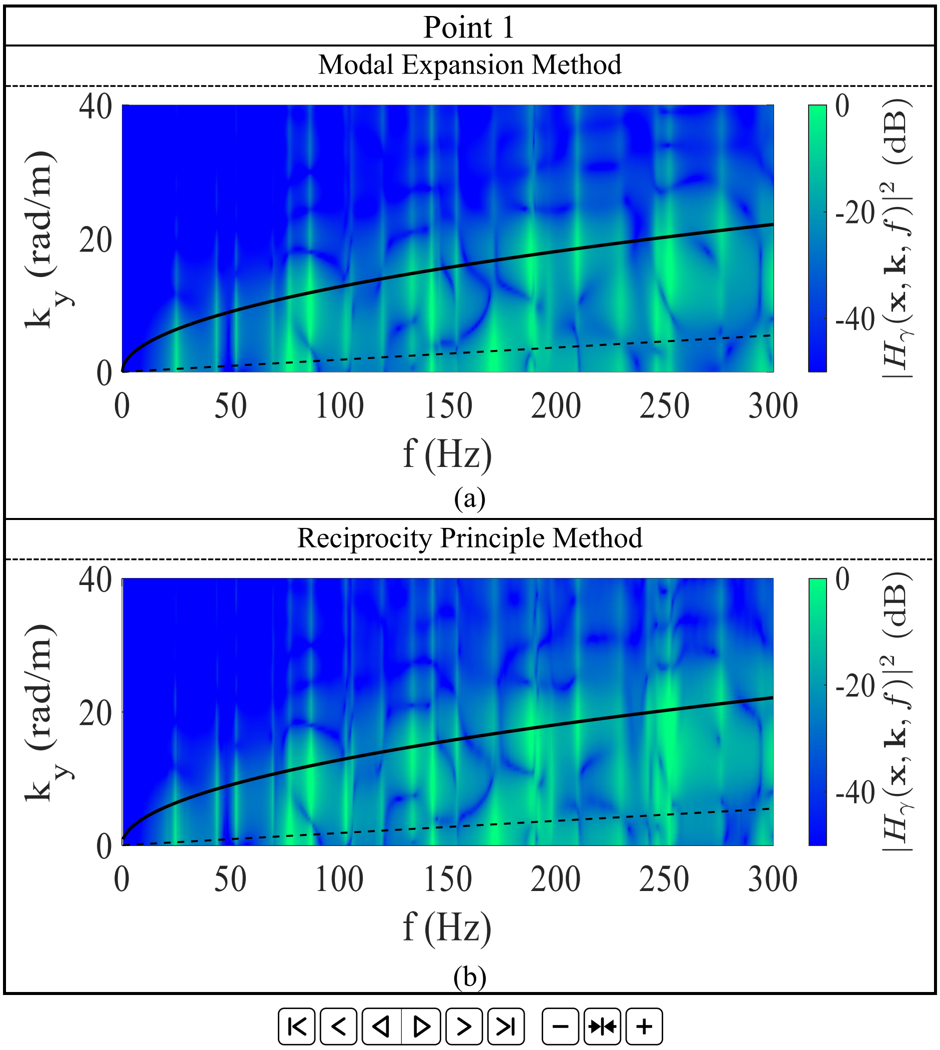

FIGURE 6.10: Interactive plots of squared absolute value of the sensitivity functions $|H_\gamma(\mathbf{x},\mathbf{k},f)|^2$ (dB, ref. 1 m^2.s^{-4}.Hz^{-1}) at 15 points specified in Table 6.2 using (a) modal expansion method and (b) reciprocity principle method as a function of frequency along $k_y \geq 0$ for $k_x = 0$. Solid line: flexural wavenumber k_f according to the Eq. (4.20). Dashed line: acoustic wavenumber of $k_0 = \omega/c_0$.

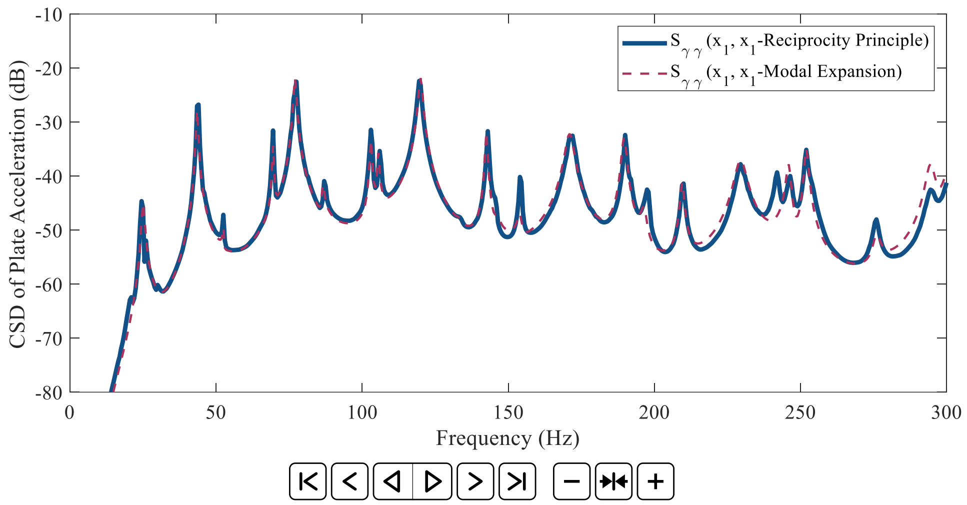

FIGURE 6.11: Interactive plots of comparing the CSD of plate acceleration $S_{\gamma\gamma}$ (dB, ref. 1 m^2.s^{-4}.Hz^{-1}) between point 1 and other points (specified in Table 6.2) achieved through the input Goody+Mellen TBL model and the computed sensitivity functions obtained via two methods: the reciprocity principle (solid line) and modal expansion (dashed line).

6.3 Summary

This chapter investigated two methods for calculating the sensitivity functions experimentally: the modal expansion and reciprocity principle. To illustrate the challenges and effectiveness of each method, an experimental study was conducted in the Acoustics Lab at UTS with a bolted plate. The sensitivity functions obtained from both methods were compared, and the experimental results showed the sensitivity functions obtained from two methods are in good agreement. The modal expansion method requires the modal properties of the structure to compute the sensitivity functions. Accurate extraction of these properties is essential but challenging, especially for complex structures and at high frequencies, as it necessitates detailed measurements of the structure's response at numerous points.

The reciprocity principle method, on the other hand, relies on measuring the vibrational response of the structure when excited at specific points where the sensitivity function is to be calculated. This method bypasses the difficulties of needing detailed modal properties and provides a practical alternative when accurate modal extraction is difficult.

In conclusion, while both methods are effective for calculating the sensitivity function, the modal expansion method's dependency on precise modal property extraction poses significant challenges. The reciprocity principle method offers a viable alternative, avoiding the limitations inherent in the modal expansion method. By applying the reciprocity principle method, one can obtain the sensitivity functions of the plate and then using the VBA technique described in Chapters 4 and 5 the low-wavenumber components of the WPF can be identified. This involves calculating the $\mathbf{Q}$ and $\bar{\mathbf{Q}}$ matrices using Eqs. (4.16) and (5.6) through the calculated sensitivity functions.

Chapter 7

Conclusions and Future Work

7.1 Conclusions

This thesis discussed and examined the ABA and VBA in estimation of the TBL WPF in the low-wavenumber domain. For each approach, the contribution to the existing research was summarized, and suggestions for future research were offered.

The first approach tackled in this thesis was the ABA. Based on the detailed findings from Chapter 3, the effectiveness of microphone arrays in estimating the TBL WPF at low-wavenumbers was thoroughly investigated. The study introduced a regularized Fourier-based method tailored for identifying these low-wavenumber components. Key array parameters—sensor spacing, co-array factor, and sensor distribution—were systematically analyzed to optimize the estimation accuracy. It was revealed that achieving precise results necessitates careful consideration of all three factors, particularly advocating for irregular array patterns with a high co-array factor ($F = 1$). Additionally, the research was extended through further investigation using virtual experiments, simulating multiple realizations of the WPF through the UWPW technique. This approach underscored that increasing the number of realizations enhances the fidelity of the estimated wall pressure spectrum, especially in discerning the convective region. However, a substantial number of realizations were indispensable for accurately capturing the low-wavenumber levels within the TBL pressure field.

An additional investigation explored the impact of convective ridges on low-wavenumber WPF identification, employing various TBL models as input references. This analysis highlighted the significant influence of convective peaks on accuracy, stressing the challenge of isolating low-wavenumber components amid convective disturbances. It was observed that as the difference between the convective peak and the low-wavenumber levels increases, the convective ridge obscures the low-wavenumber components of the TBL WPF. Consequently, a higher number of realizations is required for an accurate estimation of the WPF in the low-wavenumber domain. The study underscored the complexity in real-world scenarios where precise differentiation between convective peaks and low-wavenumber levels remains elusive, necessitating further research to determine optimal snapshot requirements for accurate estimation.

Moreover, the research illuminated practical challenges encountered during experimental setups, including limited data availability, background noise, and potential errors from instrumentation and human factors. These factors collectively underscored the intricacies and uncertainties involved in reliably estimating low-wavenumber TBL WPF using microphone arrays in experimental settings. In summary, Chapter 3 provided critical insights into the methodologies and challenges associated with estimating low-wavenumber TBL wall pressure fields using microphone arrays. The findings laid a foundation for subsequent chapters, emphasizing the need for robust methodologies and further exploration to enhance accuracy and reliability in practical applications.

Chapter 4 focused on introducing an inverse vibration method for estimating the TBL WPF within the low-wavenumber domain using single frequency analysis. The study employed an analytical model of an elastic simply-supported panel subjected to TBL excitation, utilizing acceleration data from the panel to estimate the WPF. A parametric study explored the impact of sensor number and panel size on estimation accuracy, particularly highlighting the method's efficiency compared to traditional ABA. The research demonstrated that unlike ABA methods requiring high number of sensors to meet the Nyquist criterion, the VBA achieved accurate WPF estimation with fewer sensors. Notably, increasing panel size effectively reduced error at low frequencies near the coincidence frequency, enhancing WPF estimation across a broader frequency spectrum. Virtual experiments using the UWPW technique demonstrated practical applicability, indicating that a few hundred snapshots sufficed for accurate low-wavenumber WPF estimation. Furthermore, virtual experiments affirmed the method's repeatability and accuracy when employing sufficient realizations and sensors. However, the study operated under idealized conditions—assuming a homogeneous, stationary, fully developed TBL with zero pressure gradient across the panel. With additional assumptions of non-interference between panel vibrations and the WPF, along with ergodicity of the TBL force. Variability in TBL characteristics, non-ergodic randomness, and prevalent sources of error such as background noise and instrumentation challenges posed further complexities in practice. In conclusion, Chapter 4 elucidated the effectiveness of proposed inverse vibration method in estimating low-wavenumber TBL WPF, highlighting its practical advantages over conventional acoustic methods.

Chapter 5 delved into the application of the VBA across multiple discrete frequencies to estimate the TBL WPF within the low-wavenumber domain. The study employed a frequency band formulation assuming constancy of the low-wavenumber WPF across the chosen frequency range, aimed at identifying and quantifying these specific pressure fluctuations. The research revealed that the frequency band method allowed for accurate estimation of the low-wavenumber WPF with a minimal number of realizations, underscoring its practical advantage in requiring fewer data samples per frequency. This efficiency is particularly beneficial in experimental settings where data acquisition constraints exist. To sum up, Chapter 5 advanced our understanding of utilizing vibration-based methods at multiple discrete frequencies for low-wavenumber TBL WPF estimation. While demonstrating efficacy in targeted applications, the study underscored methodological constraints that necessitate consideration in practical implementations and further research.

Chapter 6 focused on exploring two distinct methods for calculating the sensitivity function: the modal expansion and reciprocity principle. The modal expansion method entails deriving sensitivity functions based on the modal properties of the structure. This approach necessitates accurate measurement and computation of these modal properties, which becomes particularly intricate for complex structures. The method's effectiveness hinges on precise modal properties, which can be challenging. Conversely, the reciprocity principle method offers an alternative by leveraging the vibrational response of the structure when excited at specific points. This method bypasses the need for extensive modal property determination, focusing instead on practical measurement scenarios where direct excitation points are accessible. It proves especially useful in situations where accurate modal data extraction is impractical or challenging. The chapter provided a comparative analysis by conducting an experimental investigation at the Acoustics Lab at UTS using a rectangular plate bolted along all the edges to a fixed frame within a concrete wall. Results demonstrated very good agreement between experimental calculation of the sensitivity function using both methods. To sum up, while both modal expansion and reciprocity principle methods exhibit efficacy in calculating the sensitivity function, the modal expansion method's dependency on precise modal property extraction poses significant challenges, especial at high frequencies. The reciprocity principle method emerges as a robust alternative, offering practical advantages and circumventing limitations associated with complex modal analysis. This comparative assessment underscores the importance of method selection based on the specific characteristics and constraints of the structural dynamics under study.

7.2 Future work

This thesis has primarily focused on the theoretical evaluation and virtual experiments for the estimation of the WPF in the low-wavenumber domain. While significant insights have been gained, several avenues for future research can enhance the robustness and applicability of the findings presented herein.

One immediate extension of this work is to conduct real-world experiments in a controlled wind tunnel environment. By exciting a plate with airflow, the estimation of the WPF in the low-wavenumber domain can be validated experimentally. For the ABA, an array of microphones flush-mounted on the plate can be used to measure the WPF. The recorded data will then be processed using RFBA method to estimate the WPF in the low-wavenumber domain. This practical implementation will help verify the theoretical models and virtual experiments conducted in this study, providing a more comprehensive understanding of the technique's effectiveness in realistic scenarios.

Similarly, for the VBA, an array of accelerometers can be mounted on the opposite side of the plate exposed to airflow. The vibrational response of the plate, induced by the TBL, will be recorded. Using this data, the WPF in the low-wavenumber domain can be estimated using the TGSVD method investigated in Chapters 4 and 5, allowing for a comparative analysis between the ABA and VBA methods in a real experimental setup.

This dual approach will help identify the strengths and limitations of each method under practical conditions and guide future improvements.

Beyond experimental validation, further research could explore the impact of different plate materials and boundary conditions on the WPF estimation accuracy. Investigating how variations in material properties and clamping conditions influence the sensor data and subsequent WPF estimations can provide valuable insights into the adaptability and reliability of the proposed methods.

Another promising direction is the development of advanced signal processing techniques and machine learning algorithms to enhance the accuracy and efficiency of WPF estimation. By leveraging modern computational methods, it may be possible to better handle the complexities and uncertainties inherent in real-world data, such as background noise, sensor inaccuracies, and non-stationary TBL characteristics.

Additionally, the application of the proposed methods in more complex geometries and flow conditions could be explored. Extending the study to include curved surfaces, non-uniform flow fields, and varying TBL characteristics will broaden the scope of the research and its potential applications in diverse engineering contexts.

Finally, collaborative research integrating computational fluid dynamics (CFD) simulations with experimental data can further refine the estimation techniques. By comparing CFD predictions with experimental measurements, more accurate models of the WPF can be developed, enhancing the overall understanding of the TBL dynamics and their impact on structural vibrations.

In conclusion, while this thesis has laid a solid foundation for estimating the WPF in the low-wavenumber domain, substantial opportunities exist for expanding and validating this work through real-world experiments, advanced computational methods, and broader applications. Pursuing these directions will significantly contribute to the field of aeroacoustics and structural dynamics, providing practical solutions for noise control and structural health monitoring in various engineering applications.

Appendix A

TGSVD Method: Acoustic-based Approach

Using Eqs. (3.5) and (3.8), one can calculate the vector $\mathbf{S}_{pp}$ and matrix $\mathbf{Q}$. To obtain the best estimation of the WPF components, the following steps from Ref. [76] are employed:

Step 1: compute discrete first derivative operators;

```
L=get_l(size(Q,2),1);
```

Step 2: Compute the compact generalized SVD of a matrix pair;

```
[UU,sm,XX]=cgsvd(Q,L)
```

Step 3: Compute all TGSVD solutions;

```
k_tgsvd=1:size(sm,1)
[X_tgsvd,Rho,Eta]=tgsvd(UU,sm,XX,Sp,k_tgsvd);
```

Step 4: Find the corner of a discrete L-curve via an adaptive pruning algorithm;

```
k_corner=corner(Rho,Eta)
```

Step 5: Find the estimated WPF components for the optimal regularization parameter obtained from the corner method;

```
Phipp=X_tgsvd(:,k_corner)
```

Appendix B

Interactive Plot of Estimation WPF in the Low-wavenumber Domain Using ABA

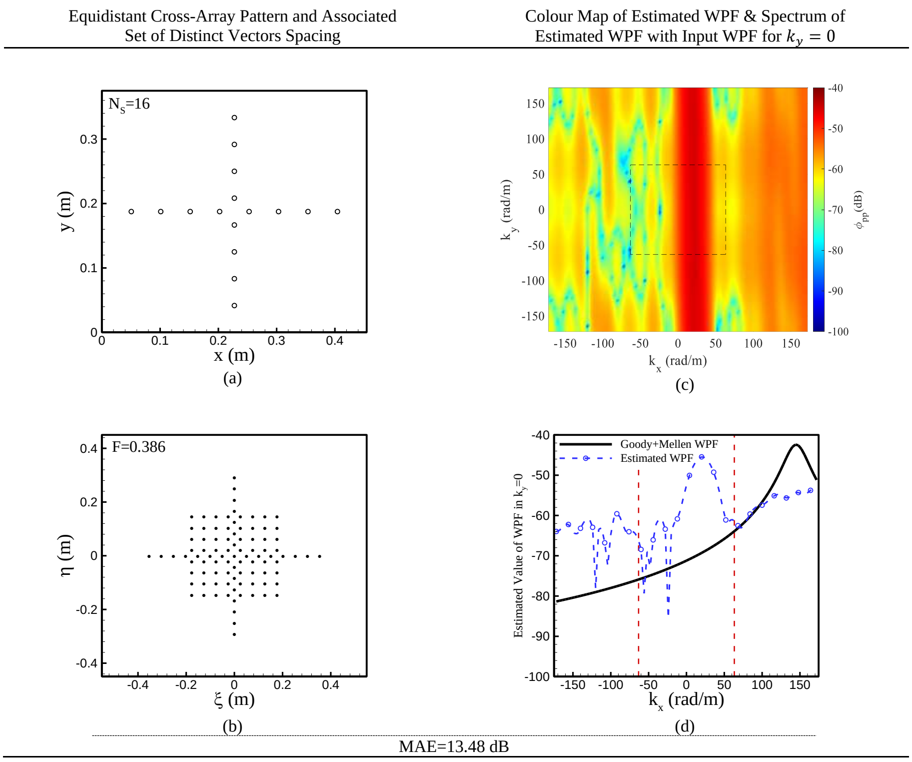

FIGURE B.1: Interactive plots of estimated WPF using RFBA method for equidistant cross-array pattern.

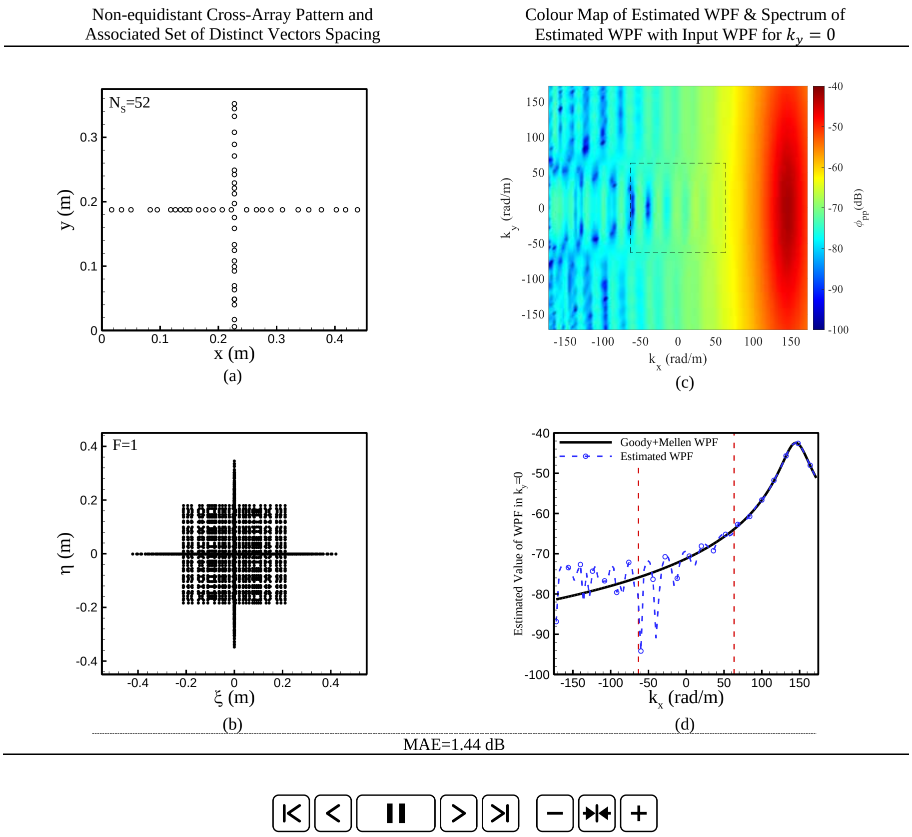

Figure B.2: Interactive plots of estimated WPF using RFBA method for non-equidistant cross-array pattern.

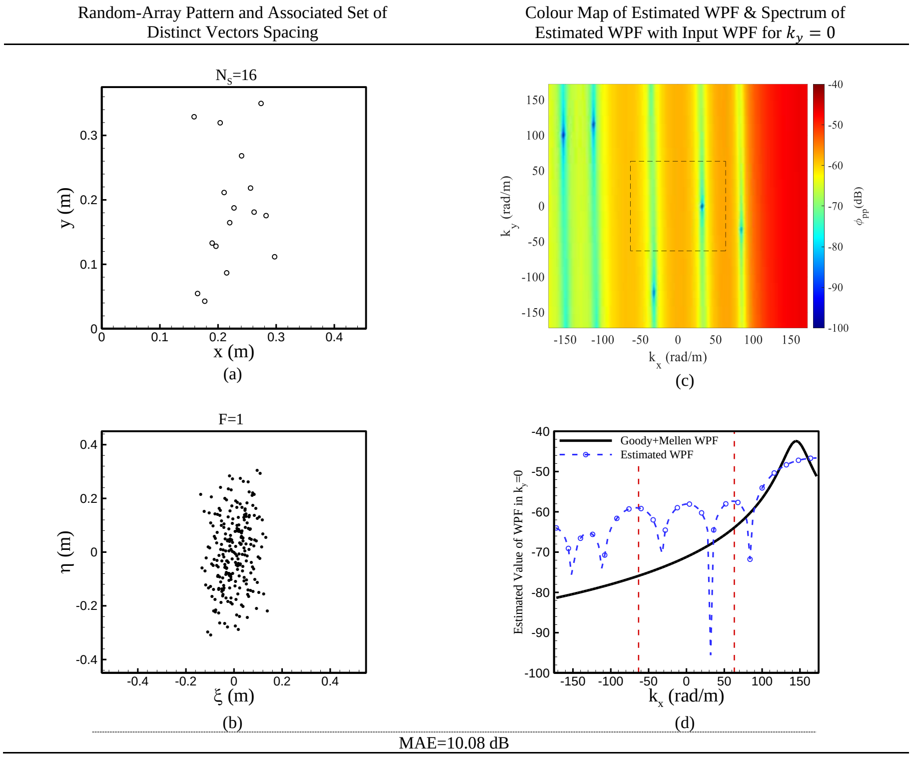

FIGURE B.3: Interactive plots of estimated WPF using RFBA method for irregular-array pattern.

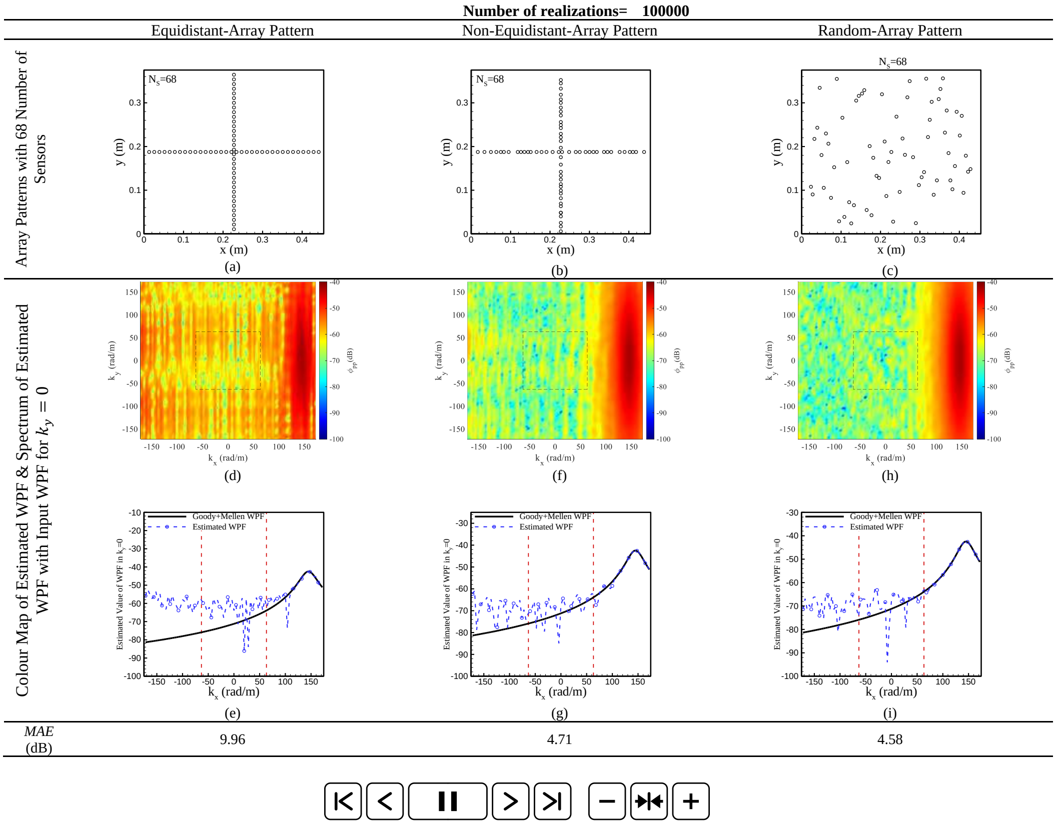

FIGURE B.4: Interactive plots of estimated WPF using the UWPW technique and different numbers of realizations for three patterns.

Appendix C

TGSVD Method: Vibration-based Approach

Using Eqs. (4.12) and (4.16), one can calculate the vector $\mathbf{S}_p(\omega)$ and matrix $\mathbf{Q}$. To obtain the best estimation of the WPF components, the following steps from [76] are employed:

Step 1: compute discrete first derivative operators;

```
L=get_l(size(Q,2),1);
```

Step 2: Compute the compact generalized SVD of a matrix pair;

```
[UU,sm,XX]=cgsvd(Q,L);
```

Step 3: Compute the TGSVD solutions (see Subsection 4.2.1.2);

```
if size(sm,1)<(M_b+N_b)^2+1
    k_tgsvd=1:size(sm,1);
else
    k_tgsvd=1:(M_b+N_b)^2;
end
[X_tgsvd,Rho,Eta]=tgsvd(UU,sm,XX,Sp,k_tgsvd);
```

Step 4: Find the corner of a discrete L-curve via an adaptive pruning algorithm;

```
k_corner=corner(Rho,Eta);
```

Step 5: Find the estimated WPF components for the optimal regularization parameter obtained from the corner method;

```
Phipp=X_tgsvd(:,k_corner);
```

Appendix D

Determining Modal Parameters of a Mechanical System by Using Complex Mode Indicator Function

Modal identification entails the estimation of structural system modal parameters from a set of Frequency Response Functions (FRFs). These parameters comprise complex-valued modal frequencies, modal vectors, and modal mass. The most prevalent form of modal testing is single reference modal testing, employing either a single fixed input or a single fixed output. Typically, a roving hammer or a shaker serves as the excitation source, while a single transducer measures the resulting acceleration. Single Input Multiple Output (SIMO) configuration is the most commonly utilized approach in single reference modal testing. However, in cases when the structure is very complex (consists of many different parts with different structural properties) or when the structure has more modes with the same or very close natural frequency (repeated roots or closely coupled modes), multiple reference testing is required in experimental modal analysis [83]. Hence, it becomes necessary to utilize two or more fixed inputs or outputs, known as multiple reference or MIMO (multiple input multiple output) modal testing. When the inputs are fixed, the FRFs are computed between each input and multiple outputs, constituting multiple columns of the FRF matrix (with the inputs serving as references).

Conversely, when two or more fixed outputs are employed, the FRFs are computed between each output and multiple inputs, forming multiple rows of the FRF matrix (with the outputs acting as references) [48]. A structure is said to have repeated roots or closely coupled modes when two or more of its modes exhibit the same or similar frequencies but possess different mode shapes. This issue arises in certain symmetrical structures or highly complex systems. To detect repeated roots or closely coupled modes, the number of rows or columns in the FRF matrix must be at least equal to the number of modes sharing the same frequency. Consequently, the number of reference points must be at least equal to the number of modes with identical frequencies. Thus, with two reference points, two repeated modes can be accurately identified; with three reference points, three repeated modes can be correctly distinguished, and so forth.

The CMIF [159] emerges as a straightforward and effective approach for discerning the modes within a complex system. By displaying the physical magnitude of each mode and the damped natural frequency for each root, the CMIF facilitates mode identification. Moreover, the CMIF has the capability to detect repeated roots and closely coupled modes, owing to the availability of multiple reference data. Additionally, the CMIF provides comprehensive modal parameters, such as damped natural frequencies, mode shapes, and modal participation vectors. The CMIF concept is realized through the SVD of the FRFs matrix at each spectral line.

In multiple references modal testing, the FRF matrix characterizes the relationship between multiple inputs and multiple outputs. At each spectral line of an N degree-of-freedom system, the FRF matrix of the structure can be represented as shown in Eq. (D.1). The size of the FRF matrix is $N_0 \times N_i$, where N_0 represents the number of response points and N_i represents the number of excitation points. For simplification, the mass matrix of the structure is assumed to be the identity matrix [159].

$$[Y(j\omega)] = \Sigma_{r=1}^{N} \frac{[A_r]}{j\omega - \lambda_r} = \Sigma_{r=1}^{N} \frac{Q_r\{\varphi\}_r\{L\}_r^H}{j\omega - \lambda_r}, \tag{D.1}$$

where:

$[Y(j\omega)]$	– FRF matrix of size $N_0 \times N_i$,
$[A_r]$	– r^{th} residue matrix of size $N_0 \times N_i$,
$\{\varphi\}_r$	– r^{th} mode shape of size $N_0 \times 1$,
$\{L\}_i$	– r^{th} modal participation factor of size $N_0 \times 1$,
Q_r	– scaling factor for r^{th} mode,
λ_r	– system pole value of r^{th} mode.

Eq. (D.1) in a compact form is [48]:

$$[Y(j\omega)] = [\Xi]\left[\frac{Q_r}{(j\omega - \lambda_r)}\right][L] \tag{D.2}$$

where:

$[\Xi]$	– mode shapes matrix of size $N_0 \times 2N$,
$[L]$	– modal participation factor matrix of size $N_i \times 2N$,
$\left[\frac{Q_r}{(j\omega - \lambda_r)}\right]$	– equivalent singular value

Eq. (D.1) represents the response of the structure, denoted by $[Y(j\omega)]$, to a unit excitation force at a specific frequency ω. This response can be expressed as the summation, or linear combination, of $2N$ residue matrices $[A_r]$ divided by the difference between the modal frequency (system pole) λ_r and the discrete frequency $j\omega$ (sampling frequency location in the Laplace domain). In conjunction with the equation, the residue matrix is defined as the product of the mode shape $\{\varphi\}_r$ and the modal participation factor $\{L\}_r^H$, weighted by a scaling factor Q_r (for r^{th} mode). This scaling factor serves as an indicator of the mode's magnitude when the mode shape and modal participation factor are scaled to be unitary vectors [48].

Through SVD [9], any matrix $[A]$ can be decomposed into the product of three matrices. When multiplied, these matrices express $[A]$ in terms of its linearly independent components. Additionally, SVD enables the determination of the rank of matrix $[A]$. The CMIF relies on the SVD of the FRF matrix. SVD is employed on the FRF matrix to identify the roots (or modes) of the system. This process decomposes the FRF matrix into three matrices for each frequency. If the number of effective modes is less than or equal to the smaller dimension (number of responses or references) of the FRF matrix, two singular vectors are obtained through singular value decomposition. Singular value decomposition can be expressed by the equation [9, 159].

$$[Y(j\omega)] = [U(j\omega)][\sigma(j\omega)][V(j\omega)]^H, \tag{D.3}$$

where:

$[U(j\omega)]$ – left singular matrix of size $N_0 \times N_0$ (unitary matrix)

$[\sigma(j\omega)]$ – singular value matrix of size $N_0 \times N_i$ (diagonal matrix)

$[V(j\omega)]$ – right singular matrix of size $N_i \times N_i$ (unitary matrix) ,

In Eq. (D.3), the middle matrix represents a diagonal matrix of singular values. When the scaling factor is constant for a mode, the magnitude of the singular value increases with the decrease in distance between the modal and discrete frequencies (as defined in Eq. (D.2)). Comparing two different modes, the singular value is larger for the mode with stronger contribution and a larger residue value (as described in Eq. (D.1)). Mode shapes are represented by the left singular vectors of the matrix $[U(\omega)]$. The right singular vectors in matrix $[V(\omega)]$ represent the corresponding modal participation factors. Both mode shapes and modal participation factors are scaled to form unitary vectors (unitary matrices) [159]. As the singular values at a particular spectral line reflects the quantity of linearly independent modes, the matrix $[Y(j\omega)]$ near resonance transforms into [141]

$$Y(j\omega) \cong \sigma_1(j\omega) u_1(j\omega) \nu_1^H(j\omega), \tag{D.4}$$

where the subscript "1" indicates the first (=highest) singular value [141].

The CMIF is determined by solving the eigenvalues from the normal matrix derived from the FRF matrix at each spectral line. Obtaining the normal matrix involves multiplying the FRF matrix (as per Eq. (D.3)) on the left by its Hermitian matrix, resulting in [159]

$$[Y(j\omega)]^H[Y(j\omega)] = [V(j\omega)][\sigma^2(j\omega)][V(j\omega)]^H. \tag{D.5}$$

CMIF is equal to the square of the magnitude of the singular value of the FRF matrix [159]

$$\mathrm{CMIF}_k(j\omega) = \vartheta_k(j\omega) = \sigma_k^2(j\omega), \tag{D.6}$$

where

$\mathrm{CMIF}_k(j\omega)$	$-$ k^{th} CMIF at frequency ω,
$\vartheta_k(j\omega)$	$-$ k^{th} eigenvalue of the normal matrix of FRF matrix at frequency ω,
$\sigma_k^2(j\omega)$	$-$ k^{th} singular value of the FRF matrix at frequency ω

The left matrix in Eq. (D.3) corresponds to mode shapes. For the k^{th} eigenvalue curve at frequency $j\omega_p$, the unscaled mode shape can be derived from the equation [159]

$$\begin{gathered} \{u(j\omega_p)\}_k = [Y(j\omega_p)]\{\nu(j\omega_p)\}_k \vartheta(j\omega_p)_k^{-1}, \\ k = 1, 2, \ldots, N_k \end{gathered} \tag{D.7}$$

where

N_k	$-$ number of repeated roots detected at frequency $j\omega_p$,
$j\omega_p$	$-$ frequency of detected peaks that is the approximate damped natural frequency of the r^{th} mode ,
$\{\boldsymbol{u}(j\omega_p)\}_k$	$-$ unscaled mode shape for k^{th} repeated root at $j\omega_p$,
$\{\boldsymbol{\nu}(j\omega_p)\}_k$	$-$ equivalent mode participation factor for k^{th} repeated root at $j\omega_p$.

The peaks identified in the CMIF plot signify the presence of modes, with the frequencies at these peaks corresponding to the damped natural frequencies. The modal shapes remain relatively consistent in the vicinity of each peak. Utilizing multiple neighboring spectral lines from the FRF matrix simultaneously can enhance the accuracy of mode shape estimation. The right matrix in Eq. (D.3) corresponds to modal participation factors, illustrating the degree to which each mode contributes to the FRFs across different reference points, essentially indicating the effectiveness of exciting each modal vector from various reference locations.

The CMIF method is able to distinguish closed and also coupled modes. Then, these identified peaks are used as initial estimate of natural frequencies to create eFRF for each mode. The eFRF method is employed to identify natural frequencies and scale an equivalent single Degree of Freedom (DOF) characteristic linked to each peak observed in the CMIF [5, 143]. The eFRF operates on the principle of transforming from physical to modal coordinates and can be described as a weighted mean of all the measured FRFs, with the left and right singular vectors serving as discrete modal filters. This method facilitates the isolation of modes. The eFRF is defined as follows [90]

$$\mathrm{eFRF}(\omega)_r = \{U(\omega_r)\}^H [Y(\omega)]\{V(\omega_r)\}, \tag{D.8}$$

where $\mathrm{eFRF}(\omega)_r$ is an enhanced frequency response function of r-th mode.

In the subsequent stage, the rational fraction polynomial method is applied to these functions to estimate modal parameters [60]. This is done by curve fitting the FRF. The FRF can be expressed in either rational (polynomial) fraction or partial fraction form. In both approaches, all modal parameters (frequency, damping, and modal coefficient) for all modes are estimated simultaneously.

The rational fraction polynomial is an iterative method used to estimate modal parameters from a function that describes the dynamic behavior of a mechanical system. This method posits that the frequency response function can be expressed as a ratio of two polynomials, as follows [57, 152]

$$Y(\omega) = \frac{\Sigma_{k=1}^{m} a_k.(\omega)^k}{\Sigma_{k=1}^{n} b_k.(\omega)^k}, \tag{D.9}$$

where a_k, b_k are sought unknown polynomial coefficients. These coefficients are determined by minimizing the error function, as defined by equation [90, 152]

$$e_i = \Sigma_{k=0}^{m} a_k(\omega_i)^k - \hbar_i[\Sigma_{k=0}^{n} b_k(\omega_i)^k + (\omega_i)^n], \tag{D.10}$$

where $\hbar_i$ represents FRF data at frequency ω_i. The error function is minimized using the least-squares technique. Equation (D.10) can also be applied to the eFRF. In this work, this estimation method is used for each of the eFRFs.

The orders of the numerator and denominator polynomials in Eq. (D.10) are independent of each other. These equations are linear, and their coefficients are identified during the curve fitting process. Eq. (D.10) represents the analytical formulation of the FRF data, with FRF being the transfer function evaluated along the frequency axis. The denominator polynomial is referred to as the characteristic polynomial of the system, with its roots corresponding to the poles of the transfer function. These roots are termed the roots of the characteristic polynomial. If the characteristic polynomial is zero, the transfer function becomes infinite. The solutions (roots) where the numerator polynomial is zero represent the values at which the transfer function is zero. These values are known as the zeros of the transfer function. Consequently, by solving the roots of the numerator and characteristic polynomials, the poles and zeros of the transfer function can be determined. A root-finding solution is then employed to ascertain the modal parameters.

Figure D.1 displays two sets of CMIF curves [9]. The upper set shows one variation of the CMIF, while the lower set illustrates another form. In understanding the CMIF, each peak signifies the presence of a mode at that particular frequency. For example, in the upper plot, the blue curve exhibits three peaks, indicating that the CMIF identifies three modes in this scenario. If a second peak appears at the same frequency as the first peak, it suggests the existence of two modes at that frequency. However, it is crucial that the second curve peaks at the same frequency as the first one; otherwise, it doesn't represent an additional mode [9].

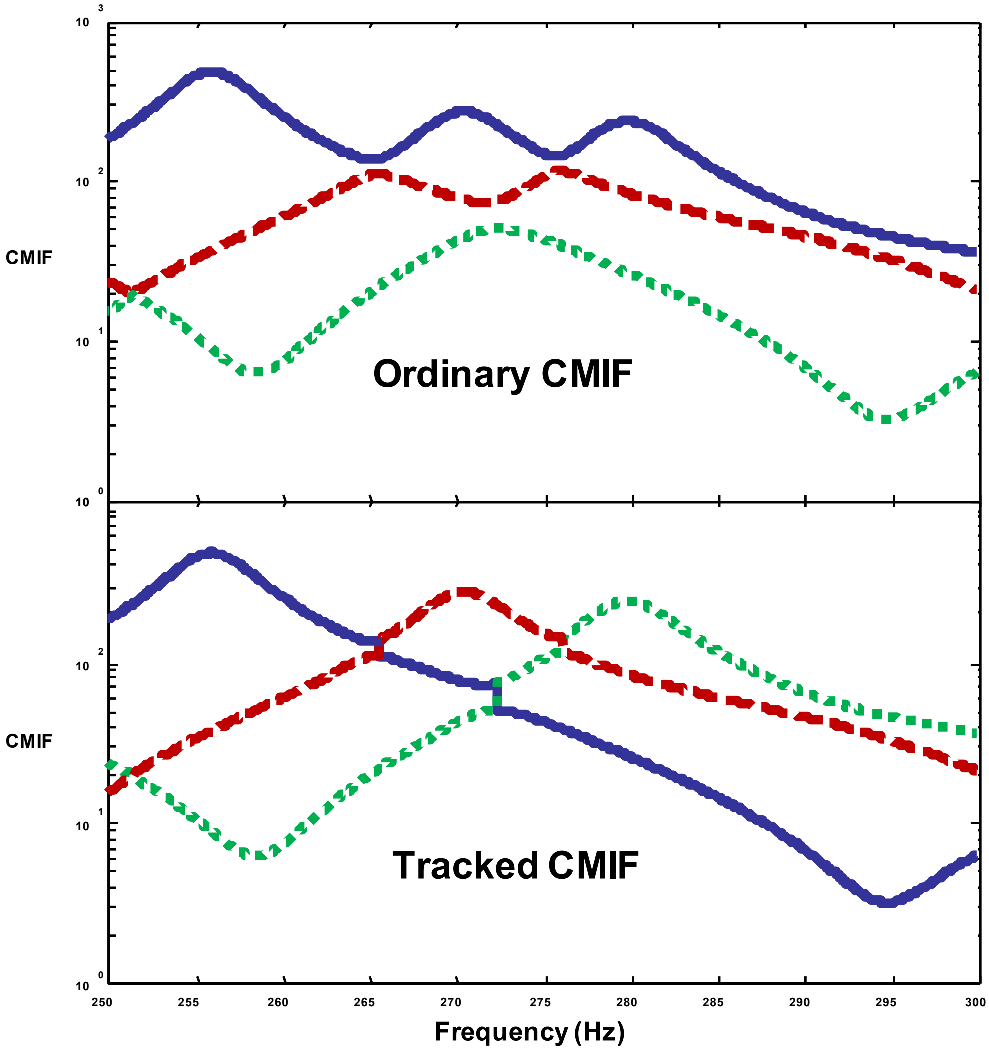

Figure D.1: CMIF (upper) and Tracked CMIF (lower). Figure from [9]

The CMIF is used to focus on the most significant singular values, while the Tracked CMIF is employed to monitor the vector associated with a singular value. In the lower plot of Fig. D.1, tracking is centered on the vector corresponding to the singular value rather than the largest singular value. Observing the blue vector, it peaks at a lower frequency before gradually decreasing. Similarly, the red vector begins with a modest amplitude, peaks midway through the frequency range, and then declines steadily. The green line starts with minimal amplitude, progressively peaking as the blue and red vectors decline. Thus, the choice between tracking the largest singular value (upper plot) or the vector linked to the singular value (lower plot) depends on the aspect of the CMIF being considered [9].

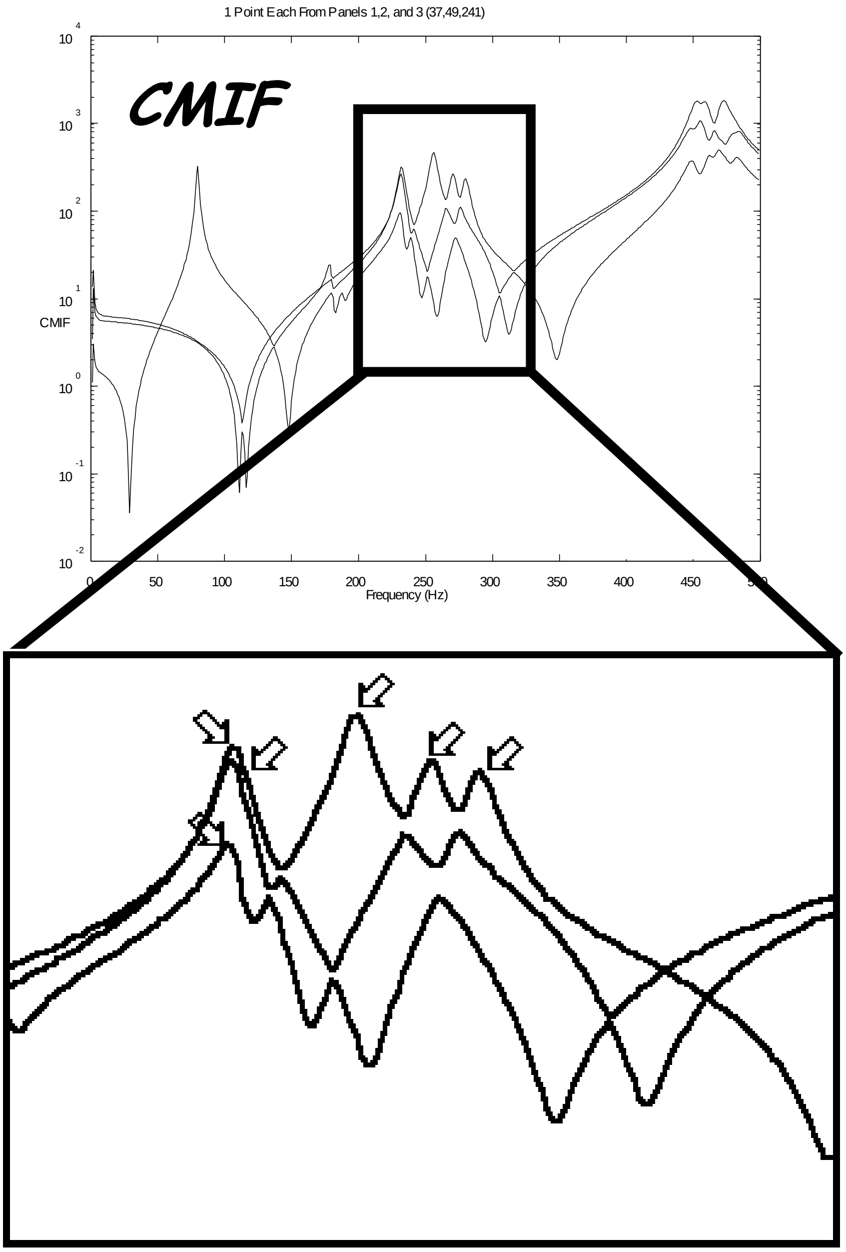

FIGURE D.2: CMIF with multiple modes. Figure from [9]

In situations where multiple modes exist at identical frequencies, the CMIF plot would exhibit one or more singular values peaking simultaneously. Figure D.2 illustrates this scenario [9], showing three modes sharing the same frequency at the initial peak in the expanded CMIF plot. Subsequently, three distinct peaks are observed at higher frequencies. Therefore, within this expanded frequency band, the CMIF plot indicates the presence of six distinct modes.

Bibliography

[1] B. M. Abraham and W. L. Keith. Direct Measurements of Turbulent Boundary Layer Wall Pressure Wavenumber-Frequency Spectra. *J. Fluids Eng*, 120(1):29–39, 03 1998.

[2] H. Abtahi, M. Karimi, and L. Maxit. On the challenges of estimating the low-wavenumber wall pressure field beneath a turbulent boundary layer using a microphone array. *J. Sound Vib.*, page 118230, 2023.

[3] H. Abtahi, M. Karimi, and L. Maxit. Identification of low-wavenumber wall pressure field beneath a turbulent boundary layer using vibration data. *J. Fluids Struct.*, 127:104135, 2024.

[4] M. Alaoui. *Coherent structures and wall-pressure fluctuations modeling in turbulent boundary layers subjected to pressure gradients.* PhD thesis, Paris, ENSAM, 2016.

[5] R. Allemang and D. Brown. A complete review of the complex mode indicator function (cmif) with applications. In *Proceedings of ISMA International Conference on Noise and Vibration Engineering, Katholieke Universiteit Leuven, Belgium*, pages 3209–3246, 2006.

[6] R. K. Amiet. Noise due to turbulent flow past a trailing edge. *J. Sound Vib.*, 47(3):387–393, 1976.

[7] B. Arguillat, D. Ricot, C. Bailly, and G. Robert. Measured wavenumber: Frequency spectrum associated with acoustic and aerodynamic wall pressure fluctuations. *J. Acoust. Soc. Am.*, 128(4):1647–1655, 2010.

[8] B. Arguillat, D. Ricot, G. Robert, and C. Bailly. Measurements of the wavenumber-frequency spectrum of wall pressure fluctuations under turbulent flows. In *11th AIAA/CEAS aeroacoustics conference*, page 2855, 2005.

[9] P. Avitabile. Modal space-in our own little world. *Exp. Tech.*, 37:4–6, 2013.

[10] A. Ben-Israel and T. N. Greville. *Generalized inverses: theory and applications*, volume 15. Springer Science & Business Media, 2003.

[11] J. S. Bendat and A. G. Piersol. *Random data: analysis and measurement procedures.* John Wiley & Sons, 2011.

[12] M. Bertero, P. Brianzi, E. R. Pike, and L. Rebolia. Linear regularizing algorithms for positive solutions of linear inverse problems. *Proc. Math. Phys. Eng. Sci.*, 415(1849):257–275, 1988.

[13] W. Bhat. Flight test measurement of exterior turbulent boundary layer pressure fluctuations on boeing model 737 airplane. *J. Sound Vib.*, 14(4):439–457, 1971.

[14] W. K. Blake. Mechanics of flow-induced sound and vibration. volume 1 general concepts and elementary source. volume 2-complex flow-structure interactions. *Appl. Math.*, 1, 1986.

[15] W. K. Blake. *Mechanics of flow-induced sound and vibration, Volume 2: Complex flow-structure interactions.* Academic press, 2017.

[16] W. K. Blake and D. M. Chase. Wavenumber-frequency spectra of turbulent-boundary-layer pressure measured by microphone arrays. *J. Acoust. Soc. Am.*, 49(3B):862–877, 1971.

[17] W. K. Bonness, D. E. Capone, and S. A. Hambric. Low-wavenumber turbulent boundary layer wall-pressure measurements from vibration data on a cylinder in pipe flow. *J. Sound Vib.*, 329(20):4166–4180, 2010.

[18] P. Bremner, C. Todter, and S. Clifton. Sideglass turbulence and wind noise sources measured with a high resolution surface pressure array. *SAE Int. J. Passeng. Cars - Mech.*, 8(2015-01-2325), 2015.

[19] T. F. Brooks and T. Hodgson. Trailing edge noise prediction from measured surface pressures. *J. Sound Vib.*, 78(1):69–117, 1981.

[20] T. F. Brooks and W. M. Humphreys. A deconvolution approach for the mapping of acoustic sources (damas) determined from phased microphone arrays. *J. Sound Vib.*, 294(4-5):856–879, 2006.

[21] M. Bull. Wall-pressure fluctuations associated with subsonic turbulent boundary layer flow. *J. Fluid Mech.*, 28(4):719–754, 1967.

[22] M. Bull. Wall-pressure fluctuations beneath turbulent boundary layers: some reflections on forty years of research. *J. Sound Vib.*, 190(3):299–315, 1996.

[23] R. Campagna, L. D'Amore, and A. Murli. An efficient algorithm for regularization of Laplace transform inversion in real case. *J. Comput. Appl. Math.*, 210(1-2):84–98, 2007.

[24] S. Caro, V. Cotoni, P. Shorter, and F. Mendonça. Turbulent surface pressure field in low speed flow. In *Flinovia-Flow Induced Noise and Vibration Issues and Aspects: A Focus on Measurement, Modeling, Simulation and Reproduction of the Flow Excitation and Flow Induced Response*, pages 91–100. Springer, 2014.

[25] M. R. Catlett, J. Forest, J. M. Anderson, and D. Stewart. Empirical spectral model of surface pressure fluctuations beneath adverse pressure gradients. In *20th AIAA/CEAS Aeroacoustics Conference*, page 2910, 2014.

[26] D. Chase. The character of the turbulent wall pressure spectrum at subconvective wavenumbers and a suggested comprehensive model. *J. Sound Vib.*, 112(1):125–147, 1987.

[27] D. Chase. Fluctuating wall-shear stress and pressure at low streamwise wavenumbers in turbulent boundary-layer flow at low mach numbers. *J. Fluids Struct.*, 6(4):395–413, 1992.

[28] D. M. Chase. Modeling the wavevector-frequency spectrum of turbulent boundary layer wall pressure. *J. Sound Vib.*, 70(1):29–67, 1980.

[29] E. Ciappi, S. De Rosa, F. Franco, J.-L. Guyader, and S. A. Hambric. *Flinovia: Flow Induced Noise and Vibration Issues and Aspects-I.* Springer, 2015.

[30] E. Ciappi, S. De Rosa, F. Franco, J.-L. Guyader, S. A. Hambric, R. C. K. Leung, and A. D. Hanford. *Flinovia: Flow Induced Noise and Vibration Issues and Aspects-II.* Springer, 2019.

[31] E. Ciappi, S. De Rosa, F. Franco, S. A. Hambric, R. C. Leung, V. Clair, L. Maxit, and N. Totaro. *Flinovia–Flow Induced Noise and Vibration Issues and Aspects-III.* Springer, 2021.

[32] E. Ciappi, F. Magionesi, S. De Rosa, and F. Franco. Hydrodynamic and hydroelastic analyses of a plate excited by the turbulent boundary layer. *J. Fluids Struct.*, 25(2):321–342, 2009.

[33] K. M. Cipolla and W. L. Keith. Measurements of the wall pressure spectra on a full-scale experimental towed array. *Ocean Eng.*, 35(10):1052–1059, 2008.

[34] J. Cockburn and J. Robertson. Vibration response of spacecraft shrouds toin-flight fluctuating pressures. *J. Sound Vib.*, 33(4):399–425, 1974.

[35] J. A. Cockburn and A. C. Jolly. *Structural-acoustic response, noise transmission losses and interior noise levels of an aircraft fuselage excited by random pressure fields.* Air Force Flight Dynamics Laboratory, Air Force Systems Command, 1968.

[36] E. Cohen. *Étude de la pression pariétale et du bruit de couches limites turbulentes avec gradients de pression.* PhD thesis, Ecole nationale supérieure d'arts et métiers-ENSAM, 2015.

[37] G. Corcos. Resolution of pressure in turbulence. *J. Acoust. Soc. Am.*, 35(2):192–199, 1963.

[38] G. Corcos. The structure of the turbulent pressure field in boundary-layer flows. *J. Fluid Mech.*, 18(3):353–378, 1964.

[39] G. Corcos. The resolution of turbulent pressures at the wall of a boundary layer. *J. Sound Vib.*, 6(1):59–70, 1967.

[40] S. Crandall. Random vibration, new york, new york: The massachusetts institute of technology & john wiley & sons, 1958.

[41] D. Crighton, A. Dowling, J. F. Williams, M. Heckl, and F. Leppington. Modern methods in analytical acoustics. *J. Fluid Mech.*, 318(1):410–412, 1996.

[42] S. Damani, E. Braaten, M. Szoke, W. N. Alexander, W. J. Devenport, N. A. Balantrapu, B. P. Pearce, T. A. Starkey, A. P. Hibbins, and J. R. Sambles. Resonator-based pressure sensor for wall pressure. In *28th AIAA/CEAS Aeroacoustics 2022 Conference*, page 2956, 2022.

[43] S. Damani, H. Butt, J. T. Banks, S. Srivastava, N. A. Balantrapu, T. Lowe, and W. J. Devenport. Low-wavenumber wall pressure measurements in zero-pressure gradient boundary layer flow. In *AIAA SCITECH 2022 Forum*, page 1795, 2022.

[44] S. Damani, H. Butt, E. Totten, S. Chaware, B. Sharma, W. J. Devenport, and T. Lowe. The characteristics of sub-convective wall pressure fluctuations in a turbulent boundary layer. In *AIAA SCITECH 2024 Forum*, page 1904, 2024.

[45] H. G. Davies. Sound from turbulent-boundary-layer-excited panels. *J. Acoust. Soc. Am.*, 49(3B):878–889, 1971.

[46] S. De Rosa and F. Franco. Exact and numerical responses of a plate under a turbulent boundary layer excitation. *J. Fluids Struct.*, 24(2):212–230, 2008.

[47] R. DeJong and R. Tubergen. A comprehensive model for the turbulent boundary layer pressure spectrum. In *INTER-NOISE and NOISE-CON Congress and Conference Proceedings*, volume 259, pages 5064–5074. Institute of Noise Control Engineering, 2019.

[48] J. Dimitrijević. Complex mode indicator function to find repeated roots or closely coupled modes. *Sci.-Tech. Rev*, 55(3-4):50–58, 2005.

[49] R. Dougherty. Extensions of damas and benefits and limitations of deconvolution in beamforming. In *11th AIAA/CEAS aeroacoustics conference*, page 2961, 2005.

[50] I. Dyer. Response of plates to a decaying and convecting random pressure field. *J. Acoust. Soc. Am.*, 31(7):922–928, 1959.

[51] B. Efimtsov. Characteristics of the field of turbulent wall pressure-fluctuations at large reynolds-numbers. *Sov. phys. Acoust.*, 28(4):289–292, 1982.

[52] B. Efimtsov. Similarity criteria for the spectra of wall pressure fluctuations in a turbulent boundary layer. *Sov. phys. Acoust.*, 30:33–35, 1984.

[53] K. Ehrenfried and L. Koop. Pressure fluctuations beneath a compressible turbulent boundary layer. In *14th AIAA/CEAS Aeroacoustics Conference (29th AIAA Aeroacoustics Conference)*, page 2800, 2008.

[54] I. Elishakoff. *Probabilistic methods in the theory of structures: strength of materials, random vibrations, and random buckling.* World Scientific, 2017.

[55] H. W. Engl, M. Hanke, and A. Neubauer. *Regularization of inverse problems*, volume 375. Springer Science & Business Media, 1996.

[56] N. D. Evans, D. E. Capone, and W. K. Bonness. Low-wavenumber turbulent boundary layer wall-pressure measurements from vibration data over smooth and rough surfaces in pipe flow. *J. Sound Vib.*, 332(14):3463–3473, 2013.

[57] D. J. Ewins. *Modal testing: theory, practice and application.* John Wiley & Sons, 2009.

[58] F. J. Fahy. *Sound and structural vibration: radiation, transmission and response.* Elsevier, 2007.

[59] T. M. Farabee and F. E. Geib. Measurement of boundary layer pressure fields with an array of pressure transducers in a subsonic flow. *ICIASF'75*, pages 311–319, 1975.

[60] A. Fasana. Modal parameters estimation in the z-domain. *Mech. Syst. Signal Process.*, 23(1):217–225, 2009.

[61] S. Finnveden, F. Birgersson, U. Ross, and T. Kremer. A model of wall pressure correlation for prediction of turbulence-induced vibration. *J. Fluids Struct.*, 20(8):1127–1143, 2005.

[62] F. Geib and T. Farabee. Measurement of boundary layer pressure fluctuations at low wavenumber on smooth and rough walls. *David Taylor Naval Ship R & D Center Report*, (84-05), 1985.

[63] A. Gelman, J. B. Carlin, H. S. Stern, and D. B. Rubin. *Bayesian data analysis.* Chapman and Hall/CRC, 1995.

[64] F. Girosi, M. Jones, and T. Poggio. Regularization theory and neural networks architectures. *Neural Comput.*, 7(2):219–269, 1995.

[65] X. Gloerfelt and J. Berland. Direct computation of turbulent boundary layer noise. In *15th AIAA/CEAS Aeroacoustics Conference (30th AIAA Aeroacoustics Conference)*, page 3401, 2009.

[66] G. H. Golub, M. Heath, and G. Wahba. Generalized cross-validation as a method for choosing a good ridge parameter. *Technometrics*, 21(2):215–223, 1979.

[67] G. H. Golub and C. F. Van Loan. *Matrix computations.* JHU press, 2013.

[68] P. Goodwin. An in-flight supersonic tbl surface pressure fluctuation model. *Contract No. NAS1-20013, Boeing Document,(D6-81571)*, 1994.

[69] M. Goody. Empirical spectral model of surface pressure fluctuations. *AIAA J.*, 42(9):1788–1794, 2004.

[70] W. Graham. Boundary layer induced noise in aircraft, Part I: The flat plate model. *J. Sound Vib.*, 192(1):101–120, 1996.

[71] W. Graham. A comparison of models for the wavenumber–frequency spectrum of turbulent boundary layer pressures. *J. Sound Vib.*, 206(4):541–565, 1997.

[72] J.-L. Guyader. *Vibration in continuous media.* John Wiley & Sons, 2013.

[73] S. Hambric and P. Lysak. Validation of a simple empirical model for calculating the vibration of flat plates excited by incompressible homogeneous turbulent boundary layer flow. In *International Conference on Flow Induced Noise and Vibration Issues and Aspects*, pages 61–85. Springer, 2019.

[74] S. A. Hambric, Y. F. Hwang, and W. K. Bonness. Vibrations of plates with clamped and free edges excited by low-speed turbulent boundary layer flow. *J. Fluids Struct.*, 19(1):93–110, 2004.

[75] P. C. Hansen. The l-curve and its use in the numerical treatment of inverse problems. 1999.

[76] P. C. Hansen. Regularization tools version 4.0 for Matlab 7.3. *Numerical algorithms*, 46(2):189–194, 2007.

[77] P. C. Hansen, T. K. Jensen, and G. Rodriguez. An adaptive pruning algorithm for the discrete L-curve criterion. *J. Comput. Appl. Math.*, 198(2):483–492, 2007.

[78] T. Hastie, R. Tibshirani, J. H. Friedman, and J. H. Friedman. *The elements of statistical learning: data mining, inference, and prediction*, volume 2. Springer, 2009.

[79] R. A. Haubrich. Array design. *Bull. Seismol. Soc. Am.*, 58(3):977–991, 1968.

[80] S. Haxter, J. Brouwer, J. Sesterhenn, and C. Spehr. Obtaining phase velocity of turbulent boundary layer pressure fluctuations at high subsonic Mach number from wind tunnel data affected by strong background noise. *J. Sound Vib.*, 402:85–103, 2017.

[81] S. Haxter and C. Spehr. Infinite beamforming: wavenumber decomposition of surface pressure fluctuations. In *Proceedings of the 5th Berlin Beamforming Conference*, pages 1–10, 2014.

[82] S. Haxter and C. Spehr. Wavenumber characterization of surface pressure fluctuations on the fuselage during cruise flight. In *Flinovia—Flow Induced Noise and Vibration Issues and Aspects-III*, pages 157–180. Springer, 2021.

[83] H. Herlufsen. Modal analysis using multi-reference and multiple-input multiple-output techniques. *Brüel & Kjær, Application Note*, 16, 2004.

[84] M. S. Howe. *Acoustics of fluid-structure interactions.* Cambridge university press, 1998.

[85] M. S. Howe. *Acoustics of fluid-structure interactions.* Cambridge university press, 2008.

[86] N. Hu. Sensor-size-related attenuation correction of wall pressure spectra measurements. *Phys. Fluids.*, 34(6), 2022.

[87] N. Hu and M. Herr. Characteristics of wall pressure fluctuations for a flat plate turbulent boundary layer with pressure gradients. In *22nd AIAA/CEAS aeroacoustics conference*, page 2749, 2016.

[88] N. Hu, N. Reiche, and R. Ewert. Simulation of turbulent boundary layer wall pressure fluctuations via poisson equation and synthetic turbulence. *J. Fluid Mech.*, 826:421–454, 2017.

[89] F. Hugues. *Modelling the vibrations generated by turbulent flows in ducts.* PhD thesis, Université de Technologie de Compiègne, 2018.

[90] R. Huňady and M. Hagara. A new procedure of modal parameter estimation for high-speed digital image correlation. *Mech. Syst. Signal Process.*, 93:66–79, 2017.

[91] Y. Hwang, W. Bonness, and S. Hambric. On modeling structural excitations by low speed turbulent boundary layer flows. Technical report, PENNSYLVANIA STATE UNIV STATE COLLEGE APPLIED RESEARCH LAB, 2003.

[92] Y. Hwang, W. K. Bonness, and S. A. Hambric. Comparison of semi-empirical models for turbulent boundary layer wall pressure spectra. *J. Sound Vib.*, 319(1-2):199–217, 2009.

[93] Y. Hwang and F. Geib. Estimation of the wavevector-frequency spectrum of turbulent boundary layer wall pressure by multiple linear regression. *Transactions of the American Society of Mechanical Engineers, Journal of Vibration, Acoustics, Stress and Reliability in Design.*, 106:334–342, 1984.

[94] Y. Hwang and G. Maidanik. A wavenumber analysis of the coupling of a structural mode and flow turbulence. *J. Sound Vib.*, 142(1):135–152, 1990.

[95] J. James and E. A. Skelton. *Theoretical acoustics of underwater structures.* World Scientific, 1997.

[96] P. Jameson. Measurement of low wavenumber component of turbulent boundary layer wall pressure spectrum. *Rap. tech. BBN Rep*, (1937), 1970.

[97] P. Jameson. Measurement of the low-wavenumber component of turbulent boundary layer pressure spectral density. 1975.

[98] L. M. Jiji and L. M. Jiji. *Heat convection.* Springer, 2006.

[99] M. Junger and D. Feit. Sound. structures and their interaction, mit press, cambridge, ma, 1986.

[100] M. Karimi, P. Croaker, L. Maxit, O. Robin, A. Skvortsov, S. Marburg, and N. Kessissoglou. A hybrid numerical approach to predict the vibrational responses of panels excited by a turbulent boundary layer. *J. Fluids Struct.*, 92:102814, 2020.

[101] M. Karimi, P. Croaker, A. Skvortsov, D. Moreau, and N. Kessissoglou. Numerical prediction of turbulent boundary layer noise from a sharp-edged flat plate. *Int. J. Numer.*, 90(10):522–543, 2019.

[102] M. Karimi and L. Maxit. Acoustic source localisation using vibroacoustic beamforming. *Mech. Syst. Signal Process.*, 199:110454, 2023.

[103] M. Karimi, L. Maxit, P. Croaker, O. Robin, A. Skvortsov, S. Marburg, N. Atalla, and N. Kessissoglou. Analytical and numerical prediction of acoustic radiation from a panel under turbulent boundary layer excitation. *J. Sound Vib.*, 479:115372, 2020.

[104] W. L. Keith, D. Hurdis, and B. Abraham. A comparison of turbulent boundary layer wall-pressure spectra. *J. Fluids Eng.*, 114:338–347, 1992.

[105] Y. Kim and A. George. Trailing-edge noise from hovering rotors. *AIAA J.*, 20(9):1167–1174, 1982.

[106] A. Klabes. Validation of a simulation model for the "statistic energyanalysis" (sea) of the airbus a320 for different flight parameters. *Airbus Operations GmbH & German Aerospace Center (DLR)*, 2012.

[107] A. Klabes. *Aircraft fuselage vibration excitation by turbulent boundary layer flow in cruise*. PhD thesis, Deutsches Institut für Luft-und Raumfahrt eV, 2017.

[108] A. Klabes, M. Herr, and S. Callsen. Fuselage excitation during cruise flight conditions: a new cfd based pressure point spectra model. In *INTER-NOISE and NOISE-CON Congress and Conference Proceedings*, volume 253, pages 1018–1029. Institute of Noise Control Engineering, 2016.

[109] P. S. Klebanoff. Characteristics of turbulence in boundary layer with zero pressure gradient. Technical report, 1955.

[110] S. H. Ko. The flush-mounted hydrophone array response to a modified corcos turbulent wall pressure spectrum (analytical approach). *J. Acoust. Soc. Am.*, 96(2):1198–1201, 1994.

[111] A. Laganelli and H. Wolfe. Prediction of fluctuating pressure in attached and separated turbulent boundary-layer flow. *J. Aircr.*, 30(6):962–970, 1993.

[112] J. Laufer. The structure of turbulence in fully developed pipe flow. Technical report, 1954.

[113] Q. Leclere, A. Dinsenmeyer, E. Salze, and J. Antoni. A comparison between different wall pressure measurement devices for the separation and analysis of tbl and acoustic contributions. In *Flinovia—Flow Induced Noise and Vibration Issues and Aspects-III*, pages 181–206. Springer, 2021.

[114] D. Lecoq, C. Pezerat, J.-H. Thomas, and W. Bi. Extraction of the acoustic component of a turbulent flow exciting a plate by inverting the vibration problem. *J. Sound Vib.*, 333(12):2505–2519, 2014.

[115] Y.-K. M. Lin. Probabilistic theory of structural dynamics. 1967.

[116] B. Liu, L. Feng, A. Nilsson, and M. Aversano. Predicted and measured plate velocities induced by turbulent boundary layers. *J. Sound Vib.*, 331(24):5309–5325, 2012.

[117] M. V. Lowson. *Prediction of boundary layer pressure fluctuations.* Air Force Flight Dynamics Laboratory, Air Force Systems Command, United . . . , 1968.

[118] P. D. Lysak, W. K. Bonness, and J. B. Fahnline. Low wavenumber models for turbulent boundary layer excitation of structures. In *Flinovia II*, pages 3–15. Springer, 2019.

[119] L. Maestrello. Measurement and analysis of the response field of turbulent boundary layer excited panels. *J. Sound Vib.*, 2(3):270–292, 1965.

[120] L. Maestrello. Use of turbulent model to calculate the vibration and radiation responses of a panel, with practical suggestions for reducing sound level. *J. Sound Vib.*, 5(3):407–448, 1967.

[121] G. Maidanik. Response of ribbed panels to reverberant acoustic fields. *J. Acoust. Soc. Am.*, 34(6):809–826, 1962.

[122] G. Maidanik. Flush-mounted pressure transducer systems as spatial and spectral filters. *J. Acoust. Soc. Am.*, 42(5):1017–1024, 1967.

[123] E. Manoha. The wavenumber-frequency spectrum of the wall pressure fluctuations beneath a turbulent boundary layer. In *Aeroacoustics Conference*, page 1758, 1996.

[124] C. Marchetto, L. Maxit, O. Robin, and A. Berry. Vibroacoustic response of panels under diffuse acoustic field excitation from sensitivity functions and reciprocity principles. *J. Acoust. Soc. Am.*, 141(6):4508–4521, 2017.

[125] C. Marchetto, L. Maxit, O. Robin, and A. Berry. Experimental prediction of the vibration response of panels under a turbulent boundary layer excitation from sensitivity functions. *J. Acoust. Soc. Am.*, 143(5):2954–2964, 2018.

[126] N. Martin and P. Leehey. Low wavenumber wall pressure measurements using a rectangular membrane as a spatial filter. *J. Sound Vib.*, 52(1):95–120, 1977.

[127] C. Maury, P. Gardonio, and S. Elliott. A wavenumber approach to modelling the response of a randomly excited panel, part i: general theory. *J. Sound Vib.*, 252(1):83–113, 2002.

[128] C. Maury, P. Gardonio, and S. Elliott. A wavenumber approach to modelling the response of a randomly excited panel, part ii: Application to aircraft panels excited by a turbulent boundary layer. *J. Sound Vib.*, 252(1):115–139, 2002.

[129] L. Maxit. Simulation of the pressure field beneath a turbulent boundary layer using realizations of uncorrelated wall plane waves. *J. Acoust. Soc. Am.*, 140(2):1268–1285, 2016.

[130] D. Mazzoni. An efficient approximation for the vibro-acoustic response of a turbulent boundary layer excited panel. *J. Sound Vib.*, 264(4):951–971, 2003.

[131] R. H. Mellen. On modeling convective turbulence. *J. Acoust. Soc. Am.*, 88(6):2891–2893, 1990.

[132] R. Merino-Martínez, P. Sijtsma, M. Snellen, T. Ahlefeldt, J. Antoni, C. J. Bahr, D. Blacodon, D. Ernst, A. Finez, S. Funke, et al. A review of acoustic imaging methods using phased microphone arrays: Part of the "aircraft noise generation and assessment" special issue. *CEAS Aeronaut. J.*, 10:197–230, 2019.

[133] T. S. Miller. *Turbulent boundary layer models for acoustic analysis.* PhD thesis, Department of Aerospace Engineering and the faculty of the Graduate School of Wichita State University, 2011.

[134] T. S. Miller, J. M. Gallman, and M. J. Moeller. Review of turbulent boundary layer models for acoustic analysis. *J. Aircr.*, 49(6):1739–1754, 2012.

[135] V. A. Morozov. *Methods for solving incorrectly posed problems.* Springer Science & Business Media, 2012.

[136] D. E. Newland. *An introduction to random vibrations, spectral & wavelet analysis.* Courier Corporation, 2012.

[137] J. Nocedal and S. J. Wright. *Numerical optimization.* Springer, 1999.

[138] A. V. Oppenheim, R. W. Schafer, and J. R. Buck. *Discrete-Time Signal Processing.* Prentice-hall Englewood Cliffs, second edition, 1999.

[139] T. L. Paez. The history of random vibrations through 1958. *Mech. Syst. Signal Process.*, 20(8):1783–1818, 2006.

[140] R. L. Panton and G. Robert. The wavenumber-phase velocity representation for the turbulent wall-pressure spectrum. *J. Fluids Eng.*, 116:477–483, 09 1994.

[141] F. Pápai and I. Szűcs. The role of singular values of measured frequency response function matrix in modal damping estimation (part i: Theory). *Tehnicki Vjesnik*, 22(3):729–734, 2015.

[142] L. Peltier and S. Hambric. Estimating turbulent-boundary-layer wall-pressure spectra from cfd rans solutions. *J. Fluids Struct.*, 23(6):920–937, 2007.

[143] A. W. Phillips, R. J. Allemang, and W. A. Fladung. The complex mode indicator function (cmif) as a parameter estimation method. In *Proceedings of the 16th International Modal Analysis Conference*, volume 3243, page 705, 1998.

[144] S. B. Pope. Turbulent flows. *Meas. Sci. Technol.*, 12(11):2020–2021, 2001.

[145] A. Powell. On the fatigue failure of structures due to vibrations excited by random pressure fields. *J. Acoust. Soc. Am.*, 30(12):1130–1135, 1958.

[146] L. Prandtl. Uber flussigkeitsbewegung bei sehr kleiner reibung. *Verhandl. 3rd Int. Math. Kongr. Heidelberg (1904), Leipzig*, 1905.

[147] S. L. Prigent, É. Salze, and C. Bailly. Deconvolution of wave-number-frequency spectra of wall pressure fluctuations. *AIAA J.*, 58(1):164–173, 2020.

[148] R. Rackl and A. Weston. Modeling of turbulent boundary layer surface pressure fluctuation auto and cross spectra-verification and adjustments based on tu-144ll data. Technical report, 2005.

[149] S. S. Rao. *Vibration of continuous systems.* John Wiley & Sons, 2019.

[150] O. Reynolds. Xxix. an experimental investigation of the circumstances which determine whether the motion of water shall be direct or sinuous, and of the law of resistance in parallel channels. *Phil. Trans. R. Soc.*, (174):935–982, 1883.

[151] H. Ribner. Response of a flexible panel to turbulent flow: Running-wave versus modal-density analysis. *J. Acoust. Soc. Am.*, 40(3):721–726, 1966.

[152] M. H. Richardson and D. L. Formenti. Parameter estimation from frequency response measurements using rational fraction polynomials. In *Proceedings of the 1st international modal analysis conference*, volume 1, pages 167–186. Citeseer, 1982.

[153] J. Robertson. Prediction of in flight fluctuating pressure environments including protuberance induced flow. Technical report, 1971.

[154] G. Rodriguez and D. Theis. An algorithm for estimating the optimal regularization parameter by the L-curve. *Rendiconti di Mat. e delle Sue Appl.*, 25:69–84, 2005.

[155] Y. Rozenberg. *Modélisation analytique du bruit aérodynamique à large bande des machines tournantes: utilisation de calculs moyennés de mécanique des fluides.* PhD thesis, Ecole Centrale de Lyon, 2007.

[156] É. Salze, C. Bailly, O. Marsden, E. Jondeau, and D. Juvé. An experimental characterisation of wall pressure wavevector-frequency spectra in the presence of pressure gradients. In *20th AIAA/CEAS Aeroacoustics Conference*, page 2909, 2014.

[157] E. Sarradj. Three-dimensional acoustic source mapping with different beamforming steering vector formulations. *Adv. Acoust. Vib.*, 2012, 2012.

[158] C. F. Schram and N. Van de Wyer. An optimized microphone array for the measurement of turbulent boundary layer wall pressure wavenumber-frequency spectra. In *2018 AIAA/CEAS Aeroacoustics Conference*, page 2968, 2018.

[159] C. Shih, Y. Tsuei, R. Allemang, and D. Brown. Complex mode indication function and its applications to spatial domain parameter estimation. *Mech. Syst. Signal Process*, 2(4):367–377, 1988.

[160] R. L. Simpson, M. Ghodbane, and B. McGrath. Surface pressure fluctuations in a separating turbulent boundary layer. *J. Fluid Mech.*, 177:167–186, 1987.

[161] A. Smol'yakov. Calculation of the spectra of pseudosound wall-pressure fluctuations in turbulent boundary layers. *Acoust. Phys.*, 46(3):342–347, 2000.

[162] A. Smol'Yakov. A new model for the cross spectrum and wavenumber-frequency spectrum of turbulent pressure fluctuations in a boundary layer. *Acoust. Phys.*, 52:331–337, 2006.

[163] P. R. Spalart. *Direct Simulation of a Turbulent Boundary Layer Up to R (sub)(theta).* 1986.

[164] W. A. Strawderman. Turbulence-induced plate vibrations: an evaluation of finite- and infinite-plate models. *J. Acoust. Soc. Am.*, 46(5B):1294–1307, 1969.

[165] A. Townsend. On the fine-scale structure of turbulence. *Proc. R. soc. Lond. Ser. A-Contain. Pap. Math. Phys.*, 208(1095):534–542, 1951.

[166] J. R. Underbrink. Aeroacoustic phased array testing in low speed wind tunnels. In *Aeroacoustic measurements*, pages 98–217. Springer, 2002.

[167] S. A. V, V. M. Tkachenko, and J. S. Wood. Model of a field of pseudosonic turbulent wall pressures and experimental data. *Sov. phys. Acoust.*, 37(6):627–631, 1991.

[168] P. H. White. Transduction of boundary-layer noise by a rectangular panel. *J. Acoust. Soc. Am.*, 40(6):1354–1362, 1966.

[169] J. F. Wilby. *The response of simple panels to turbulent boundary layer excitation.* Air Force Flight Dynamics Laboratory, Research and Technology Division, Air . . . , 1967.

[170] E. G. Williams. *Fourier acoustics: sound radiation and nearfield acoustical holography.* Academic press, 1999.

[171] J. F. Williams. Boundary-layer pressures and the corcos model: a development to incorporate low-wavenumber constraints. *J. Fluid Mech.*, 125:9–25, 1982.

[172] W. Willmarth and F. Roos. Resolution and structure of the wall pressure field beneath a turbulent boundary layer. *J. Fluid Mech.*, 22(1):81–94, 1965.

[173] W. W. Willmarth and C. E. Wooldridge. Measurements of the fluctuating pressure at the wall beneath a thick turbulent boundary layer. *J. Fluid Mech.*, 14(2):187–210, 1962.

[174] J. M. Witting. A spectral model of pressure fluctuations at a rigid wall bounding an incompressible fluid, based on turbulent structures in the boundary layer. *Noise Control Eng. J.*, 26(1):28–43, 1986.

[175] Z. Xiaojian, A. Bangcheng, L. Ziqiang, and L. Dun. A scaling procedure for panel vibro-acoustic response induced by turbulent boundary layer. *J. Sound Vib.*, 380:165–179, 2016.

[176] J. Yu and M. Joshi. On sound radiation from the trailing edge of an isolated airfoil in a uniform flow. In *5th Aeroacoustics Conference*, page 603, 1979.

[177] X. Zhao, M. Guo, and J. Lei. Updating of wavenumber-frequency spectrum models by a phased array measurement. *Aerosp. Sci. Technol.*, 107:106273, 2020.

[178] X. Zhao and J. Lei. Improved technique for evaluation of wall pressure fluctuations from turbulent boundary layer. *AIAA J.*, 58(8):3320–3331, 2020.

[179] X. Zhao and L. Zhao. Wall pressure fluctuations beneath hypersonic boundary layer over plate. *AIAA J.*, 59(5):1682–1691, 2021.